The sources and activity of ice-nucleating particles in the high latitudes

SARAH LOUISE BARR

Submitted in accordance with the requirements for the degree of
Doctor of Philosophy

The University of Leeds
School of Earth and Environment

JULY 2023

Declaration

The candidate confirms that the work submitted is their own, except where work which has formed part of jointly authored publications has been included. The contribution of the candidate and the other authors to this work has been explicitly indicated below. The candidate confirms that appropriate credit has been given within the thesis where reference has been made to the work of others.

Barr, S. L., Wyld, B., McQuaid J. B., Neely III, R. R., Murray, B. J. (2023). Southern Alaska as a source of atmospheric mineral dust and ice-nucleating particles. Published in *Science Advances* (2023). The contents of Chapter 2 are from this jointly authored publication. Author contributions are as follows: SLB (the candidate) and BJM conceived the idea and planned the study. SLB planned the fieldwork with support from JBM, BJM and BW. SLB and BW carried out the fieldwork. SLB carried out the laboratory analysis, FLEXPART modelling and data analysis. SLB wrote the initial manuscript with input from BJM. All authors discussed the results and contributed to the manuscript.

Abstract

Ice-nucleating particles play an important role in the climate system by influencing cloud radiative properties, cloud lifetime and precipitation. Understanding the sources and concentration of INPs in the atmosphere is therefore of crucial importance to accurately model clouds in the atmosphere. This is particularly pronounced in the mid to high latitudes where mixed-phase clouds, which are highly sensitive to the presence of INPs, are common and play a key role in modulating the effects of climate change through cloud-climate feedbacks. However, the sources and characteristics of INPs in the high latitudes, and their spatial and temporal variation in the atmosphere, are still not well known. This thesis applies a range of new and existing techniques to advance our understanding of the sources and concentrations of INPs, and their impact on cloud microphysical properties. In Chapter 2, I use in-situ aerosol sampling and laboratory analysis to characterise the ice-nucleating ability of glacial dust emitted from the Copper River, Alaska. The results show that this dust nucleates ice at temperatures relevant for mixed-phase clouds and is considerably more active than low-latitude desert dust due to the presence of a biogenic component that enhances the ice-nucleating activity. I then use particle dispersion modelling to show that dust can reach regions of the atmosphere where it could trigger cloud glaciation in concentrations where it would dominate over low-latitude INP sources. In Chapter 3, I test and apply a method to retrieve ice crystal number concentration from remote sensing observations to data from Summit Station, Greenland, leading to the first observations of ice crystal number concentration in clouds over the Greenland ice sheet. I combine this data with an existing dataset of INP concentrations to identify ice-formation mechanisms in these clouds and show that there is a secondary ice production process active between -10 and -18°C. Finally, in Chapter 4, I use aircraft sampling and laboratory analysis to determine INP concentrations in the northeast Atlantic. I combine this with back trajectory analysis to determine the potential sources of sampled INPs and show that the sources of INPs can vary over small spatial scales and that INP concentrations in clouds can be enhanced by contact with land.

Acknowledgements

Finishing this PhD would not have been possible without the people around me who have provided support in so many different ways. Firstly, I would like to thank my supervisors all of whom I have learnt a great deal from. I'd like to thank Ben Murray for providing me with the opportunity to do a PhD that has taken me to so many great places and for the guidance, insightful discussions and patience along the way; Ryan Neely for being willing to join the team halfway through my PhD, for bringing so much enthusiasm and for giving me the chance to tick off my long-term dream of digging a hole in the Greenland Ice Sheet; and Jim McQuaid for fieldwork support and many useful chats over coffee.

I was lucky to be part of both the ice nucleation and the remote sensing research groups in Leeds, both of which have been an endless source of help, inspiration and support. I am grateful to everyone I have worked with over the years, but I would particularly like to thank Beth Wyld for her help with fieldwork and countless discussions about dust, and Mark Tarn for his advice and friendship in the face of various unexpected situations.

A special thank you must go to Ruza Ivanovic who offered her support during a particularly difficult time. Her advice helped me get back on track and, more importantly, to get to a point where I was enjoying myself again and I am incredibly grateful for that. And to Zoe Cooke, my mentor in student disability services, who provided invaluable advice during our weekly meetings over the final 1.5 years of my PhD.

I would also like to thank Heather Guy, who has filled many roles over the past 12 years including study buddy, housemate, colleague, and covid bubble-mate, but most of all a friend who I can trust to always provide good advice, about science and about life, and even better adventures. I'm glad that skipping our undergraduate physics workshops every week in favour of eating cupcakes didn't cause too much harm in the end.

Getting to know my fellow ICAS PhD students has been one of the greatest outcomes of my PhD and their friendship has been invaluable. I'm incredibly proud to be able to say thank you to Dr Suzie Robinson, Dr Rachel Sansom, Dr Ruth Price, Dr Will Dow, Dr Heather Guy and Dr Joe Gallear. Special thanks to Ruth for brightening my days in a multitude of ways, but mostly by appearing at my office door approximately every 20 minutes for a coffee break. And to Rachel for her unwavering support since day one, including literally feeding me in the final push to finish my thesis.

My friends in Leeds and around the world have kept me going through it all. Thank you to Sophie for making me go swimming even though I (sort of) hate it, our friendship started in a lake but has progressed to a lot more than that (and to dry land, thankfully) and my life in Leeds is much

brighter for it. To Giulia, who kick-started my academic career and became a great friend in the process, for the Skype calls, the visits and for always sharing the love of mountains, cinnamon buns and Paolo Nutini. To Shannon, for always knowing the right question to ask, the right song to send and the right time to say ‘what’s the worst that could happen’. To Nel, for encouraging me from afar, for life-changing pinky promises and for not flinching when I announced with 6 days’ notice that I was coming to Canada. And to Hannah for a lot of coffee and a lot of love.

The biggest thank you of all goes to my family, without whom I could never have done this. Chris and Jo, your wedding (in 3 days’ time at the time of writing) has provided excellent motivation to finish my thesis, thanks for that and for your support along the way. Mum and Dad, you have provided me with everything I need to succeed. Your encouragement and acceptance of my choices have allowed me to find my own way in life, but your advice and help have guided me and your love and support have got me back on track when I needed it. Thank you.

This PhD was funded by the Natural Environment Research Council and the UK Met Office (Grant no. NE/R006687/1). I would like to respectfully acknowledge that the fieldwork for Chapter 2 of this thesis took place on traditional territories of the Native Village of Eyak, home of the Eyak, Chugach Region, Tlingit, and Athabaskan peoples.

Contents

List of Figures

List of Tables

1

Introduction

1.1 Clouds in the climate system

Clouds play a key role in the climate system by influencing the distribution of energy and moisture in the atmosphere. They regulate the planet's energy balance by reflecting incoming shortwave radiation back to space and trapping outgoing longwave radiation (Hartmann, 1993; Arking, 1991). Clouds are also an essential component of the hydrological cycle, delivering fresh water from Earth's atmosphere to the surface through precipitation (Pruppacher and Klett, 2010). Understanding the complex interactions between clouds, radiation, and the hydrological cycle is crucial for accurately modelling both short-term weather patterns and long-term climate changes.

On a global scale, clouds have a net cooling effect; the cooling due to the shortwave cloud radiative effect is greater than warming due to the longwave cloud radiative effect (Boucher et al., 2013). However, there are regional differences in cloud-radiative forcing driven by variations in cloud type and location. The radiative effect of clouds depends on their physical and optical properties, which are strongly controlled by cloud phase. Low-level liquid clouds are optically thick and reflect incoming solar radiation and hence tend to have a cooling effect whereas high-altitude ice clouds trap outgoing longwave radiation and have a warming effect (Chen et al., 2000). The underlying Earth's surface also influences the radiative effect of clouds. For example, low-level clouds over oceans will have a significantly higher albedo than the surface below, and there will be a cooling effect when clouds are present (Klein and Hartmann, 1993). In contrast, in the polar regions where the surface already has a high albedo due to ice and snow and there is little incoming solar radiation for much of the year, the longwave effect dominates and clouds have a net warming effect (Curry et al., 1996; Shupe et al., 2004; Lawson and Gettelman, 2014; Izeboud et al., 2020).

The radiative effect of mixed-phase clouds, which contain both ice and liquid, is particularly complicated because the cloud development, lifetime and radiative properties are affected by the ratio of ice to liquid water (Sun and Shine, 1994). Liquid water has a higher albedo than ice and hence clouds with more liquid will reflect more incoming shortwave radiation and have a greater cooling effect than clouds with more ice, as illustrated in Fig. 1.1. This variability in the radiative effect of mixed-phase clouds is important in our changing climate. As temperatures rise and isotherms shift upwards, the amount of liquid water relative to ice in clouds will increase (Murray et al., 2021). These clouds with more liquid water will reflect more shortwave radiation than clouds with more ice. The replacement of ice with liquid water can also result in longer-lived clouds because liquid droplets tend to precipitate slower than ice crystals (Tan and Storelvmo, 2019). For clouds over dark surfaces (e.g. oceans), this has a cooling effect and results in a negative climate feedback known as cloud-phase feedback (Ceppi et al., 2017; Murray et al., 2021). However, in polar regions, a higher liquid cloud fraction may have a warming effect due to an increased longwave radiative effect (Tan and Storelvmo, 2019). The strength of the cloud-phase feedback depends on the amount of ice in clouds now and in a changing climate, hence it is becoming increasingly apparent that improving our understanding of ice formation in mixed-phase clouds is vital to reduce uncertainties in climate projections (Tan et al., 2016; Storelvmo et al., 2015; Ceppi et al., 2017; Murray et al., 2021), particularly in the high-latitudes. However, ice-related processes are often poorly represented in global climate models (GCMs) due to the complexities of ice formation, which is influenced by physical processes occurring at different scales, and uncertainties associated with the interactions between ice and liquid water (Klein et al., 2009; Morrison et al., 2012; Sotiropoulou et al., 2016; Baumgardner et al., 2017b).

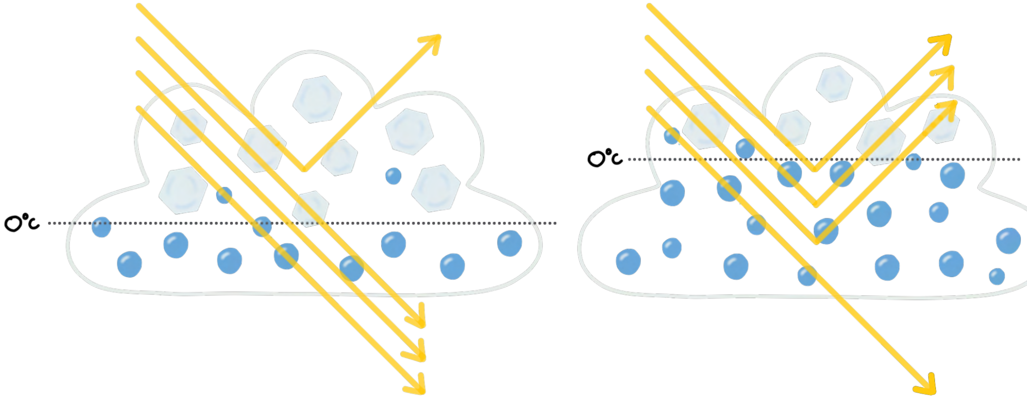

Fig. 1.1.: Schematic of the shortwave radiative effect of clouds with more ice crystals (left) or more water droplets (right). Yellow arrows represent shortwave radiation.

1.2 Aerosol-cloud interactions

Aerosols are tiny liquid or solid particles suspended in the atmosphere. These particles can be directly emitted (primary aerosol) or formed in the atmosphere by nucleation from the gas phase (secondary aerosol). Despite their diminutive size (0.001-10 μm), aerosols exert a significant influence on the global energy balance. They can have a direct effect by scattering and absorbing radiation in the atmosphere and an indirect effect through their interaction with clouds (Boucher et al., 2013). Specifically, aerosols can alter cloud properties by acting as cloud condensation nuclei (CCN) or ice-nucleating particles (INPs).

Homogeneous nucleation of a liquid droplet from the vapour phase would require supersaturations exceeding those typically found in the troposphere (Lohmann et al., 2016), hence CCN are essential in the formation of clouds and the number of CCN available for droplets to form onto (N_{CCN}) is of first-order importance for cloud droplet number concentration. This plays an important role in defining the radiative properties of clouds; higher N_{CCN} will lead to more, smaller droplets being formed which increases the albedo of the cloud, resulting in more shortwave radiation being reflected (Twomey Effect; Twomey (1977)). Droplet size can also affect cloud lifetime. On the one hand, smaller droplets reduce the collision-coalescence efficiency meaning it takes longer for droplets to grow large enough to precipitate and the lifetime of the cloud increases (Albrecht, 1989). Conversely, smaller droplets evaporate faster which reduces liquid water path through evaporation–entrainment feedbacks and results in an increase in cloud lifetime (Jiang et al., 2006; Small et al., 2009; Gryspeerdt et al., 2019). Ice in clouds often forms through the liquid-phase (De Boer et al., 2011) so modification of the droplet size distribution by CCN can also affect the number and size of ice crystals that form, with a resulting impact on the occurrence and amount of ice-phase precipitation (Cheng et al., 2010; Lance et al., 2011).

Once liquid droplets have formed, they can exist in a supercooled state down to temperatures as low as approximately -38°C (Vali, 1996), below this temperature homogeneous nucleation can occur. Between 0 and $\sim$-38°C heterogeneous nucleation can occur in the presence of INPs, a subset of atmospheric aerosols that reduce the energy barrier of ice formation by providing a surface for ice to form on to (Pruppacher and Klett, 2010; Kanji et al., 2017). The formation of ice crystals by nucleation from water vapour or supercooled liquid water is known as primary ice production (PIP). Much like CCN, the number concentration of INPs (N_{INP}) has important implications for cloud properties. N_{INP} affects the phase partitioning of the cloud by controlling how much liquid can transition to ice which modulates the radiative effect of the cloud, as outlined above. The influence of INPs is particularly pronounced in mixed-phase clouds where the formation of ice crystals results in a reduction of the liquid water content through the Wegener-Bergeron-Findeisen (WBF) process (Storelvmo and Tan, 2015). Ice has a lower saturation vapour pressure than liquid water droplets,and when the environment is supersaturated with respect to ice but sub-saturated with respect to water, ice grows rapidly by vapour deposition whereas the supercooled liquid cloud droplets evaporate. This is a key process in the formation of precipitation in cold clouds (Lau and Wu, 2003; Lohmann and Feichter, 2005; Storelvmo and Tan, 2015).

In high latitude regions, low-level mixed-phase clouds are common (Shupe and Intrieri, 2004; Lawson and Gettelman, 2014; Cossich et al., 2021; Listowski et al., 2019), forming both over the snow and ice-covered poles and in the marine boundary layer as cold polar air is advected over relatively warm oceans. These clouds are highly sensitive to the presence of INPs. Under some conditions, Arctic low-level mixed-phase clouds can persist for many days (Shupe et al., 2005; Morrison et al., 2012) but even a relatively moderate increase in N_{INP} can trigger the complete glaciation of a cloud through the WBF process whereby the growth of ice at the expense of liquid water results in the dissipation of the cloud as all the liquid evaporates and the ice crystals grow large enough to precipitate (Jiang et al., 2000; Inoue et al., 2006). Similarly, the supercooled liquid water content of high-latitude marine boundary layer clouds can be significantly altered by INPs (Komurcu et al., 2014; Vergara-Temprado et al., 2018). It is clear that understanding the role of INPs is vital to accurately model high-latitude mixed-phase clouds and their role in the climate system.

1.3 Ice nucleation

Nucleation refers to the formation of a new phase from a metastable parent state. In the case of ice nucleation, this can occur by homogeneous nucleation where nucleation of ice occurs in supercooled liquid droplets below ~-38°C (Vali, 1996; Herbert et al., 2015) or by heterogeneous nucleation involving INPs. Heterogeneous ice nucleation can occur from either the liquid or vapour phase. Fig. 1.2 illustrates possible ice formation pathways in the atmosphere, including four main modes of heterogeneous ice nucleation (Vali et al., 2015):

- **Immersion freezing** occurs when an INP is already immersed in a cloud droplet that forms at warmer temperatures via activation of CCN. Freezing is initiated once the droplet cools to the characteristic freezing temperature of the INP present.

- **Condensation freezing** occurs at temperatures below 0°C but close to water saturation, under these conditions water can condense on the surface of an INP and then freeze. This is different to the immersion mode since freezing occurs within embryos of water that have formed on the surface of an INP but before CCN activation occurs.

- **Contact freezing** occurs when an INP collides with a liquid droplet that is supercooled to below the characteristic freezing temperature of the INP. Contact freezing can also occur 'inside out' where an INP touches the air-water interface from within the droplet (Durant and Shaw, 2005).

- **Deposition nucleation** occurs when ice nucleates from the vapour phase directly on to an INP. This is the only mechanism that occurs in the absence of liquid water and requires the environment to be supersaturated with respect to ice.

Whilst these definitions are relatively well established in the literature, studies have challenged the occurrence of deposition nucleation and have instead proposed that ice formation attributed to deposition nucleation occurs due to pore condensation and freezing (PCF) (Marcolli, 2014; Wagner et al., 2016; David et al., 2019). In addition, whether condensation freezing is truly different to deposition and immersion freezing modes is still under debate (Vali et al., 2015). Observations of mixed-phase clouds show that the presence of liquid droplets is a pre-requisite of the formation of ice (Ansmann et al., 2008; De Boer et al., 2011; Field et al., 2012; Westbrook and Illingworth, 2013) and hence deposition nucleation and condensation freezing are likely to be of second-order importance in mixed-phase clouds. In laboratory experiments, contact freezing has been shown to be more efficient than immersion freezing (Ladino Moreno et al., 2013; Hoffmann et al., 2013) however in the atmosphere contact freezing is limited by the collision efficiency of droplets and INPs which is unknown (Ladino Moreno et al., 2013; Niehaus et al., 2014). In the atmosphere, where INP concentrations are low and factors such as thermophoresis (forces on particles as a result of temperature gradients) come into play, the probability of collisions between INPs and droplets may be lower than in the laboratory (Ladino Moreno et al., 2013; Phillips et al., 2007). Hence, immersion freezing is widely thought to dominate primary ice production in mixed-phase clouds (Murray et al., 2012; De Boer et al., 2011; Westbrook and Illingworth, 2013).

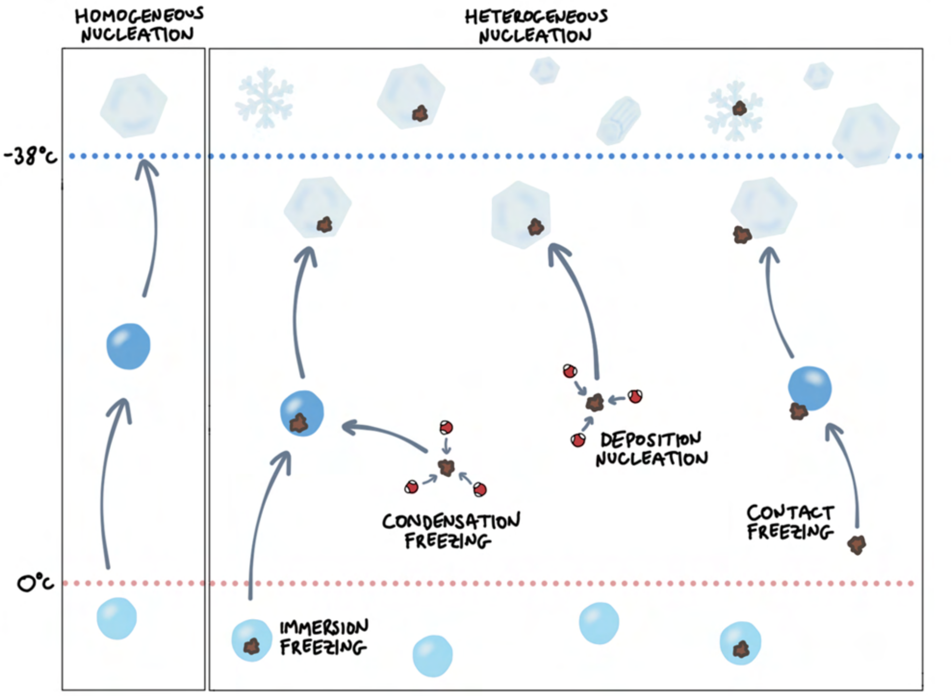

Fig. 1.2.: Schematic of primary ice production pathways. Pale blue droplets are >0°C, dark blue droplets are <0°C, brown particles represent INPs, red and white molecules represent water vapour.

1.3.1 Classical nucleation theory

Classical nucleation theory (CNT) is the most common mathematical framework to describe the formation of a new phase from a metastable parent state and has been applied in a wide range of fields since the early 20th century (Volmer and Weber, 1926), including the nucleation of ice from supercooled water or supersaturated water vapour. CNT assumes that nucleation is a stochastic (time-dependent) process that occurs as a result of random fluctuations in the system. CNT can be used to describe both homogenous and heterogeneous nucleation.

1.3.1.1 Homogenous classical nucleation theory

The nucleation process starts when small clusters of ice form spontaneously in the system. In order for these clusters to grow there is an energy barrier that must be overcome. The Gibbs free energy (ΔG) of forming a cluster considers the free energy of the new phase and that of the surrounding matrix by combining the energy associated with forming an interface, ΔG_s, and the energy associated with forming bonds in the bulk volume, ΔG_v:

$$\Delta G = \Delta G_v + \Delta G_s \tag{1.1}$$

which can also be written as:

$$\Delta G = -\frac{4\pi r^3}{3\nu} kT \ln S + 4\pi r^2 \gamma \tag{1.2}$$

where ν is the molecular volume of the condensed phase (ice in this case), k is the Boltzmann constant, T is temperature, S is saturation ratio and γ is the interfacial energy, or the energy required to form a new surface at the interface between liquid water and ice.

There is an energy cost associated with forming a liquid-ice interface hence ΔG_s is always positive. On the other hand, ΔG_v is negative due to the energy gain of cluster formation in a supercooled environment. As the radius of the cluster increases these opposing quantities compete, at smaller sizes ΔG_s dominates and the addition of molecules to the cluster is endothermic (requires energy) therefore crystal growth does not occur. However, at a certain critical radius, r_c, ΔG reaches a maximum. Above this radius growth is exothermic (releases energy) and hence crystal growth can occur (Fig. 1.3). At the critical radius $d\Delta G/dr = 0$ and so by setting the derivative of Equation 1.2 equal to 0, r_c can be written as:

$$r_c = \frac{2\gamma\nu}{kT \ln S} \tag{1.3}$$

and substituted in to Equation 1.2 to find the critical energy barrier of nucleation, ΔG^*:

$$\Delta G^* = \frac{16\pi\gamma^3\nu^2}{3(kT \ln S)^2} \tag{1.4}$$

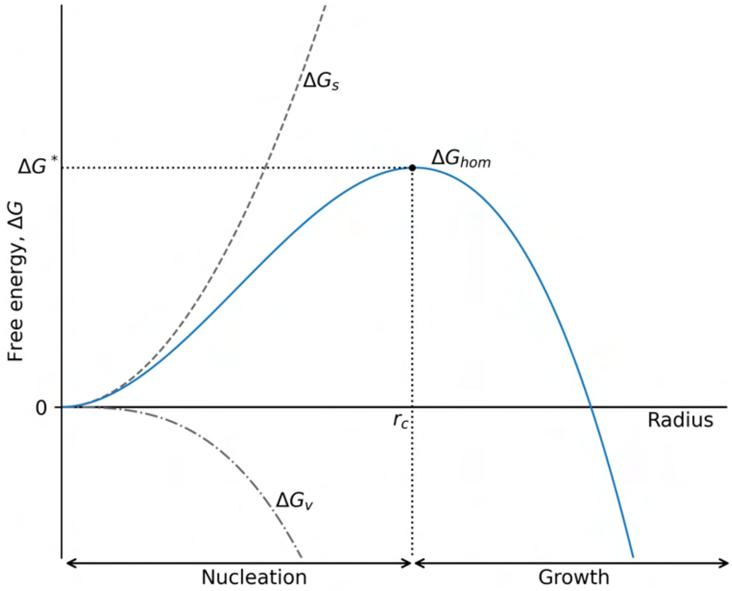

Fig. 1.3.: Schematic of the change in Gibbs free energy (ΔG) for homogeneous nucleation of an ice crystal from supercooled liquid water showing the volume term (ΔG_v), the surface term (ΔG_s), the critical energy barrier of nucleation (ΔG^*) and the critical radius (r_c).

The probability of nucleation can be described by the nucleation rate, J, which describes the number of nucleation events per unit volume per unit time and can be related to the critical Gibbs free energy:

$$J = A \exp\left(-\frac{\Delta G^*}{kT}\right) \tag{1.5}$$

where A is the pre-exponential factor.

1.3.1.2 Heterogeneous classical nucleation theory

In the presence of a suitable surface, such as an ice-nucleating particle, the energy barrier of nucleation can be reduced and heterogeneous nucleation occurs. In this case, ΔG^* is reduced by a factor between 0 and 1, leading to the critical Gibbs free energy of heterogeneous nucleation, ΔG^*_{het}:

$$\Delta G^*_{\text{het}} = \varphi \Delta G^* \tag{1.6}$$

where φ reflects the reduction in the critical energy barrier as a result of the surface and relates to the contact angle, θ, of a spherical ice nucleus on a surface:

$$\varphi = \frac{(2+\cos\theta)(1-\cos\theta)^2}{4} \tag{1.7}$$

As the contact angle decreases, φ tends to 0 and ΔG^*_{het} also decreases, hence the smaller the contact angle the greater the reduction in the energy barrier of nucleation, as illustrated in Fig. 1.4.

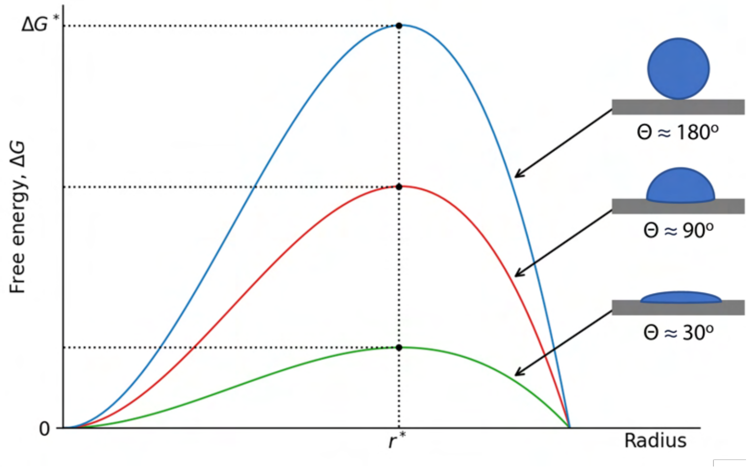

Fig. 1.4.: Schematic of the effect of contact angle on the change in Gibbs free energy (ΔG) for heterogeneous nucleation of ice from supercooled liquid water.

Equation 1.8 can be adapted to calculate the heterogeneous nucleation rate, J_{het}:

$$J_{\text{het}} = A_{\text{het}} \exp\left(-\frac{\Delta G^{*}\varphi}{kT}\right) \tag{1.8}$$

1.3.2 Singular description of heterogeneous nucleation

Whilst there has been some experimental evidence to support the stochastic nature of ice-nucleation (Murray et al., 2011; Niedermeier et al., 2011; Pinti et al., 2012; Welti et al., 2012), in immersion freezing the time dependence can be considered of secondary importance to environmental factors such as the type of INP and temperature (Vali, 1971, 2014). Ignoring the time dependence leads to a deterministic, rather than stochastic, description of heterogeneous nucleation that considers the individual characteristics of an INP rather than the average behaviour of a large number of INPs. Each INP will trigger nucleation under unique environmental conditions, and a characteristic freezing temperature can be used to specify the effectiveness of a particular particle at nucleating ice (Vali et al., 2015). The freezing behaviour of different INPs can be described quantitatively starting from an experimentally determined value of the fraction of frozen droplets at a given temperature, $f_{\text{ice}}(T)$:

$$f_{\text{ice}}(T) = \frac{n_{\text{ice}}(T)}{N_{\text{tot}}} \tag{1.9}$$

where n_{ice} is the number of frozen droplets at temperature T and N_{tot} is the total number of droplets. This can then be used to calculate the active site density, $K(T)$, that is the number of active sites per unit volume of sample, V, that have caused nucleation at a given temperature, T, as per Vali (1971):

$$K(T) = -\frac{\ln\left[1 - f_{\text{ice}}(T)\right]}{V} \tag{1.10}$$

Normalising $K(T)$ to the surface area of sampled aerosol, A, leads to the active site density per surface area of sample, $n_s(T)$:

$$n_s(T) = \frac{K(T)}{A} \tag{1.11}$$

Since $n_s(T)$ is normalised it is independent of the amount of aerosol sampled and can be used to quantitatively compare the activity of different materials.

1.4 What are INPs?

Primary aerosols are emitted into the atmosphere from natural sources such as sea spray, mineral dust, volcanoes and the biosphere. There are also anthropogenic sources of aerosols, including biomass burning and combustion of fossil fuels. However, not all aerosols can act as INPs and the concentration of INPs in the atmosphere is orders of magnitude smaller than the concentration of aerosols and CCN (Murray et al., 2021). The efficacy with which an aerosol particle may nucleate ice depends on its solubility, size, lattice structure, hydrophobicity and the presence of active sites (Pruppacher and Klett, 2010; Murray et al., 2012; Kanji et al., 2017). For insoluble particles, surface topography also plays an important role in defining the activity of the material because individual active sites can nucleate ice at characteristic temperatures (Vali, 2014; Holden et al., 2019). Determining the properties that make a 'good' INP is an ongoing area of research (Kanji et al., 2017) but several aerosol types are well-established as important INPs. These include mineral dust (DeMott et al., 2003; Chou et al., 2011; Atkinson et al., 2013; Harrison et al., 2022a; Tobo et al., 2019), volcanic ash (Isono et al., 1959; Durant et al., 2008; Maters et al., 2019), primary biogenic aerosols (Christner et al., 2008; Hoose et al., 2010; Després et al., 2012; O'Sullivan et al., 2015, 2018), fertile soil dusts (Hill et al., 2016; O'Sullivan et al., 2014; Roesch et al., 2021) and biogenic material from sea spray (Wilson et al., 2015; DeMott et al., 2016). The link between anthropogenic emissions and INPs remains under debate and depends on the aerosol in question. Some anthropogenic pollutants such as emissions from biomass burning (Prenni et al., 2012; McCluskey et al., 2014) and anthropogenically influenced organic aerosol (Tian et al., 2022) have been shown to act as INPs however, in other studies, a link between pollution and INPs has not been observed (Bi et al., 2019) and recent findings suggest that black carbon from combustion does not act as an INP under mixed-phase conditions (Mahrt et al., 2018; Adams et al., 2020; Kanji et al., 2020).

1.4.1 High-latitude sources of INPs

Despite our growing understanding of globally important sources of INPs, there is substantial temporal and spatial variability in INP concentrations in the atmosphere (Murray et al., 2012). This is driven by proximity to aerosol sources and environmental conditions (e.g. temperature). INP concentrations are also affected by atmospheric processes such as dilution of air during transport and removal of aerosol by deposition (Welti et al., 2020). The higher latitudes are remote from many major low-latitude aerosol sources meaning the concentration of low-latitude aerosols, such as dust from deserts in Africa and Asia, is reduced (Vergara-Temprado et al., 2017) and local aerosol sources may be more important (Groot Zwaaftink et al., 2016; Shi et al., 2022) for aerosol-cloud interactions. The remoteness of these environments means that making observations is challenging and there is limited data regarding INP concentrations in both the northern and southern high-latitudes. As a result, our knowledge of the sources, distribution and seasonal cycles of INPs in these regions is limited.

Many previous studies have made relatively short-term observations that have not been able to capture temporal variability in INP concentrations. However, in recent years, the first long-term observations of INPs in the Arctic and in Patagonia have been made. Wex et al. (2019) collected a year-long dataset of INP concentrations from ground-based sampling at four Arctic sites. They found a clear seasonal cycle of N_{INP} with the highest concentrations between late spring and autumn, and the lowest between autumn and early spring. A similar seasonal cycle was observed by Sze et al. (2023) from two years of measurements at Villum Research Station in northern Greenland. The annual cycle of INPs was also investigated during the year-long Multidisciplinary drifting Observatory for the Study of Arctic Climate (MOSAiC) project and the maximum INP concentrations were once again observed in summer and the minimum in winter (Creamean et al., 2022). They also report a difference in seasonality between INPs active above -15°C (warm-temperature INPs) and below -15°C (cold-temperature INPs) that they attribute to two different sources; cold-temperature INPs were from long-range transport of dust from continental sources whereas warm-temperature INPs were most likely to be proteinaceous material from local marine sources. The same seasonal cycle in INP concentrations was not observed in long-term observations made in Patagonia (Gong et al., 2022), suggesting different controls on emissions and transport of aerosol in the northern and southern hemispheres, however further observations in the southern hemisphere (particularly Antarctica) are needed.

Aerosol transport to the Arctic has a strong seasonal cycle (Stohl, 2006; Bozem et al., 2019). In summer, there is a significant temperature difference between cold Arctic air masses and warmer mid and low-latitude air masses. The cold air over the Arctic, known as the polar dome, acts as a barrier that prevents the transport of air at the surface from lower latitudes and isolates the Arctic from low-latitude aerosol sources. In contrast, in winter the polar dome can extend further south, thereby encompassing more continental aerosol sources, and it is thermodynamically easier for mid-latitude air to be transported into the polar dome, bringing more aerosols with it. This phenomenon is responsible for the accumulation of anthropogenic aerosol in the Arctic in winter and early spring, known as Arctic haze. Higher aerosol concentrations in winter are also driven by less efficient removal processes; there is less wet deposition because scavenging is less efficient in ice clouds compared to warm clouds (Browse et al., 2012), and less dry deposition because the stable stratification of the atmosphere reduces turbulent exchange (Stohl, 2006). Interestingly, the seasonal cycle of INP concentrations observed by Wex et al. (2019) and Sze et al. (2023) and the warm-temperature INP cycle observed by (Creamean et al., 2022) appears to be anti-correlated with the expected peak in Arctic aerosol which suggests two things: (i) anthropogenic aerosols do not contribute to atmospheric INP concentrations and (ii) local sources drive an increase in INP concentrations in Summer.

Other studies provide further evidence for marine and terrestrial high-latitude sources of INPs. The main source of INPs from the marine environment is biogenic aerosols that are emitted from seawater by wave breaking and bubble bursting (Schnell, 1977; Wilson et al., 2015; Creamean et al., 2019; Welti et al., 2020). In the terrestrial environment, studies have identified a multitude of possible sources of INPs. In the southern hemisphere, during the Antarctic Circumnavigation Expedition (ACE), Tatzelt et al. (2022) found the highest INP concentrations in air masses that had been in contact with ice-free land and terrestrial sources have been identified in Patagonia (López et al., 2018; Gong et al., 2022). In the northern hemisphere, Irish et al. (2019) and Creamean et al. (2018) found a correlation between INP concentrations and the time sampled air masses had spent over bare land (in Canada and Alaska), Conen et al. (2016) reported an enhancement of INP concentrations at a coastal site in Norway that they attributed to aerosols emitted from decaying leaves, Brasseur et al. (2022) identify INP sources in boreal forests in Finland and Porter et al. (2022) found high INP concentrations at the North Pole were likely to be sourced from Russia. In addition, there is a growing body of evidence to show that emissions of high-latitude dust are an important source of INPs (Paramonov et al., 2018; Tobo et al., 2019; Sanchez-Marroquin et al., 2020; Xi et al., 2022).

1.4.1.1 High-latitude dust

Mineral dust is emitted into the atmosphere in large quantities each year and makes up a substantial percentage of the total mass of aerosols globally (Gliß et al., 2021), the abundance of mineral dust and its activity make it one of the most important INPs. Much of the focus on mineral dust has been on dust from deserts in arid low-latitude regions, which makes up the largest contribution to the global dust budget (Kok et al., 2021) and has been shown to be an active INP (DeMott et al., 2003; Chou et al., 2011; Atkinson et al., 2013; Harrison et al., 2022a) with the potential to influence clouds globally (Vergara-Temprado et al., 2017; Chatziparaschos et al., 2023). However, more recent work has highlighted the importance of high-latitude regions as a source of mineral dust (Bullard et al., 2016; Groot Zwaaftink et al., 2016; Meinander et al., 2022). Dust sources have been identified in cold high-latitude regions including Alaska, Greenland, Iceland, Antarctica and Patagonia (Meinander et al., 2022), as illustrated in Fig 1.5 which shows recent observations of dust emissions from sources north of 50°N and south of 40°S. Many of these dust sources are from glaciated areas where dust is formed by the erosion of the rock underlying glaciers. This dust can be emitted directly into the atmosphere by aeolian processes in the pro-glacial environment or it can be transported by fluvial processes before being deposited and then emitted.

Recent studies by Tobo et al. (2019) and Xi et al. (2022) have investigated the ice-nucleating ability of glacial dust from Svalbard and Canada and found that these sediments nucleate ice at temperatures relevant for mixed-phase clouds. A similar observation was made by Sanchez-Marroquin et al. (2020) from airborne measurements of aerosols and INPs in Iceland, further highlighting the importance of high-latitude dust (HLD) as a source of INPs. However, despite growing research interest in this area, there are still very few measurements as shown in Fig 1.5 where the HLD sources that have been investigated for their ice nucleating activity are shown in red. In this figure, the background map shows data from the United Nations Convention to Combat Desertification (UNCCD) Global Sand and Dust Storms Source Base Map which identifies the potential for dust emissions from a location based on factors such as land cover type, moisture and windspeed (UNCCD, 2022). It is clear that there are potential emission zones across vast swathes of the northern high latitudes, as well as in Patagonia, where the dust emissions are yet to be quantified. This means we cannot yet make wider conclusions regarding the contribution of HLDs to atmospheric INP populations. It should also be noted that the UNCCD dataset does not include Antarctica but dust source regions have also been identified in ice-free areas of Antarctica (Diaz et al., 2020; Meinander et al., 2022).

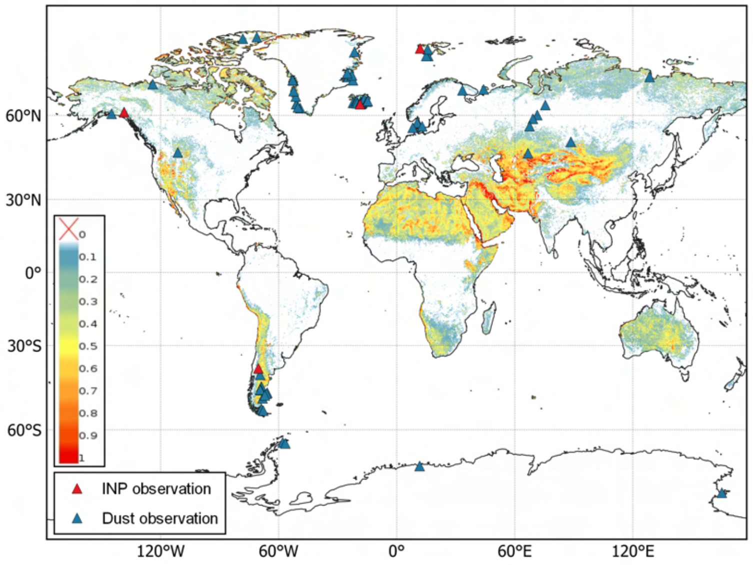

Fig. 1.5.: Map of HLD sources identified by Meinander et al. (2022) (Blue) and dust sources that have been analysed for INPs (red) (Canada: Xi et al. (2022), Iceland: Paramonov et al. (2018), Svalbard: Tobo et al. (2019), Patagonia: López et al. (2018)). Background data shows the UNCCD Global Sand and Dust Storms Source Base Map for October. Higher values represent a higher potential for dust emissions. Note: there is no UNCCD data available for Antarctica.

1.5 Secondary ice production

Observations show that the concentration of ice in clouds is often many orders of magnitude greater than the concentration of INPs (Hobbs, 1969; Hobbs and Rangno, 1985; Rangno and Hobbs, 2001a; Cantrell and Heymsfield, 2005; Sullivan et al., 2018). This is due to the enhancement of ice crystal number concentrations by secondary ice production (SIP), or ice multiplication, where ice crystals that have already formed by nucleation trigger the formation of more ice. Numerous SIP mechanisms have been proposed:

- **Rime splintering (Hallett-Mossop process)**: when a supercooled liquid droplet collides with an ice crystal, ice splinters are ejected during the riming process, this is thought to occur at temperatures between -3°C and -8°C (Hallett and Mossop, 1974)
- **Collision fragmentation**: when ice crystals break up due to turbulence or due to collisions with other particles
- **Sublimation fragmentation**: particles separate from a parent crystal during sublimation
- **Droplet shattering**: during rapid freezing of droplets pressure may build inside the droplet causing them to shatter

SIP has been observed in laboratory studies (Korolev et al., 2017; Korolev and Leisner, 2020) and observations in cloud have shown the enhancement of ice concentrations (N_{ice}) above that of INPs (Hobbs and Rangno, 1985; Cooper, 1986; Taylor et al., 2016; Lawson et al., 2017; Ladino et al., 2017, e.g.) but the contribution of different SIP mechanisms to ice concentrations in the atmosphere and the environmental conditions required for each to occur are still uncertain. In addition, whilst it is clear that PIP must occur before SIP, the relative importance of each is unknown and the concentration of primary ice crystals required to trigger SIP remains unclear (Field et al., 2017; Korolev et al., 2022). The initiation of SIP is likely to vary depending on cloud type, environmental conditions and dominant SIP mechanism. Crawford et al. (2012) and Huang et al. (2017) showed that in cumulus clouds INP concentrations of 0.01 L^{-1} may trigger secondary ice formation through the Hallett-Mossop (HM) process. In contrast, Sullivan et al. (2018) find that cloud base temperature and the presence of a modest updraft are more important than N_{INP} for SIP to occur by rime splintering but that N_{INP} is a limiting factor in collision fragmentation which can occur with N_{INP} from 0.002 to 0.15 L^{-1}.

These studies, amongst others, focus on slightly supercooled clouds with temperatures in the range where the HM process is thought to occur (-3°C $\sim$ -8°C) and SIP below -8°C is often not accounted for in numerical models. However, in high-latitude mixed-phase clouds, it is common for temperatures to fall below this temperature range. SIP has been observed down to temperatures as low as -27°C (Järvinen et al., 2022; Korolev et al., 2022; Pasquier et al., 2022) and shown to contribute up to 80% of the total ice formation in single-layer mixed-phase clouds in the Arctic (Zhao and Liu, 2022). Pasquier et al. (2022) observed that the highest concentration of secondary ice crystals in Arctic mixed-phase clouds occurs between -3°C and -8°C but that SIP occurs most frequently between -18°C and -24°C. Similarly, Järvinen et al. (2022) observed N_{ice} exceeding N_{INP} by up to 3 orders of magnitude between -14°C and -17°C in single-layer stratiform clouds in the Southern Ocean. These observations suggest an important SIP process at temperatures below -8°C but the dominant SIP mechanism at colder temperatures remains under debate. Both Pasquier et al. (2022) and Järvinen et al. (2022) propose ice-ice collision fragmentation as the possible mechanism, a theory supported by laboratory studies that show ice-ice collisions produce most ice crystals at -16°C (Takahashi et al., 1995). In contrast, in a modelling study of Arctic stratocumulus clouds, Sotiropoulou et al. (2021) found that the efficiency of ice-ice collisions was weak and it was unlikely to be the dominant factor in enhancing N_{ice}. It is clear that further observations are required in order to understand SIP processes below -8°C however concurrent observations of INPs and ice crystal number concentration are unusual, particularly over longer timescales.

1.6 Atmospheric observations

1.6.1 Sampling and characterising INPs

INPs can be sampled by offline or online techniques. Offline methods refer to those where aerosols are sampled from the environment using one instrument and then analysed for INPs separately. Online methods use instruments that sample aerosol and determine INP concentrations together.

Sampling INPs from the atmosphere for offline analysis usually involves collecting aerosol samples onto filters either from the ground (e.g. Wex et al., 2019; Adams et al., 2020; Harrison et al., 2022a), from an aircraft (e.g. Rogers et al., 2001; Price et al., 2018; Sanchez-Marroquin et al., 2020) or from balloon-borne sampling platforms (e.g. Porter et al., 2020). It can also be beneficial to collect size-resolved aerosol samples, for example by collecting aerosol onto substrates using a multi-stage cascade impactor (Porter et al., 2022). INP concentrations may also be determined from precipitation samples (Petters and Wright, 2015) and from ice cores (Schrod et al., 2020).

A common method to determine the ice-nucleating activity of samples collected by offline sampling is to use droplet freezing assays, where droplets of a suspension containing the sampled aerosol are cooled and their freezing temperatures are recorded. A multitude of instruments exist for these experiments, that vary in their cooling methods, droplet size and detectable temperature range (see Miller et al., 2021, and references therein), but each allows the experimental determination of $f_{ice}(T)$ (see Eq. 1.9) and the calculation of N_{INP}. A detailed description of this method applied to samples collected using a ground-based multistage cascade impactor is given in Chapter 2 and a modified approach for aircraft samples in Chapter 4.

Online techniques determine N_{INP} by exposing sample air to temperatures and supersaturations where aerosols can activate as INPs and then counting the number of ice crystal that forms. Cloud expansion chambers (e.g. Möhler et al., 2021) achieve this by simulating adiabatic cooling; a sample volume is drawn into a chamber and the pressure is reduced, reducing the temperature and enhancing the saturation. In continuous flow diffusion chambers (CFDCs) (e.g. Rogers, 1988; Stetzer et al., 2008; Garimella et al., 2016), the humidity is controlled by two ice-covered plates that are set at different temperatures. The temperature and humidity gradient between the plates results in a supersaturated region that the sample flow passes through. The number of ice crystals formed after the air has passed the plates are counted.

1.6.2 Observing cloud properties

Observations of cloud properties can be undertaken using in-situ and remote sensing instruments from the ground, aircraft or platforms such as tethered balloons. The use of aircraft to observe microphysical properties has been prevalent since the ‘80s (Rogers, 1988) however, in-situ observations from aircraft are susceptible to measurement biases as a result of crystal shattering (Korolev et al., 2011; Korolev and Field, 2015). Whilst improvements in cloud probe technologies have mitigated this error somewhat (Baumgardner et al., 2017a) there are still limitations to making observations in this way; for example, aircraft are limited in the time they can fly and hence aircraft observations provide only a snapshot into the cloud properties and evolution. To address this, remote sensing is increasingly used as an alternative to in-situ techniques to make observations of the atmosphere, and advances in both instrumentation and analysis techniques mean remote sensing offers a valuable way to retrieve the microphysical properties of clouds (Bühl et al., 2017). An advantage of remote sensing over in-situ observations from ground or airborne platforms is that measurements can be made over longer times and the evolution of clouds and cloud microphysical properties can be captured. In addition, vertically orientated remote sensing instruments provide valuable information on the structure of the atmosphere.

Remote sensing can either be through passive or active techniques. Active remote sensing instruments, such as radar and lidar, emit an electromagnetic pulse and the returned signal is measured. Passive remote sensing instruments, such as microwave radiometers, measure radiation emitted from objects or the atmosphere. Different remote sensing instruments are sensitive to different cloud properties and so the appropriate choice of instrument, or combination of instruments, is dictated by the atmospheric feature or particular cloud property of interest. For example, radar reflectivity is proportional to the 6th moment of the particle size distribution (diameter^6) and is therefore highly sensitive to particle size (Doviak and Zrnić, 2006). In contrast, lidar backscatter is proportional to the 2nd moment of the PSD (diameter^2) and is more sensitive to particle number concentration (Ewald et al., 2021). Hence, where lidar and radar observations are available, two moments of the particle size distribution (PSD) can be retrieved - number concentration and particle size. In addition, the different wavelengths of the instruments mean they are sensitive to different-sized targets. For example, a lidar will be able to observe optically thin clouds consisting of droplets that would be too small for radar. In contrast, in optically thick clouds the lidar signal is quickly extinguished whereas radar can penetrate. This thesis uses radar and lidar remote sensing so the background theory of both are outlined in the following sections.

1.6.2.1 Radar

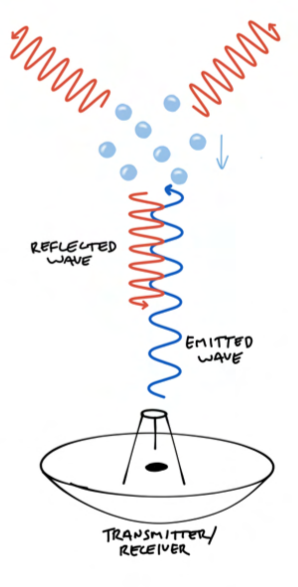

Fig. 1.6.: Illustration of the principle of radar remote sensing.

Radar (Radio Detection and Ranging) is an active remote sensing technique operating at microwave (radio) wavelengths. Radar instruments consist of a transmitter and antenna that emit a pulsed radio wave, this wave is reflected by objects in its path and the returned signal is received. The power of the returned signal is recorded along with the time elapsed from the pulse being emitted to it being received, which is used to infer the distance from the radar to the scattering object. Doppler radar also records the phase change of the backscattered signal from one pulse to the next which provides information about the movement of the target relative to the radar (Kollias et al., 2007a). Each interaction of the emitted radar pulse with a target results in a returned signal with different amplitude and phase, so the fundamental data produced by a Doppler radar is a time series of the backscattered power returns, including the phase shift between pulses, in each range sample volume. These data are processed using fast Fourier transform (FFT) techniques to compute a time series of Doppler spectra. The first three spectral moments correspond to the radar reflectivity, mean Doppler velocity and Doppler spectrum width.

Radar reflectivity (Z) is a measure of the total power of the signal that is scattered back to the receiver after interacting with particles in the atmosphere, such as cloud droplets. When electromagnetic waves encounter cloud droplets, they interact with the droplets in different ways depending on the droplet size relative to the radar wavelength. Hydrometeors in the atmosphere are considerably smaller than the wavelength of cloud radars, which tend to operate at millimetre wavelengths, and hence Rayleigh scattering dominates. In this regime, the scattering efficiency of a droplet is proportional to the sixth power of its size::

$$Z = \int D^6 N(D) dD \tag{1.12}$$

where $N(D)$ is the size distribution of hydrometeors and D is particle diameter. Z increases rapidly as D increases and the radar echo is dominated by larger particles so Z is often given as a dimensionless value on a logarithmic scale.

Mean Doppler velocity (v_D) is a measure of the motion of the target objects. When electromagnetic waves are scattered by moving objects there is a change in the frequency of the wave relative to an observer; for an object that is moving towards the observer the frequency of the wave increases and vice versa for an object moving away from the observer. The change in the frequency of the radar signal that is reflected back to the receiver is related to the radial velocity of the object (velocity parallel to the beam) and the wavelength of the radar. For vertically pointing cloud radars, Doppler velocity is the sum of the fall speed of hydrometeors and the vertical motions of the air.

The Doppler spectrum width (w) provides information on the variance in Doppler velocities in the sample volume, which is a function of the radar system parameters and meteorological conditions (Doviak and Zrnić, 2006). In the atmosphere, the Doppler spectrum is influenced by factors such as cloud droplet size distribution, atmospheric turbulence, and wind shear. For example, in a cloud with both liquid and ice particles, there would be a broad droplet size distribution and considerable variability in terminal fall velocities of hydrometeors, leading to a broad Doppler spectrum.

1.6.2.2 Lidar

Lidar (Light Detection and Ranging) works on the same principle as radar but the emitted electromagnetic waves are in the visible range. Due to the shorter wavelength (nm to μm) of the emitted pulse compared to radar (mm to cm), lidar is sensitive to smaller particles (aerosols, cloud droplets). When used to observe cloud particles the wavelength of the lidar pulse tends to be smaller than the diameter of the hydrometeors and geometric scattering occurs. In this scattering regime, the lidar backscatter is proportional to the second moment of the particle size distribution (total surface area of hydrometeors) and is therefore sensitive to the particle number concentration and backscattering cross-section (Ewald et al., 2021). The backscatter of the emitted lidar pulse from targets in the atmosphere is recorded as the number of photons at the receiver per second. Similarly to radar, the elapsed time

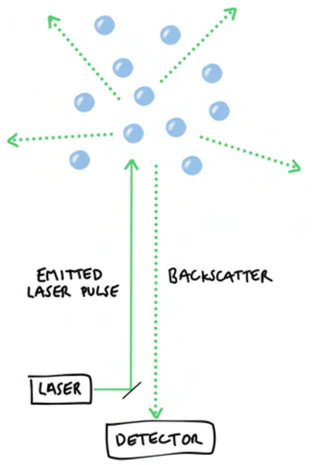

Fig. 1.7.: Illustration of the principle of lidar remote sensing.

between the beam being emitted and received is used to determine the distance to the target object.

Due to the methods used to produce the laser beam, many lidar instruments emit linearly polarised light (Sassen, 2005). The polarisation of the beam can be altered by interactions with different atmospheric targets; ice crystals depolarise both radar and lidar signals whereas liquid droplets do not depolarise the signal. This can be exploited to provide information on the phase of hydrometeors by recording both the polarised and depolarised backscatter and calculating the ratio between them, known as the depolarisation ratio. There are different ways to calculate this parameter depending on the type of polarisation employed by the lidar. Methods relevant to this thesis, including calibrations that must be applied to raw lidar data, are provided in Chapter 3

1.7 Objectives

The overriding objective of this thesis is to further our understanding of sources of ice-nucleating particles and their role in ice formation in high-latitude mixed-phase clouds. The motivation for this is to better understand ice processes in clouds that are important for climate and cloud-phase feedback. There are gaps in our understanding in three key areas: (i) high-latitude sources of INPs, (ii) the influence of INPs on cloud microphysical properties and (iii) atmospheric INP concentrations. The chapters of this thesis address each of these in turn:

(i) Chapter 2 focuses on sources of INPs and presents an investigation into a previously unstudied high-latitude dust source in Alaska. We combine field observations, laboratory analysis and modelling to answer the following questions:

  - Does dust from the Copper River, Alaska nucleate ice at temperatures relevant for mixed-phase clouds?
  - What controls the ice-nucleating activity of dust from this source and how does it compare to other high-latitude dust sources?
  - How does this dust source contribute to atmospheric INP concentrations?

(ii) Chapter 3 focuses on the influence of INPs on cloud microphysical properties. We test and apply remote-sensing techniques to data from Summit Station, Greenland to determine ice crystal number concentration (ICNC). We combine this with a year-long dataset of INP concentrations to compare ICNC with INP concentrations and answer the following questions:

  - Can ice-crystal number concentration be retrieved from remote-sensing instruments at Summit Station?
  - How do INP concentrations influence ice crystal number concentration in stratifrom mixed-phase clouds?
  - Can regions of primary and secondary ice concentration be identified?

(iii) Chapter 4 focuses on atmospheric INP concentrations using airborne sampling to investigate the following questions:

- What are the potential sources of INPs in the North East Atlantic?
- Is there a difference in the INP activity of samples collected in the marine boundary layer compared to those that have been influenced by land?

Finally, Chapter 5 discusses the overall findings of these studies and suggests future work, including proposing a study that would combine the above techniques.

2

Southern Alaska as a source of atmospheric mineral dust and ice-nucleating particles

2.1 Introduction

The presence of ice in clouds has a strong control on their physical and optical properties, and the processes they control such as radiative transfer and precipitation formation (Lohmann and Feichter, 2005; Ceppi et al., 2017). Heterogeneous freezing, triggered by the presence of ice-nucleating particles (INPs), is an important pathway for ice formation in mixed-phase clouds in the atmosphere. Hence, understanding INPs and their role in the formation of ice in clouds is of crucial importance in order to constrain the role of clouds in the climate system (Tan et al., 2016; Vergara-Temprado et al., 2018; Murray et al., 2021).

Despite their importance, our understanding of INPs is still relatively poor and their sources, concentrations and seasonal variability are poorly quantified. This is particularly pronounced in high-latitude ($\geq$ 50°N and $\geq$ 40°S) regions where mixed-phase clouds, which are highly sensitive to the presence of INPs, are common (Shupe, 2011). Many laboratory and field measurements have focused on low- and mid-latitudes where globally important sources of INPs, such as desert dust, have been identified (DeMott et al., 2003; Sassen et al., 2003; Atkinson et al., 2013; Boose et al., 2016). However, there has been less focus on INP sources in the mid- to high-latitudes (45-75 °N), a region critical for cloud-phase feedback (Murray et al., 2021). As the climate warms, the amount of liquid water relative to ice in mixed-phase clouds will increase. This leads to clouds with a higher albedo, which has a cooling effect over dark surfaces such as the ocean, and hence a negative climate feedback (Ceppi et al., 2017; Murray et al., 2021). Whilst it is clear that the cloud-phase feedback is negative there is still uncertainty over the magnitude of this feedback (Tan et al., 2016; Storelvmo et al., 2015; Ceppi et al., 2017; Murray et al., 2021). The strength of the cloud-phase feedback depends on the amount of ice in clouds so accurate modelling of the partitioning between ice and liquid water in present-day clouds, as well as in a changing climate, is key to predicting the magnitude of the cloud-phase feedback. However, ice-related processes are poorly represented in GCMs and the amount of ice is often overestimated (Tan et al., 2016; Ceppi et al., 2017; Storelvmo et al., 2015). INPs relevant for the cloud-phase feedback have not been quantified and their sources, concentration and influence on mixed-phase clouds remain a substantial uncertainty in estimates of cloud-phase feedback (Murray et al., 2021).

The high-latitudes are remote from the major low-latitude dust sources in Africa and Asia, hence the concentration of low-latitude desert dust is relatively small (Vergara-Temprado et al., 2017), there is also strong seasonal variability in aerosol concentrations relating to transport and removal mechanisms (Stohl, 2006; Hande et al., 2015; Groot Zwaaftink et al., 2016). This means that local aerosol sources can be the dominant source of mineral dust in the high-latitudes (Groot Zwaaftink et al., 2016; Shi et al., 2022). Dust emission zones in northern high-latitudes have been identified in regions including Iceland, Canada, Greenland and Alaska (Bullard et al., 2016; Meinander et al., 2022). Whilst such high-latitude dust (HLD) sources account for a relatively small fraction of global dust emissions ($\sim$5% (Bullard et al., 2016)) studies have shown that dust from sources $>$60°N contributes up to 27% of the total dust load in the Arctic which is comparable to the 32% contribution of African dust to the Arctic (Groot Zwaaftink et al., 2017; Shi et al., 2022).

HLDs have been shown to nucleate ice under conditions relevant for mixed-phase cloud formation (Tobo et al., 2019; Sanchez-Marroquin et al., 2020; Xi et al., 2022) suggesting that they could be an important source of INPs. However, there is considerable variability in the characteristics of these sources and there have been few studies investigating the transport of dust and INPs from high-latitude dust sources, meaning we cannot yet make wider conclusions regarding the contribution of HLDs to atmospheric INP populations. Tobo et al. (2019) and Xi et al. (2022) report the ice-nucleating activity of glacial outwash sediments, from Svalbard, Norway and Yukon, Canada, respectively. Sediment produced by glacial processes is one of the main contributors to high-latitude dust emissions (Bullard et al., 2016), but the physical and chemical properties are influenced by the local bedrock and environment. Dust from other origins, such as sediment derived from volcanic material in Iceland, as studied by Sanchez-Marroquin et al. (2020), again has different composition and properties (Baldo et al., 2020). Dust can also be altered by processes occurring during transport, deposition and uplift (Meinander et al., 2022). For example, glacial outwash sediment from Svalbard studied by Tobo et al. (2019) had a biogenic component to its ice-nucleating activity, rather than being controlled purely by mineralogy, suggesting mixing or growth of biological material during transport in the fluvial environment. The physical, chemical and biological processes that dust and sediments are exposed to, and the resulting effect on the ice-nucleating properties of the material, will vary depending on environmental conditions such as the local climate and land cover. Sediments studied by Tobo et al. (2019) originated from largely ice- and vegetation-free areas of Svalbard, where less than 10% of the landscape is covered in vegetation and there are no tall trees. However, in many other regions, glacial sediments are transported by rivers in vegetated or forested mountain catchments. There are biological INP sources in forests in the northern high-latitudes (Brasseur et al., 2022; Conen et al., 2017) and hence there is potential for the ice-nucleating ability of transported sediments to be enhanced by the presence of biogenic material from abundant vegetation. There have been few studies of the ice-nucleating ability of dust originating from such regions.

The south coast of Alaska is one of the most active sources of glacial dust in the northern high-latitudes (Bullard et al., 2016; Crusius et al., 2017; Meinander et al., 2022) and dust events have been observed as early as 1910 (Tarr and Martin, 1913). Here, numerous glacially fed rivers originate in the Wrangall and Chugach Mountains and flow to the Gulf of Alaska, transporting glacial sediment that is deposited on floodplains at their terminus. The largest of these rivers is the Copper River, also known as Atna'tuu (Ahtna Athabascan) or Eek̲héeni (Tlingit). The watershed of the Copper River spans 62000 km^2 of southern Alaska and encompasses ice and snow-covered mountain terrain, boreal forests, temperate rainforests and wetlands. Glaciers cover 18% of the catchment (Kargel et al., 2014) and load the river with melt-water and sediment produced by glacial processes, resulting in around 70 million tons of sediment being transported by the river each year (Brabets, 1997), the highest annual suspended-sediment load in Alaska (Jaeger et al., 1998). Some of this sediment is deposited on the Copper River Delta. In late summer or autumn, when the river levels are at their lowest and north-easterly winds down the river valley are prevalent (Crusius et al., 2017), this fine glacial sediment is lofted into the atmosphere resulting in large dust events that can last several days or weeks and extend hundreds of kilometres over the Gulf of Alaska, as shown in Fig. 2.1. Single events have been estimated to transport up to 80 kt of dust from the Copper River Valley (Crusius et al., 2011) and dust from the Copper River has been shown to play an important role in the transport of minerals to the Gulf of Alaska (Crusius et al., 2011; Schroth et al., 2017). However, the ice-nucleating ability of the dust has not yet been quantified.

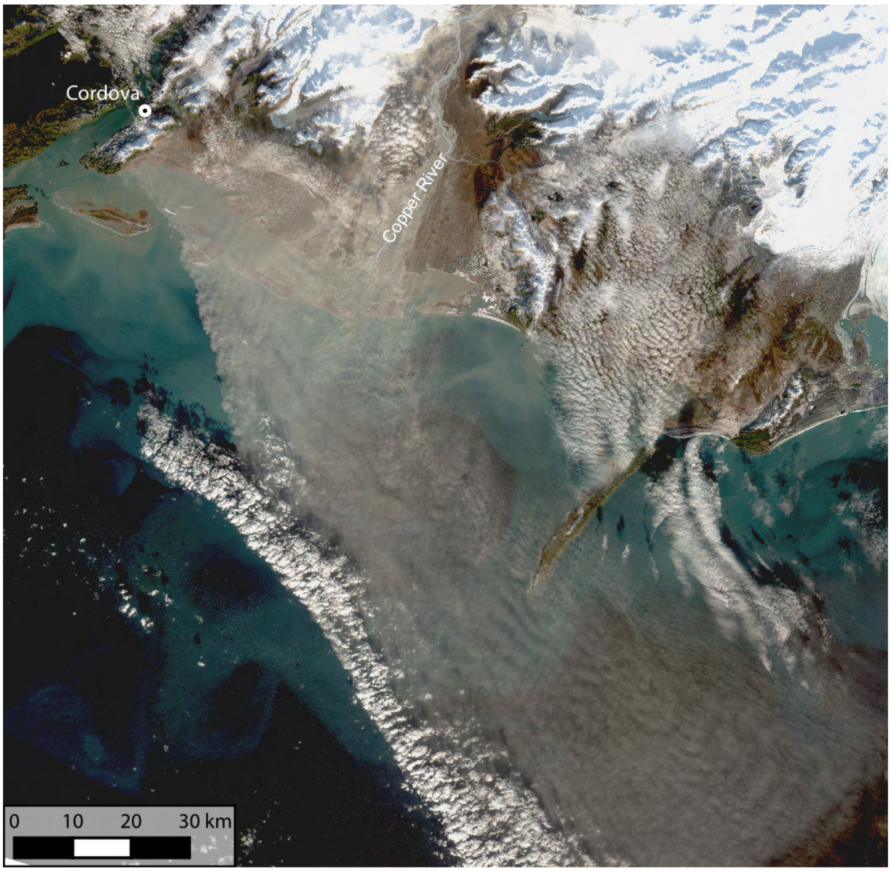

Fig. 2.1.: True colour image of the Copper River Delta derived from Landsat 8 Collection 2 Tier 1 calibrated top-of-atmosphere (TOA) reflectance of a dust event on 31st October 2020.

Here we investigate the ice-nucleating ability of glacial dust from the Copper River Delta by collecting size-segregated samples of airborne dust from the Copper River Delta and characterised its ice-nucleating activity in a laboratory study. We then use particle dispersion modelling to model the transport of this dust and estimate atmospheric INP concentrations to test the hypothesis that the Copper River Valley is an important source of INPs for the North Pacific and the northern North American continent.

2.2 Materials and Methods

Making measurements in high-latitude regions is often difficult due to their remoteness, lack of infrastructure and potentially extreme environments, hence the choice of a field site was an important consideration. As well as being an important dust source, the Copper River Delta can be accessed using a normal 4x4 vehicle via the Copper River Highway, a gravel road from the nearby town of Cordova (60.5°N, 145.8°W). This presented an excellent opportunity to access an active dust source region directly. We used portable battery-operated equipment that can easily be carried by one person, meaning sampling could be undertaken with minimal resources.

2.2.1 Sampling location and field campaign

Sampling was conducted during a field campaign between 11th and 21st October 2019. The Copper River Highway was used to access the western side of the delta where sampling locations were chosen in regions with visible dust emissions (Fig. 2.2). During the 10-day period of the field campaign dust events (i.e. days when dust emissions were observed from the surface and airborne dust was visible over a wide area) occurred on 8 days.

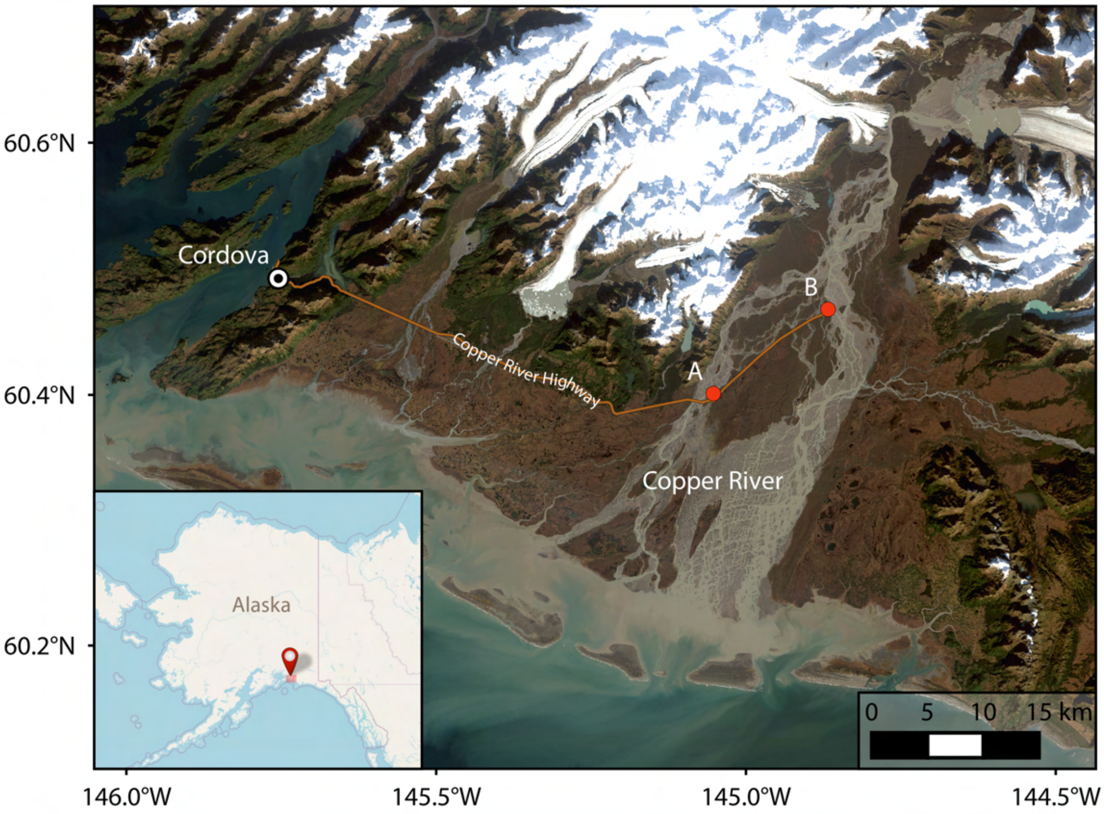

Fig. 2.2.: The Copper River Delta showing sampling locations A and B, Cordova and the Copper River Highway. Background image derived from Landsat 8 Collection 2 Tier 1 calibrated top-of-atmosphere (TOA) reflectance.

2.2.2 Sample collection

2.2.2.1 Airborne dust sampling

Airborne dust was sampled using a multistage cascade impactor (Sioutas Personal Cascade Impactor, SKC Ltd., UK), as shown in Fig. 2.3A, which collects size-resolved aerosol samples onto thin substrates for offline analysis. The impactor consists of collection stages A-D which leads to aerosol being sorted into 4 size bins: 0.25-0.5 μm, 0.5-1.0 μm, 1.0-2.5 μm and $>$2.5 μm. A flow rate of 9 L min^{-1} is required which was provided by a battery-powered pump (Leland Legacy Pump, SKC Ltd.). 25 mm diameter filters (Nuclepore track-etched membrane polycarbonate filters, Whatman, UK), with 0.05 μm pore size, were used as impactor substrates on each of the four impactor collection stages. An optical particle counter (OPC-N2, Alphasense, UK) was used alongside the cascade impactor in order to provide binned particle size distributions and both the OPC and impactor were mounted on a tripod at a height of 1 m above the surface (Fig. 2.3B). During the measurement campaign, the OPC was unable to capture the high dust concentrations and eventually failed, most likely due to the optics becoming obscured/blocked by dust, therefore an alternative gravimetric approach to determine the amount of aerosol sample was used. Wind speed was measured at hourly intervals during each sampling period using a portable three-cup anemometer (Skywatch Eole, JDC Electronic SA, Switzerland). Measurements were taken at the location of the sampler with the anemometer handheld above the observer's head and so approximately 2 m above the surface, compared to the 1 m height of the sampler. This was to ensure measurements were not influenced by the wind being blocked by the person holding the anemometer however the logarithmic wind profile means the windspeed at 2 m above the surface is likely to be higher than at 1 m. The instantaneous, 30-second average and maximum wind speed was recorded. The results presented in Table 2.1 are the 30-second average wind speed at the start of the sampling period.

Sampling efficiencies of both the impactor and the OPC are affected by wind speed and direction, the combination of which results in sampling biases; this was an important consideration during our sampling period due to the high wind speeds observed. The orientation of sampling inlets in relation to the prevailing wind direction influences the sampling efficiency and therefore sampling biases can be minimized by careful positioning of the instruments (Porter et al., 2020). Hence, to achieve optimal sampling efficiency the impactor was deployed vertically with the inlet upwards (90° to the wind) and the OPC was deployed with the inlet facing into the wind (0° to the wind). The effect of wind speed on sampling efficiency becomes more pronounced as particle size increases. We modelled the particle losses at a range of wind speeds using an open-source particle loss calculator (von der Weiden et al., 2009) the results of which are shown in Fig. A.1 in Appendix A. We found that between 0 and 2.5 μm (Stages B-D) particle losses are minimal. However, above 2.5 μm the sampling efficiency quickly decreases, reaching 0 at around 6 μm for wind speeds of 16 ms^{-1}. This implies that although Stage A has no defined upper size limit we are unlikely to have sampled particles $>$6 μm and that samples on Stage A would be biased towards smaller sizes. This was considered in the calculation of specific surface area as outlined below.

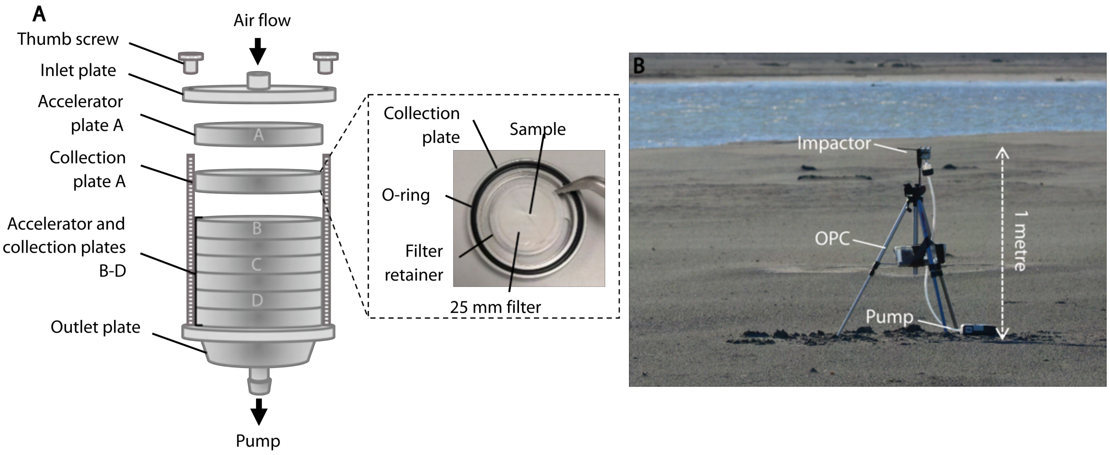

Fig. 2.3.: Size resolved dust sampling in the Copper River Valley. (A) Sioutas Personal Cascade Impactor. Sampled air passes through accelerator plates A-D in turn and particles above the cut-off size for each plate (A: >2.5 μm, B: 1.0 μm, C: 0.5 μm, D: 0.25 μm) are collected on to the corresponding collection plate. Collection plates (inset) consist of a 25 mm collection substrate, filter retainer and nitrile O-ring to maintain an airtight seal. (B) The cascade impactor and optical particle counter deployed in the Copper River Valley on a tripod.

Three sets of impactor collection stages were prepared at the University of Leeds and transported to the field site. The impactors were taken apart and cleaned with isopropyl alcohol, then rinsed with ultra-pure water (CHROMASOLV water for high-performance liquid chromatography, Sigma-Aldrich) and finally dried using dry nitrogen. Collection substrates were installed on each stage using tweezers and then each set of collection stages was wrapped in Parafilm and sealed in a sterile bag until ready to be used. Of the impactors prepared in Leeds, two were used for sampling and one as a handling blank, whereby no sample was collected on the collection substrates but they were analysed using the same protocol as the samples to assess the background INP activity. For subsequent samples the impactors were prepared in Alaska: at the end of each sampling period the impactor was sealed in a bag and transported from the field site to a nearby hotel, here the substrates were removed from the impactor using tweezers, placed into pre-rinsed 50 ml centrifuge tubes and stored in a freezer at -18°C. The collection stages and filter retainer were cleaned again using isopropyl alcohol and ultra-pure water before being reloaded with new substrates and sealed until the next sampling period. The impactors were left to dry with a sterile bag placed over them. When removing samples and installing new substrates the impactor was placed inside a freshly opened sterile polyethylene bag and then loosely closed around the hands of the person preparing the impactors; the entire process could then be completed inside the bag. In the absence of a laminar flow hood, we hoped this would reduce potential contamination, whilst the exposed filters were still exposed to potentially unclean air from the room they would be protected from particles falling onto them, for example from clothing. The handling blanks prepared in Alaska following this protocol did not show a higher level of background INP activity when compared to the handling blanks prepared in Leeds. We therefore assume that there was no additional contamination when the impactors were prepared in the field as opposed to in the laboratory in Leeds.

2.2.2.2 Surface dust sampling for X-Ray diffraction

In addition to the airborne samples, dust source material was collected close to the sampling locations shown in Fig. 2.2. Material was collected from the surface using a stainless steel scoop and briefly stored in sterile bags. Whilst still in Alaska the surface samples were sieved using a 45 μm stainless steel sieve (Fisherbrand, UK) which was cleaned in advance with isopropyl alcohol and ultra-pure water. Once sieved, the samples were stored in pre-rinsed containers (Nalgene polycarbonate jars, Thermo Scientific, UK) and frozen. The sieved samples were used to investigate the mineralogy of dust from this source using X-ray diffraction. The percentage of each mineral in the sample was determined using Total Pattern Analysis Solutions (TOPAS) analysis of Rietveld refinement of powder X-ray diffraction (XRD) patterns.

2.2.3 INP droplet freezing assay experiments

The ice-nucleating ability of airborne samples was investigated using the University of Leeds Microlitre Nucleation by Immersed Particle Instrument (μL-NIPI) for cold-stage droplet freezing experiments, following the method outlined in Whale et al. (2015). Suspensions were prepared by adding 3 ml of ultra-pure water to the centrifuge tube containing each substrate and agitated using a vortex mixer for 10 minutes. From this suspension, 1 μL droplets were pipetted onto a hydrophobic glass slide placed on a temperature-controlled cold stage. A chamber, with a digital camera, was placed on top and then flushed with dry nitrogen to inhibit condensation and frost formation. The cold stage was cooled at a rate of 1°C min^{-1} and the freezing of droplets recorded by the digital camera which, combined with concurrent measurement of the temperature of the cold stage, allowed the fraction of droplets frozen at a given temperature, $f_{\text{ice}}(T)$, to be determined. The concentration of ice-nucleating particles per volume of sampled air, N_{INP}, as a function of temperature could then be calculated according to Equation 1 (Porter et al., 2020):

$$N_{\text{INP}}(T) = -\ln\left[1 - f_{\text{ice}}(T)\right] \frac{V_{\text{wash}}}{V_{\text{drop}} V_{\text{air}}} \tag{2.1}$$

Where V_{wash} is the volume of wash-off suspension (3 ml), V_{drop} is the volume of the droplets in the freezing assay experiment (1 μL) and V_{air} is the volume of sampled air at standard temperature and pressure.

For each filter, experiments were repeated three times and combined by binning the data into 1°C temperature intervals and finding a mean number of freezing events in each bin and then the mean fraction frozen. The error bars represent the standard deviation of these repeat runs. In addition, the influence of background INP activity was removed by background subtraction, the full details of which are described in Appendix B. Briefly, for each handling blank and sample the differential freezing spectra ($k(T)$) was calculated. Then, the mean and standard deviation of $k(T)$ for all the handling blanks was calculated and taken to represent our background activity. This background $k(T)$ value was subtracted from the mean $k(T)$ of each sample, and the standard deviations combined in quadrature to represent the total error. After background subtraction

$k(T)$ was converted to a cumulative INP spectra, $K(T)$, from which N_{INP} was calculated. For data points falling in the background this subtraction results in a $k(T)$ value of zero, and no increase in $K(T)$ or N_{INP} at this temperature interval in the cumulative space, however, these points would still have an upper error bar above zero. As such, the measured INP activity at that temperature is consistent with zero but the top of the error bar represents a possible upper limit.

2.2.4 Heat tests

We performed a heat test according to the protocol defined by Daily et al. (2022). Suspensions were prepared as previously outlined and then a 1 mL aliquot of liquid containing the sample was separated. This was placed in a 15 ml centrifuge tube and then heated in a vessel of boiling water for 30 minutes. The liquid was allowed to cool and then tested using a standard μL-NIPI droplet freezing assay.

2.2.5 Gravimetric analysis and ice-active site density calculation

In order to make comparisons of ice-nucleating activity across different samples the surface area of material per droplet can be used to normalise the data and give a value of the number of active sites per unit surface area, $n_s(T)$:

$$n_s(T) = -\frac{\ln\left[1 - f_{\mathrm{ice}}(T)\right]}{A_s} \tag{2.2}$$

Where A_s is the total surface area of particles per droplet. This was estimated for each impactor size bin using the mass of sampled aerosol, the average specific surface area of particles in each bin and the known droplet and suspension volumes (1 μL and 3 mL respectively).

The mass of aerosol sampled in each size bin was determined gravimetrically. Before preparing the suspensions as described above each filter was weighed using a micro-balance (Sartorius Cubis High-Capacity Micro Balance, Sartorius Ltd.). After washing, the filter was removed from the suspension and dried in an oven at 50 °C for approximately 1 hour and weighed again. The difference in mass before and after washing was then taken as the sampled aerosol mass for that size bin. Measurements of such low masses can have a high uncertainty so each filter was weighed 5 times and the mean and standard deviation were calculated. In addition, filters were placed under an anti-static fan before every measurement to minimise errors associated with a build-up of static electricity. To ensure that the process did not alter the mass of the filters themselves 20 new filters which had not been exposed to aerosol were analysed using the same process and the uncertainty was found to be ± 5 μg, which was taken to be the limit of detection for this method. Finally, droplet freezing experiments using the wash-off suspensions from the blank filters were used to confirm that there was no increase in background INP activity and therefore we can assume the process does not introduce contamination.

The average specific surface area of particles in each size bin was estimated using Equation 3:

$$\mathrm{SSA} = \frac{6}{\rho d} \tag{2.3}$$

Where ρ is the density of the particle and d is the diameter of the particle. A value of 2.65 g cm^{-3} was used for ρ, which represents mineral dust, and d was approximated by using the diameter at the middle of each size bin. For stage A which does not have a defined upper size boundary we used a diameter of 4 μm because we were unlikely to collect particles $>$6 μm due to particle losses as a result of high wind speeds, as outlined above.

2.2.6 Particle dispersion and dust concentration modelling

The transport dust from the Copper River was modelled using the FLEXible PARTicle dispersion model (FLEXPART) (Stohl, 2006; Pisso et al., 2019). FLEXPART is a Lagrangian particle dispersion model used to simulate the transport of air parcels by mean flow as well as processes such as turbulent and diffusive transport, turbulence and convection (Pisso et al., 2019). We used FLEXPART to run 10-day forward trajectories of particles released over a four-day period, the results presented in this paper correspond to FLEXPART runs starting at 00:00 on 14th October 2019. Particles were released between 0 and 10 m above the surface in a 300 km^2 region covering the lower reaches of the Copper River Delta and encompassing our sampling sites. Model runs were driven by ERA5 meteorological reanalysis data from the European Centre for Medium Range Weather Forecast (ECMWF) (Hersbach et al., 2020) with a 3-hour temporal resolution, 0.28° x 0.28° (30 km) horizontal resolution and 137 vertical levels. We used an aerosol tracer with characteristics tuned to represent mineral dust, and in particular to accurately represent wet and dry aerosol removal processes. Wet deposition in FLEXPART is partitioned into below- and in-cloud processes, taking into account scavenging by rain and snow as well as the efficiency of particles to act as cloud condensation nuclei or INPs. Scavenging coefficients were chosen based on findings of a multi-year study of mineral dust deposition using FLEXPART (Groot Zwaaftink et al., 2016). Particle sizes in FLEXPART are defined by a log-normal distribution around a mean particle diameter, where the user can specify the mean and sigma values. We tested different particle sizes, corresponding to the size bins of the impactor stages, however the results presented in this study correspond to a mean particle diameter of 1 μm because accumulation mode dust particles dominate the number of dust INPs due to their long lifetime and high concentration. A comparison of modelled INP concentration with different mean particle sizes is shown in Fig. A.3 (Appendix A). When running forward trajectories the total mass emitted can be specified at the start of each model run. Estimates of the total dust mass from a snapshot of a dust plume during a large event in 2006 ranged from 9 to 26 kt, this event continued intermittently for 18 days and hence it was expected that the total mass emitted over the full period was considerably higher (30-80 kt) (Crusius et al., 2011). Comparing satellite imagery from this event to our sampling period suggests that the total emissions during the event we sampled are likely to be considerably less. To capture the possible range of emissions from dust events, and the resulting atmospheric

INP concentrations, we repeated FLEXPART runs with total masses ranging from 1-80 kt (Fig. A.4, Appendix A).

2.2.7 Modelled INP concentrations

From our calculations of n_s, we developed parametrisations of $n_s(T)$ representing dust from the Copper River. For each of the four impactor stages we calculated a mean $n_s(T)$ curve. We then fitted a second-order polynomial to the logarithm of these mean values to yield four different parametrisations, based on particle size. Combining $n_s(T)$ with dust concentration and temperature leads to atmospheric INP concentrations, $N_{\text{INP}}(T)$:

$$N_{\text{INP}}(T) = N_{\text{dust}}\left[1 - \exp(-n_s(T)s)\right] \tag{2.4}$$

$n_s(T)$ is the ice-active site density at temperature T, s is the surface area of an individual particle and N_{dust} is dust number concentration. In this case, N_{dust} can be determined from FLEXPART model results and T set to the ambient atmospheric temperature (T_{amb}) from ERA5 reanalysis data to determine $N_{\text{INP}}(T)$, or the number of particles that might activate to ice at T and within a cloud droplet. The results from model runs shown in this paper represent a particle size of 1 μm hence we used the n_s parametrisation for stage B, which corresponds to 1-2.5 μm, and calculations of s are based on a particle diameter of 1 μm. In addition, dust mass concentrations from FLEXPART were converted to N_{dust} based on a particle diameter of 1 μm and a density of 2.65 g cm^{-3}.

2.3 Results

2.3.1 Fraction frozen and INP concentration

We collected size-resolved samples of airborne dust during a field campaign to the Copper River in Autumn 2019. Using a multi-stage cascade impactor that collects samples onto substrates in four size bins (0.25-0.5 μm, 0.5-1.0 μm, 1.0-2.5 μm and >2.5 μm) we collected multiple samples during dust events, where the mass loading was 10 to 170 μg (see Table 2.1). Substrates from the four impactor collection stages were analysed using droplet freezing experiments, from this we determined fraction frozen (f_{ice}) and INP concentrations (N_{INP}) for each size bin. Details of each sampling period are given in Table 2.1 and the resulting size-resolved f_{ice} and N_{INP} values, as a function of temperature, in Fig. 2.4.

The majority of the data are above the mean handling blank, showing that dust from this region nucleates ice at warmer temperatures than the experimental background. Both fraction frozen and N_{INP} show some size dependence with the larger stages, A and B, freezing at warmer temperatures. This is particularly apparent in samples 191017 (AM) and 191018 which exhibit the largest difference in fraction frozen and N_{INP} between stages A and B compared to C and D.

This shows that larger particles contribute more to the INP population at the source. The sampling periods with higher INP concentrations (191017 (AM) and 191018) corresponded to the periods with greater dust loading, see Table 2.1. Other size-resolved INP concentration measurements in the North American Arctic also show that on at least some days the INP concentrations at temperatures above ∼-20°C are greater in the supermicron size range compared to the submicron range (Mason et al., 2015; Creamean et al., 2018; Si et al., 2019). Hence, this may indicate that local dust sources contribute to the super-micron INP population across the North American Arctic.

Tab. 2.1.: Overview of each sample. Locations A and B correspond to those shown on Fig. 2.2. Wind speeds refer to the measured wind speed at the start of the sampling period. PM10 is calculated from the mass on each stage and the sample volume. The uncertainty in PM10 values combines the standard deviation of the mass measurements for each stage and the instrument uncertainties.

Sample	**Location**	**Sample vol. (L)**	**Wind speed (m s^{-1})**	**Mass per stage (μg)**				**PM10 (μg m^{-3})**
				A	**B**	**C**	**D**	
191013	A	2172	13	41	16	< 5	< 5	26 ± 8
191016	A	1593	15	27	12	20	11	43 ± 11
191017 (AM)	A	1696	15	128	118	9	8	167 ± 6
191017 (PM)	B	1579	17	< 5	10	< 5	7	10 ± 7
191018	A	2255	12	40	75	27	6	66 ± 5

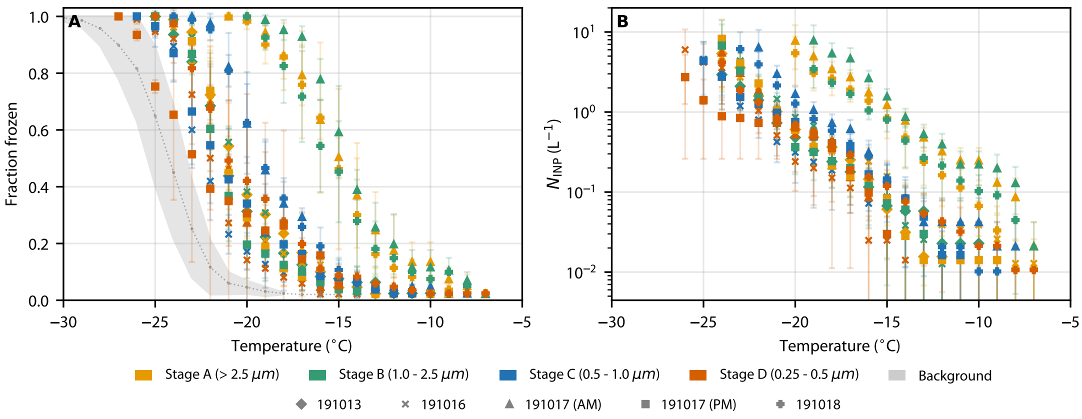

Fig. 2.4.: Size resolved ice-nucleating activity of Copper River Valley dust. (A) Fraction frozen for all samples. (B) INP concentration per standard litre of air for all samples. Different colours represent each of the four collection stages and different symbols distinguish different sampling days. The mean and standard deviation of handling blanks shown in (A) represent the background INP activity used in calculating the error shown by error bars in (B).

2.3.2 Heat sensitivity of samples

We used heat tests to further investigate the INP activity of our samples and identify potential biogenic controls of the nucleation. Ice-nucleating proteins in fungus and bacteria are known to deactivate on heating to ~100°C when immersed in water (Daily et al., 2022). In contrast, the mineral K-feldspar, which often controls the ice-nucleating activity of abiotic mineral dusts, does not deactivate under the standard wet-heat test conditions. Hence, we interpret a decrease in ice-nucleating activity after heating as the presence of an ice-nucleating proteinaceous biological component contributing to the activity of the sample.

Comparing our unheated and heated samples for all size bins (Fig. 2.5) shows a clear reduction in activity. Generally, the larger size bins experienced a greater decrease in activity on heating. Comparing heated and unheated samples in each size range shows that the most significant deactivation occurs in the larger size bins and change in the median freezing temperature, ΔT_{50}, decreases with each size bin. This deactivation, and the fact that the activity was also observed to be size-dependent (Fig. 2.4), suggests that either larger biological particles are present in the glacial dust or that large dust particles have ice-nucleating proteins attached to them. For stages A and B on the 18th October we saw a much smaller decrease in activity (~2°C, vs. a mean of 3.6°C). This perhaps indicates the presence of either heat-insensitive mineral dust (unlikely given the analysis presented below) or heat-insensitive biological materials, such as polysaccharides from pollen. Changing weather and environmental conditions, such as soil moisture, may also affect the emissions of dust. During the field campaign, we experienced rain on 12th and 13th October followed by dry conditions. This meant that throughout the field campaign the surface was drying, however the soil moisture across the delta is likely to vary and the drying itself would depend on sediment composition, particle size and location. Hence it is possible that the characteristics of the dust emissions, such as the size distribution and biological content, change as this drying process progresses and dust can be emitted from different areas. This suggests that the environmental conditions in the watershed influence the ice-nucleating activity of high-latitude dusts.

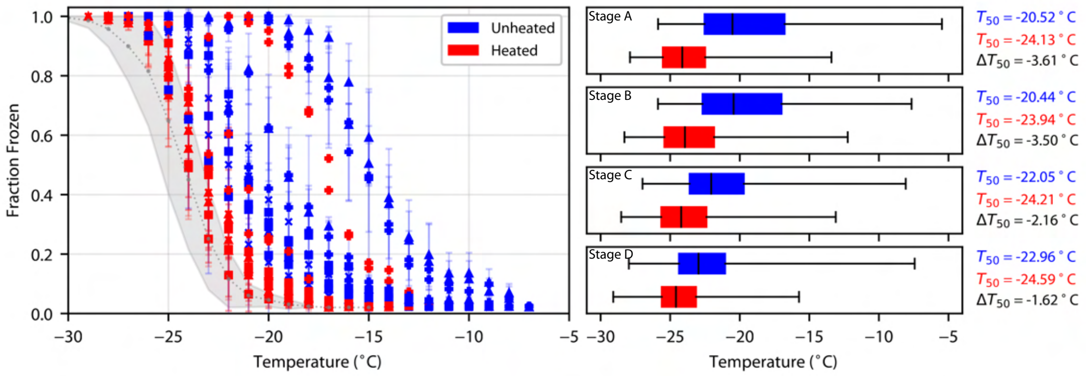

Fig. 2.5.: Heat tests for protein-based biological ice-nucleating entities. Fraction frozen before heating (blue) and after heating (red) of each sample along with box plots for each stage. The box plots include all of the samples, each box represents the 25 and 75 percentiles and the whiskers cover the full spread of the data. The median freezing temperature, ΔT_{50}, is shown with a black line.

2.3.3 Ice-active site density

To quantify the ice-nucleating activity of our Copper River dust samples we normalised the INP concentration data to the aerosol surface area derived gravimetrically to give the ice-active site density, n_s (Fig. 2.6). The general trend across the 5 samples (that we could obtain gravimetric data for) was that the larger particles had a greater n_s than the smaller ones, by approximately one order of magnitude. Reicher et al. (2018) reported that desert aerosol particles in Israel of D_{50} 3.2 μm had a slightly larger n_s than 1.0 μm particles. Similarly, in Leeds UK, Porter et al. (2022) report that the 2.5 to 10 μm size range had a greater n_s than the < 2.5 μm. However, there are other locations where the activity of aerosol does not increase with particle size, for example a measurement from Svalbard indicates that particles between 0.5 μm and 10 μm had very similar n_s values. Overall, it seems that for Copper River Valley dust the larger particles have a greater ice-nucleating activity (on a per surface area basis) than the smaller ones. Since accumulation mode particles will have a longer lifetime than the coarse mode in the atmosphere we would therefore expect the overall activity of Copper River Valley dust to decrease on transport.

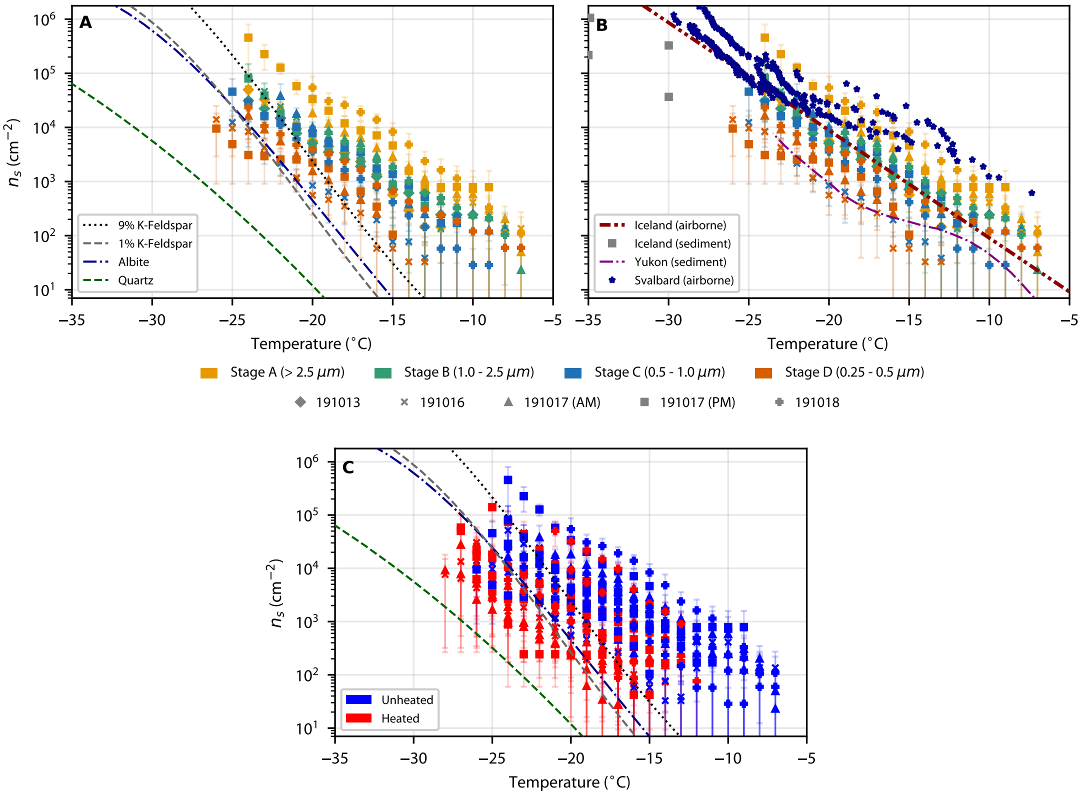

Fig. 2.6.: Size resolved active site density (n_s) of Copper River samples. (A) Comparison of n_s for Copper River dust to n_s parametrisations of ice-active minerals from Harrison et al. (2019) scaled to the mineral content of our bulk sample (from XRD analysis): 9% K-feldspar, 15% quartz and 58% albite. (B) Comparison of n_s for Copper River dust to airborne dust samples from Iceland (Sanchez-Marroquin et al., 2019) and Svalbard (Porter et al., 2020) and sediment samples from Iceland (Paramonov et al., 2018) and the Yukon (Xi et al., 2022). (C) Comparison of the n_s for Copper River dust before and after heating as well as to the same minerals as in (A).

X-Ray diffraction (XRD) of our bulk surface samples (sieved to 45 μm) highlights the presence of a number of known ice-active minerals, namely Potassium (K-) feldspar (8.94%), quartz (15.41%) and albite (57.61%) (as well as 5.86% muscovite, 7.99% calcitep, 4.19 % other). Hence, in Fig. 2.6A we plot the corresponding scaled n_s curves for the three minerals with the greatest ice-nucleating ability (K-feldspar, quartz and albite) (Harrison et al., 2019). These proportions were derived for 45 μm sieved dust and the amount of these minerals in the aerosol fractions is very likely different (most likely smaller), hence quantitative comparison with our measured n_s values should bear this in mind. Nevertheless, we can draw useful conclusions from this comparison. Due to its high ice nucleating activity and abundance, we would expect K-feldspar to be the most important mineral for ice nucleation. However, our samples show a much shallower slope and higher activity at warmer temperatures (Fig. 2.6A) compared to a scaled parametrisation of pure K-feldspar. Similarly, both albite and quartz are considerably less active than our samples. This suggests that conversely to low-latitude African desert dust (Harrison et al., 2022a; Price et al., 2018), the activity of dust from the Copper River is not controlled by K-feldspar or other ice-active minerals at temperatures above about -20°C. At temperatures below -20°C K-feldspar may account for an increasing proportion of the ice nucleating activity of our samples.

In Fig. 2.6B we compare our n_s values for Copper River Valley dust to n_s for other northern high-latitude samples. Comparing our Copper River Valley results to n_s for Icelandic dust sampled from an aircraft reveals that the dust from the two very different locations has very similar activity and the parametrisation of the Icelandic dust fits our data well. Xi et al. (2022) report the ice-nucleating activity of dust samples from a glacial valley in the Yukon, Canada (on the other side Chugach mountain range, 300 km away from the Copper River Delta). Their results fall at the low end of the range of our data. Porter et al. (2022) report size-resolved n_s values for a sample collected from a ship near Longyearbyen in Svalbard. As mentioned above, they do not observe a clear dependence on aerosol particle size, but their n_s values do overlap with the upper end of our range of n_s values. Paramonov et al. (2018) used a continuous flow diffusion chamber to study the ice nucleating activity of Icelandic dust (amongst others), their n_s values extend our literature comparison to lower temperatures. Interestingly, they found that n_s for 200 nm particles was greater than that for 400 nm particles, the opposite trend to what we observed. This comparison with the literature suggests that the ice nucleating activity of aerosol around the Arctic varies by at least two orders of magnitude and that the size dependence of n_s also varies.

In Fig. 2.6C we plot the n_s values for unheated and heated samples of Copper River Valley dust (this is the same data as in Fig. 2.5). The bulk of the samples are heat sensitive across the whole temperature range and fall into the regime defined by the minerals after heating. It is important to note that the mineral lines are defined using mineral proportions determined by XRD for a 45 μm sieved fraction and the fact that the heated n_s values fall below the K-feldspar line indicates that there is indeed less K-feldspar in the sample than the 8.94% defined by XRD. Xi et al. (2022) report that the ice-nucleating activity of dust samples from a glacial valley in the Yukon, Canada was dominated by biological material above -15°C. They did a further test using ammonium salts, which are known to enhance the ice nucleating activity of minerals (Whale et al., 2018), to show that the INP population below -15°C was dominated by mineral particles. This contrasts with dust from the Copper River Valley where there is heat sensitivity to below -25°C. This is consistent with Fig. 2.6B where we find that the Copper River valley dust is as much as 2 orders of magnitude more active than that from the Yukon. This difference is perhaps related to the watershed and vegetation cover at the two sites. Xi et al. (2022) sampled dust originating in the Äay Chù Valley and the Kaskawulsh glacier. The Äay Chù River begins at the Kaskawulsh glacier and runs approximately 25 km before terminating in Kluane Lake, this is in contrast to the Copper River which is over 450 km long and has a watershed of over 62000 km^2, much of which is vegetated. The smaller watershed means there is less vegetation and less variability in vegetation types (determined by comparing the land cover of the Copper River watershed (Fig. A.2 Appendix A)) with satellite imagery and leaf area index of the Äay Chù Valley (from NASA WorldView). Vegetation is related to the various fungal and bacterial entities that are known ice-nucleating particles. Also, ice-nucleating proteins can become bound to mineral particles when suspended in water (O'Sullivan et al., 2015); this may occur in river water leading to ice-active proteins being bound to mineral particles. Hence the greater biological INP content of the Copper River Valley dust compared to that of the Yukon samples may be evidence that the ecosystem of the watershed defines the ice-nucleating ability of the dust that is emitted.

2.3.4 Dust transport from the Copper River valley

To assess the contribution of the Copper River Valley to INP concentrations across the wider region, we used the FLEXible PARTicle dispersion model (FLEXPART) to run 10-day forward trajectories of particles released from the Copper River Delta. FLEXPART is a particle dispersion model used to simulate the transport of air parcels in the atmosphere. Tracers are given properties that represent mineral dust and removal processes, such as scavenging by rain and snow, are included (see the Methods section for details). In Fig. 2.7 we show the results of one simulation where 15 kt of dust was released over four days, starting on 14th October 2019. Emissions from the Copper River are controlled by strong winds from the north or north east. These winds arise due to a pressure gradient driven by high-pressure systems over Alaska and a low-pressure system over the Gulf of Alaska (Crusius et al., 2011; Schroth et al., 2017). On a smaller scale, wind speed and direction are influenced by local topography; air is channelled down river valleys and into the Gulf of Alaska leading to 'gap' winds (Crusius, 2021). We observed this during our sampling period where wind speeds were very low (< 2 ms^{-1}) between Cordova and the western edge of the river delta and then rapidly increased, up to as much as 25 ms^{-1}, once on the delta itself. These gap winds lead to initial emissions from the Copper River being transported southwards, as can be seen in our model results with a plume of high total dust mass extending over the Gulf of Alaska.

After 48 hours the observed pressure gradient is reduced and the dust plume is influenced by two low-pressure systems: the first to the west of the Copper River and another to the south, over the Gulf of Alaska. After 48 hours we observe two 'arms' in the modelled dust plume where dust has been entrained in both of these systems. Low-pressure systems such as those observed during this period are common in this region, in particular, the Aleutian low is a semi-permanent low-pressure system located near the Aleutian Islands (to the south west of the Copper River Delta). The position of this system has been shown to play an important role in controlling dust emissions and transport from the southern coast of Alaska (Schroth et al., 2017). After 96 hours the modelled dust has been transported over the Bering Sea and western North America. Whilst the total dust mass is relatively low in some regions a region of high concentration (0.02 g m^{-2}) remains close to the southern coast of Alaska. This pattern persists after 144 hours and after both 96 and 144 hours is associated with the centre of a low-pressure system. This suggests the circulation prevents transport over a larger area and further reinforces that the position of the Aleutian low and other low-pressure systems in the Gulf of Alaska have a strong control on the transport of dust from the Copper River. After 192 hours the low pressure system begins to dissipate and the dust begins to disperse. However, total dust mass loading of around 0.002 g m^{-2} is predicted. These mass loadings are of a similar magnitude to those predicted for dust in this region transported from lower latitude sources (Shi et al., 2022).

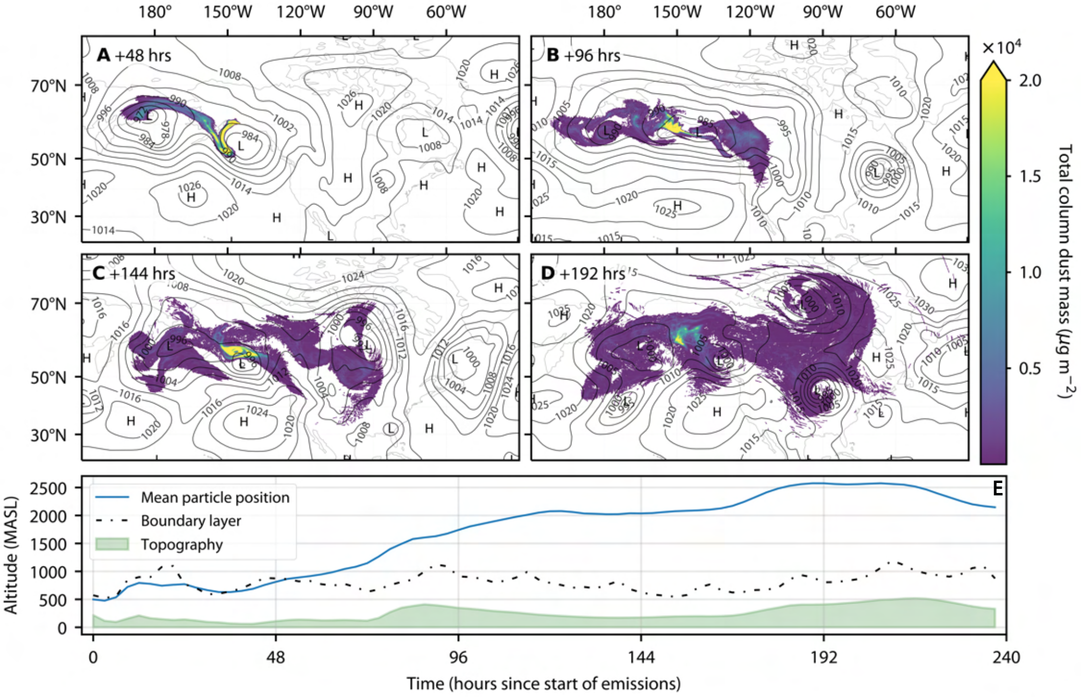

Fig. 2.7.: FLEXPART results from a 10-day simulation of a dust event at the Copper River Delta. (A to D) Transport of 15 kt of dust that was released over 4 days, starting 14th October 2019. The total column dust mass (0-10000 magl) for 48, 96, 144 and 192 hours after the start of the emission period are shown. (E) The vertical profile of the mean position of released particles (blue line), the boundary layer height (dashed line) and topography (green) along this trajectory.

The vertical profile in the lower panel of Fig. 2.7 shows the mean trajectory of emitted particles. For the initial 48 hours of the simulation, much of the dust remains within the boundary layer, however after 48 hours this trajectory begins to increase in altitude, this coincides with the interaction with low-pressure systems suggesting these systems contribute to the vertical transport of dust out of the boundary layer. The vertical trajectory reaches altitudes of 2500 metres above sea level (MASL) and shows that much of the emitted dust has been transported out of the boundary layer, meaning there is potential for this dust to reach regions in the atmosphere where temperatures are low enough for the dust to nucleate ice and influence clouds. In order to investigate this further we combined modelled dust concentrations with our parametrisation of n_s for dust from the Copper River and ambient temperatures (from ERA5 reanalysis data (Hersbach et al., 2020)) to estimate atmospheric INP concentrations.

Fig. 2.8B shows dust concentrations between 0 and 5000 MASL at 100 m vertical resolution along a transect at 62°N and, in agreement with Fig. 2.7, highlights vertical transport of dust with concentrations exceeding 15 μg m^{-3} up to 5000 MASL. We calculated mean dust concentrations in this region of high concentrations (within the red box), shown in Fig. 2.8C. It is clear from both Fig. 2.8B and C that the peak in dust concentrations is between approximately 2000 and 4000 MASL, where the temperatures range from -5 to -20°C. The ambient INP concentration reveals appreciable INP concentrations above approximately 2000 MASL, where the temperature drops below -5°C (and is therefore within the constraints of our n_s parametrisation). At approximately 4000 MASL, dust mass concentrations are still as high as 6 μg m^{-3} and N_{INP} exceeds 1 L^{-1}. This is an appreciable INP concentration and is within the range that is thought to substantially reduce supercooled water content and alter cloud radiative properties (Vergara-Temprado et al., 2018) hence INPs from the Copper River at the concentration we have estimated are likely to have an impact on mixed-phase clouds in this region.

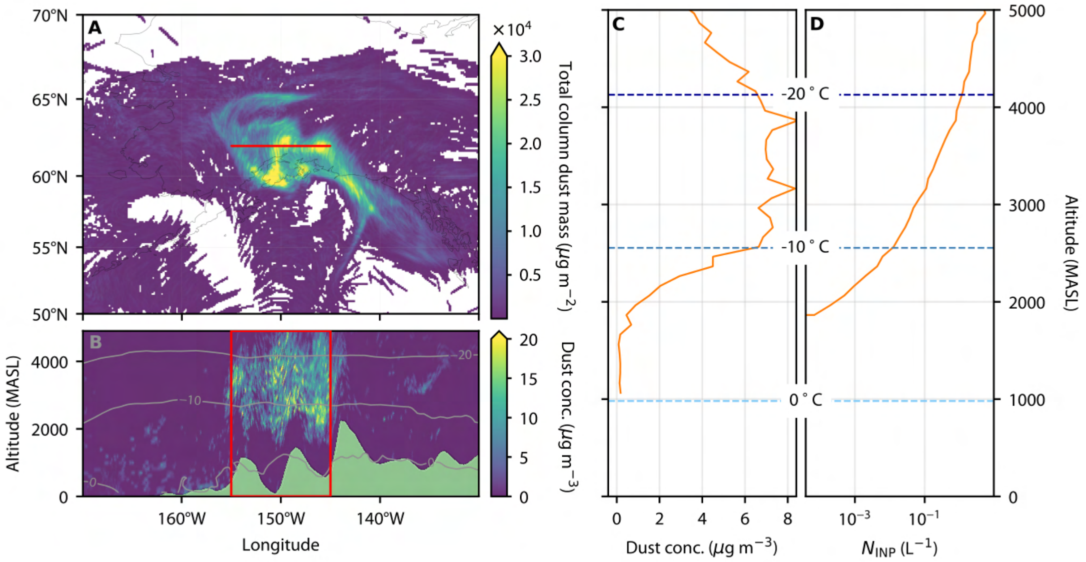

Fig. 2.8.: Case study of dust and INP concentrations after 60 hours. (A) Total dust mass integrated over 0-5000m column. (B) Vertical transect of dust concentrations along the red line shown in (A). Isotherms (from ERA5 reanalysis data) are shown in grey and topography (from FLEXPART output) is shown in green. (C) Vertical profile of mean dust concentration calculated within the red box shown in (B). Dashed lines represent isotherms of mean temperature in the same region. (D) Vertical profile of ambient INP concentration calculated using our n_s parametrisation, dust concentrations shown in (C) and the mean temperature

Vergara-Temprado et al. (2017) estimated a global distribution of INPs, based on feldspar and marine organics. Feldspar is an important component of desert dust and therefore can be used to represent the contribution of desert dust to global INP concentrations. In the region of the Copper River and Alaska, they estimate an annual mean INP concentration, based on feldspar, of approximately 1x10^{-4} L^{-1} at -15°C. This is considerably lower than the concentrations we have modelled in this study at -15°C, suggesting that INPs originating from the Copper River could dominate over those from low-latitude sources.

There are some limitations with the simple modelling approach used in this study, namely that we used an estimation of emitted dust rather than modelling it with a dedicated emission scheme. To investigate the effect of varying the initial mass of dust emitted, we completed the same analysis with total dust emissions between 1 and 80 kt. These encompass the range of total mass emissions estimated from different methods during a large dust event (Crusius et al., 2017) but could also represent dust events of different sizes or intensities. We found that the INP concentrations at -20°C ranged from $5\text{x}10^{-2}$ to $1\text{x}10^{1}$ L^{-1} (Appendix A), this shows that even with a more conservative estimate of the total dust emissions INP concentrations still exceeded 0.1 L^{-1}. In addition, in this study we have investigated emissions from one source, however, the south coast of Alaska has many similar regions where dust emissions have been observed concurrently. During such events, the total mass emitted across numerous active dust sources is likely to be considerably higher than our estimates and hence atmospheric dust and INP concentrations could also be much higher. With this in mind, our calculations represent a reasonable first estimate of INP concentrations but also highlight the need for further study and better representation of emissions from high-latitude dust sources in global models.

2.4 Discussion

In this study, we show that glacial dust from the Copper River, Alaska nucleates ice at temperatures relevant for mixed-phase clouds. Using FLEXPART for particle dispersion modelling we show that dust from the Copper River may contribute to aerosol concentrations over a large geographical area. In combination with the size-resolved ice-nucleating activity measurements, modelling shows that this dust can be lofted by meteorological phenomena typical of this region, to altitudes where it is sufficiently cold that it can contribute a substantial INP population that out-competes INPs associated with distant desert sources. The Copper River Valley is one of many such sources on the south coast of Alaska and the wider Arctic, hence these results indicate the importance of the inclusion of high-latitude dust in global models.

Using XRD analysis we identified the mineral composition of this dust and found minerals that are known to be important for ice nucleation, such as potassium feldspar. We were able to compare our results to parametrisations of these ice-active minerals and found that the parametrisations did not match the activity of our samples, suggesting that the observed ice-nucleating activity was not controlled by the mineral composition of the particles, in contrast to dust from low-latitude deserts. This was further supported by heat testing the samples which revealed that all samples were sensitive to heating, with the most deactivation observed in the larger size bins. From these results, we conclude that there is a heat-sensitive biogenic component that controls the nucleation, particularly at temperatures warmer than -20°C, and we propose that this could be a result of the mixing of glacial dust with biogenic material during transport or growth of biogenic material over time. This finding is of particular importance because it shows that not only do dust concentrations need to be correctly modelled but also that parametrisation of ice-nucleating particles must be adapted to correctly represent high-latitude sources in order to better represent primary ice production and its role in cloud properties and climate feedbacks. In addition, we found that our samples differed from those from other similar high-latitude sources, such as glacial dust studied by Xi et al. (2022), and were considerably more active (higher n_s values) which may be due to greater biogenic content in our samples. This suggests that the local environment, specifically the river catchment, influences the processing of glacial dust and alters the ice-nucleating properties of transported sediments. This is also an important consideration when representing high-latitude dust sources in global models but further studies are needed to better understand the variability in ice-nucleating activity of high-latitude dust.

We have investigated one important high-latitude dust source however there are still very few studies of this nature and there are many dust emissions regions in northern and southern high latitudes that have not been studied. Linking field observations with modelling of dust transport is a crucial step in determining the contribution of high-latitude dust to atmospheric INP concentrations however many previous studies have focused on either observations or modelling. For example, Tobo et al. (2019) and Xi et al. (2022) identified high-latitude sources of INPs but did not investigate the transport and atmospheric concentration of INPs from these sources whereas Shi et al. (2022) and Kawai et al. (2023) studied the contribution of HLDs to INPs in the Arctic but used a single parameterisation to represent all HLDs. In addition, studies such as Sanchez-Marroquin et al. (2020) and Kawai et al. (2023), use global aerosol models that require significant resources and expertise to run. The approach outlined in this paper offers a methodology to investigate potential INP sources, from observations at the source through to modelling atmospheric concentrations, that could easily be applied to other high-latitude dust sources. Using portable battery-powered sampling equipment, which is easy to carry and deploy in the field, opens up the possibility of making measurements in more inaccessible regions where larger field campaigns would be impractical and expensive. In addition, we chose to use FLEXPART over a more complex aerosol model because it is a computationally inexpensive, open-source model that can be easily tailored to different scenarios and run without extensive modelling experience. Applying this approach to other high-latitude dust sources would provide a comprehensive first estimate of INP concentrations which can be used to help inform which dust sources need to be included in global models.

3

Using remote sensing to explore ice formation in mixed-phase stratiform clouds at Summit Station, Greenland

3.1 Introduction

The Greenland Ice Sheet (GrIS) has been losing mass at an accelerating rate since the late 1990s, primarily due to changes in the surface mass balance (SMB) driven by increased surface melt (Hanna et al., 2013; van den Broeke et al., 2016; Slater et al., 2020). As a result, the GrIS is currently the largest single contributor, by mass, to sea-level rise (Bamber et al., 2018; Hofer et al., 2020), making up 60% of the contribution to sea-level rise from ice sheets (Slater et al., 2020). Clouds play a fundamental role in the surface mass balance (SMB) of the GrIS, influencing both mass loss and mass gain. Clouds control the amount and distribution of precipitation on the ice sheet, which provides a mass input and drives inter-annual SMB variability (van den Broeke et al., 2009). They also modulate the surface energy budget (SEB) which in turn influences surface melt (Bennartz et al., 2013; Miller et al., 2017). Hence, understanding the role of clouds in the SMB is crucial. Low-level mixed-phase clouds are of particular interest due to their warming effect over the ice sheet (Miller et al., 2015) which can increase ice sheet runoff (Van Tricht et al., 2016) and enhance both the intensity and extent of extreme melt events (Niwano et al., 2019; Gallagher et al., 2020; Bennartz et al., 2013). As outlined in Chapter 1, mixed-phase clouds are highly sensitive to the presence of aerosols and can be influenced by both cloud condensation nuclei (CCN) and ice-nucleating particles (INPs). The modification of cloud properties and precipitation processes by aerosols over the GrIS has a resulting effect on the SMB, hence understanding the interactions between aerosols and clouds is vital for accurate predictions of GrIS melt.

Almost half of the snowfall falling on the GrIS each year is from precipitation events associated with mixed-phase clouds (McIlhattan et al., 2020; Pettersen et al., 2018). In the accumulation zone, precipitation from mixed-phase clouds is a major driver of changes to the SMB, contributing over 50% of the total annual accumulation (Pettersen et al., 2018). Comparisons of observations with model predictions of precipitation show that models generally overestimate precipitation frequency and accumulation (Kay et al., 2018; Lenaerts et al., 2020b), whilst simultaneously underestimating the presence of liquid-bearing clouds (McIlhattan et al., 2017). This suggests that ice-related processes such as the Wegener-Bergeron-Findheisen (WBF) process are overactive in these models, causing over-efficient scavenging of supercooled liquid (McIlhattan et al., 2017). The WBF process is strongly linked to INP concentrations (N_{INP}) and in other regions of the world, improving the representation of N_{INP} has reduced similar biases in model predictions of liquid cloud fraction (Vergara-Temprado et al., 2017). However, to date, there have not been any observations of INPs on the GrIS and N_{INP} remains a major uncertainty in accurately modelling precipitation associated with mixed-phase clouds in Greenland.

The amount of ice in clouds is not only affected by primary ice production (PIP), which is modulated by N_{INP}, but also by secondary ice production (SIP) which can result in N_{ice} being several orders of magnitude larger than N_{INP} (Hobbs, 1969; Mossop, 1985; Rangno and Hobbs, 2001a; Korolev and Leisner, 2020). Several pathways by which SIP contributes to N_{ice} have been proposed (as outlined in Chapter 1) however the relative importance of different SIP mechanisms, and the environmental conditions under which they occur, is still not well understood. In addition, the minimum concentration of INPs required to trigger SIP is not well defined (Sullivan et al., 2018). Many previous studies have focused on the Hallet-Mossop (HM) process which takes place at temperatures between -3 and -8°C (Hallett and Mossop, 1974), however, observations in mixed-phase clouds at colder temperatures have also shown N_{ice} of many orders of magnitude more than N_{INP} Korolev et al. (2022); Pasquier et al. (2022). The dominant SIP mechanism at temperatures below -8°C has not yet been clearly identified. Observations at Summit Station, at the highest point on the GrIS, show that the mean (1992–2019) surface temperature in the summer months is around -13°C (Hanna et al., 2021) and that clouds are present more than 85% of the time (Shupe et al., 2013). Therefore, SIP processes that occur below the HM regime are likely to be important.

Investigating PIP and SIP requires knowledge of both N_{INP} and N_{ice}. Whilst there has been a resurgence in INP measurements in recent years (DeMott et al., 2018; Burrows et al., 2022), there are limited concurrent observations of N_{INP} and N_{ice}; hence, the link between them is poorly understood and the relative importance of primary and secondary ice formation in mixed-phase clouds remains unclear (Zhao and Liu, 2022). This dearth of observations is, in part, because making observations of both INPs and ice in clouds is challenging. INPs are rare, with concentrations often much lower than the overall aerosol concentration, so long sampling times are required. Measuring N_{ice} has its own challenges; in-situ observations, such as from an aircraft, are limited in their spatial and temporal resolution and are affected by sampling biases as a result of crystal shattering while sampling at high speeds. Measurements in Greenland have also been limited by the remoteness of the region. This means that observations of INPs in Greenland have been limited to atmospheric sampling at coastal sites (Wex et al., 2019; Sze et al., 2023) or analysis of ice cores (Schrod et al., 2020) and observations of N_{ice} in clouds over the GrIS have not been made.

In recent years, remote sensing techniques have increasingly been used to make observations of clouds. Satellite observations, such as *CloudSat* (Stephens et al., 2002) and *Cloud Aerosol Lidar and Infrared Pathfinder Satellite Observations* (CALIPSO; Winker et al., 2010) and networks of ground-based remote sensing instruments, such as the Atmospheric Radiation Measurement (ARM) program and Cloudnet (Illingworth et al., 2007), allow measurements of cloud properties around the globe. However, determining microphysical properties from remote sensing observations is not a trivial task. Retrieving N_{ice} is particularly challenging, and the strong variability in the shape and size of ice crystals means prior knowledge of crystal size is a requirement of many retrieval methods. As outlined in Section 1.6.2, radar and lidar operate at different wavelengths making the received signals sensitive to distinct moments of the particle size distribution. Several approaches have been developed to exploit this wavelength dependence to estimate N_{ice} when concurrent radar and lidar observations are available (Delanoë and Hogan, 2010; Cazenave et al., 2019; Sourdeval et al., 2018; Gryspeerdt et al., 2018). However, when dealing with optically thick clouds, the lidar signal is quickly extinguished, rendering such retrieval methods ineffective. Bühl et al. (2019) propose an alternative approach that uses terminal fall velocity (v_{t}) to determine particle size and estimate N_{ice}. This method offers a viable solution for clouds or cloud regions that cannot be penetrated by lidar.

In this study, we make use of a unique year-long dataset of INP measurements and long-term remote sensing observations from Summit Station, at the highest point of the GrIS, to investigate primary and secondary ice production and the role of INPs in Arctic clouds. We apply the method from Bühl et al. (2019) to the instrumentation available at Summit Station to determine N_{ice} at Summit Station for the first time. By comparing these observations with meteorological measurements and INP data we identify regions of potential primary and secondary ice production. Summit Station has a unique environment due to its high-altitude location on the Greenland Ice Sheet, however stratiform mixed-phase clouds observed here have a similar structure to those elsewhere in the Arctic (Shupe et al., 2013) hence this study provides valuable insights into ice production in climatically important mixed-phase clouds.

3.2 Methods

3.2.1 Measurement location and instrument setup

Summit Station (Summit) is a high-altitude, high-latitude year-round Arctic research station located at the highest point of the Greenland Ice Sheet (Fig. 3.1a). Summit is operated by the US National Science Foundation. Since 2010, a suite of ground-based remote sensing instruments (Fig. 3.1b) has been deployed at Summit as part of the ICECAPS (Integrated Characterization of Energy, Clouds, Atmospheric State, and Precipitation at Summit) project (Shupe et al., 2008a). In 2019, the ICECAPS project was expanded to include surface measurements of aerosols, including INPs, for the Aerosol Cloud Experiment (ICECAPS-ACE) (Guy et al., 2021). In this study, we make use of ICECAPS observations from June-November 2019. An overview of instruments used for cloud and meteorological observations is provided in Table 3.1, and key data processing procedures are outlined in Sections 3.2.2-3.2.5. INP sampling and analysis are described in Section 3.2.6. Finally, the retrieval of ice crystal number concentration is described in Section 3.2.7.

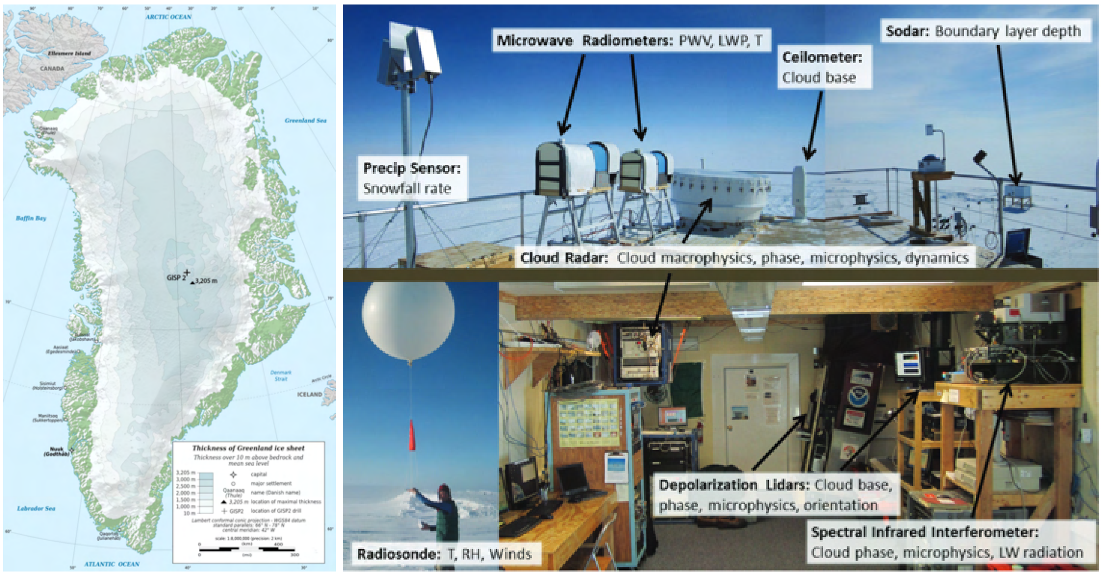

Fig. 3.1.: Map of Greenland (by Eric Gaba under CC BY-SA 3.0) and overview of ICECAPS instruments (from Shupe et al., 2013). Summit Station is at the location of the GISP2 drill site.

Tab. 3.1.: Instrument specifications and measurements used in this study

Instrument	Key Specifications	Measurements	Application
Millimeter cloud radar (MMCR)	Ka-band (35 GHz), 8 mm wavelength, 2 s time res., 45 m vertical res.	Reflectivity, Doppler velocity, Doppler spectrum width	N_{ice} retrieval, IWC, vertical air motion
Micropulse lidar (MPL)	532 nm wavelength, 15 s time res., 15 m vertical res.	Backscatter, depolarization ratio	N_{ice} retrieval, cloud phase
Microwave radiometer (HATPRO)	7 channels 22-32 GHz, 7 channels 51-59 GHz, 2-4 s time res.	Downwelling brightness temperature	LWP, PWV, atmospheric temperature
Sodar	2100 Hz, 1 s time res., $<$1m vertical res.	Reflectivity	Boundary layer structure
Precipitation occurrence sensor system (POSS)	X-band (10.5 GHz), 1 min time res.	Reflectivity, Doppler spectra	Snowfall occurrence at the surface
Vaisala RS41-SG radiosondes	1 s time res., 00:00 and 12:00 UTC	Temperature, relative humidity, pressure, wind	Temperature, atmospheric structure
Ice particle images (icePIC)	Canon D50 DSLR, 5.6x magnification, 1 μm resolution	Digital photographs	Ice crystal shape

3.2.2 Millimeter cloud radar

The Millimeter cloud radar (MMCR; Moran et al. (1998)) is a zenith-pointing, Ka-band (35 GHz), single-polarization, Doppler cloud radar operating at an 8 mm wavelength. Doppler spectra are produced from the backscatter signals in each range gate of the radar using fast Fourier transform (FFT) techniques (Kollias et al., 2007c). The first three moments of the Doppler spectra correspond to the reflectivity, mean Doppler velocity, and Doppler spectrum width. Four different data acquisition modes each with slightly different operational parameters (e.g. vertical resolution, number of FFT points, Spectral averaging time) are cycled through sequentially whilst the MMCR is in operation (Moran et al., 1998; Clothiaux et al., 1999; Widener and Johnson, 2005). Each of these modes enhances the sensitivity of the radar in a different way, allowing data to be recorded concurrently that is suitable for a range of intended applications. In this study mode 1 is used because in the lowest 3 km of the atmosphere it is the most sensitive of the four modes, making it the most suitable for investigating boundary layer clouds (Widener and Johnson, 2005; Clothiaux et al., 1999). In mode 1 the Doppler spectral moments are determined using 64 FFT points and spectral averaging uses 64 Doppler spectra. The radar reflectivity, mean Doppler velocity and Doppler spectrum width are calculated at 2 s time resolution and 45 m vertical resolution with a measurement uncertainty 0.5 dB for reflectivity and 0.1 ms^{-1} for Doppler velocity and Doppler spectrum. For the applications in this study, the full Doppler spectrum data were not required so the ICECAPS data product containing the calculated moments was used (Shupe, 2020).

The data also include the signal-to-noise ratio (SNR) which expresses the relative intensity of the radar return signal from a cloud compared to the noise in the receiver and is used to remove data where there is no atmospheric signal (Kollias et al., 2005, 2007b). SNR values are associated with potentially large errors in the Doppler moments, to account for this data where SNR was less than -14 were removed. It is sometimes necessary to correct for attenuation of radar signals due to atmospheric gases and hydrometeors (Illingworth et al., 2007; Kalogeras and Battaglia, 2022), however in this case attenuation corrections were deemed unnecessary. At millimetre wavelengths, liquid precipitation is an important source of attenuation (Moran et al., 1998) but at Summit rainfall has only been observed once since records began (NSIDC, 2021) so this does not need to be considered (yet...(Lenaerts et al., 2020a)). Correcting for attenuation due to liquid water was also deemed unnecessary. For a 94 GHz radar and a cloud with a liquid water path (LWP) of 500 g m^{-3} the attenuation would be around 4.5 dB (Illingworth et al., 2007) however, at Summit where LWP rarely exceeds 50 g m^{-3} (Shupe et al., 2013), and at the 35 GHz frequency of the MMCR, the attenuation would be substantially smaller and can be considered negligible (Moran et al., 1998). Attenuation due to ice crystals is also negligible for mm-wavelength radar (Lhermitte, 1990; Moran et al., 1998; Bühl et al., 2019; Kalogeras and Battaglia, 2022).

A number of secondary parameters were calculated from the MMCR dataset. First, the radar reflectivity was used to determine cloud top height (CTH), the MMCR was used for this rather than a combined lidar/radar approach (e.g. Clothiaux et al., 2000) because the lidar is more quickly attenuated by liquid water and often cannot penetrate to the very top of clouds with a supercooled liquid layer. Hence, cloud boundaries were defined from the radar echo at each timestep of the MMCR data. The top of the lowest cloud layer was determined by finding the highest consecutive radar pixel with a signal-to-noise ratio of >-14 dB and a reflectivity of >-40 dBZ before a gap of at least two height intervals (90 vertical m). CTH determined in this way was validated against the height of cloud layers determined from twice-daily radiosonde launches and found to provide an acceptable estimate of CTH.

Radar reflectivity was also used to derive ice water content (IWC) according to the relationship between radar reflectivity, temperature and IWC as per Hogan et al. (2006):

$$\mathrm{IWC} = 0.072Z - 0.0233T - 1.70 \tag{3.1}$$

where Z is reflectivity in dBZ and T the atmospheric temperature in °C. Since IWC is used to make qualitative comparisons between case studies the uncertainties in the calculation were not calculated.

A key part of the algorithm for calculating ice crystal number concentration (Section 3.2.7) relies on the relationship between particle size and terminal fall velocity, so Doppler velocity was used to calculate the terminal fall velocity of hydrometeors. The mean Doppler velocity (v_D) measured by a vertically pointing radar measures the relative speed of hydrometeors moving towards or away from the detector however, these measured velocities include both the reflectivity-weighted terminal fall velocity of hydrometeors (v_t) and the vertical air motion (v_air): $v_D = v_t + v_{air}$. To determine v_t from the measured Doppler velocity, a method to estimate v_air is necessary. While Bühl et al. (2019) employed radar wind profiler (RWP) measurements, Summit lacks an RWP. Hence, we explored alternative methods to obtain v_t.

In uniform stratiform cloud systems, vertical air motion tends to be small compared to the fall velocity of hydrometeors (Protat and Williams, 2011; Matrosov and Heymsfield, 2000; Orr and Kropfli, 1999) and, over a sufficiently long time period, the small-scale vertical air motions average to zero. Under this assumption, establishing a power-law relationship between Z and v_t ($v_\mathrm{t} = aZ^b$) and assuming that deviations from this curve are due to vertical air motion enables a statistical determination of v_t (Orr and Kropfli, 1999; Delanoë et al., 2007). However, this approach assumes the $v_\mathrm{t} - Z$ relationship is uniform throughout the cloud which is unlikely to be true, especially in the vertical direction, due to microphysical processes such as crystal growth and aggregation (Protat and Williams, 2011). To account for this, here we used a v_t-Z relationship that also includes height (H) as a parameter, as proposed by Protat and Williams (2011) and further developed by Kalesse and Kollias (2013). Following this method, the cloud is considered in time segments of 20 minutes and the data is grouped into Z-H pairs by separating the reflectivities into 2 dBZ bins and the heights into 45 m vertical bins (the native resolution of the MMCR). A time interval of 20 minutes was chosen as this is deemed long enough to filter the vertical air motion when averaging v_D without smoothing out small-scale features (Kalesse and Kollias, 2013). In each time interval, the average v_D was found for each Z-H pair and taken to equal v_t. Then the linear regression coefficients of the $v_\mathrm{t} = aZ^b$ relationship were computed for each time interval. From this, v_t was computed at the 10 s time resolution and 45 m vertical resolution of the radar reflectivity data. An example of the result of this calculation is shown in Fig. 3.2. Finally, the uncertainty in v_t was calculated by combining the measurement uncertainty of v_D with the sum of the squared residuals from the $v_\mathrm{t} = aZ^b$ fit in quadrature.

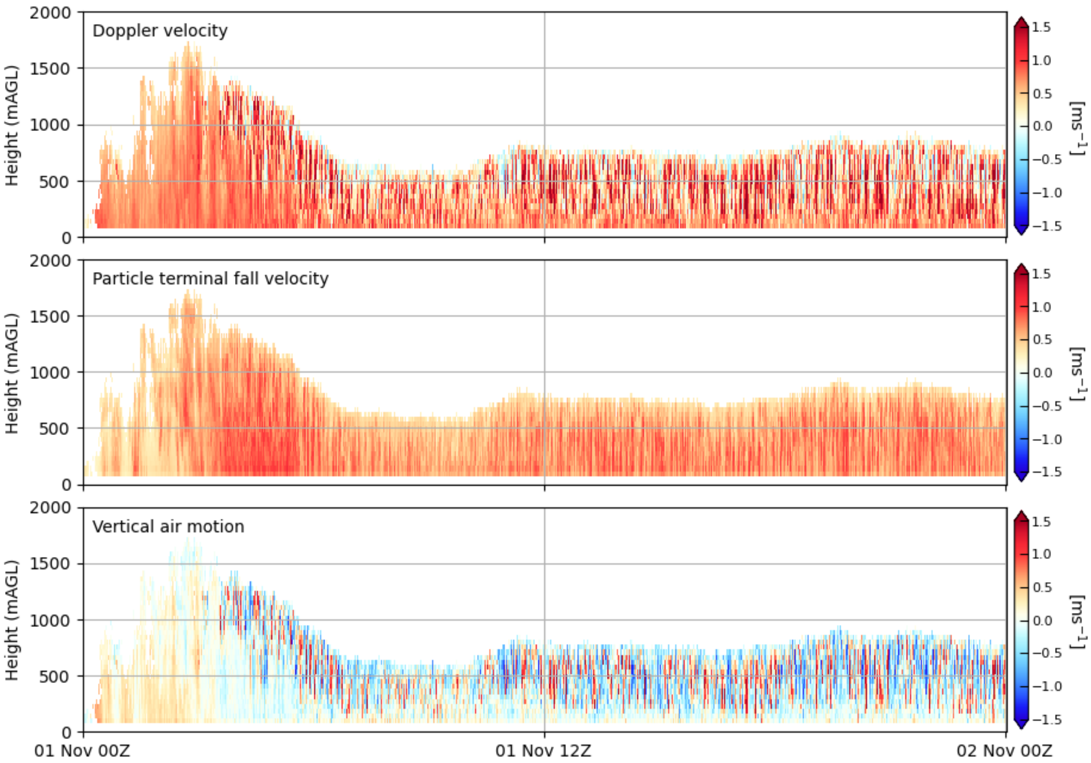

Fig. 3.2.: Time-height plot of Doppler velocity (a) from MMCR on 1st November 2019, particle terminal fall velocity (b) and vertical air velocity (c) calculated using $v_t - Z - H$ approach. Positive (red) values indicate motion towards the radar

An alternative approach for calculating v_{air} and v_{t} is to identify different populations of hydrometeors (e.g. liquid and ice) in individual Doppler spectra and calculate the vertical air motions based on the velocity of small liquid droplets (Shupe et al., 2008b; Radenz et al., 2019). However, this relies on being able to identify distinct peaks in the Doppler spectrum, in particular a liquid droplet mode, which was not always possible in these case studies.

3.2.3 MicroPulse Lidar

The MicroPulse Lidar (MPL; Campbell et al. (2002); Flynn et al. (2007)) is a ground-based, eye-safe lidar operating at 532 nm and oriented 2°-4° off zenith. The MPL is a dual-polarization lidar that detects the backscatter in two polarization channels: 'cross-polarized' (channel 1, denoted with the subscript $\perp$) and 'co-polarized' (channel 2, denoted with the subscript $\|$). Channel 1 is more sensitive to non-spherical particles (e.g. ice) whereas channel 2 is more sensitive to spherical particles (e.g. water). This configuration means the ratio between the two signals, the de-polarization ratio (Flynn et al., 2007), can be used to distinguish between spherical and non-spherical particles. The MPL at Summit is 'fast-switching' meaning it alternates between channels on every pulse (2500 Hz rate). The ICECAPS MPL data product contains vertical profiles of backscatter in each channel at a time resolution of 5 seconds and a vertical resolution of 15 metres. The backscatter data are provided as raw counts that were corrected for background noise and instrument effects following Campbell et al. (2002). The raw photon counts detected in each range bin per microsecond can be expressed as:

$$n(r) = \frac{O_c(r)CE\beta(r)T(r)^2}{D[n(r)]r^2} + \frac{n_b}{D[n(r)]} + \frac{n_{ap}(r)}{D[n(r)]} \tag{3.2}$$

which when rearranged yields the normalized relative backscatter (NRB):

$$\text{NRB} = C\beta(r)T(r)^2 = \frac{r^2}{O_c(r)E}\Big[\big(n(r)D[n(r)]\big) - n_{ap}(r) - n_b\Big] \tag{3.3}$$

where n is the counts measured at the detector per microsecond in the range r, O_c is the overlap correction to account for the reduction in signal strength where the transmitted and received signals overlap, C is a system calibration constant, E is the transmitted laser pulse energy, β is the backscatter cross section due to all types of atmospheric scattering, T is the atmospheric transmittance, n_b is the background correction to remove noise due to sunlight, n_{ap} is the after-pulse correction to remove the noise induced by the laser firing and $D[n(r)]$ is the dead-time correction to remove the saturation effect at high count rates.

$D[n(r)]$, $n_{ap}(r)$ and E are provided by the instrument manufacturer, n_b is determined by taking the maximum value of the counts above 10 km for each dead-time-corrected and afterpulse-corrected profile, O_c has previously been measured at Summit. Once these corrections have been applied, dividing NRB by the lidar calibration constant C yields the attenuated backscatter (in sr^{-1}m^{-1}).

$$\beta_{\text{att}} = \frac{\text{NRB}}{C} \tag{3.4}$$

After calculating the NRB for both the cross- and co-polarised channels the MPL depolarisation ratio (δ_{MPL}; Flynn et al. (2007)) was calculated:

$$\delta_{\text{MPL}} = \frac{\text{NRB}_{||}}{\text{NRB}_{||} + \text{NRB}_{\perp}} \tag{3.5}$$

Finally, lidar extinction was calculated from the attenuated backscatter by multiplication with the lidar ratio (S):

$$E = \beta_{\text{att}}S \tag{3.6}$$

For this study we used a value of 25 sr for S to represent ice clouds (Balmes et al., 2019) and calculated E using channel 1 backscatter, since this is most sensitive to ice which is of interest for this study.

3.2.4 Ice particle imaging

We made use of manually captured images from the ice particle imaging camera (icePIC) to provide qualitative information about ice crystal habits. These images were taken by the Summit Station science technicians. Particles were collected on glass slides that were left outside in a location sheltered from horizontal winds (to prevent contamination from blowing snow) until falling ice crystals had accumulated on them. The slides were transported to the Mobile Science Facility where they were photographed using a Nikon D50 digital camera attached to a Thorlabs RMS4X microscope (5.6 x magnification) with a resolution of 1.5 μm.

3.2.5 Meteorological measurements

A two-channel humidity and temperature profiler (HATPRO) microwave radiometer (Rose et al., 2005) was used to retrieve temperature and humidity profiles, including liquid water path (LWP) and precipitable water vapour (PWV). The HATPRO is zenith pointing and measures brightness temperatures at specific microwave frequencies, it has seven channels near the water vapour absorption line and seven channels near the oxygen absorption line. In this study, we use values of atmospheric temperature and liquid water path retrieved using the TROPoe iterative optimal estimation physical retrieval algorithm (Turner and Löhnert, 2014; Turner and Blumberg, 2019; Guy et al., 2022). The atmospheric temperature profiles were further constrained by combining them with data from twice daily radiosondes launches. Data from these radiosonde launches were also used to determine the atmospheric structure, such as to identify the presence of inversion layers. This was aided by data from a bi-static sodar that was used to provide information on boundary layer depth and structure. Precipitation occurrence was identified using snowfall rates from the precipitation occurrence sensor system (POSS).

3.2.6 INP sampling

For this analysis, we make use of a dataset of INP concentrations determined by laboratory analysis of filter samples collected at Summit Station from 6th June 2019 until 22nd July 2020 as part of the ICECAPS-ACE project. This was managed by PhD student Bethany Wyld and the measurements and laboratory analysis were undertaken by technicians working on the ICECAPS-ACE project.

A semi-automated Digitel DPA14 Low Volume Sampler was deployed in the Atmospheric Watch Observatory (AWO) at Summit Station with its inlet on the roof of the building. This sampler can be loaded with up to 15 filters and programmed to change to the next filter after a pre-set sampling time. AWO is located approximately 700 m from the main station in the clear air zone (CAZ). The CAZ is oriented such that wind-blown emissions from the station (e.g. combustion aerosol) are less likely to influence sensitive operations, such as aerosol sampling, in this area. The sampler was fitted with a heated total suspended particulate (TSP) inlet head which was positioned 1.7 m above the roof of the building, which itself was approximately 4 metres above the snow surface. After an initial testing period, and considering the low aerosol concentrations observed at Summit, a sampling time of 56 hours was chosen as a compromise between time resolution and maximising the probability of having a signal above the technique's limit of detection. The sampling flow rate was set to 33.8 L min^{-1} as per the manufacturers recommendation and 47 mm diameter track-etched membrane polycarbonate filters with a pore size of 0.4 μm were used (Nuclepore, Whatman, UK).

Filters were prepared and analysed by technicians in a laboratory in the Mobile Science Facility (MSF) at Summit. After being removed from the sampler the filter holder tube was sealed to prevent contamination and transported (on foot) from AWO to a laminar flow hood in MSF. Filter holders were removed and each filter was placed in a pre-rinsed polypropylene centrifuge tube. 5 ml of ultra-pure water was then added to each centrifuge tube containing a filter and agitated for 10 minutes using a vortex mixer to remove aerosol from the filter. These suspensions were then used for droplet freezing experiments using the Microlitre Nucleation by Immersed Particle Instrument (μL-NIPI) as described in detail by Whale et al. (2015) and in Chapter 2 of this thesis. Three freezing experiments were undertaken for each filter sample, along with a handling blank. The ICECAPS-ACE INP data product consists of the raw data from these freezing experiments. Background subtraction was applied following the method described in Chapter 2 and Appendix B and INP concentrations were calculated following the method in Chapter 2.

3.2.7 Ice crystal number concentration retrieval

Ice crystal number concentration (N_{ice}) was retrieved using a forward modelling approach as described in Bühl et al. (2019). This technique compares measured to simulated values of observational variables in pre-calculated lookup tables that are computed for a range of input variables. Where the highest probability of the measured values matching the simulated values is found the corresponding properties of the particle size distribution that would lead to those measurements are retrieved. The principle of this is illustrated in Fig. 3.3. The retrieval method is described in detail in Bühl et al. (2019) but an overview is included here for completeness.

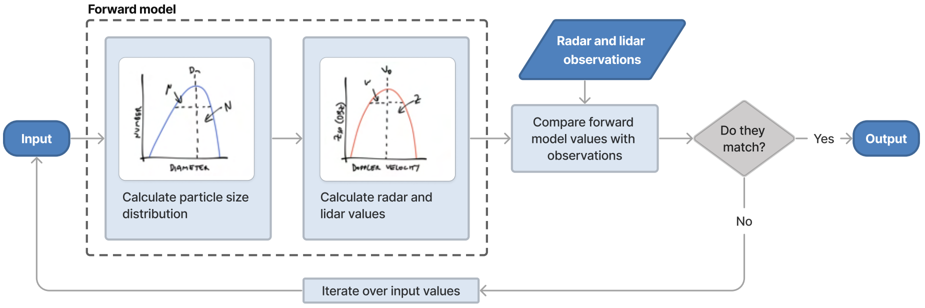

Fig. 3.3.: Schematic illustrating the principle of forward modelling, applied to retrieving ice-crystal number concentration from radar and lidar data

The measurement variables are radar reflectivity (Z), terminal fall velocity of hydrometeors (v_t), Doppler spectrum width (w) and lidar extinction (E). These measurements are stored in the observation vector $\mathbf{m} = (Z/E, v_t, w)$. A range of simulated values of each of the variables in $\mathbf{m}$ are calculated by iterating over input variables that describe the properties of the size distribution, median particle size (D_m) and a shape parameter (μ). Environmental factors, pressure (P), temperature (T), spectral broadening (σ) are also varied. These input variables are stored in the state vector $\mathbf{s} = (D_m, \mu, P, T, \sigma)$.

3.2.7.1 Computing lookup tables

Lookup tables are computed by first calculating particle size distributions (PSDs) for a range of realistic inputs and then simulating each of the variables in the observation vector, leading to a table in the dimensions of $\mathbf{s} \times \mathbf{m}$. In the following, variables with the subscript $_\mathrm{L}$ represent those in the lookup table. The PSDs are calculated based on a normalized PSD for ice clouds represented using the modified gamma distribution described in Delanoë et al. (2005):

$$N(D) = N_\mathrm{tot} C \left(\frac{D}{D_m}\right)^{\mu} \exp\left[-(4+\mu)\frac{D}{D_m}\right] \tag{3.7}$$

where D_m is the median particle maximum diameter (the diameter of a sphere encircling the ice crystal (Mitchell, 1996), μ is a shape parameter describing the tilt of the distribution, C is a normalization factor and N_tot is the total ice number concentration. Since N_tot is an unknown, the PSDs are calculated for a particle number concentration of 1 m^{-3} and the resulting calculations of Z, E are therefore also normalized to 1 m^{-3}. As a result, directly observed values of Z and E cannot be used in the retrieval but the ratio $Z_1/E_1 = Z/E$ can.

The relationship between fall velocity and particle size is then exploited to calculate v_t from each PSD. These calculations following an analytical approach that describes the mass and area of particles as a function of crystal shape and size (Mitchell, 1996; Heymsfield and Westbrook, 2010; Khvorostyanov and Curry, 2014). These calculations are described in detail in Bühl et al. (2019) and Khvorostyanov and Curry (2014) however the key formula is:

$$v_{\mathrm{t_L}}(D) = A_v(D) \cdot D^{B_v(D)} \tag{3.8}$$

where A_v and B_v are functions of D and the properties of the surrounding air which depend on air pressure and temperature. The mass, m, and area, A, of particles are calculated using the following equations:

$$m(D) = \alpha D^{\beta} \tag{3.9}$$

$$A(D) = \gamma D^{\sigma} \tag{3.10}$$

where α, β, γ and σ are shape dependent parameters (Khvorostyanov and Curry, 2014). These parameters must be chosen depending on the ice crystal shapes present, this is discussed in Section 3.3.2.

The radar reflectivity is then calculated by first simulating a Doppler spectrum based on the relation between Z, $N(D)$ and $m(D)$:

$$Z(D) = \frac{{}^{K}\!/_{0.93}({}^{6}\!/_{917\pi})^2 N(D) m(D)^2}{0.001^6} \tag{3.11}$$

where K is the dielectric constant for ice at 35 GHz, $N(D)$ is the PSD from Eq. 3.7 and $m(D)$ is particle mass from Eq. 3.9.

From this spectrum, w_{L} (Spectrum width) was determined and the normalised radar reflectivity calculated:

$$Z_{1_{\mathrm{L}}} = \int Z(D) dD \tag{3.12}$$

The normalised lidar particle extinction coefficient, E, was calculated based on the relation between extinction and particle area:

$$E_{1_{\mathrm{L}}} = 2 \int N(D) A(D) dD \tag{3.13}$$

The above calculations are repeated for every possible combination of values in **s** and the output stored in the lookup table vector, $\mathbf{L} = (Z_{1_{\mathrm{L}}}/E_{1_{\mathrm{L}}}, v_{\mathrm{t_L}}, w_{\mathrm{L}})$.

3.2.7.2 Retrieving properties of the PSD from the lookup table

To retrieve a result from the lookup table each of the measured variables are compared with corresponding simulated values in the lookup table and a matching probability is calculated. The measurement error of the observations (in vector **e**) is included in the calculation:

$$P = \exp\left[-0.5 \sum_i \frac{\mathbf{L}_i^2 - \mathbf{m}_i^2}{\mathbf{e}_i^2}\right] \tag{3.14}$$

This leads to a distribution of values of P, one for each simulation in **L**. At the position of the highest value of this distribution, the properties of the size distribution that would lead to the observed radar spectra are retrieved. A simplified illustration of this retrieval process is provided in Fig. 3.4.

Finally, the normalized size distribution determined from the retrieved parameters is scaled to the true ice crystal number concentration, N_{ice}, using the ratio of the normalised reflectivity Z_{1_L} to measured reflectivity Z. The uncertainty of the retrieval of N_{ice} is determined by calculating the full-width half maximum (FWHM) of the distribution of P as a function of N.

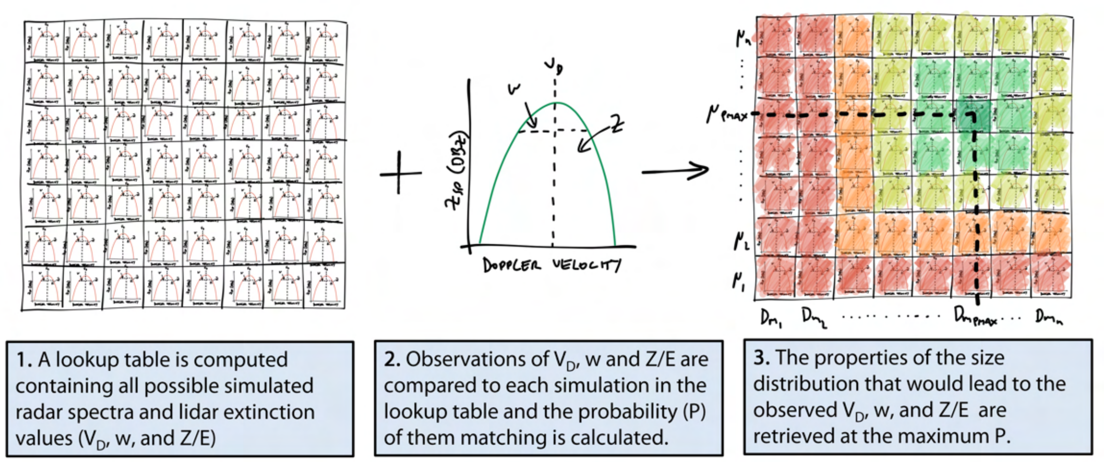

1. A lookup table is computed containing all possible simulated radar spectra and lidar extinction values (V_D, w, and Z/E)

2. Observations of V_D, w and Z/E are compared to each simulation in the lookup table and the probability (P) of them matching is calculated.

3. The properties of the size distribution that would lead to the observed V_D, w, and Z/E are retrieved at the maximum P.

Fig. 3.4.: Illustration of steps to retrieve properties of the particle size distribution from the lookup tables

3.3 Results and discussion

3.3.1 N_{ice} retrieval evaluation and uncertainties

As outlined in Section 3.2.7.2, the retrieval algorithm produces a distribution of possible results for each retrieved parameter. The full-width half maximum of this distribution is used to quantify the retrieval uncertainty. The retrieval can be done with different combinations v_{t}, w and Z/E which were tested and the output and uncertainties were compared. When using v_{t}, w and Z/E as the variational parameters in the retrieval, there were often many pixels where a successful retrieval was not possible. One reason for this is that in optically thick clouds containing liquid water, the lidar signal is quickly extinguished and therefore a measurement of E was not available. Where a retrieval with Z/E and w or with Z/E, v_{t} and w was possible, both predicted more ice than when using v_{t} and w without Z/E by up to an order of magnitude. This was most pronounced in clouds, or regions of a cloud, that were optically thicker, particularly where there was more liquid water. This is likely to be because lidar is sensitive to very small droplets in supercooled layers and these droplets will result in higher concentrations of ice being erroneously retrieved, when in fact some of this is liquid water (Delanoë and Hogan, 2010). Since we are interested in investigating ice concentrations at cloud tops, where the lidar may not be able to penetrate or the retrieval may be biased by liquid, we retrieve N_{ice} using v_{t} and w, and exclude Z/E. Bühl et al. (2019) found that the retrieval uncertainties when using v_{t} and w, compared to Z/E and w or Z/E, v_{t} and w were slightly larger however we found that the mean uncertainty in the retrieval was approximately a factor of 5, in agreement with Bühl et al. (2019) and Ramelli et al. (2021). Ramelli et al. (2021) also used a radar-only approach and found an acceptable agreement between retrieved N_{ice} and in-situ observations.

3.3.2 Ice crystal shape

The retrieval of N_{ice} requires knowledge of the dominant ice crystal shape. This is a difficult parameter to determine with the instruments available since it generally requires in-situ observations of individual crystals. We made a first estimate of the appropriate shape using the well-known relationship between ice crystal shape and temperature (Fig. 3.5) to define three temperature regimes and choose the corresponding lookup table used for the retrieval.

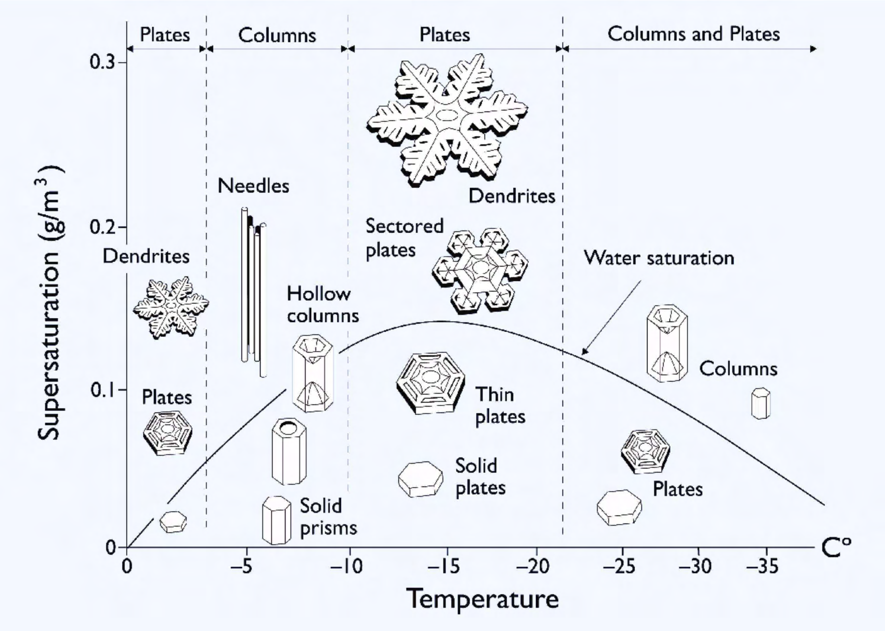

Fig. 3.5.: Theoretical relationship between temperature, supersaturation and ice crystal habit (from Libbrecht (2008).

Between -5 and -10°C and between -10 and -20°C combined particle types from Bühl et al. (2019) were chosen: column-like for $-5 > T > -10$°C and plate-like for $-10 > T > -20$°C. At temperatures colder than -20°C, particle shapes from Mitchell (1996) were used. Details of the temperature regimes and particle shapes are outlined in Table 3.2.

Tab. 3.2.: Temperature regimes and crystal shapes used to choose appropriate lookup table for N_{ice} retrieval

Temperature (°C)	Crystal size	Shape
$-5 > T > -10$	30-600 μm	Hexagonal columns
	600-2000 μm	Rimed long columns
$-10 > T > -20$	15 - 600 μm	Hexagonal plates
	600 - 3000 μm	Aggregates mixture
$T < -20$	30-600 μm	Hexagonal columns, bullets
	600-3000 μm	Aggregates of plates, columns, bullets

To validate this, we made use of icePIC images which were available on 14 days between July to October 2019. Comparing these images with the surface temperatures recorded during the observations (Fig. 3.6) showed that at temperatures below approximately -20°C, column-shaped ice crystals were predominant, accompanied by some small hexagonal and triangular plates. Between -20°C and -10°C, we commonly see hexagonal plates, stellar plates, stellar crystals, and aggregates. There were limited observations above -10°C; however, based on the available images and accompanying written observations, we identified columns and needles with some aggregates. These observations provides qualitative evidence that in most cases the temperature regimes defined in Table 3.2 represent the observed ice crystal shapes well.

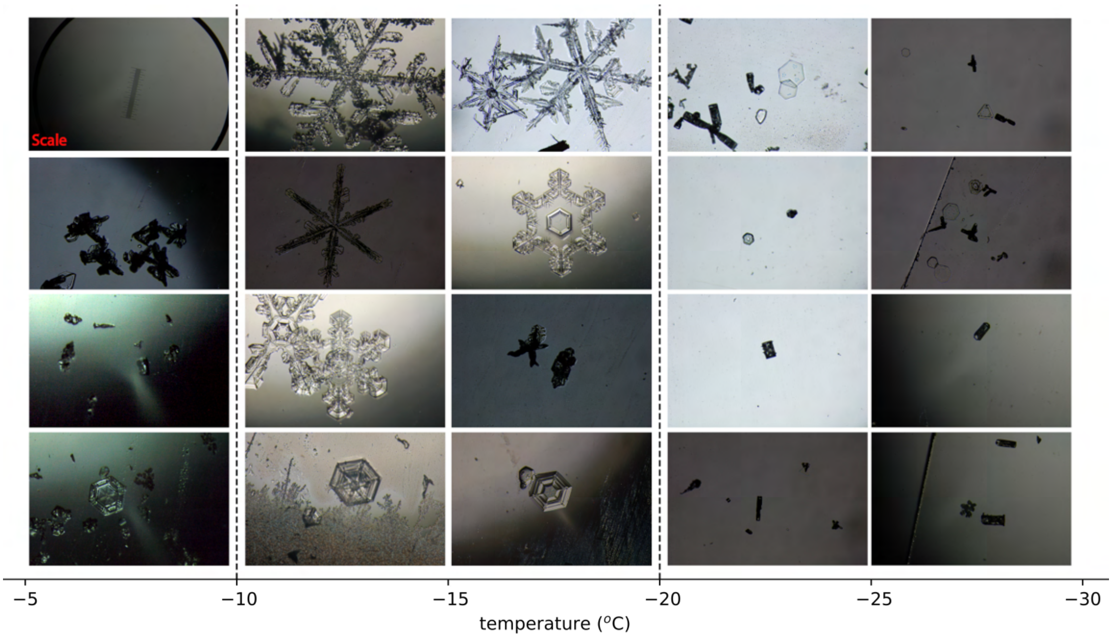

Fig. 3.6.: Ice particle images taken at Summit Station in Summer 2019, grouped by surface temperature at the time of observation (to the nearest 5°C). Calibration scale = 1 mm with 10 μm ticks.

3.3.3 Overview of case studies

To investigate the relationship between ice nucleating particle concentrations and ice crystal number concentrations the above methodology was applied to 12 case studies from 2019 where stratiform clouds that are capped by a temperature inversion were observed (canonical stratiform clouds) and persisted for at least 6 hours. These clouds were all mixed-phase with a supercooled liquid layer at the top. For the purposes of this study, we define cloud as occurring when hydrometeors are observed above 100 m in the atmosphere by ground-based sensors (Shupe et al., 2013). By this definition, cloud is observed to the lowest observational height of the instruments (250 mAGL) in all 12 cases. Where there are multiple cloud layers, precipitation from the layer above can initiate ice formation in the layer below (Vassel et al., 2019) so cases where there is a second cloud layer less than 1000 m above the top of the lower layer and where precipitation was observed by radar from higher cloud layers were excluded from this study. In the following sections, three case studies are presented in detail followed by the results from all 12 cases.

3.3.4 Case study 1: enhanced ice concentrations at low temperatures

On 28th August 2019 a precipitating stratiform cloud was observed. For the majority of the time, hydrometeors were observed from 250 m AGL to a cloud top height of up to 1400 m AGL, as shown in the radar reflectivity in Fig. 3.7a. The increased backscatter (Fig. 3.7e) and low LDR values (Fig. 3.7f) at the cloud top show the presence of a supercooled liquid layer between 1200 and 1400 m AGL. Below this, the LDR values suggest that between 06:00 and 13:00 the cloud is predominantly ice but from 00:00 to 06:00 and after 13:00 liquid is present at lower levels, with some regions where the cloud does not reach the surface. This can also be seen in the radar data where there is a general increase in reflectivity and spectral width between 05:00 and 14:00, indicating the presence of large crystals. During this time there are bands of particularly high reflectivity reaching the surface, likely due to precipitation.

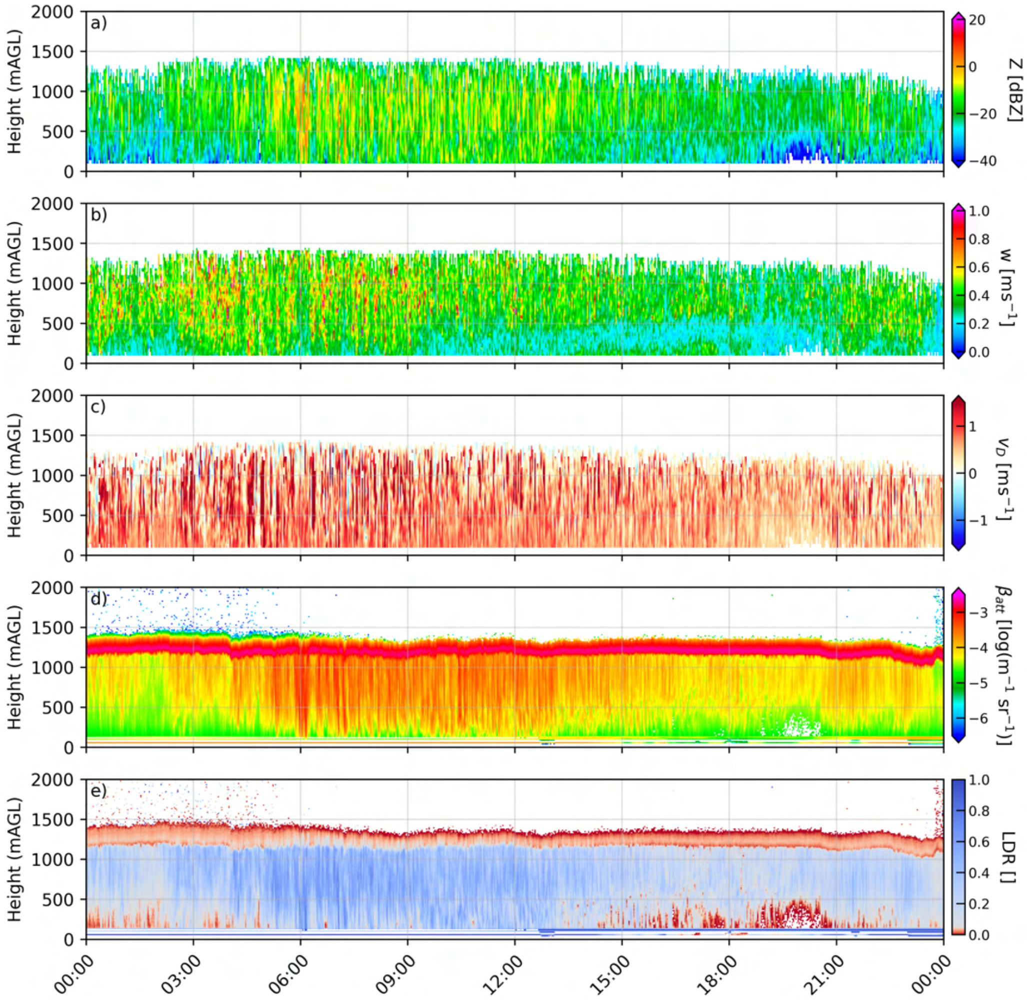

Fig. 3.7.: Remote sensing observations on 28th August 2019. a) MMCR reflectivity, b) MMCR spectral width, c) MMCR Doppler velocity, d) MPL total backscatter (sum of cross- and co-polarised channels), e) MPL depolarisation ratio - blue represents ice crystals and red represents liquid droplets

The cloud tops decrease in altitude slightly over the 24-hour period, which corresponds with the decreasing altitude of the temperature inversion in the temperature profiles from radiosonde launches at 11:19 AM and 11:15 PM (Fig. 3.8a). The vertical profiles of potential temperature (Fig. 3.8b) show a slight surface-based temperature inversion (SBI) in the evening and a stable surface layer to around 250 m in both ascents. In the morning there is also a decoupling layer at around 600 m which is not apparent in the evening profile where there is well-mixed layer above around 250 m until the temperature inversion at 1500 m. The observed SBI may mean that N_{INP} measured at the surface is not representative of N_{INP} in cloud, this is discussed further in Sect. 3.3.6.

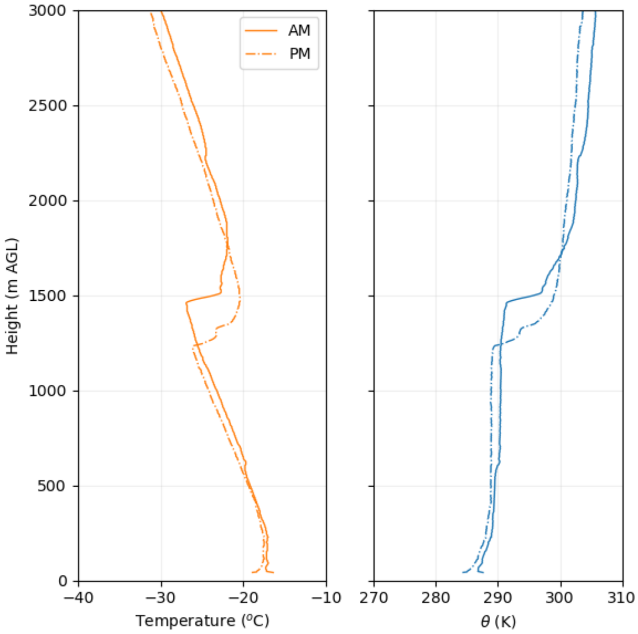

Fig. 3.8.: Vertical profiles of temperature (left) and potential temperature (right) from radiosonde launches at 11:19 AM and 11:15 PM on 28th August 2019. (Note: photographs and observations from POSS as presented in the following case studies were unavailable on 28th August 2019.)

Fig. 3.9 shows the results of the ice crystal number concentration retrieval. The increased amount of ice between 05:00 and 14:00 can be seen clearly in the IWP as well as the ice concentration. Fig. 3.9c shows ambient INP concentrations, calculated using the cloud top temperature, and the ice concentration at different heights in the cloud. At certain times, N_{ice} closely matches N_{INP} throughout the depth of the cloud. However, between 05:00 and 14:00, N_{ice} at 500 m and 1000 m is enhanced by up to an order of magnitude compared to N_{INP}. Interestingly, this enhancement is generally not observed at the cloud top. Comparing median N_{INP} and N_{ice} before, during and after this time period (Table 3.3) confirms that across all time periods, N_{ice} at the cloud top remains within an order of magnitude of N_{INP}. In contrast, between 05:00 and 14:00 the median N_{ice} is an order of magnitude larger than N_{INP} at both 1000 m and 500 m. N_{ice} at 1000 m is slightly higher than at 500 m at all times, this variability is within the uncertainty of the retrieval but could be an indication that ice is sublimating. The fact that N_{ice} does not show the same increase at the cloud top suggests that primary production is the dominant ice production pathway at cloud top and N_{ice} is limited by N_{INP}. In contrast, the enhancement of N_{ice} in the cloud suggests secondary ice production is occurring.

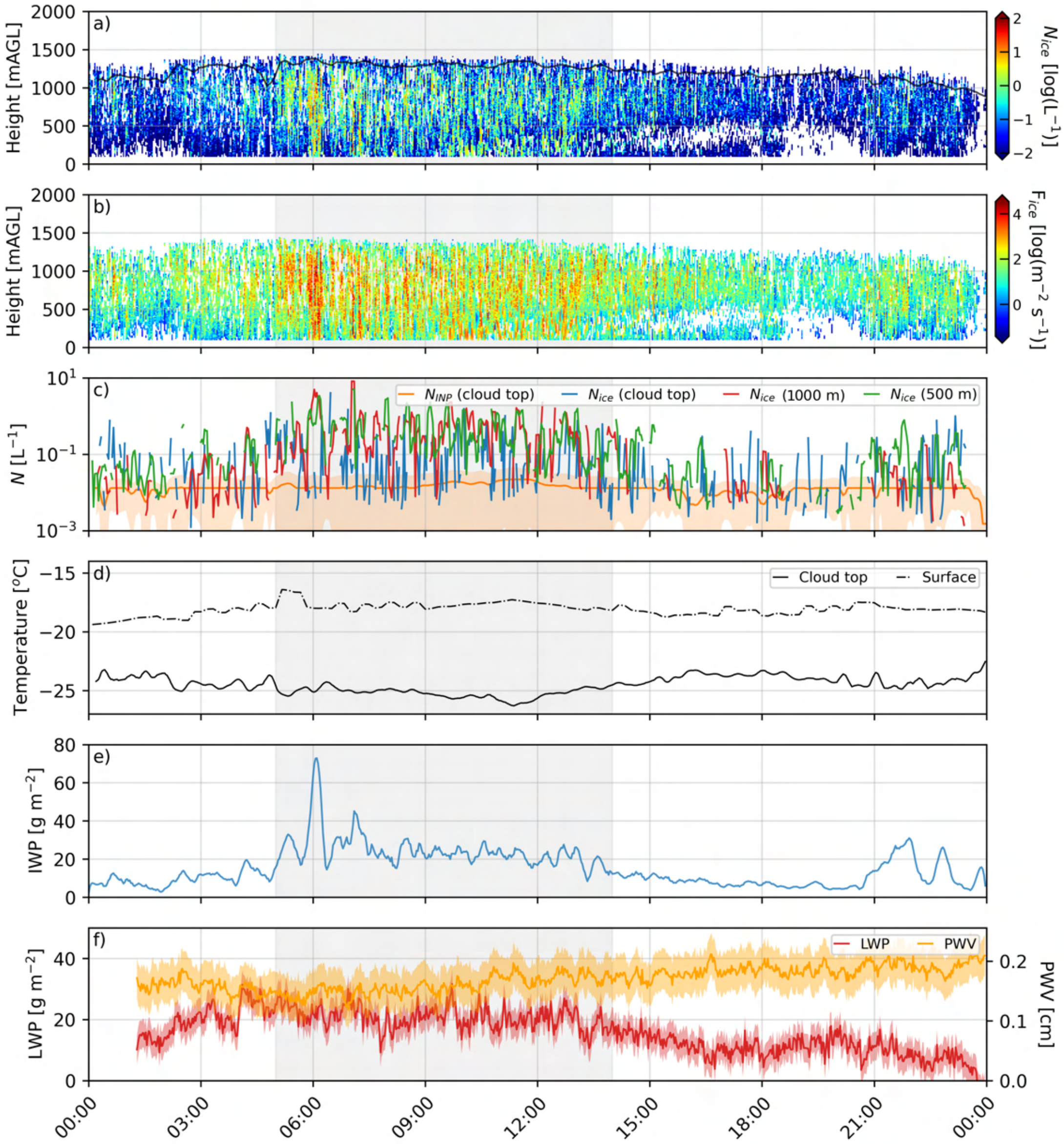

Fig. 3.9.: Retrieved cloud properties on 28th August 2019. a) ice crystal number concentration, b) ice crystal number concentration at the cloud top (blue), 500 m AGL (green) and 250 m AGL (red) along with ambient INP concentration at the cloud top (orange), c) Surface and cloud top temperature (from MWR), c) ice water path (from MMCR), e) liquid water path and precipitable water vapour (from MWR). Shaded regions (i)-(iii) correspond to the times in Table 3.3.

Tab. 3.3.: Median N_{INP} at the cloud top and N_{ice} at the cloud top, 1000 m AGL and 500 m AGL on 28th August 2019. Time periods (i)-(iii) correspond to the shaded regions labelled in Fig. 3.9.

Time	N_{INP} **(L^{-1})**	N_{ice} **(L^{-1})**		
		Cloud top	**1000 m**	**500 m**
(i) 00:00-05:00	1.4×10^{-2}	5.4×10^{-2}	9.9×10^{-2}	2.8×10^{-2}
(ii) 05:00-14:00	2.2×10^{-2}	5.2×10^{-2}	2.2×10^{-1}	1.5×10^{-1}
(iii) 14:00-00:00	1.3×10^{-2}	1.9×10^{-2}	2.9×10^{-2}	1.2×10^{-2}

3.3.5 Case study 2: high ice concentrations in a moderately supercooled stratiform cloud

On 5th July 2019 surface temperatures were relatively warm for Summit at around -10°C and a persistent stratiform cloud was observed from 16:00 on 4th July until 10:00 on 6th July. The MSF webcam (Fig. 3.10a) shows that there is low visibility with low-level cloud. The POSS shows snowfall starting at 03:00 and increasing to a maximum snowfall rate of 0.5 mm h^{-1} at 13:00. The temperature profiles from 5th July (Fig. 3.10c) show a temperature inversion at around 750 m with little change in the 12 hours between the radiosonde launches. The profiles of potential temperature (Fig. 3.10d) show a well mixed-layer from the surface to this inversion with no decoupling layers.

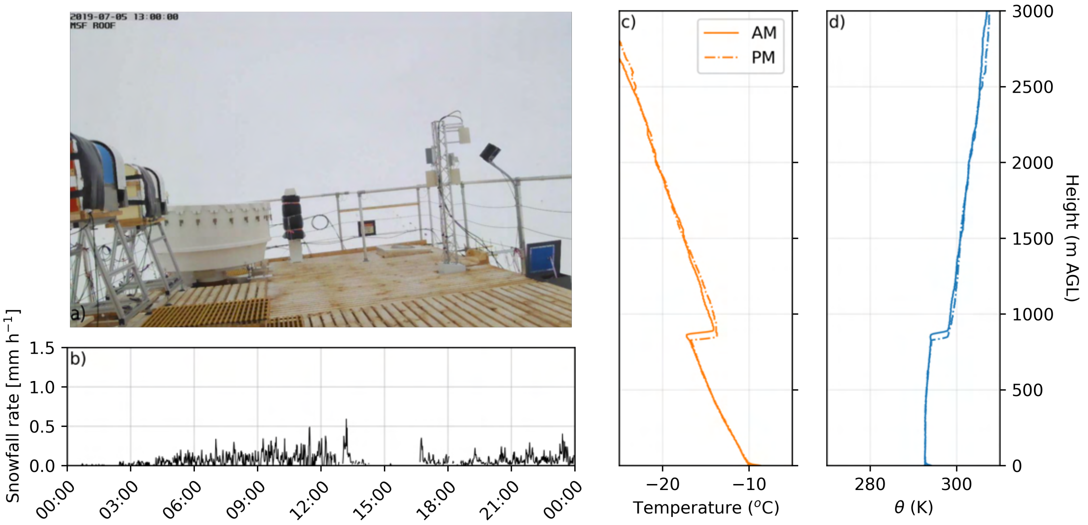

Fig. 3.10.: Meteorological observations on 5th July 2019. a) photograph taken at 13:00 from a webcam on the roof of the MSF b) snowfall rate (from the POSS) c) vertical temperature profile from radiosonde launches at 11:10 AM and 11:15 PM d) potential temperature from the same radiosondes

The radar reflectivity (Fig. 3.11) shows cloud tops of around 750m at the time of the radiosonde launches, consistent with cloud being capped by the inversion, but cloud tops increase from just above 500 m at 00:00 to just below 1000 m at 12:00. During this time, the radar reflectivity and attenuated backscatter increase, particularly from 05:00 until 14:00 where there are regions of enhanced reflectivity that indicate the development of large ice crystals and the initiation of snowfall, in agreement with the POSS observations. Much like case study 1, the high attenuated backscatter and low LDR values at the cloud top show the presence of a supercooled liquid layer, below which the cloud is predominantly ice. In this case, the Doppler velocity shows turbulent motion from the surface to the cloud tops and both the radar and lidar show hydrometeors to the surface at all times during the 24-hour period. The LDR values are generally smaller than those observed in case study 1, which could be indicative of more column or bullet-shaped crystals in 5th July compared to 28th August 2019, this is in agreement with the icePIC observations discussed in Sect. 3.3.2 where columns were observed at surface temperatures of -10°C and above.

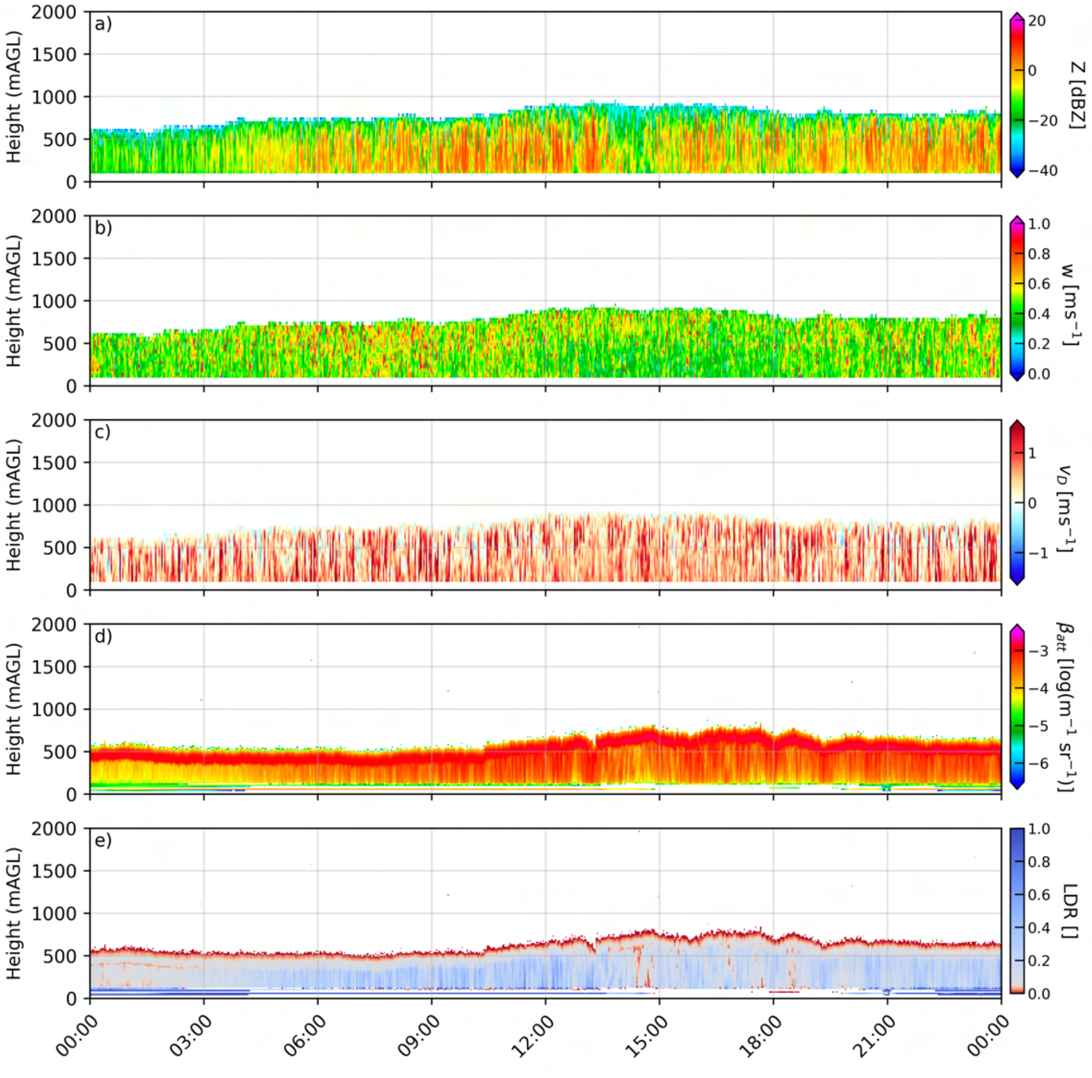

Fig. 3.11.: Remote sensing observations on 5th July 2019. Panels a)-e) show the same variables as Fig. 3.7

The retrieved ice crystal number concentration (Fig. 3.12a) shows considerably higher N_{ice} compared to 28th August, despite cloud top temperatures being up to 10° warmer on 5th July. At these warmer temperatures, N_{INP} is below the limit of detection of our instruments for some of the time but the upper limit of N_{INP}, shown by the orange shading in Fig. 3.12c, does not exceed 1.0×10^{-3} L^{-1}. Comparing this to the median N_{ice} for the whole 24-hour period (Table 3.4) reveals that N_{ice} is enhanced by at least four orders of magnitude in the cloud. These temperatures are lower than where the Hallet-Mossop process would be expected to be the dominant SIP mechanism, suggesting there is an alternative pathway for SIP at lower temperatures. Identifying this process is challenging without further in-situ observations, such as in-cloud measurements of ice crystal habit, however, ice-ice collisions have been shown to be most efficient at -16°C (Takahashi et al., 1995). It is also possible that ice forms elsewhere, where temperatures could be warmer, and remains in the cloud until it is observed at Summit. However, due to the location of Summit Station and the homogeneity of the topography and environment surrounding it, it is unlikely that there are substantial differences in environmental conditions in the vicinity of the station. A Lagrangian approach would be required to investigate this further, for example by making observations of developing cloud systems from an aircraft.

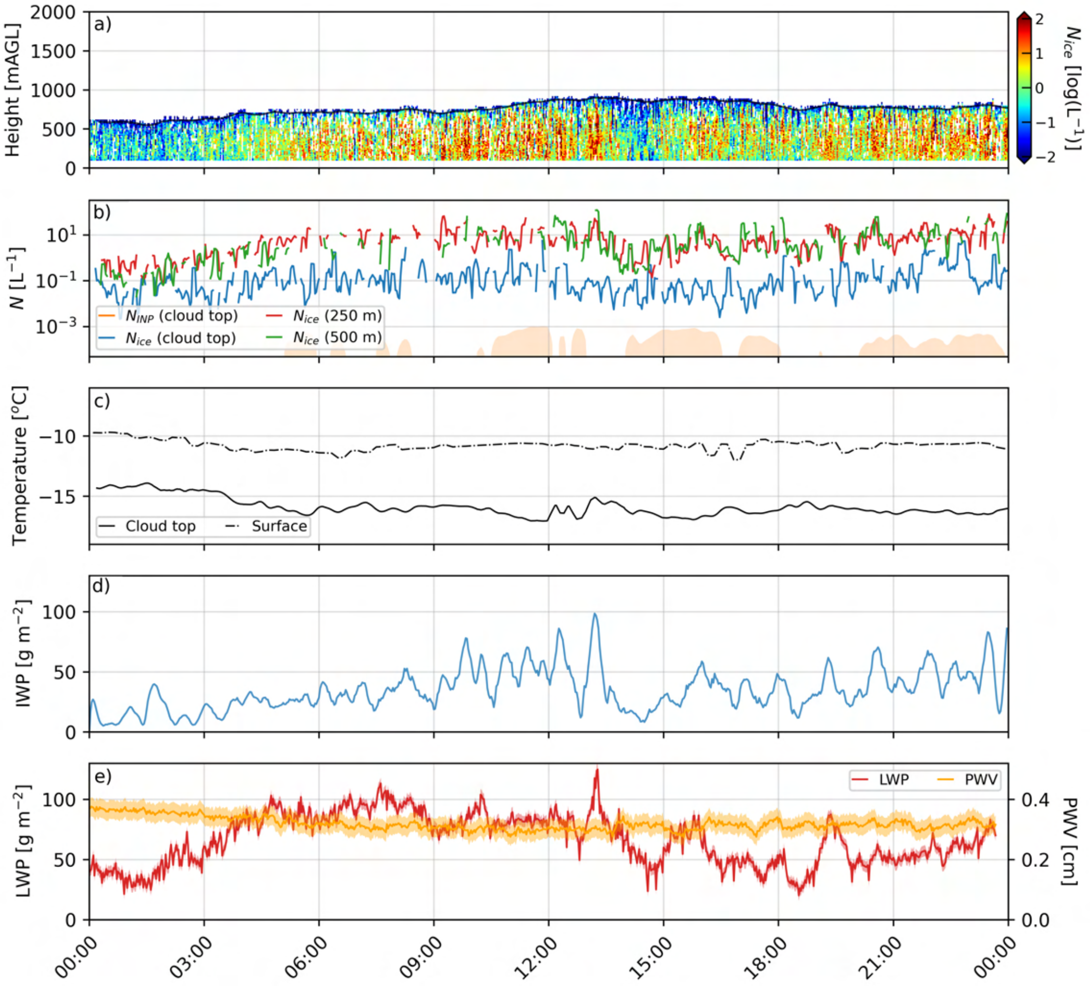

Fig. 3.12.: Retrieved cloud properties on 5th July 2019. Panels a)-f) show the same variables as Fig. 3.9.

Tab. 3.4.: Median N_{INP} at the cloud top and N_{ice} at the cloud top, 500 m AGL and 250 m AGL on 5th July 2019

Time	N_{INP} **(L $^{-1}$)**	N_{ice} **(L $^{-1}$)**		
		Cloud top	**500 m**	**250 m**
00:00-00:00	$<1.0\times10^{-3}$	8.1×10^{-2}	1.9×10^{1}	2.4×10^{1}

3.3.6 Case study 3: investigating the decoupled boundary layer

In the final case study, we focus on a cloud layer where we also observed a surface-based temperature inversion (SBI). When inversions occur, the mixing of air and aerosols to the surface can be inhibited (Igel et al., 2017) meaning INP measurements made at the surface may not be representative of those within the cloud, hence we generally excluded such cases from this analysis. However, SBIs occur more than 70% of the time at Summit (Miller et al., 2013) so investigating cloud development in the presence of SBIs is of interest.

On 1st November 2019 the MSF webcam (Fig. 3.13a) shows very low visibility and low-level cloud. The POSS (Fig. 3.13b) shows very low snowfall rates so we consider this a non-precipitating cloud. The temperature profiles from the 11:16 and 23:24 radiosonde launches (Fig. 3.13b and c) show that there is a strong temperature inversion and an increase in potential temperature from the surface to around 200 m indicating a decoupled surface mixed layer.

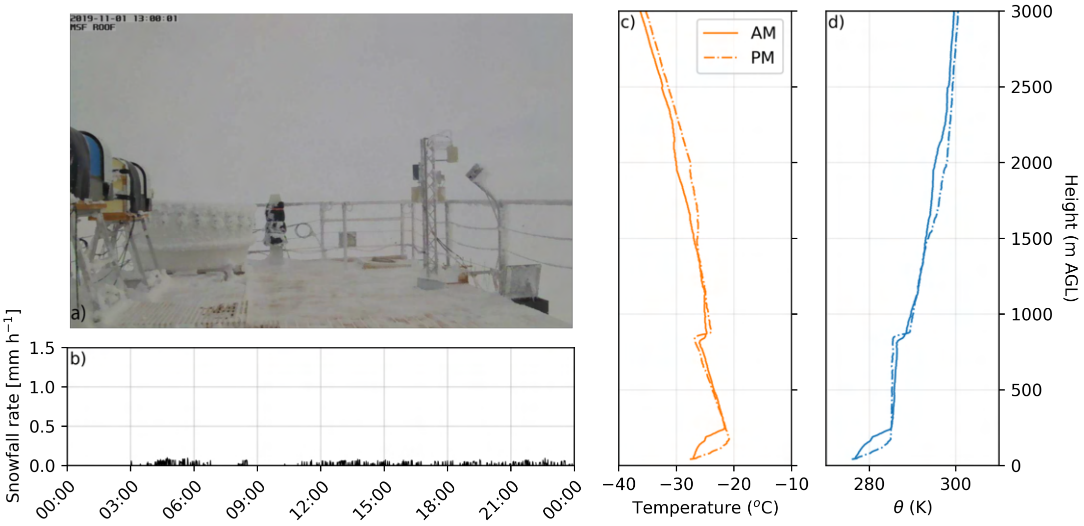

Fig. 3.13.: Meteorological observations on 1st November 2019. Panels a)-d show the same variables as Fig. 3.10)

From 00:00 until 03:00 low values of radar reflectivity, spectral width and Doppler velocity (Fig. 3.14) are consistent with small liquid particles, but bands of higher reflectivity and low LDR indicate the presence of some ice. After 04:00, a more uniform cloud with a supercooled liquid layer at the cloud top and ice below forms. This transition can be observed in the Sodar (Fig.

3.15) which shows that throughout 31st October there is a clear surface layer, consistent with a shallow SBI, which develops throughout the day. At around 04:00 on 1st November, when the stratiform clouds form, this layer breaks down and a deeper mixing layer is observed (to >140 m). The radar reflectivity (Fig. 3.14a) between 04:00 and 06:00 shows a region of enhanced reflectivity but the spectral width remains low, and the Doppler velocity is generally positive (towards the radar) suggesting there is a period with less turbulence. Between 06:00 and 12:00 the cloud top height decreases and the backscatter (Fig. 3.14d) and LDR (Fig. 3.14e) indicate a supercooled liquid layer in the cloud, as well as at the cloud top, most likely forming at the top of the SBI. After 12:00, this layer dissipates and a single-layer cloud persists for approximately 18 hours.

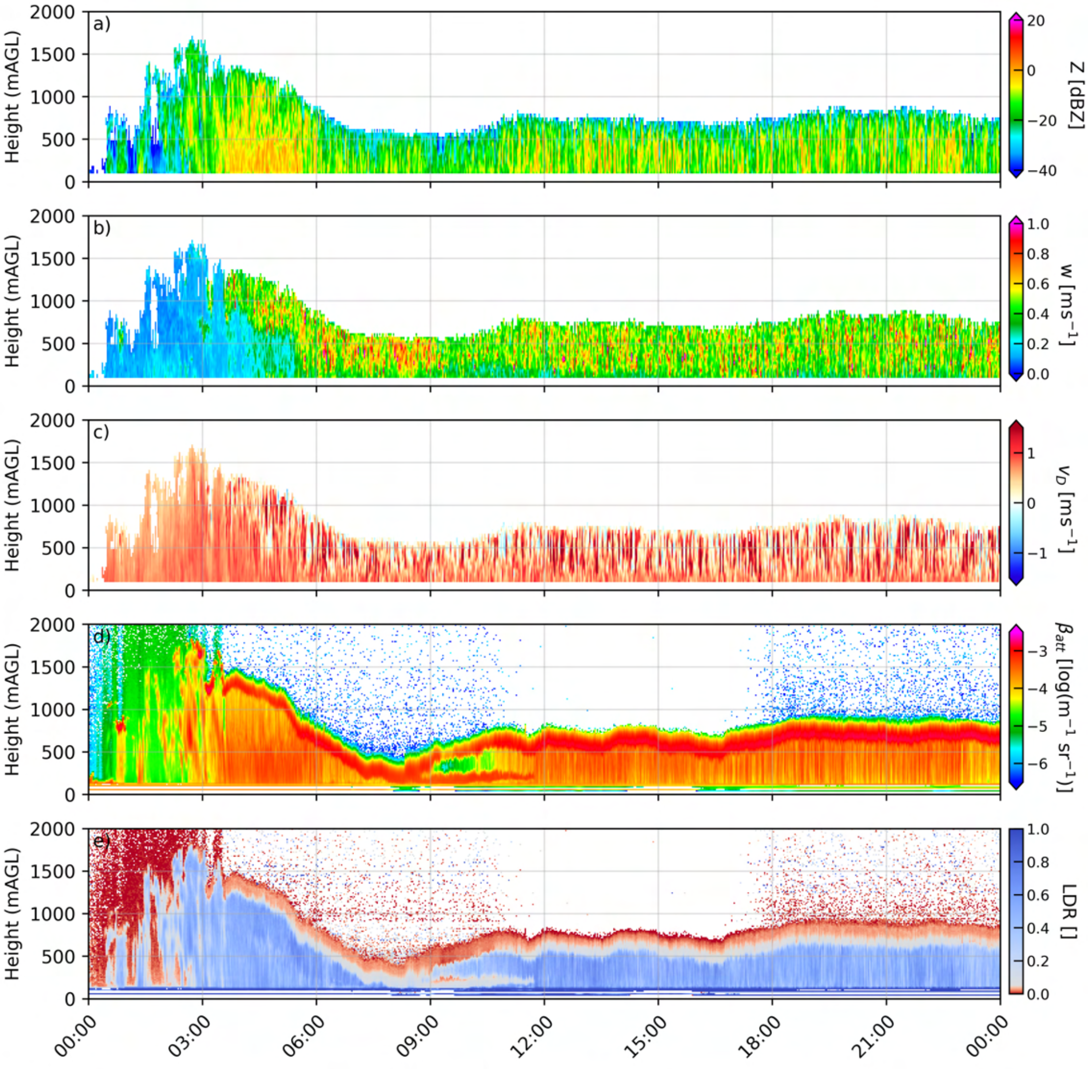

Fig. 3.14.: Remote sensing observations on 1st November 2019. Panels a)-e) show the same variables as Fig. 3.7

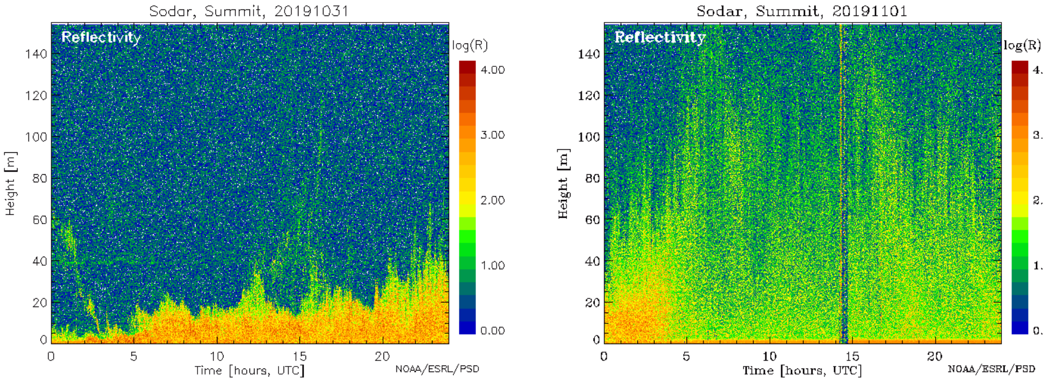

Fig. 3.15.: Sodar reflectivity observations on 31st October 2019 (left) and 1st November 2019 (right)

In Fig. 3.16, we highlight these three separate regimes and compare N_{INP} with N_{ice} in them. We observe high N_{ice} in-cloud shortly after the cloud forms at 04:00, which then reduces as the cloud heights decrease and more liquid forms. This transition can also be seen in a peak in IWP followed by a peak in LWP. At this transition, higher vertical velocities were observed, which could contribute to the increase of liquid water, whilst an increase in precipitation, as seen in Fig. 3.13b, depletes the ice. Between 03:00 and 06:00 median N_{ice} at the cloud top is approximately 7 x higher than N_{INP}. Within the cloud, N_{ice} is observed to be 2 orders of magnitude greater than N_{INP} at both 500 m and 250 m. Between 06:00 and 10:00 N_{INP} and N_{ice} at the cloud top both decrease, due to the increase in temperature, but remain in agreement with each other. In this time period the cloud tops are close to 500 m, hence N_{ice} at 500 m is the same order of magnitude as N_{ice} at the cloud top. In contrast, N_{ice} at 250 m, which is between the two liquid layers, is an order of magnitude larger. After 10:00, median N_{INP} and N_{ice} at the cloud top are still in agreement but N_{ice} at 250 m and at 500 m is larger compared to N_{INP} by an order of magnitude. This shows that, similarly to case study 1, there is an enhancement of ice in cloud at low temperatures. Given the SBI, the coldest temperatures in the cloud are not at the cloud top in this case so the highest N_{INP} may not be at the cloud top and it is possible that primary production is also higher in-cloud than at the cloud top. Since the concentration of primary ice influences SIP, assuming there are no other sources of ice, this could also have an impact on where SIP is occurring in clouds. The lowest in cloud temperatures are outside detection limits of the N_{INP} measurements and so we were not able to determine N_{INP} in the cloud.

The cloud top temperatures observed in case study 1 on 28th August are similar to those in this case study, however N_{ice} is an order of magnitude greater on 1st November compared to 28th August. On 28th August the precipitable water vapour is double that of 1st November, suggesting the higher N_{ice} is not a result of moisture availability. Two noticeable differences between the two case studies are 1) N_{INP} is an order of magnitude greater on 1st November and 2) there is an SBI on 1st November. The clear agreement between N_{INP} and N_{ice} at the cloud tops in both cases suggests that N_{INP} could be a controlling factor. Lower N_{INP} could also explain why more liquid persists in cloud on 28th August than on 1st November. It is interesting that N_{INP} and N_{ice} show good agreement in this case, despite the presence of the SBI. This implies that measurements of aerosols at the surface may be representative of those above the surface mixing layer if there was previously a well-mixed boundary layer. However, it's clear that further observations of this are required, for example using a tethered balloon system to make observations above the surface.

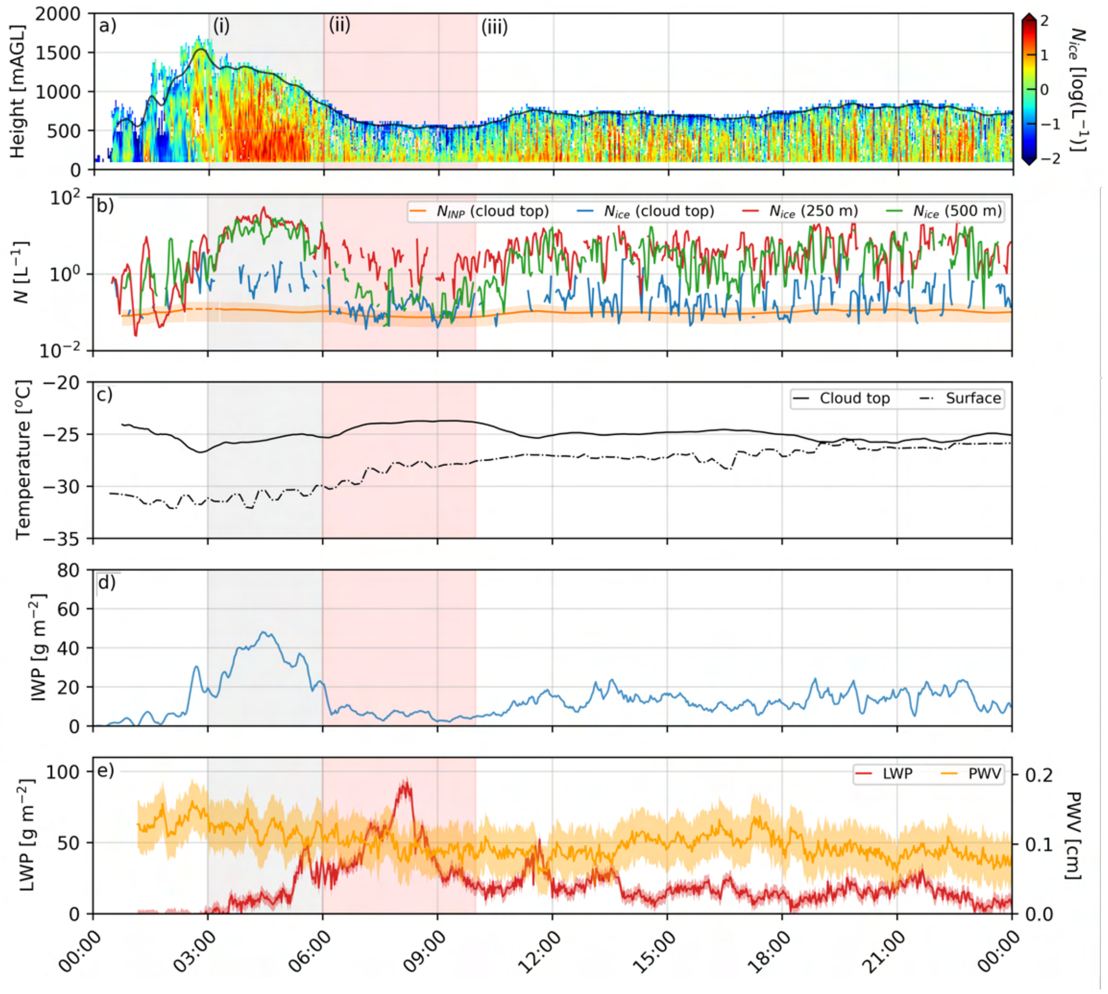

Fig. 3.16.: Retrieved cloud properties on 1st November 2019. Panels a)-f) show the same variables as Fig. 3.9. Shaded regions (i)-(iii) correspond to the time periods in Table 3.5.

Tab. 3.5.: Median N_{INP} at the cloud top and N_{ice} at the cloud top, 500 m AGL and 250 m AGL on 1st November 2019. Time periods (i)-(iii) correspond to the shaded regions labelled in Fig. 3.16.

Time	N_{INP} **(L** $^{-1}$**)**	N_{ice} **(L** $^{-1}$**)**		
		Cloud top	**500 m**	**250 m**
(i) 03:00-06:00	1.1×10^{-1}	7.3×10^{-1}	1.0×10^{1}	1.7×10^{1}
(ii) 06:00-10:00	8.4×10^{-2}	1.2×10^{-1}	1.9×10^{-1}	1.2×10^{0}
(iii) 10:00-00:00	1.1×10^{-1}	2.4×10^{-1}	1.5×10^{0}	1.2×10^{0}

3.3.7 Ice concentrations in Arctic boundary layer clouds

Fig. 3.17 shows the relationship between retrieved N_{ice} and local in-cloud temperature for all 12 case studies, along with the measured cumulative N_{INP} spectra. The median N_{ice} across all observations was 0.22 L^{-1} but there is considerable variability, with 5th and 95th percentiles of 7.9×10^{-3} L^{-1} and 14 L^{-1} respectively. The highest N_{ice} across all observations was 320 L^{-1}. When comparing each temperature bin, the highest median N_{ice} was between -26 and -27°C (1.57 L^{-1}) and the lowest was between -6 and -7°C (6.4×10^{-3}). These values are in agreement with other observations of arctic clouds (e.g. Rangno and Hobbs, 2001b; Hobbs, 1969; Pasquier et al., 2022). There is a clear decrease in N_{ice} to a minimum between -19 and -20°C, where the median is 4.0×10^{-2} L^{-1}, and increase to a maximum between -14 and -15°C, where the median is 0.46 L^{-1}. A similar peak in N_{ice}, but at slightly colder temperatures, was observed by Järvinen et al. (2022), who found the highest median ice concentration in stratocumulus clouds in the Southern Ocean to be at -16°C

The green points show N_{INP} for each case study. The points show the mean of three experimental values and the error bars show the standard deviation. The highest N_{INP} measured was 0.56 L^{-1} and the lowest was 4.9 $\times10^{-4}$ L^{-1}, although values of zero were recorded where the measurements fell in the background data. Across all temperatures, the median N_{ice} tends to be larger than N_{INP} but between -18°C and -26°C the data overlap and N_{ice} increases in line with N_{INP}, suggesting N_{ice} is limited by N_{INP} in this temperature range. Above -16°C there is a clear enhancement of N_{ice} compared to N_{INP}. In Case Study 2 we observed high concentrations between -10°C and -16°C, in agreement with the results shown here, which include a further 4 case studies within this temperature range.

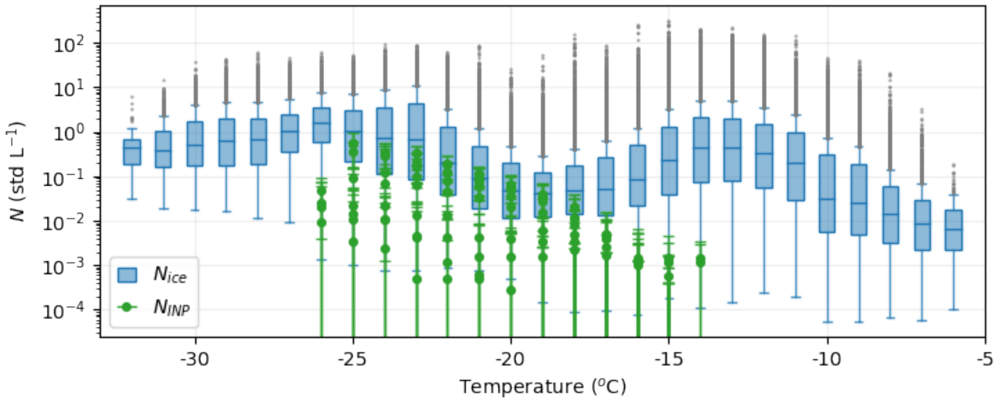

Fig. 3.17.: Retrieved ice crystal number concentrations (blue) for all case studies as a function of in-cloud temperatures and measured INP concentrations (green). N_{ice} is shown as a boxplot for each 1°C temperature bin. The boxes span the interquartile range while the whiskers are 2 x the interquartile range. The centre line of the box represents the median. Outliers are shown as grey points. Each N_{INP} spectra corresponds to one sampling period, the points represent the mean of three experimental values while the error bars represent the standard deviation of these values.

The investigate further, an ice multiplication factor (IMF) (Wieder et al., 2022) was calculated by dividing N_{ice} by N_{INP}, as shown in Fig. 3.18. Cloud top N_{INP} was used since this (usually) represents the coldest part of the cloud and therefore the highest N_{INP} and the upper limit of the primary ice production. Due to the detection limits of the measurement technique, the N_{INP} spectra do not extend to temperatures warmer than -14°C or colder than -26°C meaning the calculation was not possible when the cloud top temperature fell outside the range of the INP data, hence the narrower temperature range of the data in Fig. 3.18 compared to Fig. 3.17. Across all the data, the median IMF was 8.5 and, similarly to N_{ice}, there is substantial variability in IMF values with 5th and 95th percentile values of 0.30 and 1185. In Fig. 3.18 we see there is a peak -14°C to -15°C where the median IMF reaches 35. This, along with high N_{ice} shown in Fig. 3.17, provides further evidence for a SIP mechanism below the Hallet Mossop regime, down to around -18°C. Both droplet shattering and ice-ice collisions have been proposed as possible mechanisms for SIP from -10 to -18°C (Rangno and Hobbs, 2001b) but determining the dominant mechanism here is not possible with the instrumentation available.

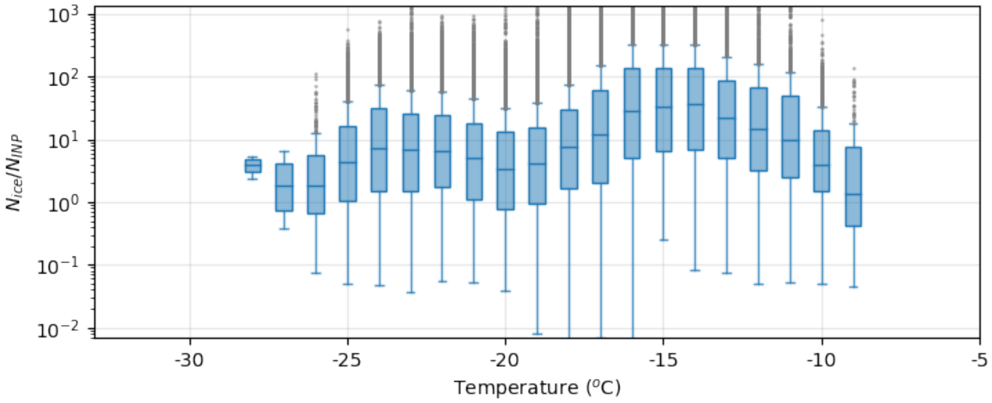

Fig. 3.18.: Calculated ice multiplication factor (IMF) for periods where the cloud top temperature was within the range of the INP data. The components of the box plots represent the same parameters as in Fig. 3.17

3.4 Conclusions

In this study, we investigate the microphysical properties of low-level Arctic stratiform clouds using remote sensing and in-situ observations. We present the first measurements of ice crystal number concentration (N_{ice}) in clouds on the Greenland Ice Sheet (GrIS), retrieved using remote sensing observations from Summit Station. N_{ice} had a median of 0.22 L^{-1} with variability between 10^{-3} and 10^{2} L^{-1}, values which agree with other observations in Arctic stratiform clouds. The highest N_{ice} was around -26°C and there was a secondary peak at around -15°C.

Comparing N_{ice} to N_{INP} revealed N_{ice} often greatly exceeds N_{INP}, providing evidence for secondary ice production in these clouds. The fact that in many cases N_{ice} and N_{INP} were in agreement at the cloud tops, where primary production would be expected to occur, but N_{ice} was enhanced in cloud provides further evidence for secondary ice production. Between -18°C and -26°C, we observe that N_{ice} appears to be directly related to N_{INP} but at temperatures warmer than -18°C there is a substantial enhancement of N_{ice} compared to N_{INP}. We calculated an ice multiplication factor which also showed the highest values above -18°C, with a peak of 35 at around -15°C. From this, we deduce that a SIP mechanism that is active at temperatures below the Hallett-Mossop regime is contributing to N_{ice}. We also compared two case studies at similar temperatures, in both we observed enhanced N_{ice} at temperatures as low as -30°C, once again confirming the importance of SIP well below the Hallet-Mossop regime. However, there is an order of magnitude difference in N_{INP} and in retrieved N_{ice}, suggesting that low concentrations of N_{INP} are limiting PIP and SIP.

A limitation of this study is the lack of in-situ observations of cloud properties to validate the retrieval of N_{ice}. However, other studies have applied the same method with concurrent in-situ observations and found acceptable agreement between observed and retrieved N_{ice} (Bühl et al., 2019; Pasquier et al., 2022; Ramelli et al., 2021; Wieder et al., 2022). The retrieval uncertainties and calculated ice multiplication factors are in agreement with these studies, and N_{ice} is consistent with other observations of Arctic mixed-phase clouds. In the absence of in-situ measurements, this provides some confidence to the results presented but it is clear that further observations are required. The different timescales of the observations, in particular the fact that the INP measurements are made over 56 hours, is also a limitation. Addressing this is challenging due to the difficulty in measuring such low concentrations of INPs and highlights the need to develop methods to make continuous measurements of INPs in these environments.

Observations of both N_{INP} and N_{ice} are essential to improving the modelling of clouds and their impact on the surface mass balance of the Greenland Ice Sheet. This study makes an important step by providing a method to observe N_{ice} using the instrumentation at Summit Station, and making the first comparisons of N_{INP} and N_{ice}. The ICECAPS project has been collecting data at Summit Station since 2010, the combination of this unique dataset and the techniques developed in this thesis open up the possibility of long-term observations of ice in clouds over the Greenland Ice Sheet.

4

Sources of ice-nucleating particles in the North East Atlantic

4.1 Introduction

Shallow supercooled clouds over oceans are climactically important due to their overall cooling effect. How these clouds respond as the climate warms is a crucial modulator of the expected warming, through a multitude of cloud feedbacks (Boucher et al., 2013; Ceppi and Nowack, 2021; Forster et al., 2021). Liquid-only marine clouds in the low latitudes are expected to reduce in amount due to a transition from stratus to stratocumulus and cumulus (Klein and Hartmann, 1993), which will have a warming effect and therefore a positive climate feedback (Forster et al., 2021). However, in the middle to high latitudes where temperatures are below $0°C$ and mixed-phase clouds are common, warming will result in a change in the composition of the clouds, with a shift towards there being more liquid and less ice (Gettelman and Sherwood, 2016; Forster et al., 2021; Murray et al., 2021). This will result in clouds with a higher albedo, and hence a negative climate feedback. This cloud-phase feedback has been shown to have a significant impact on predictions of equilibrium climate sensitivity (ECS), a measure of how climate models respond to a doubling of CO_2 in the atmosphere, but the exact magnitude of the feedback remains uncertain (Ceppi et al., 2017; Ceppi and Nowack, 2021; Gettelman et al., 2019; Storelvmo et al., 2015; Tan et al., 2016). Some of this uncertainty stems from the uncertainties associated with aerosol-cloud interactions, including the role of INPs, both in the present day and in a changing climate. Studies have shown that ice processes in models of present-day clouds are often too active and too much liquid water is removed (Vergara-Temprado et al., 2017), resulting in an overestimation of the magnitude of the negative cloud-phase feedback and an underestimation of ECS (Tan et al., 2016). As outlined throughout this thesis, the ratio of ice to liquid water in mixed-phase clouds is strongly dependent on INPs, hence it is clear that having an understanding of sources and concentrations of INPs in the mid to high latitudes is crucial to better constrain the magnitude of the cloud-phase feedback.

However, there is still a lack of understanding of the role of different aerosol particles as INPs (Murray et al., 2012) and there is a dearth of field observations, in particular of airborne measurements. Many studies have focused on the very high latitudes (e.g. Porter et al., 2022; Tatzelt et al., 2022; Shi et al., 2022; Kawai et al., 2023) or the low-latitudes (e.g. Sassen et al., 2003; Atkinson et al., 2013; Boose et al., 2016; Harrison et al., 2022b) with less focus on INP sources in the mid- to high-latitudes (50°-70°). The INP population at these latitudes can be influenced by numerous sources, including dust from low-latitude deserts, fertile soils and biogenic aerosol from both the marine and terrestrial environment. For example, in the United Kingdom and North East Atlantic, Easterly flow brings continental air masses that are likely dominated by organic and anthropologically sourced aerosols (Tunved et al., 2005) whereas northerly or westerly flow brings polar or maritime air which has not made contact with land for many 100s of kilometres and is therefore likely to have a less organic aerosol as well as lower aerosol mass concentrations (Dall'osto et al., 2010). Local aerosol sources such as biogenic particles (O'Sullivan et al., 2015) as well as long-range transport from dust sources which are known to be important for INPs such as the Sahara, or high-latitude dust from Iceland (Sanchez-Marroquin et al., 2020) or Svalbard (Tobo et al., 2019), can also contribute to the total INP population. This potentially complicated situation, combined with a lack of measurements, means that INP concentrations and sources are poorly constrained.

Here we present the results of airborne INP measurements from a field campaign based in Scotland. We use droplet freezing assays to quantify INP concentrations and optical probes on the aircraft to determine the aerosol size distribution. We utilise the FLEXible PARTicle dispersion model (FLEXPART) for back trajectory analysis to determine potential sources of INPs in this region. More specifically we investigate if INP concentrations are significantly higher when sampled air masses have been in contact with land in order to identify if there is a terrestrial source of INPs in the UK. We also identify potential sources and inputs to the regional aerosol population. The results show a significant variation in observed INP which highlights the need for further measurements in this region in order to understand spatial and temporal variation in atmospheric INP concentrations.

4.2 Methods

4.2.1 PIKnMIX-F field campaign

The PIKnMIX-F field campaign took place in March 2019. For the duration of the campaign, the UK's Facility for Airborne Atmospheric Measurements (FAAM) BAe-146 research aircraft was based in Stornoway on the Isle of Lewis - an island situated approximately 50 miles off the west coast of Scotland. Research flights took place in regions around the north of the UK, the North Sea, and the North Atlantic up to a maximum latitude of 64°N. The filter inlet system on board the aircraft was used to sample accumulation and coarse mode aerosol (up to $\sim$20 μm) onto filters and offline analysis was used to determine INP concentrations. In addition, aerosol size distributions were determined using underwing optical particle probes.

4.2.2 Sample collection

Aerosol samples were collected onto filters on board the FAAM BAe-146 aircraft using the methods outlined by Price et al. (2018) and Sanchez-Marroquin et al. (2020). The aircraft is fitted with a filter inlet system (Fig. 4.1) consisting of two parallel inlets and two filter holders. The inlets are positioned outside the aircraft and aligned with the local airflow. Air passes through the inlets, aided by a vacuum pump and the ram of the aircraft, and into the aircraft where the airstream passes through the filter holder. A mass flow meter on each inlet measures the flow volume (in standard pressure and temperature) so that the total sample volume is known. Manually operated valves allow the flow to be turned on or off in-flight thereby exposing or isolating the filters.

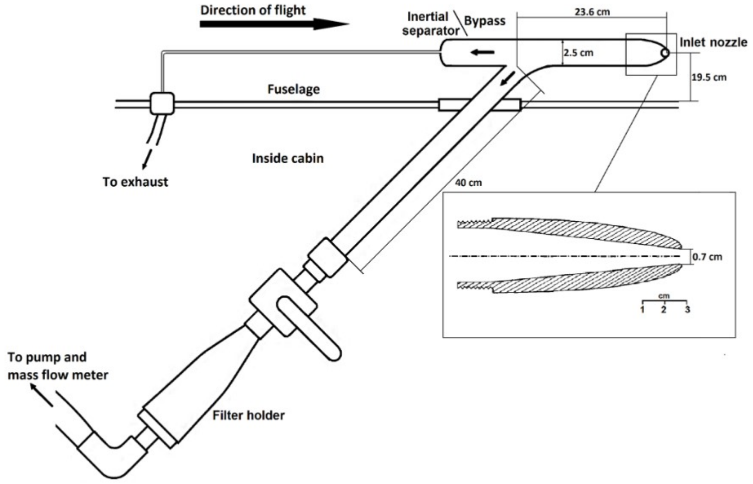

Fig. 4.1.: Schematic of one of the lines of the filter inlet system on the FAAM BAe-146 research aircraft (From Sanchez-Marroquin et al., 2019)

For INP analysis, samples were collected onto 47 mm Sartorius polytetrafluoroethylene (PTFE) filters with a pore size of 1.2 μm. In the parallel inlet, samples were collected onto Whatman Nuclepore polycarbonate track-etched filters with a pore size of 0.45 μm to be analysed using scanning electron microscopy (SEM). The results of this analysis are not presented due to delays as a result of the COVID-19 pandemic. Hence, any further reference to the filters relates to the PTFE filters used for INP experiments.

Previous studies utilising the inlet system on the FAAM BAe-146 to collect samples for for INP analysis used PTFE filters with a pore size of 0.4 μm (Price et al., 2018; Sanchez-Marroquin et al., 2020, 2021). Here a larger pore size was used in order to increase the flow rate through the system and thereby increase the sample volume during each run and the mass loading on the filters. Testing showed that the INP concentrations between the filters of different pore size were in agreement and the increase in pore size had no effect on the ice-nucleating ability of the filters themselves. Increasing the pore size in this way resulted in approximately a 3 x increase in flow rate. Given the low concentration of INPs in the atmosphere and the short sample times possible during aircraft measurements increasing the flow rate increases the likelihood of the INP signal in the samples being higher than the limit of detection of the technique and therefore improves the quantification of the INP concentrations.

22 filters were sampled during 9 flights, shown in Fig. 4.2. Filters were exposed during straight and level runs at altitudes ranging from 100 metres above sea level (mASL) to 4000 mASL and for

between 15 and 45 minutes. Sampling was paused when passing through clouds and precipitation and when the aircraft was cornering or ascending/descending. For each pair of filters, a PTFE handling blank was also collected in order to quantify the background INP concentrations. These handling blanks were treated the same as the samples but did not have any airflow through them.

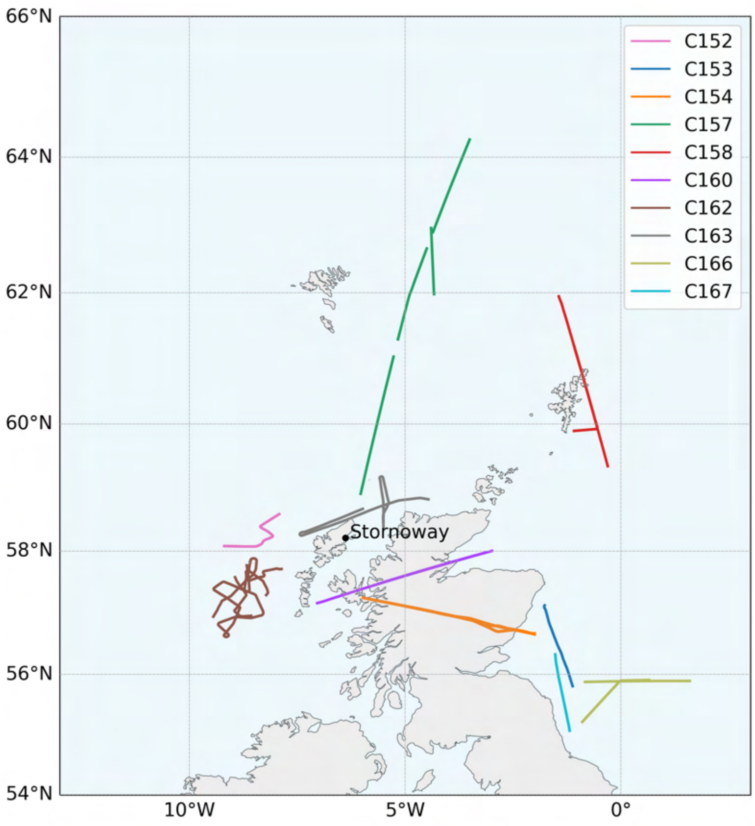

Fig. 4.2.: Sampling location for all filter samples collected during the PIKnMIX-F field campaign, grouped by flight

4.2.3 Droplet freezing experiments

Samples collected on PTFE filters using the filter inlet system on the FAAM BAe-146 were analysed for INPs using an adaptation of the droplet assay technique outlined in Chapter 2. A different approach is required when sampling INPs from an aircraft because sampling times are short (< 30 minutes) and the amount of INPs sampled is often very low. In such a situation, the technique of washing the sampled aerosol off the filters into a suspension and then pipetting droplets from this is not sensitive enough because there are a small number of INPs in a relatively large volume of water (5 ml for 47 mm filters). To increase the sensitivity of the droplet freezing assay technique a larger proportion of the sample needs to be in a smaller volume of water, this is achieved by placing droplets directly onto the sampling substrate rather than making a suspension. The droplet-on-filter technique used in this study is described in detail in Price et al. (2018) and has been used in other measurements of INPs sampled from the FAAM aircraft (Sanchez-Marroquin et al., 2020, 2021).

A hydrophobic glass slide (Ted Pella cover glass, 48 × 60 × 0.15 mm, coated with Turtle Wave ClearVue Rain Repellent solution) was positioned on the temperature-controlled cold stage on top of the University of Leeds Microlitre Nucleation by Immersed Particle (μL-NIPI) instrument (Whale et al., 2015) and held in place using a drop of silicon oil, which improves the thermal contact between the slide and the top of the cold stage. The PTFE filters were placed on to this slide and 50-70 2 μL drops of pure water (Sigma-Aldrich, Water - HPLC grade) dropped onto the filter with a pipette. A chamber, with a digital camera, was placed on top. In order to inhibit condensation and frost formation the chamber was flushed with air which passed from an air compressor (Titan Precision 22L Silent Quiet Dental Medical Clinic Oil Free Air Compressor) through a two-stage drying process, consisting of a silica gel drying column and a Drierite drying tube, and a HEPA filter. The cold stage was then cooled at a rate of 1 °C min^{-1} and the freezing of droplets and the corresponding temperature of the cold stage were recorded. Some of these videos were manually analysed to identify freezing events in each frame however some were analysed using a newly developed automatic analysis technique, which is outlined in Appendix C. The freezing temperature data, combined with the known sampling volume was then used to calculate the concentration of INP per unit litre of sampled air, N_{INP}:

$$N_{\text{INP}}(T) = \frac{-\ln(1 - f_{\text{ice}}(T))A_{\text{fil}}}{V_{\text{air}}\alpha} \tag{4.1}$$

where f_{ice} is the fraction of droplets frozen at temperature T, A_{fil} is the surface area of the filter exposed during sampling (11 ± 2 cm^2), V_{air} is the volume of sampled air and α is the area of each drop in contact with the filter (1.35 ±0.1 mm^2). α was calculated assuming spherical cap geometry with a droplet volume of 2 ±0.1 μL and a contact angle of 126 ±3° (measured by Price et al. (2018) using a contact angle goniometer).

A portable laboratory was set up during the field campaign which allowed the droplet freezing experiments to be completed within 24 hours of filter samples being collected so that they did not have to be stored and transported. After unloading from the filter holder, samples were placed into individual Petri dishes and sealed until they were analysed. If analysis could not be completed on the day that samples were collected (for example if there were two flights on the same day) then they were frozen at -18°C and analysed the next day. Due to the sensitivity of INP experiments to contamination an air quality monitor (AirVisual Pro) was used in conjunction with an air purifier (Vax Pure Air 200 AC02AMV1 Air Purifier) in order to monitor and reduce potential aerosol contaminants in the temporary lab and filters were loaded and unloaded from the filter holders inside a laminar flow hood. Blank filters and handling blanks were tested in the same way as the samples in order to quantify background INP concentrations. This background INP concentration was then subtracted from the sampled data following the method introduced in Chapter 2 and in Appendix B. With the droplet-on-filter technique, each experiment can only be completed once per sample so the uncertainty cannot be expressed using the standard deviation, unlike in Chapter 2 and Chapter 3. Here the standard deviation of a Poisson distribution of the number of freezing events in each temperature interval is used to express the uncertainty, this is described in Appendix B.

4.2.4 Aerosol size distribution

Aerosol particle size distributions were measured by underwing optical particle probes: the passive cavity aerosol spectrometer probe Probe 100-X (PCASP) and the cloud droplet probe (CDP). The PCASP measures particle with diameters of approximately 0.1-3 μm and the CDP measures particles with diameters of approximately 2-50 μm. The PCASP draws an air sample into an optical chamber where it measures the aerosol particles in the sample. The CDP is an open path optical particle counter (OPC). The data from the optical probes were calibrated and optical property corrections applied following the method in Rosenberg et al. (2012). This method uses Mie theory and therefore assumes that particles are spherical, which has been shown to be a reasonable approximation for airborne dust despite mineral dust particles generally being non-spherical (Rosenberg et al., 2012). A value of $1.56 + 0i$ was used for the refractive index when applying optical property corrections, following recommendations in Sanchez-Marroquin et al. (2020). Uncertainty in the particle size distributions from the PCASP and CDP measurements were calculated by combining the uncertainty of the number of particles in each bin (Poisson counting uncertainty) and the uncertainty in the bin widths (calculated from optical property corrections).

Representative sampling of aerosol from an aircraft is challenging due to sampling biases that arise as a result of the high speed of the aircraft (Brockmann, 2011; von der Weiden et al., 2009; Sanchez-Marroquin et al., 2019). This is particularly true for coarse-mode aerosols that can be both enhanced and lost to different processes. Under sub-isokinetic conditions (velocity of air surrounding the sampling is greater than the velocity of air entering the sampling inlet) coarse-mode aerosols are enhanced because their high inertia means they don't follow the streamlines of the air as it is deflected around the inlet. However, coarse-mode aerosol may also be under-represented due to inertial impaction or gravitational settling in the inlet system (Brockmann, 2011). This means that the measurements of aerosol size distribution from the optical probes may not be representative of what has been collected on the filters. The sampling biases differ depending on sampling conditions such as the flow rate, which is partially dependent on the filters used, and the type of aerosol being sampled. The filter system on the FAAM BAe-146 also has a bypass line, designed to remove water droplets or ice crystals, which is controlled independently from the main sampling line and affects the flow rate and the sub-isokinetic conditions. Comparisons of the size distributions measured by the FAAM BAe-146 optical probes and on filters collected using the filter system have been made on numerous occasions, with differing results. Andreae et al. (2000) and Young et al. (2016) did not observe an enhancement of coarse-mode aerosol on the filters, whereas Chou et al. (2008), Price et al. (2018) and Ryder et al. (2018) observed an enhancement of coarse-mode aerosol consistent with oversampling under sub-isokinetic conditions. More recently, Sanchez-Marroquin et al. (2019) characterised the filter inlet system on the FAAM aircraft in detail and compared size distribution observed by the optical probes to the size distribution of aerosol on filters determined using scanning electron microscopy (SEM). They observed an enhancement of particles of sizes above around 8 μm on filters of up to an order of magnitude but found that this enhancement could be minimized by keeping the bypass line open and by keeping the sampling flow rate between 50 and 80 L min^{-1} to reduce the sub-isokinetic enhancement. These recommendations were followed for all samples collected in this study. The filters used can also affect the sampling efficiencies. Sanchez-Marroquin et al. (2019) used polycarbonate filters with a 0.45 μm pore size for the SEM analysis whereas sampling in this study used PTFE filters with 1.2 μm pore size. The flow rate when using 0.4 μm polycarbonate filters is approximately 3 x greater than 0.4 μm PTFE filters (Price et al., 2018), however the 1.2 μm PTFE filters we used increased the flow rate by a factor of three compared to 0.4 μm PTFE filters, as outlined above. This brings the flow rate of the 1.2 μm PTFE filters in line with that of the 0.4 μm polycarbonate filters used by Sanchez-Marroquin et al. (2019) and suggests the sampling efficiencies may be similar to those observed by Sanchez-Marroquin et al. (2019). However, the discrepancy between the optical probes and the filters is still not fully quantified and varies under different corrections so it was not corrected for when calculating the aerosol surface area used to determine n_s, but it should be considered when interpreting the results.

4.2.5 FLEXPART back trajectory analysis

The origin of the sampled air masses and potential aerosol sources was investigated using the FLEXible PARTicle Dispersion Model (FLEXPART) (Stohl et al., 2011; Pisso et al., 2019). FLEXPART is a Lagrangian particle dispersion model used to simulate the transport of air parcels by mean flow as well as processes such as turbulent and diffusive transport, turbulence and convection. Loss processes such as radioactive decay and wet and dry deposition are also considered. In this case, the model was driven by ERA5 meteorological reanalysis data from the European Centre for Medium Range Weather Forecast (ECMWF) (Hersbach et al., 2020). FLEXPART can be used in forward mode, as demonstrated in Chapter 2, where particles are released from a source, or in backward mode where the release location represents a receptor (i.e. a measurement site) (Pisso et al., 2019). Backward trajectories are based on the theory of a source-receptor (s-r) matrix (Seibert and Frank, 2004), whereby the sensitivity of a ‘receptor’ to a ‘source’ is described. The output is a regular latitude-longitude-altitude grid of potential emission sensitivity (PES). PES represents a residence time of particles in a given grid cell and is proportional to the contribution a source in the grid cell would make to the mass concentration at the receptor. Hence, multiplying PES (in seconds) by a known emission flux (kg m^{-3} s^{-1}) results in the actual contribution of the grid cell to the mass concentration at the receptor (kg m^{-3}). Where an emission flux is not known, as in this case, the emission sensitivity on its own is an indicator of the likelihood that a particle released from a grid cell (source) would have been detected at the measurement location (receptor).

We used FLEXPART in backward mode by releasing particles along flight paths such that the receptors of the source-receptor matrix correspond to our filter samples. Since the exact nature of aerosols sampled is not known we used a default aerosol tracer. In order to account for the movement of the aircraft multiple particle releases were initiated for each filter sampling period;

five evenly sized boxes were created along each flight path and 10000 particles were released from each box (50000 particles in total). The start and end time of each release were set to correspond with the times at which the aircraft was sampling within each box and therefore the combined time of the five releases was equal to the total sampling time (i.e. the time the filter was exposed to the air). These simulated particles were followed backwards for seven days and the output was generated at 3-hour intervals on a grid with 0.1° x 0.1° horizontal resolution. For each sampling period, the five individual releases were combined and the resulting output was integrated over all timesteps to create total potential emission sensitivity plots. Since emissions from the surface are of particular interest when determining possible aerosol sources, the PES footprint was calculated for the surface (0 to 100 metres above ground level).

4.3 Results and Discussion

4.3.1 INP measurements

Details of the 22 samples collected for INP analysis are given in Table 4.1. Fraction frozen for each sample was determined using the droplet-on-filter technique described in Sect. 4.2.3 and N_{INP} was calculated using Eq. 4.1. The fraction frozen results for all the samples, grouped by flight, are shown in Fig. 4.3A and the background subtracted INP concentrations in Fig. 4.3B. It should be noted that the fraction frozen results are the raw, un-binned data whereas N_{INP} data is binned into 1°C temperature bins. The fraction frozen curves show considerable variability between samples, with the temperature at which half of the droplets are frozen (T_{50}) varying between -26.7 and -18.9°C. In approximately 1/2 of the samples, there is a clear difference between the fraction frozen curves of the samples and the handling blanks, however many of the samples show a low activity, similar to or lower than that of the handling blanks. However, after applying background subtraction most of the samples were above the average background INP spectra. The corresponding INP concentrations also show considerable variability and cover a broad temperature range. The temperature at which N_{INP} exceeds 0.1 L^{-1} ranges from approximately -21°C to -14°C and N_{INP} at -20°C spans more than an order of magnitude from $< 10^{-1}$ L^{-1} to $>$ 10^{0} L^{-1}.

To investigate the drivers of the variability in observed INP concentrations and determine possible aerosol sources we categorised the dataset into three groups based on the synoptic conditions observed. The first group consisted of samples where there was a westerly flow during sampling and samples were collected over the sea, the second where there was a northerly flow and samples were collected over the sea and the third where there was westerly flow over orography and samples were collected over land.

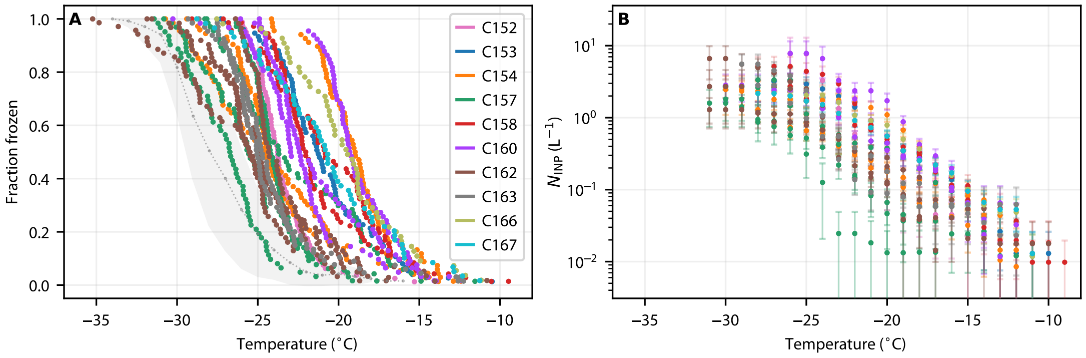

Fig. 4.3.: Measured fraction frozen (A) and INP concentration (B) for all filter samples during the PIKnMIX-F field campaign. Samples from the same flight are grouped together and the colours correspond to those used for the flight tracks in Fig. 4.2. Fraction frozen data shows the raw data, N_{INP} data is in 1°C temperature bins. The grey area in (A) shows the mean and standard deviation of the handling blanks.

Tab. 4.1.: Summary of samples collected during PIKnMIX-F. The symbol * indicates that sampling was interrupted at least once between the start and end time (e.g. when in cloud, when the aircraft was cornering, when changing altitude). The symbol † indicates that the altitude changed during the run, the altitudes given are the start altitude and the end altitude. Aerosol surface area was derived from the underwing Cloud Droplet Probe and Passive Cavity Aerosol Spectrometer Probe.

Sample	Date	Start (UTC)	End (UTC)	Altitude (mASL)	Aerosol surface area (μm^2 cm^{-3})	Description
C152a	12/03/19	09:45:15	10:07:50*	774	349	W. flow, in BL
C153a	13/03/19	14:08:05	14:34:00*	405	30.4	W. flow, in BL
C154a	14/03/19	12:03:00	12:38:30	3968	N/A	Lee wave, above BL
C154b	14/03/19	12:47:20	13:13:00*	2755	1.10	Lee wave, in BL
C154c	14/03/19	13:19:30	13:45:10*	2062	2.10	Lee wave, in BL
C157a	17/03/19	12:40:40	13:10:20	3654	0.62	N. flow, above BL
C157b	17/03/19	13:14:00	13:33:00	3656	0.33	N. flow, above BL
C157c	17/03/19	13:36:20	13:55:10	3654	N/A	N. flow, above BL
C157d	17/03/19	15:29:11	15:43:30	386	68.8	N. flow, in BL
C158a	18/03/19	14:36:30	15:01:40	437	44.1	N. flow, in BL
C158b	18/03/19	15:18:10	15:53:20	3965	3.00	N. flow, above BL
C160b	20/03/19	17:22:20	17:47:50	3665	3.45	Lee wave, above BL
C160c	20/03/19	17:53:06	18:04:05*	2747	12.9	Lee wave, above BL
C160d	20/03/19	18:10:20	18:29:20*	2135	N/A	Lee wave, above BL
C162a	23/03/19	11:40:10	11:54:50*	394	85.6	W. flow, in BL
C162b	23/03/19	12:04:30	12:51:30*	945-1823†	10.8	W. flow, in BL
C162c	23/03/19	13:02:50	13:35:40*	2287-3352†	3.44	W. flow, above BL
C162d	23/03/19	14:32:20	14:54:20*	494-960†	72.5	W. flow, in BL
C163a	24/03/19	13:37:30	14:03:10*	419	137	W. flow, in BL
C163b	24/03/19	15:58:40	16:38:20	4571-3658†	N/A	W. flow, above BL
C166a	27/03/19	12:54:20	13:14:40*	780	28.3	W. flow, in BL
C167a	27/03/19	15:34:30	15:55:01	2437	5.48	W. flow, above BL

4.3.2 Category 1: westerly flow

Fig. 4.4 shows the sampling locations during six flights where there was predominantly westerly flow. We have further categorised these samples into two groups based on the sampling location. Given the westerly flow, the air masses sampled to the east of the UK will have passed over the UK and may be influenced by terrestrial aerosol sources. In contrast, air masses sampled to the west of the UK will not have been in contact with land for many days and therefore the aerosol sources are more likely to be from the marine environment.

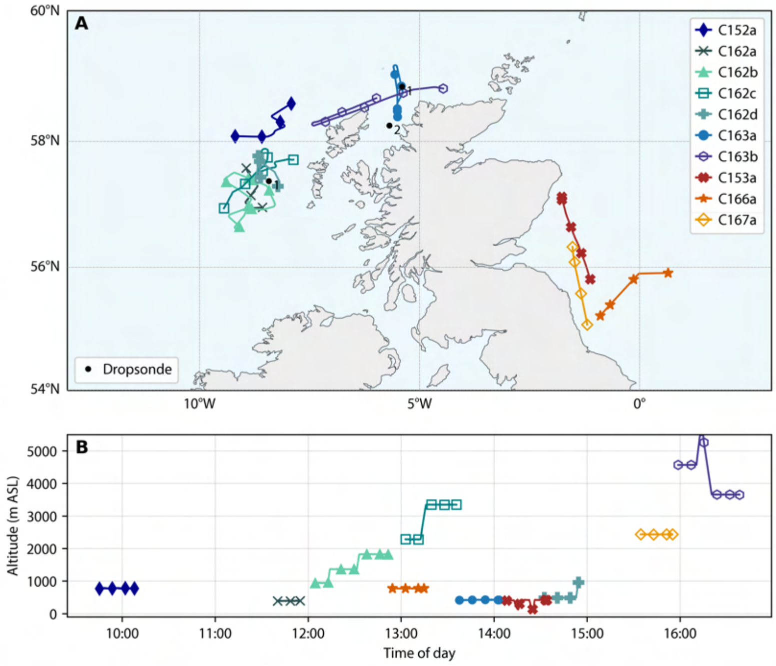

Fig. 4.4.: (A) Sampling location for samples in category 1. Dropsonde launches are shown in black and numbered to match Fig. 4.5. (B) Sampling altitude for samples in category 1. Samples with hollow symbols were above the boundary layer and samples with filled symbols were in the boundary layer.

During flight C152 there was a low-pressure system to the west of the UK and the flight focussed on measurements of these frontal clouds, sample C152a was collected below cloud. Flights C162 and C163 aimed to observe the microphysical properties of supercooled cumulus clouds. The vertical temperature profiles from dropsondes launched during these flights (Fig. 4.5) show a cloud layer at around 2000 mASL on both days. Therefore, samples C162a, C162d and C163a were all below cloud. During sampling of C162b the altitude increased from ∼1000 mASL to ∼2000 mASL which is below the cloud layer observed in the dropsonde profiles, however, there was considerable spatial heterogeneity in the cloud cover throughout both flights and observations recorded during sampling show that the aerosol sample collection was paused multiple times during the run due to the presence of clouds, hence we assume that this sample was collected in the cloud-free air at the altitude of the cloud layer. Flight C153 took place in clear air. Flights C166 and C167 were on the same day and both focussed on measurements of stratocumulus, there were no dropsondes on C166 and C167 but observations during the flight confirm that C166a was below cloud and C167a was above cloud.

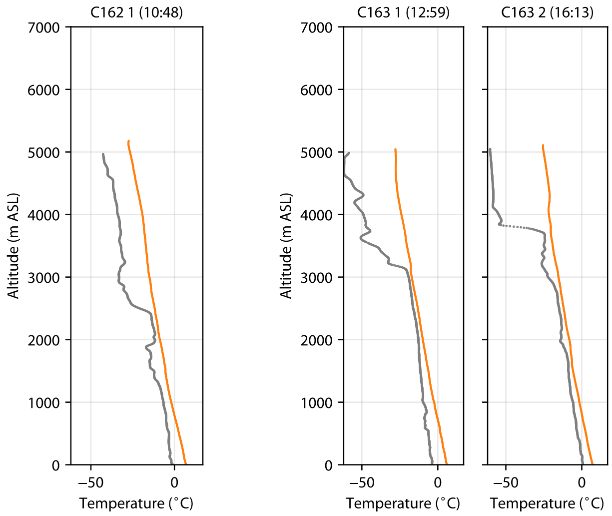

Fig. 4.5.: Temperature (orange) and dew point (grey) from dropsondes launched during flights C162 and C163

The fraction frozen curves in Fig. 4.6 highlight a clear difference between the flights hypothesised to be influenced by the marine environment and those influenced by the terrestrial environment (which shall now be referred to as simply marine or terrestrial samples). N_{INP} of the terrestrial samples is also noticeably greater than the marine samples. At -20°C, median N_{INP} for the terrestrial samples is 0.55 L^{-1} compared to 0.13 L^{-1} for the marine samples. In addition, the median temperature at which N_{INP} exceeds 0.1 L^{-1} is 4 degrees warmer for the terrestrial samples (-16°C) compared to the marine samples (-20°C). The differences in N_{INP} are most pronounced between -15 and -20°C, below -20°C the INP spectra converge. However, at temperatures below -25°C some of the data points are in the background data and the observed flattening of the

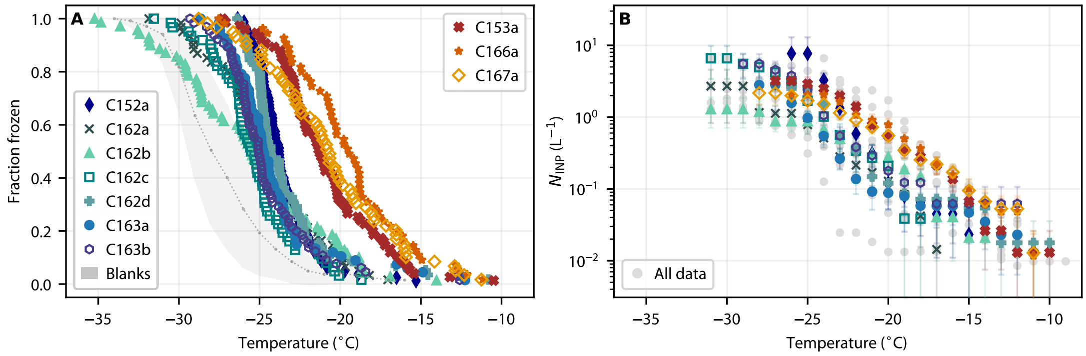

Fig. 4.6.: Measured fraction frozen (A) and INP concentration per standard litre of air (B) for samples in category 1. The mean and standard deviation of the handling blanks shown in (A) represent the background INP activity used in calculating the error shown by error bars in (B). N_{INP} of all samples in this study are shown in grey in (B). Blue colours represent samples collected to the west of the UK and orange colours to the east of the UK

INP spectra below -25°C may be due to reaching the limit of detection of the droplet-on-filter technique.

The size distribution data (Fig. 4.7A) show that, in general, the marine samples have a higher aerosol concentration (by number), particularly in the coarse mode (1-10 μm). In terms of surface area, the mean aerosol surface area in marine cases was 109.7 μm^2 cm^{-3} compared to 21.4 μm^2 cm^{-3} in the terrestrial cases. This suggests that the observed increase in N_{INP} is not due to higher total aerosol concentration but due to a different population of aerosols, containing more active INPs. There is also a difference in the particle size distribution of samples collected above cloud (hollow symbols) compared to those below cloud (filled symbols). Those sampled below cloud exhibit an enhancement of course mode aerosol, with a peak at around 5 μm, which is not seen in the above cloud samples. This suggests that the population of aerosols above and below cloud is different and that the number concentration of samples below cloud is enhanced by a surface source of aerosol.

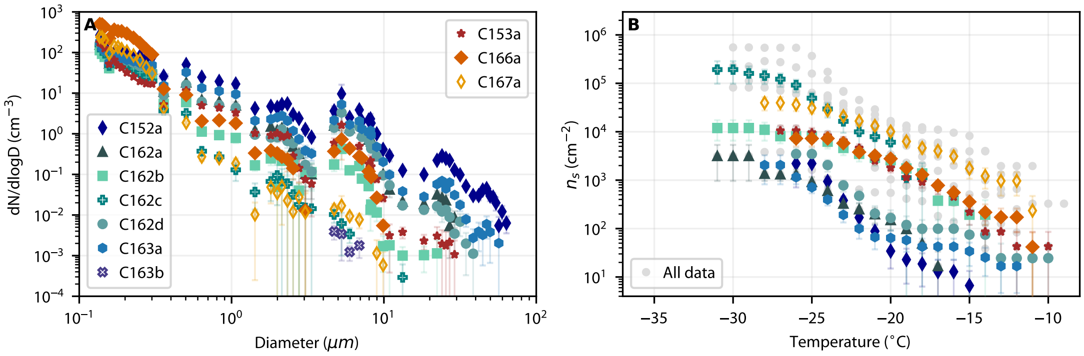

Fig. 4.7.: Size distribution of samples in category 1 determined from the PCASP and CDP optical probes (A) and active site density (n$_s$) of each sample (B). n_s of all samples in this study are shown in grey in (B).

n_s values were calculated by normalising N_{INP} by the aerosol surface area determined using the underwing optical probes. Quantitative comparisons of n_s calculated in this study must consider the different sampling biases of the filter inlet system compared to the optical probes, as described in Sect. 4.2.4, nevertheless, the n_s values provide valuable information and allow comparison of the activity of different samples. The results in Fig. 4.7B show considerable variability in n_s and three distinct groups in the samples. The lowest n_s values are observed in below cloud marine samples C152a, C162a, C162d and C163a. These samples also have the highest aerosol concentrations, meaning that despite the higher aerosol loading this population of aerosols is relatively low in ice-nucleating activity (compared to other samples in this study). Interestingly, samples C153a and C166a have a similar particle size distribution to C152a, C162a, C162d and C163a but a higher n_s by more than an order of magnitude (at -20°C). The main difference in sampling location between these two groups is that C153a and C166a were sampled to the east of the UK and C152a, C162a, C162d and C163a to the west. Given the westerly flow observed during these flights, this enhanced INP activity may be due to the presence of terrestrial aerosol in the boundary layer that has been transported from the UK. The highest n_s is observed in samples C162c and C167a that we collected above the boundary layer (there is not enough data from the optical probes to calculate n_s for sample C163b). Sample C162b appears to show a similar n_s to the terrestrial samples despite being collected to the west of the UK, this sample was collected at varying altitudes within cloud layers so it is possible that this is because the different air masses above and below cloud have both been sampled on this filter.

From these observations, we propose that the samples to the east of the UK in the boundary layer, to the west of the UK in the boundary layer and above the boundary layer capture three distinct aerosol populations. To identify possible sources, we used FLEXPART to run 7-day back trajectories, as described in Sect. 4.2.5, and calculated a potential emission sensitivity (PES) footprint. Fig. 4.8 compares the mean PES for samples collected to the east of the UK in the boundary layer (A), to the west of the UK in the boundary layer (B) and above cloud (C). This shows that, on average, the highest emission sensitivity for the samples collected to the east of the UK is close to land and there was circulation over land in the 7 days preceding the sampling. This suggests that the sampled air masses have been influenced by the terrestrial environment of the UK which has contributed to the higher N_{INP} and n_s seen in samples C153a and C166a. In contrast, in the samples collected to the west of the UK there was less circulation close to the land and instead more pronounced transport from the west. Therefore, in the samples collected within the boundary layer to the west of the UK there is unlikely to be a local terrestrial source of aerosol and the presence of coarse mode in the aerosol size distribution is most likely due to sea spray aerosol. During flights, the sea state (on the Beaufort scale) is recorded based on qualitative observations by the pilots. During flight C152, which has the greatest peak in coarse mode aerosol and the highest total aerosol surface area, the Beaufort number was observed to be 9 (*High waves. Dense streaks of foam along the direction of the wind. Crests of waves begin to topple, tumble and roll over. Spray may affect visibility*). This is the highest at any point during the PIKnMIX-F measurement campaign, and the correlation between the enhancement of coarse mode aerosol and the high wind speeds provides qualitative evidence that samples below the cloud are dominated by sea spray aerosol. The PES of the samples collected above the boundary layer do not exhibit the same high PES values or spatial coverage, this means that the sampled air masses have had less contact with the surface during the 7-day back trajectory and implies that particles at the sampling location have descended from higher in the atmosphere rather than being from a local surface source. The observation of there being less coarse mode aerosol above the cloud also suggests that is likely that INPs in samples C162b and C167a are predominantly from long-range transport of aerosol above the boundary layer.

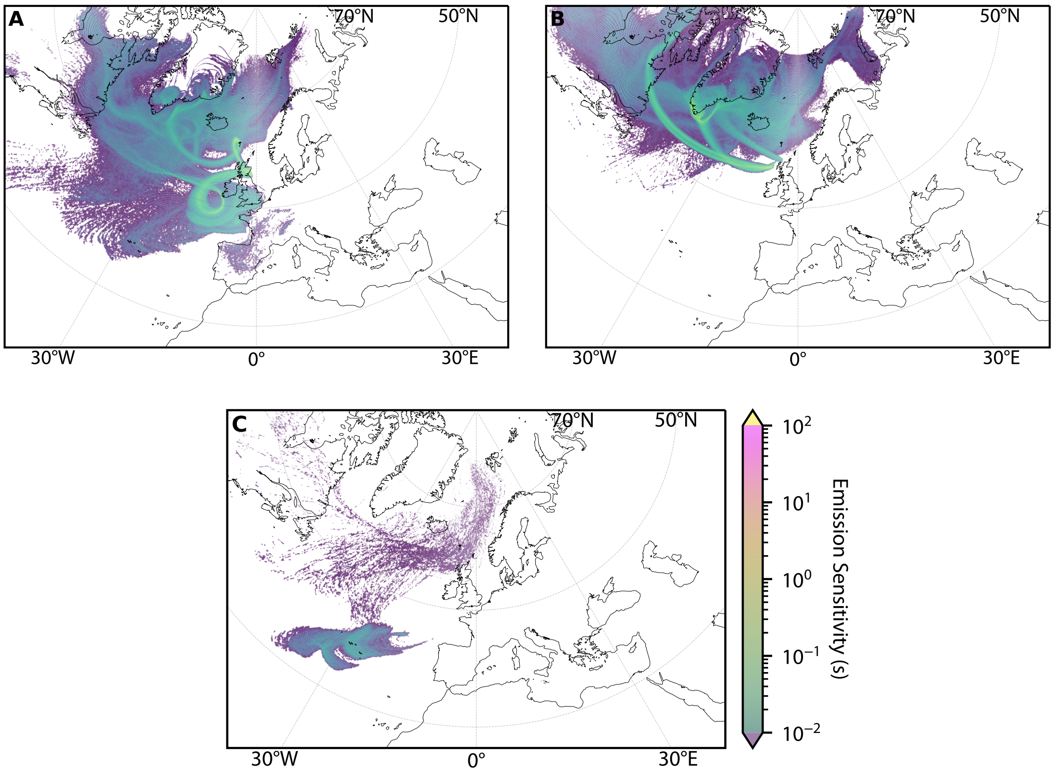

Fig. 4.8.: Potential emission sensitivity (PES) from 7-day FLEXPART back trajectory analysis. (A) average PES of samples in the boundary layer to the east of the UK (C153a, C166a), (B) average PES of samples in the boundary layer to the west of the UK (C152a, C162a, C162b, C162d, C163a) and (C) average PES of samples above the boundary layer (C162c, C163b, C167a)

4.3.3 Category 2: northerly flow

Flight C157 and C158 took place to the north of the UK, as shown in Fig. 4.9. The aim of flight C157 was to investigate the boundary layer structure and cloud properties in a cold-air outbreak (CAO). CAOs are a common feature where cold polar air is transported by northerly flow towards the UK (Abel et al., 2017). As cold, dry air is transported over the relatively warm open ocean the boundary layer evolves due to the addition of heat and moisture. Stratiform cloud decks form further north and transition to open cellular convection further south. There were no dropsondes during flight C157 but during the flight, cloud tops were observed to be at around 3000 mASL. Samples C157a, b and c were collected above the cloud tops and C157d was below the cloud base. C157a was in the convective regime of the CAO, C157b in the transition regime and C157c in the stratiform regime. Flight C158 took place the following day, the aim of this flight was to make clear-sky radiation measurements. The flow was also northerly, there was less cloud during flight C158 than C157 but patchy cumulus from open cellular convection was observed. The temperature and humidity profiles (Fig. 4.10) show that the cloud layer was at around 1000 mASL. Sample C160a was collected below this and C160b was collected above.

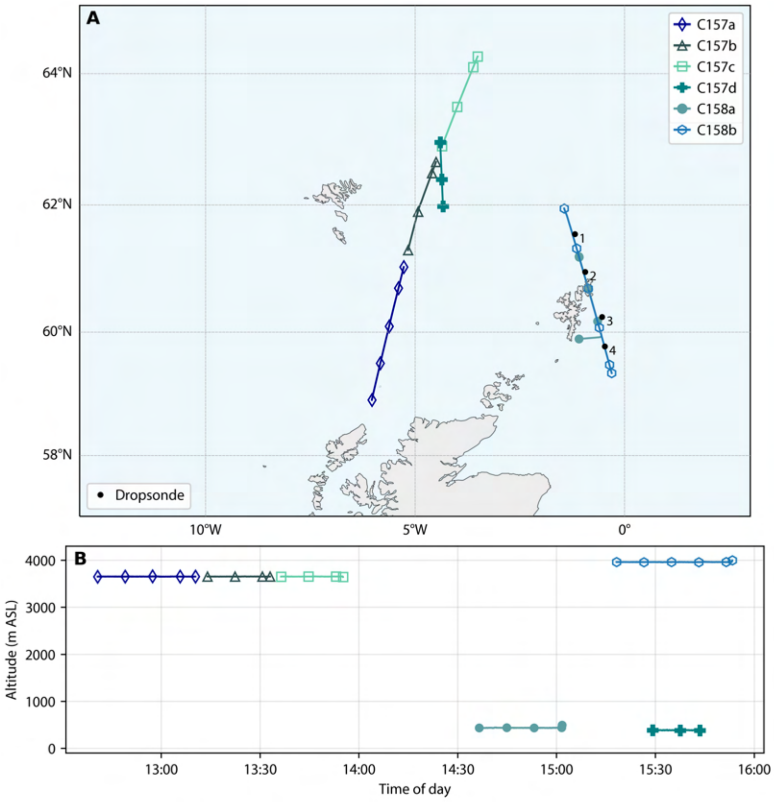

Fig. 4.9.: (A) Sampling location for samples in category 2. Dropsonde launches are shown in black and numbered to match Fig. 4.10. (B) Sampling altitude for samples in category 2. Samples with hollow symbols were above the boundary layer and samples with filled symbols were in the boundary layer.

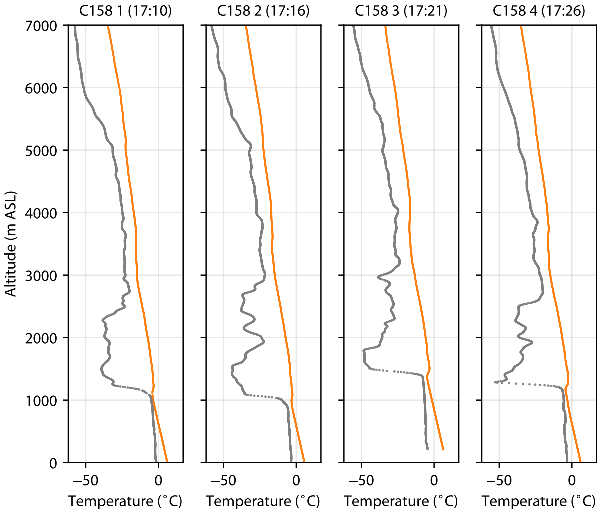

Fig. 4.10.: Temperature (orange) and dew point (grey) from dropsondes launched during flight C158

The INP spectra in Fig. 4.11B show that samples C157a, b and c that were collected above cloud have low N_{INP} (compared to other samples in this study) but C158b, which was also collected above cloud, has much higher N_{INP}. High N_{INP} is also observed in samples C157d and C158a which were both below cloud.

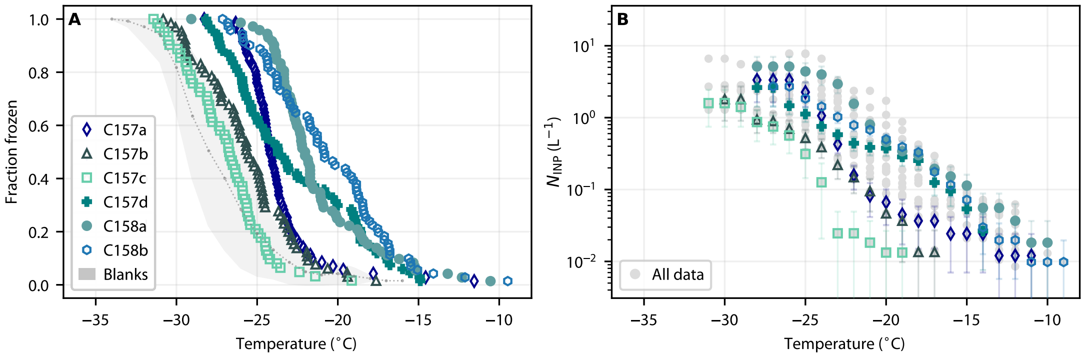

Fig. 4.11.: Measured fraction frozen (A) and INP concentration per standard litre of air (B) for samples in category 2.

Fig. 4.12A shows that, similarly to in category 1, the samples collected below cloud (C157d and C158a) show a clear enhancement of coarse mode aerosol that is not present in the samples collected above the cloud. Due to the observed northerly flow and lack of local terrestrial aerosol sources, it is likely that this is due to sea spray. The total aerosol surface area of the two below cloud samples, C157d and C158a were 68.8 and 44.1 μm^2 cm^{-3}, respectively.These are some of the highest values observed across all samples in this study which suggests that the high N_{INP} may be as a result of high aerosol loading, rather than the presence of particularly active INPs. This is confirmed by the n_s values for these samples, which are relatively low. In contrast, the total aerosol surface area for sample C158b, which also exhibited high N_{INP}, was much lower at 3.00 μm^2 cm^{-3}. This suggests that N_{INP} of sample C158b was enhanced by the activity of the aerosol itself rather than a high aerosol concentration, which is confirmed by the high n_s values for this sample. The samples collected above cloud during flight C157 have a similar size distribution to C168b but do not show the same high N_{INP}, however, the n_s values are similar to those observed in sample C158b. They also do not have the same enhancement in coarse mode aerosol as the below cloud samples. These observations once again suggest different populations of aerosol have been sampled, or that the samples have been diluted by inactive sea spray aerosol.

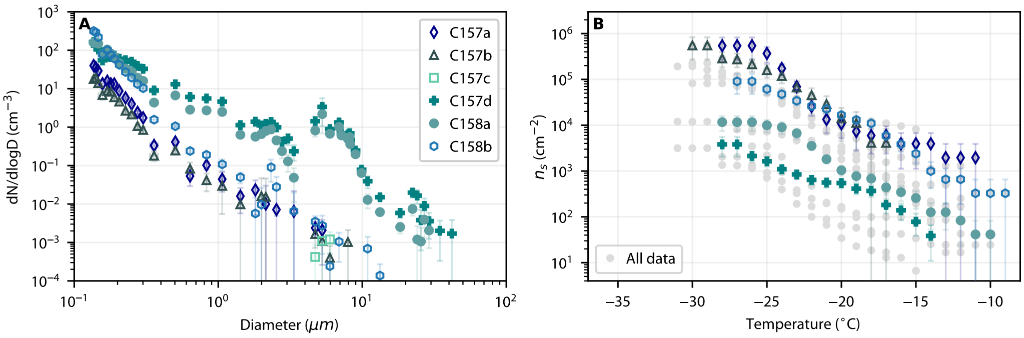

Fig. 4.12.: Size distribution of samples in category 2 determined from the PCASP and CDP optical probes (A) and active site density (n$_s$) of each sample (B).

Fig. 4.13 shows the mean PES footprint for the below cloud samples (A), the above cloud samples from flight C157 (B) and the above cloud sample from flight C158 (C). It is clear that there are different potential aerosol sources in the three groups of samples identified from the N_{INP} and n_s results. Fig. 4.13A shows that air masses sampled below cloud originate predominantly from the north, and there is a high surface emission sensitivity. This means that it is probable that the aerosol in samples C157d and C158b has been emitted from the marine environment north of the UK and the enhancement in coarse mode aerosol in samples C157d and C158b is most likely due to sea spray aerosol. In addition, the size distribution, n_s, N_{INP} and back trajectories of these samples are comparable to the marine samples identified in the previous case study suggesting a similar type of aerosol. Fig. 4.13B shows the back trajectories for samples C157a, b and c which were collected above cloud and Fig. 4.13B shows the back trajectory for C158b which was also collected above cloud. These examples have been considered separately due to the observed difference in N_{INP}.

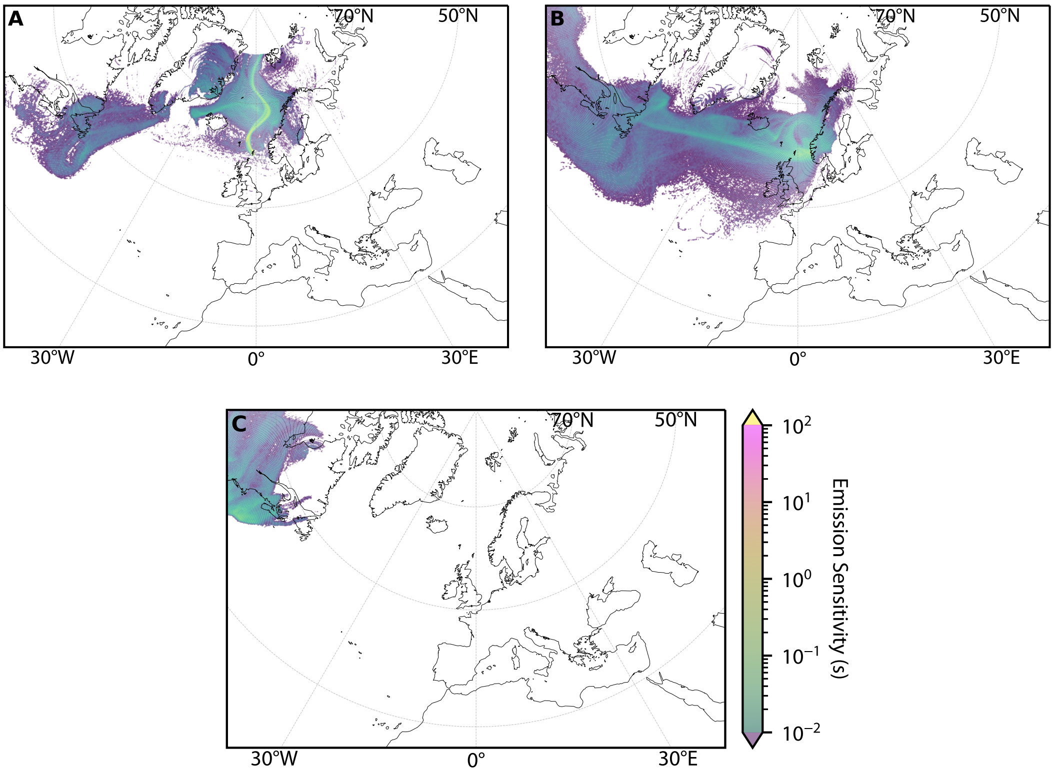

Fig. 4.13.: Potential emission sensitivity (PES) from 7-day FLEXPART back trajectory analysis. (A) average PES of samples in the boundary layer to the north of the UK (C157d, C158a), (B) average PES of samples above the boundary layer during flight C157 (C157a, C157b, C157d) and (C) average PES of samples above the boundary layer during flight C158 (C158b)

It is clear that the back trajectories of particles from above the boundary layer during flight C157 is quite different to those in C158, which is likely to have driven the observed differences in N_{INP}. On flight C157 the air masses have had contact with the surface in the days preceding sampling. This suggests that aerosol in samples C157a, b and c has been mixed into the cloud from below. The surface emission sensitivity covers a broad area which encompasses the marine environment but also highlights potential emissions from land in Scandinavia. Given the relatively high n_s values for these samples, especially compared to samples with no potential terrestrial influence, it is likely that the INP population in samples C157a, b and c has been enhanced by terrestrial aerosol. However, the size distribution is different to the terrestrial samples in the boundary layer identified in the previous case in that there is no enhancement in coarse-mode aerosol. This may be because the coarse mode aerosol has a shorter residence time in the atmosphere and hence at higher altitudes the larger sizes have been removed preferentially by wet or dry deposition. In contrast to flight C157, during C158 the sampled air masses are isolated from the surface which again implies that particles have descended from higher in the atmosphere. n_s and N_{INP} of C158b are also in agreement with the above cloud samples in the previous study. From this, we conclude that, like samples C162b and C167a, the INP activity of sample C158b is driven by aerosol from long-range transport above the boundary layer.

4.3.4 Category 3: westerly flow over orography

Flights C154 and C160 took place over the UK to investigate clouds forming due to lee waves in stable flow over orography. On both flights, sampling took place along transects over Scotland at varying altitudes.

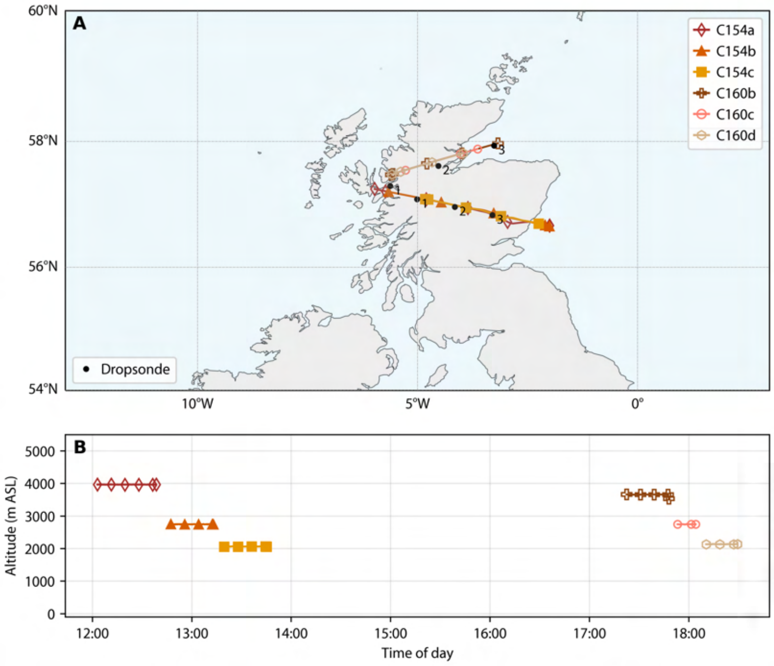

Fig. 4.14.: (A) Sampling location for samples in category 3. Dropsonde launches are shown in black and numbered to match Fig. 4.5. (B) Sampling altitude for samples in category 3. Samples with hollow symbols were above the boundary layer and samples with filled symbols were in the boundary layer.

The temperature and humidity profiles from dropsondes during the flights are shown in Fig 4.15. In both cases, a temperature inversion is observed with saturated air below the inversion and dry air above, however, during flight C154 this inversion is at around 3700 mASL compared to 2300 mASL during flight C160. This means that filter samples C154b and c are in the boundary layer, whereas the rest of the samples are above the boundary layer and above cloud.

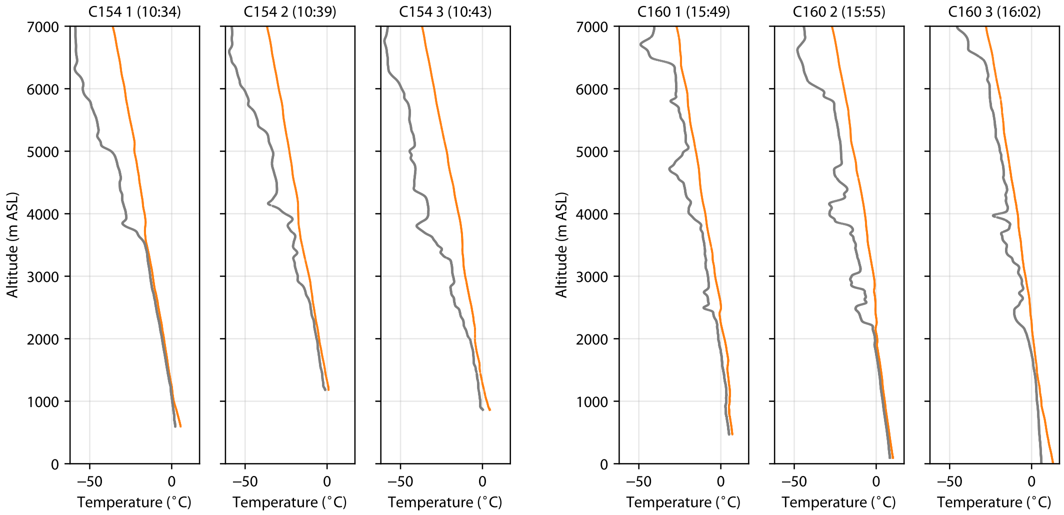

Fig. 4.15.: Temperature (orange) and dew point (grey) from dropsondes launched during flights C154 and C160

From the samples collected on flight C154, the highest N_{INP} of around 1 L^{-1} at -20°C, is observed in C154a which was collected above the boundary layer at close to 4000 mASL. N_{INP} then decreases to around 0.1 L^{-1} in samples C154b and C154c, which are in the boundary layer. N_{INP} is also lower in samples C154b and C154c than all of the samples during flight C160, which are all above the boundary layer. This difference between the samples collected in or above the boundary layer is in agreement with the previous two case studies and it is once again likely that the air masses sampled are different resulting in the observed differences in N_{INP}.

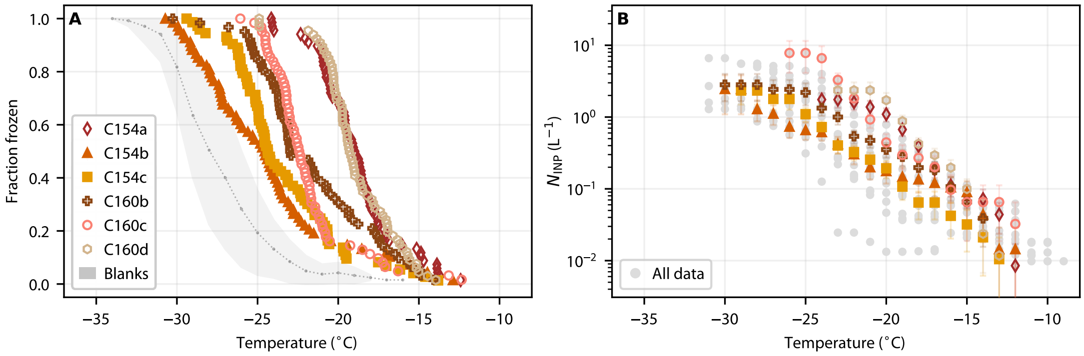

Fig. 4.16.: Measured fraction frozen (A) and INP concentration per standard litre of air (B) for samples in category 3.

The size distributions shown in Fig. 4.17A follow a similar pattern to N_{INP} with the samples in the boundary layer having the lowest number concentrations, suggesting that the observed differences in N_{INP} are due to less aerosol overall. The large peak in the size distribution of C160d is interesting however this sample was collected close to the cloud tops and it is therefore likely that this is a result of cloud droplets. The data from the optical probes were filtered to remove the potential influence of liquid or swollen aerosols due to high humidity, however, some erroneous results can still occur. This run was therefore excluded from the calculation of n_s. Fig. 4.17B presents n_s for these samples. These results are relatively high (compared to others in this study) and all of the samples exhibit similar n_s; there is very little difference in the samples collected above or below the boundary layer. This may be due to similar activity in two different INP populations, or it may suggest vertical mixing between the boundary layer and the air above.

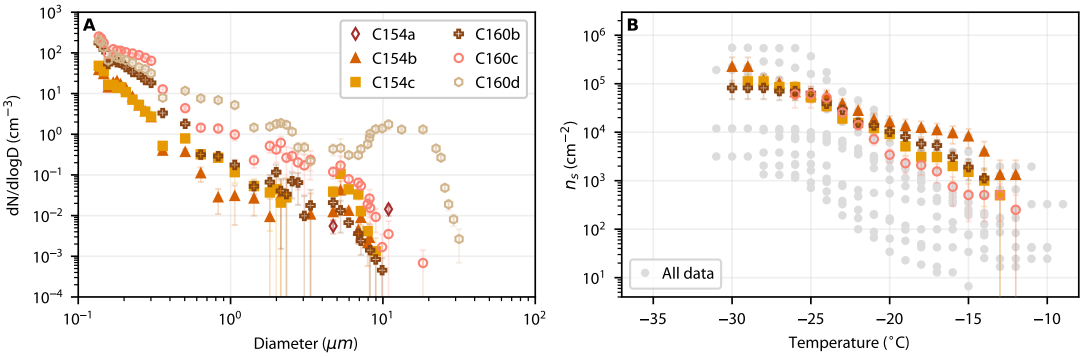

Fig. 4.17.: Size distribution of samples in category 3 determined from the PCASP and CDP optical probes (A) and active site density (n_s) of each sample (B).

Fig 4.18 shows the mean PES footprint for samples collected in the boundary layer (A) and above the boundary layer (B). The PES footprint of samples in the boundary layer are similar to those observed in the marine samples in case 1, however, in this case, there is contact with land over the UK suggesting a potential terrestrial aerosol source. n_s of samples C154b and C154c is similar to n_s of the terrestrial samples in case study one, and much larger than the marine samples in both of the previous cases, suggesting that N_{INP} of samples C154b and C154c is enhanced by terrestrial aerosol from the UK. The dropsonde profiles show that below the boundary layer the atmosphere is well mixed to the surface, and vertical motion was observed during the flight hence it is likely that these samples contain terrestrial aerosol. In contrast, and as observed in the previous two case studies, the air masses sampled above the boundary layer have not been in contact with the surface for most of the preceding 7 days. This suggests that air masses are predominantly descending from above and any aerosol present is likely to be from long-range transport.

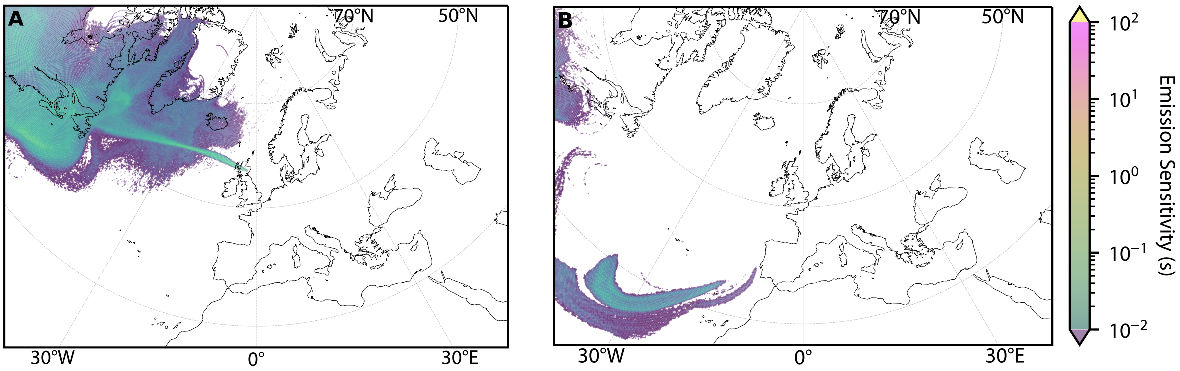

Fig. 4.18.: Potential emission sensitivity (PES) from 7-day FLEXPART back trajectory analysis. (A) average PES of samples in the boundary layer (C154b, C154c) and (B) average PES of samples above the boundary layer (C154a, C160b, C160c, C160d)

4.3.5 Sources of ice-nucleating particles in the North East Atlantic

We have highlighted three potential aerosol sources in the samples collected during PIKnMIX-F: a local marine source, a surface terrestrial source (UK and Scandinavia) and a long-range source. Fig. 4.19 shows the median N_{INP} and n_s for the samples in each of these groups. The highest median N_{INP} is observed in the terrestrial samples and the lowest is in the marine samples, with there being a difference of around half an order of magnitude at -20°C. However, this difference is only observed between around -15 and -25°C, above and below these temperatures median N_{INP} is similar across all three categories. Below -25°C this is likely due to the limit of detection of the technique, as outlined above. Above -15°C there is a ‘hump’ in the marine data which may be due to the presence of a population of INPs that are more active at warmer temperatures.

Fig. 4.19A also compares the results of this study with other observations. The blue shaded area shows INP concentrations from field and laboratory measurements of sea spray (adapted from DeMott et al. (2016)). The median N_{INP} of the marine samples in our study overlaps with this dataset. The pink shading shows N_{INP} from samples collected in Leeds, UK by (O’Sullivan et al., 2018). In this study, they identify a fraction of their samples that are heat-sensitive and a fraction that are heat-insensitive. They attribute the INP activity of the heat-sensitive samples to be due to biological INPs from the UK, and the heat-insensitive fraction to be mineral dust. The pink shading includes all samples in (O’Sullivan et al., 2018) whereas the purple shading includes only those that were heat-insensitive and therefore likely to be dominated by mineral dust. Between -18 and -25°C the O’Sullivan dataset overlaps with N_{INP} from the terrestrial and long-range samples in our study. However, at warmer temperatures, O’Sullivan et al. (2018) observe much higher N_{INP} than what is seen in this study. They attribute these high INP concentrations to the presence of biogenic aerosols. The fact that our results match well with the heat-insensitive portion of the samples in O’Sullivan et al. (2018) but there is a discrepancy at warmer temperatures suggests that below -20°C the activity of our samples is dominated by mineral dust but we have not sampled the highly active biogenic INPs as observed by O'Sullivan et al. (2018) at temperatures above -20°C.

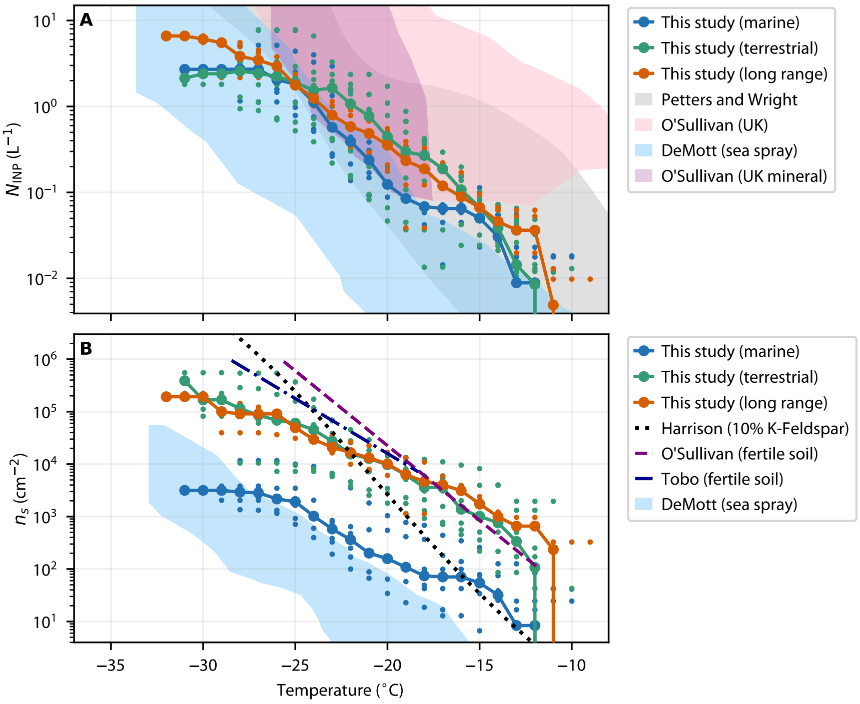

Fig. 4.19.: INP concentrations (A) and n_s (B) for all samples collected during PIKnMIX-F. Samples are grouped by potential aerosol sources: local marine (blue), local terrestrial (green) and long-range terrestrial (orange). (A) shows INP concentrations from Petters and Wright (2015), O'Sullivan et al. (2018), DeMott et al. (2016) and (B) shows n_s from Harrison et al. (2019), O'Sullivan et al. (2014), Tobo et al. (2013) and DeMott et al. (2016)

Fig. 4.19B shows the median n_s, again grouped by potential aerosol source. n_s of the samples identified as having a local and long-range terrestrial source are very similar to each other, meaning the ice-nucleating activity of samples collected above and below the boundary layer in this study is similar. However, there is a considerable difference between the marine and terrestrial samples. At -20°C, n_s of the terrestrial and long-range transport samples is almost 2 orders of magnitude greater than the marine samples, this provides clear evidence for there being distinct populations of INPs in our samples. Comparing our results to other studies reveals that n_s of the marine samples in this study is similar to that observed by DeMott et al. (2016), however our results are slightly higher, especially at warmer temperatures. The sampling biases of the filter system on the aircraft mean that there tends to be more coarse mode aerosol, particularly above $\sim$8 μm, sampled on filters than observed by the optical probes (Price et al., 2018; Sanchez-Marroquin et al., 2019). This oversampling means that the calculation of n_s is likely to be biased high, which could explain the discrepancy between our marine sample and those of DeMott et al. (2016). Correcting for this would bring the results in good agreement with DeMott et al. (2016). n_s of our terrestrial samples does not agree with the potassium (K) feldspar parametrisation of Harrison et al. (2019), the data overlap but the slope of our n_s curves is much shallower and at temperatures above -20°C we observe higher n_s than the K-feldpsar parameterization.

A minor fraction of the aerosol sampled is likely to be mineral dust so the magnitude of the parametrized and measured n_s values would not be expected to match, however comparing the slope is informative and the difference observed implies that something else is responsible for the ice-nucleating activity in our samples. Comparing our results to n_s of fertile soil sampled in the UK by (O'Sullivan et al., 2014) shows that the ice-nucleating ability at warmer temperatures in our samples could be explained by fertile soil. There is also good agreement between our data and that of Tobo et al. (2013) which is also for fertile soil. Below -20°C, our results are lower than that of the two fertile soil studies and the K-feldspar parameterization. This may be because only a minor component of the aerosol is fertile soil or mineral dust.

4.4 Conclusions

In this study, aerosol samples were collected using the filter system on board the FAAM BAe-146 aircraft during the PIKnMIX-F field campaign in March 2019. These filters were analysed using the droplet-on-filter technique to quantify atmospheric ice-nucleating particle concentrations. Aerosol data was obtained from underwing optical probes to calculate an aerosol surface area which was then used to calculate ice-active sight density for our samples. This analysis shows that there is variability in ice-nucleating particle concentrations and activity in samples driven by different sampling locations and whether samples were collected in or above the boundary layer. We categorised samples based on the synoptic conditions in which they were sampled and used FLEXPART back trajectories to identify potential sources of aerosol and drivers of the difference in observed ice-nucleating activity.

Three categories of samples were identified: samples collected in the boundary layer with a local marine aerosol source, samples collected in the boundary layer with a local terrestrial source, samples collected above the boundary layer with a terrestrial source from long-range transport. The INP concentrations of these samples show only a small amount of variability, however normalising these results to the surface area of aerosol to calculate n_s revealed significant differences between the marine and terrestrial samples.

Samples collected in the marine boundary layer where sampled air masses had minimal contact with land in the preceding 7 days had high aerosol concentration but relatively low ice-nucleating activity. These samples had an enhancement of coarse mode aerosol suggesting a surface aerosol source that is likely to be sea spray. Qualitative observations of sea state showed the highest aerosol concentrations were measured on the days with the roughest seas, providing further evidence for this conclusion. We compared our N_{INP} and n_s values to sea spray observations from DeMott et al. (2016) and find N_{INP} in a similar range. Our observed n_s values are slighter higher than DeMott et al. (2016) but this could be explained by the oversampling of course mode aerosol on the filters compared to the observations from the optical probes that were used to calculate the aerosol surface area. Hence, we conclude that the aerosol population of these samples is dominated by sea spray aerosol. In contrast, samples where there had been contact with land showed much higher ice-nucleating activity. This was apparent in samples collected in the marine boundary layer where air masses has passed over the UK before sampling, in samples collected above cloud to the north of the UK where the FLEXPART results highlight potential aerosol emissions from Scandinavia and in samples collected over land where FLEXPART results show potential aerosol emissions from the UK and vertical motion was observed during the flight. Since we do not know the exact composition of the samples, quantitative comparisons of n_s calculated from the total aerosol surface area with parametrizations would not necessarily show a good agreement in magnitude. However, comparing the slope of observed n_s with other observations and a K-feldspar parametrisation reveals that the activity of these samples most likely cannot be explained entirely by K-feldspar but at temperatures above -20°C our results are in good agreement with observations of n_s of fertile soils. These results provide evidence for a terrestrial source of aerosols. Finally, we identified samples that were collected above the boundary layer that had low aerosol concentration but relatively high ice-nucleating activity. Samples in this category were collected to the north, east and west of the UK. FLEXPART back trajectories showed that it was unlikely that aerosols in these samples were emitted from the surface in the 7 days before sampling, implying that particles had descended from higher in the atmosphere before being sampled.

These results highlight that sources of INPs can vary drastically over small spatial scales and show that the INP concentration in air masses can be enhanced by contact with land. The samples collected to the east of the UK were less than 350 km from those collected on the west but N_{INP} and n_s were more than an order of magnitude greater. The results also show that whether INPs are mixed into clouds from above or below is an important consideration because, in many cases, we observed that the ice-nucleating activity of the samples collected above cloud was much greater than was sampled below cloud. This was particularly pronounced in the marine environment where sea spray aerosol dominates in the boundary layer but is not such an active ice-nucleating material as terrestrial aerosol that may be present above the boundary layer. This has important implications for accurately modelling ice-formation processes in shallow marine clouds, which are common in the mid- to high-latitudes and are particularly important for cloud-phase feedback (Murray et al., 2021; Ceppi et al., 2017).

Conclusions

5.1 Overview

This thesis applies a range of measurement and analysis techniques to address gaps in our understanding of the sources and characteristics of INPs in the high-latitudes, as well as their impact on cloud microphysical properties. Chapter 2 focuses on high-latitude INP sources and uses ground-based sampling and particle dispersion modelling to quantify the ice-nucleating ability and potential atmospheric impact of dust from the Copper River, Alaska. Chapter 3 focuses on the impact of INPs on cloud microphysical properties using remote sensing observations from Summit Station, Greenland to make measurements of ice-crystal number concentration in clouds over the Greenland Ice Sheet. These measurements are compared to INP concentrations measured as part of the ICECAPS Aerosol Cloud Experiment (ICECAPS-ACE) to identify contributions of primary and secondary ice production to the observed ice crystal number concentrations in clouds. Chapter 4 focuses on atmospheric concentrations of INPs using measurements made from the FAAM BAe-146 research aircraft and uses back trajectory analysis to identify different aerosol source regions in climatically important mixed-phase clouds. This chapter summarises the key findings of this thesis and makes recommendations for future work.

5.2 Summary of findings

5.2.1 High-latitude sources of INPs

Glacial dust from the Copper River, Alaska nucleates ice at temperatures relevant for mixed-phase clouds and is transported to regions where it could cause cloud glaciation.

Chapter 2 presents a novel approach to investigate potential INP sources from observations at the source through to modelling atmospheric concentrations. Samples of glacial dust for INP analysis were collected at the Copper River, Alaska using portable battery-powered equipment and an open-source particle dispersion model was used to investigate the transport of dust emissions from this source and predict atmospheric INP concentrations. This methodology offers a template that can be applied in other regions to provide a first estimate of INP concentrations without the need for large field campaigns and computationally expensive modelling.

The results show that dust from the Copper River is an effective ice-nucleating material under conditions relevant for mixed-phase clouds. X-ray diffraction analysis showed the presence of ice-active minerals in the dust (e.g. potassium feldspar) but comparing the ice-nucleating activity of our samples with known parameterizations of these minerals showed that the parameterizations under-predicted the activity of the Copper River dust. This means the ice-nucleating activity is different to that of low-latitude dust and is controlled by something other than the mineral content. All of the Copper River samples were sensitive to heat, particularly at temperatures warmer than -20°C, hence we conclude that the activity of dust from the Copper River is predominantly controlled by heat-sensitive biogenic material that is mixed with the dust during transport in the fluvial environment. This finding is in agreement with studies of other high-latitude dust sources (Tobo et al., 2013; Xi et al., 2022), however, the ice-active site density of samples from the Copper River was higher than those observed by Xi et al. (2022). This we attribute to the presence of more biogenic material in the Copper River samples, which leads to the conclusion that the ecosystem of the watershed in which glacial sediment is transported and deposited defines the ice-nucleating ability of the dust that is emitted. FLEXPART modelling showed that dust could be lofted to altitudes of up to 5000 mASL and that the highest dust mass concentrations (after 60 hours) were between 2000 mASL and 4000 mASL, where temperatures were between -5 and -20°C. At 4000 mASL, N_{INP} exceeded 1 L^{-1}, a concentration that could alter cloud radiative properties and liquid water content (Vergara-Temprado et al., 2018). We also found that at certain times of the year, the contribution to atmospheric INP concentrations over North American and the Gulf of Alaska was greater from the Copper River than from mineral dust from low-latitude sources (Vergara-Temprado et al., 2017) meaning that the Copper River may be the dominant INP source.

These findings confirm the importance of high-latitude dust as a source of INPs and show that high-latitude dust emissions must be included in global climate models to accurately represent primary ice production. The results show that parametrisations of ice-nucleating particles must be adapted to correctly represent high-latitude sources because the activity can differ considerably compared to INPs from low-latitude sources. This highlights the need for further observations in both the northern and southern high latitudes to investigate the variability in ice-nucleating activity across different high-latitude dust sources.

5.2.2 The influence of INPs on cloud microphysical properties

Ice crystal number concentration can be retrieved using remote sensing instrumentation at Summit Station, Greenland and provides evidence for a secondary ice production mechanism that is active between -10 and -18°C.

In Chapter 3, a technique to retrieve ice crystal number concentration (N_{ice}) from clouds using radar and lidar remote sensing observations was adapted and tested for use with observations from the Integrated Characterization of Clouds, Energy, Atmospheric state, and Precipitation at Summit (ICECAPS) project. We found that the method was most successful using a radar-only retrieval which was applied to case studies of stratiform mixed-phase clouds observed at Summit

Station, Greenland in Summer and Autumn 2019. Using this approach, the retrieval uncertainties are similar to other studies (Bühl et al., 2019; Ramelli et al., 2021) and observed N_{ice} is in agreement with previous observations of Arctic boundary layer clouds (Hobbs and Rangno, 1985; Rangno and Hobbs, 2001b; Pasquier et al., 2022). These results present the first observations of N_{ice} in clouds over the Greenland Ice Sheet. The ICECAPS project has been making remote sensing observations at Summit for over 13 years; the methods applied in this thesis open up the possibility of using this dataset for a long-term investigation into ice in clouds over the Greenland Ice Sheet. This would provide valuable insights into the radiative budget and precipitation patterns on the ice sheet, both of which need to be properly constrained in order to accurately model the surface mass balance. Given the similarity between clouds at Summit and other regions in the Arctic (Shupe et al., 2013) such a study would also be applicable to Arctic mixed-phase clouds more broadly. Comparing N_{ice} with INP concentrations determined from aerosol samples collected at Summit Station reveals that at the cloud top N_{ice} and N_{INP} are often in agreement but in cloud N_{ice} often exceeds N_{INP} by many orders of magnitude. This provides evidence that secondary ice production is enhancing ice crystal number concentration in these clouds. Comparing N_{INP} and N_{ice} as a function of temperature shows that between around -18 and -26°C N_{ice} increases in line with N_{INP}, suggesting N_{INP} modulates N_{ice} at these temperatures. However, at temperatures warmer than -18°C N_{ice} is significantly enhanced and the highest ice multiplication factor ($N_{\text{ice}}/N_{\text{INP}}$) is at -15°C. From this, we conclude that there is a secondary ice process that is active between -10 and -18°C.

Many previous studies have focussed on secondary ice production between -3 and -8°C where the Hallet-Mossop process is thought to dominate SIP, these results add to a growing body of evidence showing that SIP is important at considerably colder temperatures (Korolev et al., 2022; Pasquier et al., 2022; Järvinen et al., 2022). Determining what SIP mechanism is responsible for the observed enhancement of N_{ice} from remote sensing alone is not possible, this highlights the need for more in-situ observations of cloud microphysical properties (e.g. N_{ice}, ice crystal shape, crystal size) in order to fully understand ice formation pathways in clouds.

5.2.3 INP concentrations in the atmosphere

Sources of INPs measured in the atmosphere can vary drastically over small spatial scales and INP concentrations in air masses can be enhanced after coming into contact with land.

In Chapter 4, measurements were made from the FAAM BAe-146 research aircraft during the PIKnMIX-F field campaign in March 2019 to investigate atmospheric INP concentrations. N_{INP} was determined from samples using droplet-on-filter freezing assay experiments and found to vary by more than one order of magnitude, and the temperature at which N_{INP} exceeds 0.1 L^{-1} ranged from $\sim$-14 to $\sim$-21°C. Measurements from under-wing optical probes were used to measure aerosol size distribution and determine an aerosol size distribution that was used to calculate ice-active site density (n_s) from N_{INP}. The n_s values showed even greater variability, with the n_s at -20°C ranging from less than 10^2 to greater than 10^4 cm^{-2}. Samples collected in the marine boundary generally showed the highest aerosol loading and an enhancement in coarse-mode aerosol, which is likely to be due to sea spray aerosol. Of these samples, those where FLEXPART analysis showed that potential emissions were predominantly from the marine environment had low N_{INP} and low n_s (relative to other samples in this study). In contrast, those where FLEXPART analysis showed potential aerosol emissions from land had a similar size distribution but higher N_{INP} and n_s suggesting a terrestrial source of INPs that contributes to the atmospheric INP population when air masses come into contact with land. Samples collected above the boundary layer had relatively high N_{INP} and n_s values but FLEXPART analysis showed that it was most likely that the sampled aerosol had descended from higher in the atmosphere rather than having been emitted from the surface in the previous 7-days, which suggests the observed INP activity is due to aerosol from long-range transport rather than emissions from an aerosol source at the surface in the last 7-days. We conclude that the aerosol loading of samples collected in the boundary layer is dominated by sea spray aerosol, which does not have high ice-nucleating ability, but there is a terrestrial source of aerosols that enhances the INP population when air comes into contact with land. We also propose that there is a population of INPs in the free troposphere that can be mixed into the boundary layer and enhance the INP population.

These results show that the source of the INPs in the atmosphere varies over small scales and show that INPs have the potential to be entrained into clouds from above and below. This has important implications for modelling mid to high-latitude mixed-phase clouds and quantifying the role of INPs in modulating the cloud-phase feedback.

5.3 Future work

The findings of this thesis contribute to our knowledge in different areas of ice nucleating research but also highlight several open questions. In Chapter 2, size-resolved measurements quantify the characteristics of INPs as they are emitted from a source but how the size distribution and INP population evolves in time and space requires further measurements. In addition, the modelling in Chapter 2 provides insights into the contribution to INP concentrations in the atmosphere from the source but without observations of cloud properties the impact of these INPs on clouds cannot be quantified. In Chapter 3, the comparison of INPs and ice-crystal number concentration provides insights into primary and secondary ice production but the composition of the INPs sampled is unknown meaning the exact controls on the nucleation cannot be determined. Furthermore, the samples collected at the surface may not be representative of the observations made in the cloud and a lack of in-situ cloud measurements means validation of the results is challenging. In Chapter 4, atmospheric INP concentrations are quantified and different source regions are identified but the composition of these particles was not measured. In addition, comparisons between the observed INP concentrations and ice crystal number concentration in cloud were not made. It is clear that linking all of these measurements is a crucial step to understanding INPs and their impact on clouds. Here I propose a possible study that combines all of the techniques used in this thesis and what was learned when applying them in isolation to provide much-needed observations of the role of INPs from source through to their impact on cloud properties.

For such a study, there needs to be a known INP source with regular emissions to a region with sufficiently supercooled clouds, the potential to make airborne measurements and the potential to deploy ground or ship-based remote-sensing and aerosol instrumentation. The Gulf of Alaska offers such a 'natural laboratory'. First, we have shown that the Copper River is a known INP source and temperatures are sufficiently low that these INPs could cause cloud glaciation. Secondly, there are accessible and nearby airports where an aircraft campaign could be based. Finally, as well as the potential for ship-based measurements, there is a small uninhabited island, Middleton Island, located approximately 130 km south of Cordova in the Gulf of Alaska as shown in Fig. 5.1. Due to previously being the site of a US Air Force Station, and now the site of regular sea-bird research, the island has a well-maintained runway and is accessible for research.

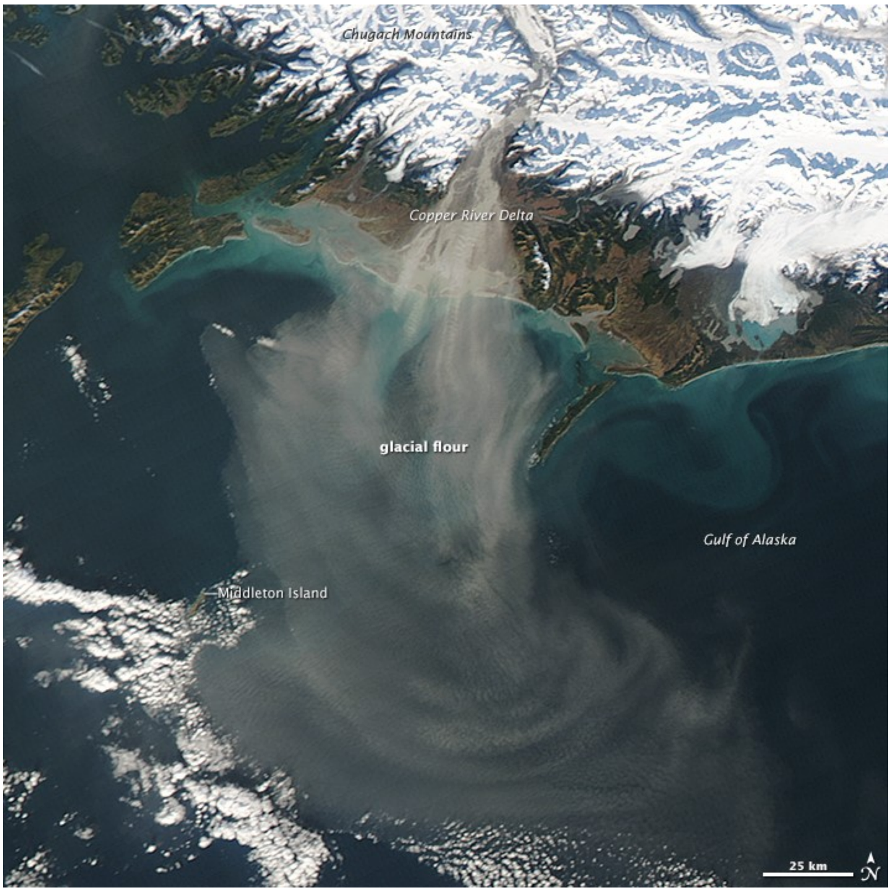

Fig. 5.1.: True colour image of the Gulf of Alaska during a dust storm on 28th October 2014, captured by NASA's Aqua Moderate Resolution Imaging Spectroradiometer (MODIS). Adapted from NASA Earth Observatory (2014).

Fig 5.2 illustrates a potential experimental set-up at this location. All of the instruments described are currently available and have previously been used in the ways described herein, but it should be noted that this hypothetical experiment optimistically assumes that funding is no object. Four main categories of measurements are proposed: in-situ INP sampling, in-situ aerosol observations, in-situ cloud observations and remote sensing observations.

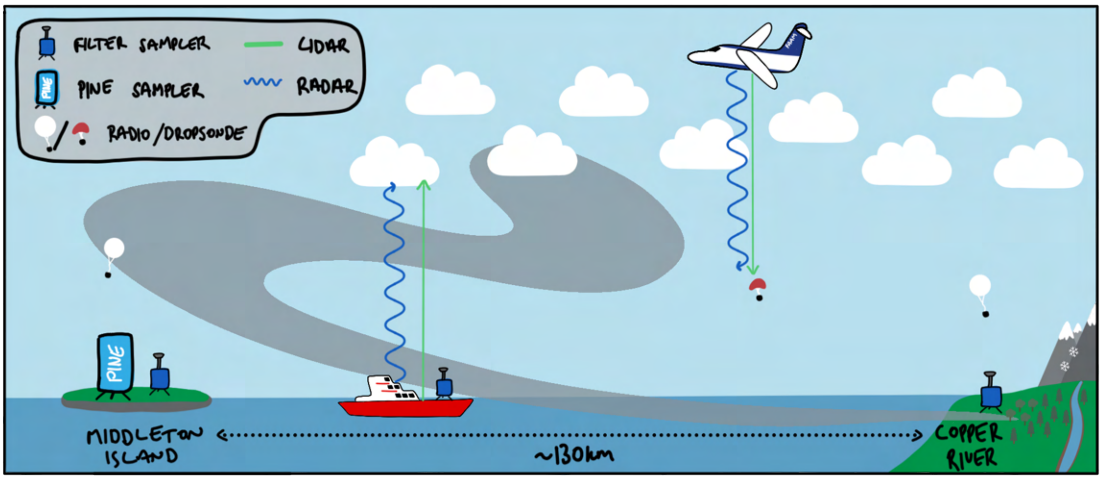

Fig. 5.2.: Schematic of proposed study to investigate ice formation in clouds in the Gulf of Alaska. Not to scale.

Deploying the multi-stage cascade impactor used in Chapter 2 and/or the semi-automated digitel filter sampler used in Chapter 3 to the Copper River Delta, on board a research vessel and on Middleton Island to collect filter samples for INP analysis would provide insights into the evolution of the INP population in the boundary layer with increasing horizontal distance from the source. Concurrent filter sampling from the FAAM BAe-146 research aircraft, following the method outlined in Chapter 4, would capture the vertical distribution of aerosol and INPs in the atmosphere and add more certainty that the INPs sampled are representative of those at the altitude of the clouds. Samples in the boundary layer and in the free troposphere can also help identify different potential INP sources, as seen in Chapter 4. One of the limitations of offline filter sampling is the need for samples to be collected over many hours which may mean short-term temporal variability is not captured, as was highlighted in Chapter 3 of this thesis. On the other hand, sampling is not autonomous so is hard to implement over long timescales. The inclusion of online methods for INP analysis would improve the spatial and temporal resolution of the INP measurements. The portable ice nucleating experiment (PINE; Möhler et al. (2021)), is an expansion chamber capable of making automated long-term field observations of INPs that could be deployed on Middleton island for an extended period to capture seasonal cycles of dust and INP emissions from this source. The Met Office Ice Nucleus counter (INC) is a continuous-flow diffusion chamber currently under development for use on board the FAAM aircraft that could be used to capture spatial variability in INP concentrations (horizontal and vertical).

Quantifying the evolution and variability of the total aerosol loading in the atmosphere and the particle size distribution is vital and can be achieved using ground and aircraft-based optical instruments alongside the INP measurements. The University of Leeds has a suite of aerosol instruments contained in a shipping container (the IcePod) that has been deployed for field measurement around the world (O'Sullivan et al., 2018; Porter et al., 2022; Harrison et al., 2022b) and could be used on the research vessel in this proposed study. The instruments available include a scanning mobility particle sizer (SMPS) and aerodynamic particle sizer (APS) spectrometer that combined can measure aerosol from 10 nm to 20 μm. From the FAAM aircraft, particle size distribution measurements can be made using the under-wing optical probes as outlined in Chapter 4. Identifying the controls of ice nucleating activity in samples requires knowledge of the aerosol composition. In Chapter 2, this was achieved using X-ray diffraction analysis but the analysis was done on bulk material collected from the surface and sieved to 45 μm, rather than samples collected from the atmosphere. It is likely that the composition of the material that is aerosolised differs from the bulk due to the different size distribution (Glaccum and Prospero, 1980) but this could not be confirmed. Furthermore, in Chapter 4, variability between aerosol populations in the boundary layer and in the free troposphere was observed but the composition of these aerosol populations could not be determined with the observations available. Collecting filter samples to determine size-resolved aerosol composition by scanning electron microscopy with energy-dispersive X-ray spectroscopy (SEM-EDS), following the methods in Sanchez-Marroquin et al. (2019), would address both of these open questions. Samples could be collected using ground-based filter samplers at the Copper River Delta and on Middleton Island to investigate the aerosol composition at the source and after transport. In addition, samples could be collected from the aircraft; the inlet system has two parallel inlets meaning one filter can be collected for INP analysis and one for SEM-EDS analysis at the same time. This would help to identify what controls the ice-nucleating activity of dust from the Copper River and identify if there is an additional aerosol source in the free troposphere as observed in Chapter 4. Determining the surface area of aerosol sampled onto filters on the aircraft using SEM-EDS rather than the underwing optical probes would also address the uncertainties associated with biases when sampling aerosol from an aircraft that are outlined in Chapter 4.

In-situ observations of cloud microphysical and bulk properties from the FAAM BAe-146 aircraft would allow validation of remote sensing retrievals and comparison of cloud properties (e.g. liquid water path) with measured INP concentrations. In addition, in Chapter 3 regions where secondary ice production was likely to be enhancing the ice crystal number concentration in cloud were identified but determining the mechanism responsible for this was not possible. Imaging probes on the aircraft can capture particles from 15 μm to 6 mm to quantify their shape and determine the particle size distribution. The size of ice crystals can be used to identify how they have formed (Korolev and Leisner, 2020), hence this data may allow SIP mechanisms to be identified.

Finally, remote sensing observations are needed to investigate cloud properties over a longer time scale than is possible to measure from an aircraft, specifically to apply the method outlined in Chapter 3 to retrieve ice crystal number concentration. Radar and lidar instruments installed on Middleton Island could be used to make long-term observations in conjunction with the proposed (almost) continuous INP observations from PINE. This would be a significant improvement over the INP sampling approach in Chapter 3 where the samples were collected over 56 hours. A further uncertainty of the approach in Chapter 3 is associated with the measurement of the vertical air motions. To address this, a radar wind profiler could be installed with the radar and lidar and the vertical air motion determined following the approach in Radenz et al. (2018). Remote sensing instruments can also be deployed on moveable platforms which allows more flexibility in measurement location, hence the proposed remote sensing instruments could be installed on a ship. This presents additional challenges due to the motion of the platform but instruments can be stabilised or the motion recorded and corrected for (Moran et al., 2012; Protat and McRobert, 2020). The FAAM BAe-146 aircraft also offers the potential for remote sensing that would allow observations to be made from above and below cloud. At present the aircraft is not equipped with radar however radar, doppler wind lidar and aerosol lidar instruments have been proposed for the upcoming mid-life upgrade of the aircraft. Lidar can also be used to investigate aerosols and INPs. Ansmann et al. (2008) and Wieder et al. (2022) propose methods to determine INP concentrations by combining parametrisations of INPs with lidar data. The availability of ship or aircraft-borne aerosol lidar alongside the multitude of aerosol and INP observations proposed here opens up the possibility of testing and validating these methods.

5.4 Closing remarks

The formation and evolution of mixed-phase clouds is governed by complex and intertwined processes; from the nucleation of ice at a scale of just a few nanometres, to the influence of synoptic-scale weather systems spanning 100s of kilometres. Quantifying these processes is of crucial importance to better understand our climate, now and in a rapidly warming world. This thesis approaches the gaps in our knowledge of ice-nucleating particles and ice formation in clouds from different angles in an attempt to untangle some of these complexities. The work has provided new observations in diverse regions around the world and developed novel techniques that can be applied to many more, both of which contribute to our overall understanding of the role of ice-nucleating particles in the climate system.

Bibliography

Abel, S. J., Boutle, I. A., Waite, K., Fox, S., Brown, P. R. A., Cotton, R., Lloyd, G., Choularton, T. W., and Bower, K. N. (2017). The Role of Precipitation in Controlling the Transition from Stratocumulus to Cumulus Clouds in a Northern Hemisphere Cold-Air Outbreak. *Journal of the Atmospheric Sciences*, 74(7):2293–2314.

Adams, M. P., Tarn, M. D., Sanchez-Marroquin, A., Porter, G. C. E., O'Sullivan, D., Harrison, A. D., Cui, Z., Vergara-Temprado, J., Carotenuto, F., Holden, M. A., Daily, M. I., Whale, T. F., Sikora, S. N. F., Burke, I. T., Shim, J.-U., McQuaid, J. B., and Murray, B. J. (2020). A Major Combustion Aerosol Event Had a Negligible Impact on the Atmospheric Ice-Nucleating Particle Population. *Journal of Geophysical Research: Atmospheres*, 125(22):e2020JD032938.

Albrecht, B. A. (1989). Aerosols, Cloud Microphysics, and Fractional Cloudiness. *Science*, 245(4923):1227–1230.

Andreae, M. O., Elbert, W., Gabriel, R., Johnson, D. W., Osborne, S., and Wood, R. (2000). Soluble ion chemistry of the atmospheric aerosol and SO2 concentrations over the eastern North Atlantic during ACE-2. *Tellus B: Chemical and Physical Meteorology*, 52(4):1066–1087.

Ansmann, A., Tesche, M., Althausen, D., Müller, D., Seifert, P., Freudenthaler, V., Heese, B., Wiegner, M., Pisani, G., Knippertz, P., and Dubovik, O. (2008). Influence of Saharan dust on cloud glaciation in southern Morocco during the Saharan Mineral Dust Experiment. *Journal of Geophysical Research: Atmospheres*, 113(D4).

Arking, A. (1991). The Radiative Effects of Clouds and their Impact on Climate. *Bulletin of the American Meteorological Society*, 72(6):795–814.

Atkinson, J. D., Murray, B. J., Woodhouse, M. T., Whale, T. F., Baustian, K. J., Carslaw, K. S., Dobbie, S., O'Sullivan, D., Malkin, T. L., O'Sullivan, D., and Malkin, T. L. (2013). The importance of feldspar for ice nucleation by mineral dust in mixed-phase clouds. *Nature*, 498(7454):355–358.

Baldo, C., Formenti, P., Nowak, S., Chevaillier, S., Cazaunau, M., Pangui, E., Di Biagio, C., Doussin, J.-F., Ignatyev, K., Dagsson-Waldhauserova, P., Arnalds, O., MacKenzie, A. R., and Shi, Z. (2020). Distinct chemical and mineralogical composition of Icelandic dust compared to northern African and Asian dust. *Atmospheric Chemistry and Physics*, 20(21):13521–13539.

Balmes, K. A., Fu, Q., and Thorsen, T. J. (2019). Differences in Ice Cloud Optical Depth From CALIPSO and Ground-Based Raman Lidar at the ARM SGP and TWP Sites. *Journal of Geophysical Research: Atmospheres*, 124(3):1755–1778.

Bamber, J. L., Westaway, R. M., Marzeion, B., and Wouters, B. (2018). The land ice contribution to sea level during the satellite era. *Environmental Research Letters*, 13(6):063008.

Baumgardner, D., Abel, S. J., Axisa, D., Cotton, R., Crosier, J., Field, P., Gurganus, C., Heymsfield, A., Korolev, A., Krämer, M., Lawson, P., McFarquhar, G., Ulanowski, Z., and Um, J. (2017a). Cloud Ice Properties: In Situ Measurement Challenges. *Meteorological Monographs*, 58(1):9.1–9.23.

Baumgardner, D., McFarquhar, G. M., and Heymsfield, A. J., editors (2017b). *Ice Formation and Evolution in Clouds and Precipitation*. Number Volume 58 in Meteorological Monographs. American Meteorological Society, Boston.

Bennartz, R., Shupe, M. D., Turner, D. D., Walden, V. P., Steffen, K., Cox, C. J., Kulie, M. S., Miller, N. B., and Pettersen, C. (2013). July 2012 Greenland melt extent enhanced by low-level liquid clouds. *Nature*, 496(7443):83–86.

Bi, K., McMeeking, G. R., Ding, D. P., Levin, E. J. T., DeMott, P. J., Zhao, D. L., Wang, F., Liu, Q., Tian, P., Ma, X. C., Chen, Y. B., Huang, M. Y., Zhang, H. L., Gordon, T. D., and Chen, P. (2019). Measurements of Ice Nucleating Particles in Beijing, China. *Journal of Geophysical Research: Atmospheres*, 124(14):8065–8075.

Boose, Y., Sierau, B., García, M. I., Rodríguez, S., Alastuey, A., Linke, C., Schnaiter, M., Kupiszewski, P., Kanji, Z. A., and Lohmann, U. (2016). Ice nucleating particles in the Saharan Air Layer. *Atmospheric Chemistry and Physics*, 16(14):9067–9087.

Boucher, O., Randall, D., Artaxo, P., Bretherton, C., Feingold, G., Forster, P., Kerminen, V.-M., Kondo, Y., Liao, H., Lohmann, U., Rasch, P., Satheesh, S. K., Sherwood, S., Stevens, B., and Zhang, X. Y. (2013). Clouds and Aerosols. In *Climate Change 2013: The Physical Science Basis. Contribution of Working Group I to the Fifth Assessment Report of the Intergovernmental Panel on Climate Change.* [Stocker, T.F., D. Qin, G.-K. Plattner, M. Tignor, S.K. Allen, J. Boschung, A. Nauels, Y. Xia, V. Bex and P.M. Midgley (eds.)]. Cambridge University Press, Cambridge, United Kingdom and New York, NY, USA.

Bozem, H., Hoor, P., Kunkel, D., Köllner, F., Schneider, J., Herber, A., Schulz, H., Leaitch, W. R., Aliabadi, A. A., Willis, M. D., Burkart, J., and Abbatt, J. P. D. (2019). Characterization of transport regimes and the polar dome during Arctic spring and summer using in situ aircraft measurements. *Atmospheric Chemistry and Physics*, 19(23):15049–15071.

Brabets, T. P. (1997). *Geomorphology of the Lower Copper River, Alaska*. Number 1581 in U.S. Geological Survey Professional Paper. U.S. G.P.O. ; For sale by U.S. Geological Survey, Information Services, Washington : Denver, CO.

Bradski, G. (2000). The OpenCV Library.

Brasseur, Z., Castarède, D., Thomson, E. S., Adams, M. P., Drossaart van Dusseldorp, S., Heikkilä, P., Korhonen, K., Lampilahti, J., Paramonov, M., Schneider, J., Vogel, F., Wu, Y., Abbatt, J. P. D., Atanasova, N. S., Bamford, D. H., Bertozzi, B., Boyer, M., Brus, D., Daily, M. I., Fösig, R., Gute, E., Harrison, A. D., Hietala, P., Höhler, K., Kanji, Z. A., Keskinen, J., Lacher, L., Lampimäki, M., Levula, J., Manninen, A., Nadolny, J., Peltola, M., Porter, G. C. E., Poutanen, P., Proske, U., Schorr, T., Silas Umo, N., Stenszky, J., Virtanen, A., Moisseev, D., Kulmala, M., Murray, B. J., Petäjä, T., Möhler, O., and Duplissy, J. (2022). Measurement report: Introduction to the HyICE-2018 campaign for measurements of ice-nucleating particles and instrument inter-comparison in the Hyytiälä boreal forest. *Atmospheric Chemistry and Physics*, 22(8):5117–5145.

Brockmann, J. E. (2011). Aerosol Transport in Sampling Lines and Inlets. In Kulkarni, P., Baron, P. A., and Willeke, K., editors, *Aerosol Measurement*, pages 68–105, Hoboken, NJ, USA. John Wiley & Sons, Inc.

Browse, J., Carslaw, K. S., Arnold, S. R., Pringle, K., and Boucher, O. (2012). The scavenging processes controlling the seasonal cycle in Arctic sulphate and black carbon aerosol. *Atmospheric Chemistry and Physics*, 12(15):6775–6798.

Bühl, J., Alexander, S., Crewell, S., Heymsfield, A., Kalesse, H., Khain, A., Maahn, M., Tricht, K. V., and Wendisch, M. (2017). Remote Sensing. *Meteorological Monographs*, 58(1):10.1–10.21.

Bühl, J., Seifert, P., Radenz, M., Baars, H., and Ansmann, A. (2019). Ice crystal number concentration from lidar, cloud radar and radar wind profiler measurements. *Atmospheric Measurement Techniques*, 12(12):6601–6617.

Bullard, J. E., Matthew, B., Tom, B., John, C., Eleanor, D., Diego, G., Santiago, G., Gudrun, G., Richard, H., Robert, M., Cheryl, M.-N., Tom, M., Helena, S., and Thorsteinsson, T. (2016). High latitude dust in the Earth system. *Reviews of Geophysics*, 54:447–485.

Burrows, S. M., McCluskey, C. S., Cornwell, G., Steinke, I., Zhang, K., Zhao, B., Zawadowicz, M., Raman, A., Kulkarni, G., China, S., Zelenyuk, A., and DeMott, P. J. (2022). Ice-Nucleating Particles That Impact Clouds and Climate: Observational and Modeling Research Needs. *Reviews of Geophysics*, 60(2):e2021RG000745.

Campbell, J. R., Hlavka, D. L., Welton, E. J., Flynn, C. J., Turner, D. D., Spinhirne, J. D., Scott, V. S., and Hwang, I. H. (2002). Full-Time, Eye-Safe Cloud and Aerosol Lidar Observation at Atmospheric Radiation Measurement Program Sites: Instruments and Data Processing. *Journal of Atmospheric and Oceanic Technology*, 19(4):431–442.

Cantrell, W. and Heymsfield, A. (2005). Production of Ice in Tropospheric Clouds: A Review. *Bulletin of the American Meteorological Society*, 86(6):795–808.

Cazenave, Q., Ceccaldi, M., Delanoë, J., Pelon, J., Groß, S., and Heymsfield, A. (2019). Evolution of DARDAR-CLOUD ice cloud retrievals: New parameters and impacts on the retrieved microphysical properties. *Atmospheric Measurement Techniques*, 12(5):2819–2835.

Ceppi, P., Brient, F., Zelinka, M. D., and Hartmann, D. L. (2017). Cloud feedback mechanisms and their representation in global climate models. *WIREs Climate Change*, 8(4):e465.

Ceppi, P. and Nowack, P. (2021). Observational evidence that cloud feedback amplifies global warming. *Proceedings of the National Academy of Sciences*, 118(30):e2026290118.

Chatziparaschos, M., Daskalakis, N., Myriokefalitakis, S., Kalivitis, N., Nenes, A., Gonçalves Ageitos, M., Costa-Surós, M., Pérez García-Pando, C., Zanoli, M., Vrekoussis, M., and Kanakidou, M. (2023). Role of K-feldspar and quartz in global ice nucleation by mineral dust in mixed-phase clouds. *Atmospheric Chemistry and Physics*, 23(3):1785–1801.

Chen, T., Rossow, W., and Zhang, Y. (2000). Radiative Effects of Cloud-Type Variations. *Journal of Climate - J CLIMATE*, 13:264–286.

Cheng, C.-T., Wang, W.-C., and Chen, J.-P. (2010). Simulation of the effects of increasing cloud condensation nuclei on mixed-phase clouds and precipitation of a front system. *Atmospheric Research*, 96(2):461–476.

Chou, C., Formenti, P., Maille, M., Ausset, P., Helas, G., Harrison, M., and Osborne, S. (2008). Size distribution, shape, and composition of mineral dust aerosols collected during the African Monsoon Multidisciplinary Analysis Special Observation Period 0: Dust and Biomass-Burning Experiment field campaign in Niger, January 2006. *Journal of Geophysical Research: Atmospheres*, 113(D23).

Chou, C., Stetzer, O., Weingartner, E., Jurányi, Z., Kanji, Z. A., and Lohmann, U. (2011). Ice nuclei properties within a Saharan dust event at the Jungfraujoch in the Swiss Alps. *Atmospheric Chemistry and Physics*, 11(10):4725–4738.

Christner, B. C., Cai, R., Morris, C. E., McCarter, K. S., Foreman, C. M., Skidmore, M. L., Montross, S. N., and Sands, D. C. (2008). Geographic, seasonal, and precipitation chemistry influence on the abundance and activity of biological ice nucleators in rain and snow. *Proceedings of the National Academy of Sciences*, 105(48):18854–18859.

Clothiaux, E. E., Ackerman, T. P., Mace, G. G., Moran, K. P., Marchand, R. T., Miller, M. A., and Martner, B. E. (2000). Objective Determination of Cloud Heights and Radar Reflectivities Using a Combination of Active Remote Sensors at the ARM CART Sites. *Journal of Applied Meteorology and Climatology*, 39(5):645–665.

Clothiaux, E. E., Moran, K. P., Martner, B. E., Ackerman, T. P., Mace, G. G., Uttal, T., Mather, J. H., Widener, K. B., Miller, M. A., and Rodriguez, D. J. (1999). The Atmospheric Radiation Measurement Program Cloud Radars: Operational Modes. *Journal of Atmospheric and Oceanic Technology*, 16(7):819–827.

Conen, F., Eckhardt, S., Gundersen, H., Stohl, A., and Yttri, K. E. (2017). Rainfall drives atmospheric ice-nucleating particles in the coastal climate of southern Norway. *Atmospheric Chemistry and Physics*, 17:11065–11073.

Conen, F., Stopelli, E., and Zimmermann, L. (2016). Clues that decaying leaves enrich Arctic air with ice nucleating particles. *Atmospheric Environment*, 129:91–94.

Cooper, W. A. (1986). *Ice Initiation in Natural Clouds*, pages 29–32. American Meteorological Society, Boston, MA.

Cossich, W., Maestri, T., Magurno, D., Martinazzo, M., Di Natale, G., Palchetti, L., Bianchini, G., and Del Guasta, M. (2021). Ice and mixed-phase cloud statistics on the Antarctic Plateau. *Atmospheric Chemistry and Physics*, 21(18):13811–13833.

Crawford, I., Bower, K. N., Choularton, T. W., Dearden, C., Crosier, J., Westbrook, C., Capes, G., Coe, H., Connolly, P. J., Dorsey, J. R., Gallagher, M. W., Williams, P., Trembath, J., Cui, Z., and Blyth, A. (2012). Ice formation and development in aged, wintertime cumulus over the UK: Observations and modelling. *Atmospheric Chemistry and Physics*, 12(11):4963–4985.

Creamean, J. M., Barry, K., Hill, T. C. J., Hume, C., DeMott, P. J., Shupe, M. D., Dahlke, S., Willmes, S., Schmale, J., Beck, I., Hoppe, C. J. M., Fong, A., Chamberlain, E., Bowman, J., Scharien, R., and Persson, O. (2022). Annual cycle observations of aerosols capable of ice formation in central Arctic clouds. *Nature Communications*, 13(1):3537.

Creamean, J. M., Cross, J. N., Pickart, R., McRaven, L., Lin, P., Pacini, A., Hanlon, R., Schmale, D. G., Ceniceros, J., Aydell, T., Colombi, N., Bolger, E., and DeMott, P. J. (2019). Ice Nucleating Particles Carried From Below a Phytoplankton Bloom to the Arctic Atmosphere. *Geophysical Research Letters*, 46(14):8572–8581.

Creamean, J. M., Kirpes, R. M., Pratt, K. A., Spada, N. J., Maahn, M., De Boer, G., Schnell, R. C., and China, S. (2018). Marine and terrestrial influences on ice nucleating particles during continuous springtime measurements in an Arctic oilfield location. *Atmospheric Chemistry and Physics*, 18(24):18023–18042.

Crusius, J. (2021). Dissolved Fe Supply to the Central Gulf of Alaska Is Inferred to Be Derived From Alaskan Glacial Dust That Is Not Resolved by Dust Transport Models. *Journal of Geophysical Research: Biogeosciences*, 126(6):e2021JG006323.

Crusius, J., Schroth, A. W., Gassó, S., Moy, C. M., Levy, R. C., and Gatica, M. (2011). Glacial flour dust storms in the Gulf of Alaska: Hydrologic and meteorological controls and their importance as a source of bioavailable iron. *Geophysical Research Letters*, 38(6):1–5.

Crusius, J., Schroth, A. W., Resing, J. A., Cullen, J., and Campbell, R. W. (2017). Seasonal and spatial variabilities in northern Gulf of Alaska surface water iron concentrations driven by shelf sediment resuspension, glacial meltwater, a Yakutat eddy, and dust. *Global Biogeochemical Cycles*, 31(6):942–960.

Curry, J. A., Schramm, J. L., Rossow, W. B., and Randall, D. (1996). Overview of Arctic Cloud and Radiation Characteristics. *Journal of Climate*, 9(8):1731–1764.

Daily, M. I., Tarn, M. D., Whale, T. F., and Murray, B. J. (2022). An evaluation of the heat test for the ice-nucleating ability of minerals and biological material. *Atmospheric Measurement Techniques*, 15(8):2635–2665.

Dall'osto, M., Ceburnis, D., Martucci, G., Bialek, J., Dupuy, R., Jennings, S. G., Berresheim, H., Wenger, J., Healy, R., Facchini, M. C., Rinaldi, M., Giulianelli, L., Finessi, E., Worsnop, D., Ehn, M., Mikkilä, J., Kulmala, M., and O'dowd, C. D. (2010). Aerosol properties associated with air masses arriving into the North East Atlantic during the 2008 Mace Head EUCAARI intensive observing period: An overview. *Atmospheric Chemistry and Physics*, 10:8413–8435.

David, R. O., Marcolli, C., Fahrni, J., Qiu, Y., Perez Sirkin, Y. A., Molinero, V., Mahrt, F., Brühwiler, D., Lohmann, U., and Kanji, Z. A. (2019). Pore condensation and freezing is responsible for ice formation below water saturation for porous particles. *Proceedings of the National Academy of Sciences*, 116(17):8184–8189.

De Boer, G., Morrison, H., Shupe, M. D., and Hildner, R. (2011). Evidence of liquid dependent ice nucleation in high-latitude stratiform clouds from surface remote sensors. *Geophysical Research Letters*, 38(1):1–5.

Delanoë, J. and Hogan, R. J. (2010). Combined CloudSat-CALIPSO-MODIS retrievals of the properties of ice clouds. *Journal of Geophysical Research: Atmospheres*, 115(D4).

Delanoë, J., Protat, A., Bouniol, D., Heymsfield, A., Bansemer, A., and Brown, P. (2007). The Characterization of Ice Cloud Properties from Doppler Radar Measurements. *Journal of Applied Meteorology and Climatology*, 46(10):1682–1698.

Delanoë, J., Protat, A., Testud, J., Bouniol, D., Heymsfield, A. J., Bansemer, A., Brown, P. R. A., and Forbes, R. M. (2005). Statistical properties of the normalized ice particle size distribution. *Journal of Geophysical Research: Atmospheres*, 110(D10).

DeMott, P. J., Hill, T. C. J., McCluskey, C. S., Prather, K. A., Collins, D. B., Sullivan, R. C., Ruppel, M. J., Mason, R. H., Irish, V. E., Lee, T., Hwang, C. Y., Rhee, T. S., Snider, J. R., McMeeking, G. R., Dhaniyala, S., Lewis, E. R., Wentzell, J. J. B., Abbatt, J., Lee, C., Sultana, C. M., Ault, A. P., Axson, J. L., Diaz Martinez, M., Venero, I., Santos-Figueroa, G., Stokes, M. D., Deane, G. B., Mayol-Bracero, O. L., Grassian, V. H., Bertram, T. H., Bertram, A. K., Moffett, B. F., and Franc, G. D. (2016). Sea spray aerosol as a unique source of ice nucleating particles. *Proceedings of the National Academy of Sciences*, 113(21):5797–5803.

DeMott, P. J., Möhler, O., Cziczo, D. J., Hiranuma, N., Petters, M. D., Petters, S. S., Belosi, F., Bingemer, H. G., Brooks, S. D., Budke, C., Burkert-Kohn, M., Collier, K. N., Danielczok, A., Eppers, O., Felgitsch, L., Garimella, S., Grothe, H., Herenz, P., Hill, T. C. J., Höhler, K., Kanji, Z. A., Kiselev, A., Koop, T., Kristensen, T. B., Krüger, K., Kulkarni, G., Levin, E. J. T., Murray, B. J., Nicosia, A., O'Sullivan, D., Peckhaus, A., Polen, M. J., Price, H. C., Reicher, N., Rothenberg, D. A., Rudich, Y., Santachiara, G., Schiebel, T., Schrod, J., Seifried, T. M., Stratmann, F., Sullivan, R. C., Suski, K. J., Szakáll, M., Taylor, H. P., Ullrich, R., Vergara-Temprado, J., Wagner, R., Whale, T. F., Weber, D., Welti, A., Wilson, T. W., Wolf, M. J., and Zenker, J. (2018). The Fifth International Workshop on Ice Nucleation phase 2 (FIN-02): Laboratory intercomparison of ice nucleation measurements. *Atmospheric Measurement Techniques*, 11(11):6231–6257.

DeMott, P. J., Sassen, K., Poellot, M. R., Baumgardner, D., Rogers, D. C., Brooks, S. D., Prenni, A. J., and Kreidenweis, S. M. (2003). African dust aerosols as atmospheric ice nuclei. *Geophysical Research Letters*, 30(14).

Després, V. R., Alex Huffman, J., Burrows, S. M., Hoose, C., Safatov, A. S., Buryak, G., Fröhlich-Nowoisky, J., Elbert, W., Andreae, M. O., Pöschl, U., and Jaenicke, R. (2012). Primary biological aerosol particles in the atmosphere: A review. *Tellus, Series B: Chemical and Physical Meteorology*, 64(1).

Diaz, M. A., Welch, S. A., Sheets, J. M., Welch, K. A., Khan, A. L., Adams, B. J., McKnight, D. M., Cary, S. C., and Lyons, W. B. (2020). Geochemistry of aeolian material from the McMurdo Dry Valleys, Antarctica: Insights into Southern Hemisphere dust sources. *Earth and Planetary Science Letters*, 547:116460.

Doviak, R. J. and Zrnić, D. S. (2006). *Doppler Radar and Weather Observations*. Dover Publications, Mineola, N.Y, 2nd ed., dover ed edition.

Durant, A. J. and Shaw, R. A. (2005). Evaporation freezing by contact nucleation inside-out. *Geophysical Research Letters*, 32(20).

Durant, A. J., Shaw, R. A., Rose, W. I., Mi, Y., and Ernst, G. G. J. (2008). Ice nucleation and overseeding of ice in volcanic clouds. *Journal of Geophysical Research: Atmospheres*, 113(D9).

Ewald, F., Groß, S., Wirth, M., Delanoë, J., Fox, S., and Mayer, B. (2021). Why we need radar, lidar, and solar radiance observations toconstrain ice cloud microphysics.

Field, P. R., Heymsfield, A. J., Shipway, B. J., DeMott, P. J., Pratt, K. A., Rogers, D. C., Stith, J., and Prather, K. A. (2012). Ice in Clouds Experiment–Layer Clouds. Part II: Testing Characteristics of Heterogeneous Ice Formation in Lee Wave Clouds. *Journal of the Atmospheric Sciences*, 69(3):1066–1079.

Field, P. R., Lawson, R. P., Brown, P. R. A., Lloyd, G., Westbrook, C., Moisseev, D., Miltenberger, A., Nenes, A., Blyth, A., Choularton, T., Connolly, P., Buehl, J., Crosier, J., Cui, Z., Dearden, C., DeMott, P., Flossmann, A., Heymsfield, A., Huang, Y., Kalesse, H., Kanji, Z. A., Korolev, A., Kirchgaessner, A., Lasher-Trapp, S., Leisner, T., McFarquhar, G., Phillips, V., Stith, J., and Sullivan, S. (2017). Secondary Ice Production: Current State of the Science and Recommendations for the Future. *Meteorological Monographs*, 58(1):7.1–7.20.

Flynn, C. J., Mendoza, A., Zheng, Y., and Mathur, S. (2007). Novel polarization-sensitive micropulse lidar measurement technique. *Optics Express*, 15(6):2785–2790.

Forster, P., Storelvmo, T., Armour, K., Collins, W., Dufresne, J.-L., Frame, D., Lunt, D. J., Mauritsen, T., Palmer, M. D., Watanabe, M., Wild, M., and Zhang, H. (2021). The Earth's Energy Budget, Climate Feedbacks, and Climate Sensitivity. In *Climate Change 2021 – The Physical Science Basis: Working Group I Contribution to the Sixth Assessment Report of the Intergovernmental Panel on Climate Change*. [Masson-Delmotte, V., P. Zhai, A. Pirani, S.L. Connors, C. Péan, S. Berger, N. Caud, Y. Chen, L. Goldfarb, M.I. Gomis, M. Huang, K. Leitzell, E. Lonnoy, J.B.R. Matthews, T.K. Maycock, T. Waterfield, O. Yelekçi, R. Yu, and B. Zhou (eds.)]. Cambridge University Press, 1 edition.

Gallagher, M. R., Chepfer, H., Shupe, M. D., and Guzman, R. (2020). Warm Temperature Extremes Across Greenland Connected to Clouds. *Geophysical Research Letters*, 47(9):e2019GL086059.

Garimella, S., Kristensen, T. B., Ignatius, K., Welti, A., Voigtländer, J., Kulkarni, G. R., Sagan, F., Kok, G. L., Dorsey, J., Nichman, L., Rothenberg, D. A., Rösch, M., Kirchgäßner, A. C. R., Ladkin, R., Wex, H., Wilson, T. W., Ladino, L. A., Abbatt, J. P. D., Stetzer, O., Lohmann, U., Stratmann, F., and Cziczo, D. J. (2016). The SPectrometer for Ice Nuclei (SPIN): An instrument to investigate ice nucleation. *Atmospheric Measurement Techniques*, 9(7):2781–2795.

Gettelman, A., Hannay, C., Bacmeister, J. T., Neale, R. B., Pendergrass, A. G., Danabasoglu, G., Lamarque, J.-F., Fasullo, J. T., Bailey, D. A., Lawrence, D. M., and Mills, M. J. (2019). High Climate Sensitivity in the Community Earth System Model Version 2 (CESM2). *Geophysical Research Letters*, 46(14):8329–8337.

Gettelman, A. and Sherwood, S. C. (2016). Processes Responsible for Cloud Feedback. *Current Climate Change Reports*, 2(4):179–189.

Glaccum, R. A. and Prospero, J. M. (1980). Saharan aerosols over the tropical North Atlantic — Mineralogy. *Marine Geology*, 37(3-4):295.

Gliß, J., Mortier, A., Schulz, M., Andrews, E., Balkanski, Y., Bauer, S. E., Benedictow, A. M. K., Bian, H., Checa-Garcia, R., Chin, M., Ginoux, P., Griesfeller, J. J., Heckel, A., Kipling, Z., Kirkevåg, A., Kokkola, H., Laj, P., Le Sager, P., Lund, M. T., Lund Myhre, C., Matsui, H., Myhre, G., Neubauer, D., van Noije, T., North, P., Olivié, D. J. L., Rémy, S., Sogacheva, L., Takemura, T., Tsigaridis, K., and Tsyro, S. G. (2021). AeroCom phase III multi-model evaluation of the aerosol life cycle and optical properties using ground- and space-based remote sensing as well as surface in situ observations. *Atmospheric Chemistry and Physics*, 21(1):87–128.

Gong, X., Radenz, M., Wex, H., Seifert, P., Ataei, F., Henning, S., Baars, H., Barja, B., Ansmann, A., and Stratmann, F. (2022). Significant continental source of ice-nucleating particles at the tip of Chile's southernmost Patagonia region. *Atmospheric Chemistry and Physics*, 22(16):10505–10525.

Groot Zwaaftink, C. D., Arnalds, Ó., Dagsson-Waldhauserova, P., Eckhardt, S., Prospero, J. M., Stohl, A., and Zwaaftink, C. G. (2017). Temporal and spatial variability of Icelandic dust emissions and atmospheric transport. *Atmospheric Chemistry and Physics*, 17:10865–10878.

Groot Zwaaftink, C. D., Grythe, H., Skov, H., and Stohl, A. (2016). Substantial contribution of northern high-latitude sources to mineral dust in the Arctic. *Journal of Geophysical Research*, 121(22):13,678–13,697.

Gryspeerdt, E., Goren, T., Sourdeval, O., Quaas, J., Mülmenstädt, J., Dipu, S., Unglaub, C., Gettelman, A., and Christensen, M. (2019). Constraining the aerosol influence on cloud liquid water path. *Atmospheric Chemistry and Physics*, 19(8):5331–5347.

Gryspeerdt, E., Sourdeval, O., Quaas, J., Delanoë, J., Krämer, M., and Kühne, P. (2018). Ice crystal number concentration estimates from lidar–radar satellite remote sensing – Part 2: Controls on the ice crystal number concentration. *Atmospheric Chemistry and Physics*, 18(19):14351–14370.

Guy, H., Brooks, I. M., Carslaw, K. S., Murray, B. J., Walden, V. P., Shupe, M. D., Pettersen, C., Turner, D. D., Cox, C. J., Neff, W. D., Bennartz, R., and Iii, R. R. N. (2021). Controls on surface aerosol particle number concentrations and aerosol-limited cloud regimes over the central Greenland Ice Sheet. *Atmospheric Chemistry and Physics*, 21:15351–15374.

Guy, H., Turner, D. D., Walden, V. P., Brooks, I. M., and Neely, R. R. (2022). Passive ground-based remote sensing of radiation fog. *Atmospheric Measurement Techniques*, 15(17):5095–5115.

Hallett, J. and Mossop, S. C. (1974). Production of secondary ice particles during the riming process. *Nature*, 249(5452):26–28.

Hande, L. B., Engler, C., Hoose, C., and Tegen, I. (2015). Seasonal variability of Saharan desert dust and ice nucleating particles over Europe. *Atmospheric Chemistry and Physics*, 15:4389–4397.

Hanna, E., Cappelen, J., Fettweis, X., Mernild, S. H., Mote, T. L., Mottram, R., Steffen, K., Ballinger, T. J., and Hall, R. J. (2021). Greenland surface air temperature changes from 1981 to 2019 and implications for ice-sheet melt and mass-balance change. *International Journal of Climatology*, 41(S1):E1336–E1352.

Hanna, E., Navarro, F. J., Pattyn, F., Domingues, C. M., Fettweis, X., Ivins, E. R., Nicholls, R. J., Ritz, C., Smith, B., Tulaczyk, S., Whitehouse, P. L., and Zwally, H. J. (2013). Ice-sheet mass balance and climate change. *Nature*, 498(7452):51–59.

Harrison, A. D., Lever, K., Sanchez-Marroquin, A., Holden, M. A., Whale, T. F., Tarn, M. D., McQuaid, J. B., and Murray, B. J. (2019). The ice-nucleating ability of quartz immersed in water and its atmospheric importance compared to K-feldspar. *Atmospheric Chemistry and Physics*, 19(17):11343–11361.

Harrison, A. D., O'Sullivan, D., Adams, M. P., Porter, G. C. E., Blades, E., Brathwaite, C., Chewitt-Lucas, R., Gaston, C., Hawker, R., Krüger, O. O., Neve, L., Pöhlker, M. L., Pöhlker, C., Pöschl, U., Sanchez-Marroquin, A., Sealy, A., Sealy, P., Tarn, M. D., Whitehall, S., McQuaid, J. B., Carslaw, K. S., Prospero, J. M., and Murray, B. J. (2022a). The ice-nucleating activity of African mineral dust in the Caribbean boundary layer. *Atmospheric Chemistry and Physics*, 22(14):9663–9680.

Harrison, A. D., O'Sullivan, D., Adams, M. P., Porter, G. C. E., Blades, E., Brathwaite, C., Chewitt-Lucas, R., Gaston, C., Hawker, R., Krüger, O. O., Neve, L., Pöhlker, M. L., Pöhlker, C., Pöschl, U., Sanchez-Marroquin, A., Sealy, A., Sealy, P., Tarn, M. D., Whitehall, S., McQuaid, J. B., Carslaw, K. S., Prospero, J. M., and Murray, B. J. (2022b). The ice-nucleating activity of African mineral dust in the Caribbean boundary layer. *Atmospheric Chemistry and Physics*, 22(14):9663–9680.

Hartmann, D. L. (1993). Chapter 6 Radiative Effects of Clouds on Earth's Climate. In Hobbs, P. V., editor, *International Geophysics*, volume 54 of *Aerosol–Cloud–Climate Interactions*, pages 151–173. Academic Press.

Herbert, R. J., Murray, B. J., Dobbie, S. J., and Koop, T. (2015). Sensitivity of liquid clouds to homogenous freezing parameterizations. *Geophysical Research Letters*, 42(5):1599–1605.

Hersbach, H., Bell, B., Berrisford, P., Hirahara, S., Horányi, A., Muñoz-Sabater, J., Nicolas, J., Peubey, C., Radu, R., Schepers, D., Simmons, A., Soci, C., Abdalla, S., Abellan, X., Balsamo, G., Bechtold, P., Biavati, G., Bidlot, J., Bonavita, M., Chiara, G., Dahlgren, P., Dee, D., Diamantakis, M., Dragani, R., Flemming, J., Forbes, R., Fuentes, M., Geer, A., Haimberger, L., Healy, S., Hogan, R. J., Hólm, E., Janisková, M., Keeley, S., Laloyaux, P., Lopez, P., Lupu, C., Radnoti, G., Rosnay, P., Rozum, I., Vamborg, F., Villaume, S., and Thépaut, J.-N. (2020). ERA5 hourly data on pressure levels from 1959 to present. 10.24381/cds.bd0915c6.

Heymsfield, A. J. and Westbrook, C. D. (2010). Advances in the estimation of ice particle fall speeds using laboratory and field measurements. *Journal of the Atmospheric Sciences*, 67(8):2469–2482.

Hill, T. C., Demott, P. J., Tobo, Y., Fröhlich-Nowoisky, J., Moffett, B. F., Franc, G. D., and Kreidenweis, S. M. (2016). Sources of organic ice nucleating particles in soils. *Atmospheric Chemistry and Physics*, 16(11):7195–7211.

Hobbs, P. V. (1969). Ice Multiplication in Clouds. *Journal of the Atmospheric Sciences*, 26(2):315–318.

Hobbs, P. V. and Rangno, A. L. (1985). Ice Particle Concentrations in Clouds. *Journal of the Atmospheric Sciences*, 42(23):2523–2549.

Hofer, S., Lang, C., Amory, C., Kittel, C., Delhasse, A., Tedstone, A., and Fettweis, X. (2020). Greater Greenland Ice Sheet contribution to global sea level rise in CMIP6. *Nature Communications*, 11(1):6289.

Hoffmann, N., Duft, D., Kiselev, A., and Leisner, T. (2013). Contact freezing efficiency of mineral dust aerosols studied in an electrodynamic balance: Quantitative size and temperature dependence for illite particles. *Faraday Discussions*, 165(0):383–390.

Hogan, R. J., Mittermaier, M. P., and Illingworth, A. J. (2006). The Retrieval of Ice Water Content from Radar Reflectivity Factor and Temperature and Its Use in Evaluating a Mesoscale Model. *Journal of Applied Meteorology and Climatology*, 45(2):301–317.

Holden, M. A., Whale, T. F., Tarn, M. D., O'Sullivan, D., Walshaw, R. D., Murray, B. J., Meldrum, F. C., and Christenson, H. K. (2019). High-speed imaging of ice nucleation in water proves the existence of active sites. *Science Advances*, 5(2):eaav4316.

Hoose, C., Kristjánsson, J. E., and Burrows, S. M. (2010). How important is biological ice nucleation in clouds on a global scale? *Environmental Research Letters*, 5(2).

Huang, Y., Blyth, A. M., Brown, P. R. A., Choularton, T. W., and Cui, Z. (2017). Factors controlling secondary ice production in cumulus clouds. *Quarterly Journal of the Royal Meteorological Society*, 143(703):1021–1031.

Igel, A. L., Ekman, A. M. L., Leck, C., Tjernström, M., Savre, J., and Sedlar, J. (2017). The free troposphere as a potential source of arctic boundary layer aerosol particles. *Geophysical Research Letters*, 44(13):7053–7060.

Illingworth, A. J., Hogan, R. J., O'Connor, E., Bouniol, D., Brooks, M. E., Delanoé, J., Donovan, D. P., Eastment, J. D., Gaussiat, N., Goddard, J. W. F., Haeffelin, M., Baltink, H. K., Krasnov, O. A., Pelon, J., Piriou, J.-M., Protat, A., Russchenberg, H. W. J., Seifert, A., Tompkins, A. M., van Zadelhoff, G.-J., Vinit, F., Willén, U., Wilson, D. R., and Wrench, C. L. (2007). Cloudnet. *Bulletin of the American Meteorological Society*, 88(6):883–898.

Inoue, J., Liu, J., Pinto, J. O., and Curry, J. A. (2006). Intercomparison of Arctic Regional Climate Models: Modeling Clouds and Radiation for SHEBA in May 1998. *Journal of Climate*, 19(17):4167–4178.

Irish, V. E., Hanna, S. J., Willis, M. D., China, S., Thomas, J. L., Wentzell, J. J. B., Cirisan, A., Si, M., Leaitch, W. R., Murphy, J. G., Abbatt, J. P. D., Laskin, A., Girard, E., and Bertram, A. K. (2019). Ice nucleating particles in the marine boundary layer in the Canadian Arctic during summer 2014. *Atmospheric Chemistry and Physics*, 19:1027–1039.

Isono, K., Komabayasi, M., and Ono, A. (1959). Volcanoes as a Source of Atmospheric Ice Nuclei. *Nature*, 183(4657):317–318.

Izeboud, M., Lhermitte, S., Van Tricht, K., Lenaerts, J. T. M., Van Lipzig, N. P. M., and Wever, N. (2020). The Spatiotemporal Variability of Cloud Radiative Effects on the Greenland Ice Sheet Surface Mass Balance. *Geophysical Research Letters*, 47(12):e2020GL087315.

Jaeger, J. M., Nittrouer, C. A., Scott, N. D., and Milliman, J. D. (1998). Sediment accumulation along a glacially impacted mountainous coastline: North-east Gulf of Alaska. *Basin Research*, 10(1):155–173.

Järvinen, E., McCluskey, C. S., Waitz, F., Schnaiter, M., Bansemer, A., Bardeen, C. G., Gettelman, A., Heymsfield, A., Stith, J. L., Wu, W., D'Alessandro, J. J., McFarquhar, G. M., Diao, M., Finlon, J. A., Hill, T. C. J., Levin, E. J. T., Moore, K. A., and DeMott, P. J. (2022). Evidence for Secondary Ice Production in Southern Ocean Maritime Boundary Layer Clouds. *Journal of Geophysical Research: Atmospheres*, 127(16):e2021JD036411.

Jiang, H., Cotton, W. R., Pinto, J. O., Curry, J. A., and Weissbluth, M. J. (2000). Cloud Resolving Simulations of Mixed-Phase Arctic Stratus Observed during BASE: Sensitivity to Concentration of Ice Crystals and Large-Scale Heat and Moisture Advection. *Journal of the Atmospheric Sciences*, 57(13):2105–2117.

Jiang, H., Xue, H., Teller, A., Feingold, G., and Levin, Z. (2006). Aerosol effects on the lifetime of shallow cumulus. *Geophysical Research Letters*, 33(14).

Kalesse, H. and Kollias, P. (2013). Climatology of High Cloud Dynamics Using Profiling ARM Doppler Radar Observations. *Journal of Climate*, 26(17):6340–6359.

Kalogeras, P. and Battaglia, A. (2022). Improving Millimeter Radar Attenuation Corrections in High-Latitude Mixed-Phase Clouds via Radio Soundings and a Suite of Active and Passive Instruments. *IEEE Transactions on Geoscience and Remote Sensing*, 60:1–11.

Kanji, Z. A., Ladino, L. A., Wex, H., Boose, Y., Burkert-Kohn, M., Cziczo, D. J., and Krämer, M. (2017). Overview of Ice Nucleating Particles. *Meteorological Monographs*, 58:1.1–1.33.

Kanji, Z. A., Welti, A., Corbin, J. C., and Mensah, A. A. (2020). Black Carbon Particles Do Not Matter for Immersion Mode Ice Nucleation. *Geophysical Research Letters*, 47(11):e2019GL086764.

Kargel, J. S., Beedle, M. J., Bush, A. B., Carreño, F., Castellanos, E., Haritashya, U. K., Leonard, G. J., Lillo, J., Lopez, I., Pleasants, M., Pollock, E., and Wolfe, D. F. (2014). Multispectral image analysis of glaciers and glacier lakes in the Chugach Mountains, Alaska. In Kargel, J. S., Leonard, G. J., Bishop, M. P., Kääb, A., and Raup, B. H., editors, *Global Land Ice Measurements from Space*, Springer Praxis Books, pages 297–332. Springer, Berlin, Heidelberg.

Kawai, K., Matsui, H., and Tobo, Y. (2023). Dominant Role of Arctic Dust With High Ice Nucleating Ability in the Arctic Lower Troposphere. *Geophysical Research Letters*, 50(8):e2022GL102470.

Kay, J. E., L'Ecuyer, T., Pendergrass, A., Chepfer, H., Guzman, R., and Yettella, V. (2018). Scale-Aware and Definition-Aware Evaluation of Modeled Near-Surface Precipitation Frequency Using CloudSat Observations. *Journal of Geophysical Research: Atmospheres*, 123(8):4294–4309.

Khvorostyanov, V. I. and Curry, J. A. (2014). *Thermodynamics, Kinetics, and Microphysics of Clouds*. Cambridge University Press, 1 edition.

Klein, S. A. and Hartmann, D. L. (1993). The Seasonal Cycle of Low Stratiform Clouds. *Journal of Climate*, 6(8):1587–1606.

Klein, S. A., McCoy, R. B., Morrison, H., Ackerman, A. S., Avramov, A., de Boer, G., Chen, M., Cole, J. N. S., Del Genio, A. D., Falk, M., Foster, M. J., Fridlind, A., Golaz, J.-C., Hashino, T., Harrington, J. Y., Hoose, C., Khairoutdinov, M. F., Larson, V. E., Liu, X., Luo, Y., McFarquhar, G. M., Menon, S., Neggers, R. A. J., Park, S., Poellot, M. R., Schmidt, J. M., Sednev, I., Shipway, B. J., Shupe, M. D., Spangenberg, D. A., Sud, Y. C., Turner, D. D., Veron, D. E., von Salzen, K., Walker, G. K., Wang, Z., Wolf, A. B., Xie, S., Xu, K.-M., Yang, F., and Zhang, G. (2009). Intercomparison of model simulations of mixed-phase clouds observed during the ARM Mixed-Phase Arctic Cloud Experiment. I: Single-layer cloud. *Quarterly Journal of the Royal Meteorological Society*, 135(641):979–1002.

Kok, J. F., Adebiyi, A. A., Albani, S., Balkanski, Y., Checa-Garcia, R., Chin, M., Colarco, P. R., Hamilton, D. S., Huang, Y., Ito, A., Klose, M., Li, L., Mahowald, N. M., Miller, R. L., Obiso, V., Pérez García-Pando, C., Rocha-Lima, A., and Wan, J. S. (2021). Contribution of the world's main dust source regions to the global cycle of desert dust. *Atmospheric Chemistry and Physics*, 21(10):8169–8193.

Kollias, P., Albrecht, B. A., Clothiaux, E. E., Miller, M. A., Johnson, K. L., and Moran, K. P. (2005). The Atmospheric Radiation Measurement Program Cloud Profiling Radars: An Evaluation of Signal Processing and Sampling Strategies. *Journal of Atmospheric and Oceanic Technology*, 22(7):930–948.

Kollias, P., Clothiaux, E. E., Miller, M. A., Albrecht, B. A., Stephens, G. L., and Ackerman, T. P. (2007a). Millimeter-Wavelength Radars: New Frontier in Atmospheric Cloud and Precipitation Research. *Bulletin of the American Meteorological Society*, 88(10):1608–1624.

Kollias, P., Clothiaux, E. E., Miller, M. A., Albrecht, B. A., Stephens, G. L., and Ackerman, T. P. (2007b). Millimeter-Wavelength Radars: New Frontier in Atmospheric Cloud and Precipitation Research. *Bulletin of the American Meteorological Society*, 88(10):1608–1624.

Kollias, P., Miller, M. A., Luke, E. P., Johnson, K. L., Clothiaux, E. E., Moran, K. P., Widener, K. B., and Albrecht, B. A. (2007c). The Atmospheric Radiation Measurement Program Cloud Profiling Radars: Second-Generation Sampling Strategies, Processing, and Cloud Data Products. *Journal of Atmospheric and Oceanic Technology*, 24(7):1199–1214.

Komurcu, M., Storelvmo, T., Tan, I., Lohmann, U., Yun, Y., Penner, J. E., Wang, Y., Liu, X., and Takemura, T. (2014). Intercomparison of the cloud water phase among global climate models. *Journal of Geophysical Research: Atmospheres*, 119(6):3372–3400.

Korolev, A., DeMott, P. J., Heckman, I., Wolde, M., Williams, E., Smalley, D. J., and Donovan, M. F. (2022). Observation of secondary ice production in clouds at low temperatures. *Atmospheric Chemistry and Physics*, 22(19):13103–13113.

Korolev, A. and Field, P. R. (2015). Assessment of the performance of the inter-arrival time algorithm to identify ice shattering artifacts in cloud particle probe measurements. *Atmospheric Measurement Techniques*, 8(2):761–777.

Korolev, A. and Leisner, T. (2020). Review of experimental studies of secondary ice production. *Atmospheric Chemistry and Physics*, 20(20):11767–11797.

Korolev, A., McFarquhar, G., Field, P. R., Franklin, C., Lawson, P., Wang, Z., Williams, E., Abel, S. J., Axisa, D., Borrmann, S., Crosier, J., Fugal, J., Krämer, M., Lohmann, U., Schlenczek, O., Schnaiter, M., Wendisch, M., Korolev, A., McFarquhar, G., Field, P. R., Franklin, C., Lawson, P., Wang, Z., Williams, E., Abel, S. J., Axisa, D., Borrmann, S., Crosier, J., Fugal, J., Krämer, M., Lohmann, U., Schlenczek, O., Schnaiter, M., and Wendisch, M. (2017). Mixed-Phase Clouds: Progress and Challenges. *Meteorological Monographs*, 58:5.1–5.50.

Korolev, A. V., Emery, E. F., Strapp, J. W., Cober, S. G., Isaac, G. A., Wasey, M., and Marcotte, D. (2011). Small Ice Particles in Tropospheric Clouds: Fact or Artifact?: Airborne Icing Instrumentation Evaluation Experiment. *Bulletin of the American Meteorological Society*, 92(8):967–973.

Ladino, L. A., Korolev, A., Heckman, I., Wolde, M., Fridlind, A. M., and Ackerman, A. S. (2017). On the role of ice-nucleating aerosol in the formation of ice particles in tropical mesoscale convective systems. *Geophysical Research Letters*, 44(3):1574–1582.

Ladino Moreno, L. A., Stetzer, O., and Lohmann, U. (2013). Contact freezing: A review of experimental studies. *Atmospheric Chemistry and Physics*, 13(19):9745–9769.

Lance, S., Shupe, M. D., Feingold, G., Brock, C. A., Cozic, J., Holloway, J. S., Moore, R. H., Nenes, A., Schwarz, J. P., Spackman, J. R., Froyd, K. D., Murphy, D. M., Brioude, J., Cooper, O. R., Stohl, A., and Burkhart, J. F. (2011). Cloud condensation nuclei as a modulator of ice processes in Arctic mixed-phase clouds. *Atmospheric Chemistry and Physics*, 11(15):8003–8015.

Lau, K. M. and Wu, H. T. (2003). Warm rain processes over tropical oceans and climate implications. *Geophysical Research Letters*, 30(24).

Lawson, P., Gurganus, C., Woods, S., and Bruintjes, R. (2017). Aircraft Observations of Cumulus Microphysics Ranging from the Tropics to Midlatitudes: Implications for a “New” Secondary Ice Process. *Journal of the Atmospheric Sciences*, 74(9):2899–2920.

Lawson, R. P. and Gettelman, A. (2014). Impact of Antarctic mixed-phase clouds on climate. *Proceedings of the National Academy of Sciences*, 111(51):18156–18161.

Lenaerts, J. T. M., Camron, M. D., Wyburn-Powell, C. R., and Kay, J. E. (2020a). Present-day and future Greenland Ice Sheet precipitation frequency from CloudSat observations and the Community Earth System Model. *The Cryosphere*, 14(7):2253–2265.

Lenaerts, J. T. M., Gettelman, A., Van Tricht, K., van Kampenhout, L., and Miller, N. B. (2020b). Impact of Cloud Physics on the Greenland Ice Sheet Near-Surface Climate: A Study With the Community Atmosphere Model. *Journal of Geophysical Research: Atmospheres*, 125(7):e2019JD031470.

Lhermitte, R. (1990). Attenuation and Scattering of Millimeter Wavelength Radiation by Clouds and Precipitation. *Journal of Atmospheric and Oceanic Technology*, 7(3):464–479.

Libbrecht, K. G. (2008). Crystal Growth in the Presence of Surface Melting and Impurities: An Explanation of Snow Crystal Growth Morphologies.

Listowski, C., Delanoë, J., Kirchgaessner, A., Lachlan-Cope, T., and King, J. (2019). Antarctic clouds, supercooled liquid water and mixed phase, investigated with DARDAR: Geographical and seasonal variations. *Atmospheric Chemistry and Physics*, 19(10):6771–6808.

Lohmann, U. and Feichter, J. (2005). Global indirect aerosol effects: A review. *Atmospheric Chemistry and Physics*, 5:715–737.

Lohmann, U., Lüönd, F., and Mahrt, F. (2016). *An Introduction to Clouds: From the Microscale to Climate*. Cambridge University Press, 1 edition.

López, M. L., Borgnino, L., and Ávila, E. E. (2018). The role of natural mineral particles collected at one site in Patagonia as immersion freezing ice nuclei. *Atmospheric Research*, 204(January):94–101.

Mahrt, F., Marcolli, C., David, R. O., Grönquist, P., Barthazy Meier, E. J., Lohmann, U., and Kanji, Z. A. (2018). Ice nucleation abilities of soot particles determined with the Horizontal Ice Nucleation Chamber. *Atmospheric Chemistry and Physics*, 18(18):13363–13392.

Marcolli, C. (2014). Deposition nucleation viewed as homogeneous or immersion freezing in pores and cavities. *Atmospheric Chemistry and Physics*, 14(4):2071–2104.

Mason, R. H., Si, M., Li, J., Chou, C., Dickie, R., Toom-Sauntry, D., Pöhlker, C., Yakobi-Hancock, J. D., Ladino, L. A., Jones, K., Leaitch, W. R., Schiller, C. L., Abbatt, J. P. D., Huffman, J. A., and Bertram, A. K. (2015). Ice nucleating particles at a coastal marine boundary layer site: Correlations with aerosol type and meteorological conditions. *Atmospheric Chemistry and Physics*, 15(21):12547–12566.

Maters, E. C., Dingwell, D. B., Cimarelli, C., Müller, D., Whale, T. F., and Murray, B. J. (2019). The importance of crystalline phases in ice nucleation by volcanic ash. *Atmospheric Chemistry and Physics*, 19(8):5451–5465.

Matrosov, S. Y. and Heymsfield, A. J. (2000). Use of Doppler radar to assess ice cloud particle fall velocity-size relations for remote sensing and climate studies. *Journal of Geophysical Research: Atmospheres*, 105(D17):22427–22436.

McCluskey, C. S., DeMott, P. J., Prenni, A. J., Levin, E. J. T., McMeeking, G. R., Sullivan, A. P., Hill, T. C. J., Nakao, S., Carrico, C. M., and Kreidenweis, S. M. (2014). Characteristics of atmospheric ice nucleating particles associated with biomass burning in the US: Prescribed burns and wildfires. *Journal of Geophysical Research: Atmospheres*, 119(17):10458–10470.

McIlhattan, E. A., L'Ecuyer, T. S., and Miller, N. B. (2017). Observational Evidence Linking Arctic Supercooled Liquid Cloud Biases in CESM to Snowfall Processes. *Journal of Climate*, 30(12):4477–4495.

McIlhattan, E. A., Pettersen, C., Wood, N. B., and L'Ecuyer, T. S. (2020). Satellite observations of snowfall regimes over the Greenland Ice Sheet. *The Cryosphere*, 14(12):4379–4404.

Meinander, O., Dagsson-Waldhauserova, P., Amosov, P., Aseyeva, E., Atkins, C., Baklanov, A., Baldo, C., Barr, S. L., Barzycka, B., Benning, L. G., Cvetkovic, B., Enchilik, P., Frolov, D., Gassó, S., Kandler, K., Kasimov, N., Kavan, J., King, J., Koroleva, T., Krupskaya, V., Kulmala, M., Kusiak, M., Lappalainen, H. K., Laska, M., Lasne, J., Lewandowski, M., Luks, B., McQuaid, J. B., Moroni, B., Murray, B., Möhler, O., Nawrot, A., Nickovic, S., O'Neill, N. T., Pejanovic, G., Popovicheva, O., Ranjbar, K., Romanias, M., Samonova, O., Sanchez-Marroquin, A., Schepanski, K., Semenkov, I., Sharapova, A., Shevnina, E., Shi, Z., Sofiev, M., Thevenet, F., Thorsteinsson, T., Timofeev, M., Umo, N. S., Uppstu, A., Urupina, D., Varga, G., Werner, T., Arnalds, O., and Vukovic Vimic, A. (2022). Newly identified climatically and environmentally significant high-latitude dust sources. *Atmospheric Chemistry and Physics*, 22(17):11889–11930.

Miller, A. J., Brennan, K. P., Mignani, C., Wieder, J., David, R. O., and Borduas-Dedekind, N. (2021). Development of the drop Freezing Ice Nuclei Counter (FINC), intercomparison of droplet freezing techniques, and use of soluble lignin as an atmospheric ice nucleation standard. *Atmospheric Measurement Techniques*, 14(4):3131–3151.

Miller, N. B., Shupe, M. D., Cox, C. J., Noone, D., Persson, P. O. G., and Steffen, K. (2017). Surface energy budget responses to radiative forcing at Summit, Greenland. *The Cryosphere*, 11(1):497–516.

Miller, N. B., Shupe, M. D., Cox, C. J., Walden, V. P., Turner, D. D., and Steffen, K. (2015). Cloud Radiative Forcing at Summit, Greenland. *Journal of Climate*, 28(15):6267–6280.

Miller, N. B., Turner, D. D., Bennartz, R., Shupe, M. D., Kulie, M. S., Cadeddu, M. P., and Walden, V. P. (2013). Surface-based inversions above central Greenland. *Journal of Geophysical Research: Atmospheres*, 118(2):495–506.

Mitchell, D. L. (1996). Use of Mass- and Area-Dimensional Power Laws for Determining Precipitation Particle Terminal Velocities. *Journal of the Atmospheric Sciences*, 53(12):1710–1723.

Möhler, O., Adams, M., Lacher, L., Vogel, F., Nadolny, J., Ullrich, R., Boffo, C., Pfeuffer, T., Hobl, A., Weiß, M., Vepuri, H. S. K., Hiranuma, N., and Murray, B. J. (2021). The Portable Ice Nucleation Experiment (PINE): A new online instrument for laboratory studies and automated long-term field observations of ice-nucleating particles. *Atmospheric Measurement Techniques*, 14(2):1143–1166.

Moran, K., Pezoa, S., Fairall, C., Williams, C., Ayers, T., Brewer, A., de Szoeke, S. P., and Ghate, V. (2012). A Motion-Stabilized W-Band Radar for Shipboard Observations of Marine Boundary-Layer Clouds. *Boundary-Layer Meteorology*, 143(1):3–24.

Moran, K. P., Martner, B. E., Post, M. J., Kropfli, R. A., Welsh, D. C., and Widener, K. B. (1998). An Unattended Cloud-Profiling Radar for Use in Climate Research. *Bulletin of the American Meteorological Society*, 79(3):443–456.

Morrison, H., de Boer, G., Feingold, G., Harrington, J., Shupe, M. D., and Sulia, K. (2012). Resilience of persistent Arctic mixed-phase clouds. *Nature Geoscience*, 5(1):11–17.

Mossop, S. C. (1985). Secondary ice particle production during rime growth: The effect of drop size distribution and rimer velocity. *Quarterly Journal of the Royal Meteorological Society*, 111(470):1113–1124.

Murray, B. J., Broadley, S. L., Wilson, T. W., Atkinson, J. D., and Wills, R. H. (2011). Heterogeneous freezing of water droplets containing kaolinite particles. *Atmospheric Chemistry and Physics*, 11(9):4191–4207.

Murray, B. J., Carslaw, K. S., and Field, P. R. (2021). Opinion: Cloud-phase climate feedback and the importance of ice-nucleating particles. *Atmospheric Chemistry and Physics*, 21(2):665–679.

Murray, B. J., O'Sullivan, D., Atkinson, J. D., and Webb, M. E. (2012). Ice nucleation by particles immersed in supercooled cloud droplets. *Chemical Society Reviews*, 41(19):6519–6554.

Niedermeier, D., Shaw, R. A., Hartmann, S., Wex, H., Clauss, T., Voigtländer, J., and Stratmann, F. (2011). Heterogeneous ice nucleation: Exploring the transition from stochastic to singular freezing behavior. *Atmospheric Chemistry and Physics*, 11(16):8767–8775.

Niehaus, J., Bunker, K. W., China, S., Kostinski, A., Mazzoleni, C., and Cantrell, W. (2014). A Technique to Measure Ice Nuclei in the Contact Mode. *Journal of Atmospheric and Oceanic Technology*, 31(4):913–922.

Niwano, M., Hashimoto, A., and Aoki, T. (2019). Cloud-driven modulations of Greenland ice sheet surface melt. *Scientific Reports*, 9(1):10380.

NSIDC (2021). Rain at the summit of Greenland | Greenland/Antarctic Ice Sheet Today.

Orr, B. W. and Kropfli, R. A. (1999). A Method for Estimating Particle Fall Velocities from Vertically Pointing Doppler Radar. *Journal of Atmospheric and Oceanic Technology*, 16(1):29–37.

O'Sullivan, D., Adams, M. P., Tarn, M. D., Harrison, A. D., Vergara-Temprado, J., Porter, G. C. E., Holden, M. A., Sanchez-Marroquin, A., Carotenuto, F., Whale, T. F., McQuaid, J. B., Walshaw, R., Hedges, D. H. P., Burke, I. T., Cui, Z., and Murray, B. J. (2018). Contributions of biogenic material to the atmospheric ice-nucleating particle population in North Western Europe. *Scientific Reports*, 8(1):13821.

O'Sullivan, D., Murray, B. J., Malkin, T. L., Whale, T. F., Umo, N. S., Atkinson, J. D., Price, H. C., Baustian, K. J., Browse, J., and Webb, M. E. (2014). Ice nucleation by fertile soil dusts: Relative importance of mineral and biogenic components. *Atmospheric Chemistry and Physics*, 14:1853–1867.

O'Sullivan, D., Murray, B. J., Ross, J. F., Whale, T. F., Price, H. C., Atkinson, J. D., Umo, N. S., and Webb, M. E. (2015). The relevance of nanoscale biological fragments for ice nucleation in clouds. *Scientific Reports*, 5:1–7.

Paramonov, M., David, R. O., Kretzschmar, R., and Kanji, Z. A. (2018). A laboratory investigation of the ice nucleation efficiency of three types of mineral and soil dust. *Atmospheric Chemistry and Physics*, 18(22):16515–16536.

Pasquier, J. T., Henneberger, J., Ramelli, F., Lauber, A., David, R. O., Wieder, J., Carlsen, T., Gierens, R., Maturilli, M., and Lohmann, U. (2022). Conditions favorable for secondary ice production in Arctic mixed-phase clouds. *Atmospheric Chemistry and Physics*, 22(23):15579–15601.

Petters, M. D. and Wright, T. P. (2015). Revisiting ice nucleation from precipitation samples. *Geophysical Research Letters*, 42(20):8758–8766.

Pettersen, C., Bennartz, R., Merrelli, A. J., Shupe, M. D., Turner, D. D., and Walden, V. P. (2018). Precipitation regimes over central Greenland inferred from 5 years of ICECAPS observations. *Atmospheric Chemistry and Physics*, 18(7):4715–4735.

Phillips, V. T. J., Donner, L. J., and Garner, S. T. (2007). Nucleation Processes in Deep Convection Simulated by a Cloud-System-Resolving Model with Double-Moment Bulk Microphysics. *Journal of the Atmospheric Sciences*, 64(3):738–761.

Pinti, V., Marcolli, C., Zobrist, B., Hoyle, C. R., and Peter, T. (2012). Ice nucleation efficiency of clay minerals in the immersion mode. *Atmospheric Chemistry and Physics*, 12(13):5859–5878.

Pisso, I., Sollum, E., Grythe, H., Kristiansen, N. I., Cassiani, M., Eckhardt, S., Arnold, D., Morton, D., Thompson, R. L., Groot Zwaaftink, C. D., Evangeliou, N., Sodemann, H., Haimberger, L., Henne, S., Brunner, D., Burkhart, J. F., Fouilloux, A., Brioude, J., Philipp, A., Seibert, P., and Stohl, A. (2019). The Lagrangian particle dispersion model FLEXPART version 10.4. *Geosci. Model Dev*, 12:4955–4997.

Porter, G. C., Sikora, S. N., Adams, M. P., Proske, U., Harrison, A. D., Tarn, M. D., Brooks, I. M., and Murray, B. J. (2020). Resolving the size of ice-nucleating particles with a balloon deployable aerosol sampler: The SHARK. *Atmospheric Measurement Techniques*, 13(6):2905–2921.

Porter, G. C. E., Adams, M. P., Brooks, I. M., Ickes, L., Karlsson, L., Leck, C., Salter, M. E., Schmale, J., Siegel, K., Sikora, S. N. F., Tarn, M. D., Vüllers, J., Wernli, H., Zieger, P., Zinke, J., and Murray, B. J. (2022). Highly Active Ice-Nucleating Particles at the Summer North Pole. *Journal of Geophysical Research: Atmospheres*, 127(6):e2021JD036059.

Prenni, A. J., DeMott, P. J., Sullivan, A. P., Sullivan, R. C., Kreidenweis, S. M., and Rogers, D. C. (2012). Biomass burning as a potential source for atmospheric ice nuclei: Western wildfires and prescribed burns. *Geophysical Research Letters*, 39(11).

Price, H. C., Baustian, K. J., McQuaid, J. B., Blyth, A., Bower, K. N., Choularton, T., Cotton, R. J., Cui, Z., Field, P. R., Gallagher, M., Hawker, R., Merrington, A., Miltenberger, A., Neely, R. R., Parker, S. T., Rosenberg, P. D., Taylor, J. W., Trembath, J., Vergara-Temprado, J., Whale, T. F., Wilson, T. W., Young, G., and Murray, B. J. (2018). Atmospheric Ice-Nucleating Particles in the Dusty Tropical Atlantic. *Journal of Geophysical Research: Atmospheres*, 123(4):2175–2193.

Protat, A. and McRobert, I. (2020). Three-dimensional wind profiles using a stabilized shipborne cloud radar in wind profiler mode. *Atmospheric Measurement Techniques*, 13(7):3609–3620.

Protat, A. and Williams, C. R. (2011). The Accuracy of Radar Estimates of Ice Terminal Fall Speed from Vertically Pointing Doppler Radar Measurements. *Journal of Applied Meteorology and Climatology*, 50(10):2120–2138.

Pruppacher, H. and Klett, J. (2010). *Microphysics of Clouds and Precipitation*, volume 18. Springer Netherlands, Dordrecht.

Radenz, M., Bühl, J., Lehmann, V., Görsdorf, U., and Leinweber, R. (2018). Combining cloud radar and radar wind profiler for a value added estimate of vertical air motion and particle terminal velocity within clouds. *Atmospheric Measurement Techniques*, 11(10):5925–5940.

Radenz, M., Bühl, J., Seifert, P., Griesche, H., and Engelmann, R. (2019). peakTree: A framework for structure-preserving radar Doppler spectra analysis. *Atmospheric Measurement Techniques*, 12(9):4813–4828.

Ramelli, F., Henneberger, J., David, R. O., Bu¨hl, J., Radenz, M., Seifert, P., Wieder, J., Lauber, A., Pasquier, J. T., Engelmann, R., Mignani, C., Hervo, M., and Lohmann, U. (2021). Microphysical investigation of the seeder and feeder region of an Alpine mixed-phase cloud. *Atmospheric Chemistry and Physics*, 21(9):6681–6706.

Rangno, A. L. and Hobbs, P. V. (2001a). Ice particles in stratiform clouds in the Arctic and possible mechanisms for the production of high ice concentrations. *Journal of Geophysical Research: Atmospheres*, 106(D14):15065–15075.

Rangno, A. L. and Hobbs, P. V. (2001b). Ice particles in stratiform clouds in the Arctic and possible mechanisms for the production of high ice concentrations. *Journal of Geophysical Research: Atmospheres*, 106(D14):15065–15075.

Reicher, N., Segev, L., and Rudich, Y. (2018). The WeIzmann Supercooled Droplets Observation on a Microarray (WISDOM) and application for ambient dust. *Atmospheric Measurement Techniques*, 11(1):233–248.

Roesch, C., Roesch, M., Wolf, M. J., Zawadowicz, M. A., AlAloula, R., Awwad, Z., and Cziczo, D. J. (2021). CCN and INP activity of middle eastern soil dust. *Aeolian Research*, 52:100729.

Rogers, D. C. (1988). Development of a Continuous Flow Thermal Gradient Diffusion Chamber for Ice Nucleation Studies. *Atmospheric Research*, 22:149–181.

Rogers, D. C., Demott, P. J., Kreidenweis, S. M., and Chen, Y. (2001). A Continuous-Flow Diffusion Chamber for Airborne Measurements of Ice Nuclei. *Journal of Atmospheric and Oceanic Technology*.

Rose, T., Crewell, S., Löhnert, U., and Simmer, C. (2005). A network suitable microwave radiometer for operational monitoring of the cloudy atmosphere. *Atmospheric Research*, 75(3):183–200.

Rosenberg, P. D., Dean, A. R., Williams, P. I., Dorsey, J. R., Minikin, A., Pickering, M. A., and Petzold, A. (2012). Particle sizing calibration with refractive index correction for light scattering optical particle counters and impacts upon PCASP and CDP data collected during the Fennec campaign. *Atmospheric Measurement Techniques*, 5(5):1147–1163.

Ryder, C. L., Marenco, F., Brooke, J. K., Estelles, V., Cotton, R., Formenti, P., McQuaid, J. B., Price, H. C., Liu, D., Ausset, P., Rosenberg, P. D., Taylor, J. W., Choularton, T., Bower, K., Coe, H., Gallagher, M., Crosier, J., Lloyd, G., Highwood, E. J., and Murray, B. J. (2018). Coarse-mode mineral dust size distributions, composition and optical properties from AER-D aircraft measurements over the tropical eastern Atlantic. *Atmospheric Chemistry and Physics*, 18(23):17225–17257.

Sanchez-Marroquin, A., Arnalds, O., Baustian-Dorsi, K. J., Browse, J., Dagsson-Waldhauserova, P., Harrison, A. D., Maters, E. C., Pringle, K. J., Vergara-Temprado, J., Burke, I. T., McQuaid, J. B., Carslaw, K. S., and Murray, B. J. (2020). Iceland is an episodic source of atmospheric ice-nucleating particles relevant for mixed-phase clouds. *Science Advances*, 6(26):eaba8137.

Sanchez-Marroquin, A., Hedges, D. H. P., Hiscock, M., Parker, S. T., Rosenberg, P. D., Trembath, J., Walshaw, R., Burke, I. T., McQuaid, J. B., and Murray, B. J. (2019). Characterisation of the filter inlet system on the FAAM BAe-146 research aircraft and its use for size-resolved aerosol composition measurements. *Atmospheric Measurement Techniques*, 12(11):5741–5763.

Sanchez-Marroquin, A., West, J. S., Burke, I. T., McQuaid, J. B., and Murray, B. J. (2021). Mineral and biological ice-nucleating particles above the South East of the British Isles. *Environmental Science*, 1(4):176–191.

Sassen, K. (2005). Polarization in Lidar. In Weitkamp, C., editor, *Lidar*, volume 102, pages 19–42. Springer-Verlag, New York.

Sassen, K., DeMott, P. J., Prospero, J. M., and Poellot, M. R. (2003). Saharan dust storms and indirect aerosol effects on clouds: CRYSTAL-FACE results. *Geophysical Research Letters*, 30(12).

Schnell, R. (1977). Ice Nuclei in Seawater, Fog Water and Marine Air off the Coast of Nova Scotia: Summer 1975. *Journal of Atmospheric Sciences*, 34:1299–1305.

Schrod, J., Kleinhenz, D., Hörhold, M., Erhardt, T., Richter, S., Wilhelms, F., Fischer, H., Ebert, M., Twarloh, B., Della Lunga, D., Jensen, C. M., Curtius, J., and Bingemer, H. G. (2020). Ice-nucleating particle concentrations of the past: Insights from a 600-year-old Greenland ice core. *Atmospheric Chemistry and Physics*, 20(21):12459–12482.

Schroth, A. W., Crusius, J., Gassó, S., Moy, C. M., Buck, N. J., Resing, J. A., and Campbell, R. W. (2017). Atmospheric deposition of glacial iron in the Gulf of Alaska impacted by the position of the Aleutian Low. *Geophysical Research Letters*, 44(10):5053–5061.

Seibert, P. and Frank, A. (2004). Source-receptor matrix calculation with a Lagrangian particle dispersion model in backward mode. *Atmospheric Chemistry and Physics*, 4(1):51–63.

Shi, Y., Liu, X., Wu, M., Zhao, X., Ke, Z., and Brown, H. (2022). Relative importance of high-latitude local and long-range-transported dust for Arctic ice-nucleating particles and impacts on Arctic mixed-phase clouds. *Atmospheric Chemistry and Physics*, 22(4):2909–2935.

Shupe, M. (2020). Millimeter Cloud Radar measurements taken at Summit Station, Greenland, 2019.

Shupe, M. D. (2011). Clouds at Arctic Atmospheric Observatories. Part II: Thermodynamic Phase Characteristics. *Journal of Applied Meteorology and Climatology*, 50(3):645–661.

Shupe, M. D., Daniel, J. S., de Boer, G., Eloranta, E. W., Kollias, P., Long, C. N., Luke, E. P., Turner, D. D., and Verlinde, J. (2008a). A Focus On Mixed-Phase Clouds: The Status of Ground-Based Observational Methods. *Bulletin of the American Meteorological Society*, 89(10):1549–1562.

Shupe, M. D. and Intrieri, J. M. (2004). Cloud Radiative Forcing of the Arctic Surface: The Influence of Cloud Properties, Surface Albedo, and Solar Zenith Angle. *Journal of Climate*, 17(3):616–628.

Shupe, M. D., Kollias, P., Matrosov, S. Y., and Schneider, T. L. (2004). Deriving Mixed-Phase Cloud Properties from Doppler Radar Spectra. *Journal of Atmospheric and Oceanic Technology*, 21(4):660–670.

Shupe, M. D., Kollias, P., Poellot, M., and Eloranta, E. (2008b). On Deriving Vertical Air Motions from Cloud Radar Doppler Spectra. *Journal of Atmospheric and Oceanic Technology*, 25(4):547–557.

Shupe, M. D., Turner, D. D., Walden, V. P., Bennartz, R., Cadeddu, M. P., Castellani, B. B., Cox, C. J., Hudak, D. R., Kulie, M. S., Miller, N. B., Neely, R. R., Neff, W. D., and Rowe, P. M. (2013). High and dry: New observations of tropospheric and cloud properties above the greenland ice sheet. *Bulletin of the American Meteorological Society*, 94(2):169–186.

Shupe, M. D., Uttal, T., and Matrosov, S. Y. (2005). Arctic Cloud Microphysics Retrievals from Surface-Based Remote Sensors at SHEBA. *Journal of Applied Meteorology and Climatology*, 44(10):1544–1562.

Si, M., Evoy, E., Yun, J., Xi, Y., Hanna, S. J., Chivulescu, A., Rawlings, K., Veber, D., Platt, A., Kunkel, D., Hoor, P., Sharma, S., Richard Leaitch, W., Bertram, A. K., Leaitch, W. R., and Bertram, A. K. (2019). Concentrations, composition, and sources of ice-nucleating particles in the Canadian High Arctic during spring 2016. *Atmospheric Chemistry and Physics*, 19(5):3007–3024.

Slater, T., Hogg, A. E., and Mottram, R. (2020). Ice-sheet losses track high-end sea-level rise projections. *Nature Climate Change*, 10(10):879–881.

Small, J. D., Chuang, P. Y., Feingold, G., and Jiang, H. (2009). Can aerosol decrease cloud lifetime? *Geophysical Research Letters*, 36(16).

Sotiropoulou, G., Ickes, L., Nenes, A., and Ekman, A. M. L. (2021). Ice multiplication from ice–ice collisions in the high Arctic: Sensitivity to ice habit, rimed fraction, ice type and uncertainties in the numerical description of the process. *Atmospheric Chemistry and Physics*, 21(12):9741–9760.

Sotiropoulou, G., Sedlar, J., Forbes, R., and Tjernström, M. (2016). Summer Arctic clouds in the ECMWF forecast model: An evaluation of cloud parametrization schemes. *Quarterly Journal of the Royal Meteorological Society*, 142(694):387–400.

Sourdeval, O., Gryspeerdt, E., Krämer, M., Goren, T., Delanoë, J., Afchine, A., Hemmer, F., and Quaas, J. (2018). Ice crystal number concentration estimates from lidar–radar satellite remote sensing – Part 1: Method and evaluation. *Atmospheric Chemistry and Physics*, 18(19):14327–14350.

Stephens, G. L., Vane, D. G., Boain, R. J., Mace, G. G., Sassen, K., Wang, Z., Illingworth, A. J., O'connor, E. J., Rossow, W. B., Durden, S. L., Miller, S. D., Austin, R. T., Benedetti, A., and Mitrescu, C. (2002). THE CLOUDSAT MISSION AND THE A-TRAIN: A New Dimension of Space-Based Observations of Clouds and Precipitation. *Bulletin of the American Meteorological Society*, 83(12):1771–1790.

Stetzer, O., Baschek, B., Lüönd, F., and Lohmann, U. (2008). The Zurich Ice Nucleation Chamber (ZINC) - A new instrument to investigate atmospheric ice formation. *Aerosol Science and Technology*, 42(1):64–74.

Stohl, A. (2006). Characteristics of atmospheric transport into the Arctic troposphere. *Journal of Geophysical Research*, 111(D11):D11306.

Stohl, A., Sodemann, H., Eckhardt, S., Frank, A., Seibert, P., and Wotawa, G. (2011). The Lagrangian particle dispersion model FLEXPART The Lagrangian particle dispersion model FLEXPART version 8.2. *FLEXPART user guide, url: http://zardoz. nilu. no/flexpart/flexpart/flexpart82. pdf (March 14, 2012)*.

Storelvmo, T. and Tan, I. (2015). The Wegener-Bergeron-Findeisen process-Its discovery and vital importance for weather and climate. *Meteorologische Zeitschrift*.

Storelvmo, T., Tan, I., and Korolev, A. V. (2015). Cloud Phase Changes Induced by CO2 Warming—a Powerful yet Poorly Constrained Cloud-Climate Feedback. *Current Climate Change Reports*, 1(4):288–296.

Sullivan, S. C., Hoose, C., Kiselev, A., Leisner, T., and Nenes, A. (2018). Initiation of secondary ice production in clouds. *Atmospheric Chemistry and Physics*, 18(3):1593–1610.

Sun, Z. and Shine, K. P. (1994). Studies of the radiative properties of ice and mixed-phase clouds. *Quarterly Journal of the Royal Meteorological Society*, 120(515):111–137.

Sze, K. C. H., Wex, H., Hartmann, M., Skov, H., Massling, A., Villanueva, D., and Stratmann, F. (2023). Ice-nucleating particles in northern Greenland: Annual cycles, biological contribution and parameterizations. *Atmospheric Chemistry and Physics*, 23(8):4741–4761.

Takahashi, T., Nagao, Y., and Kushiyama, Y. (1995). Possible High Ice Particle Production during Graupel–Graupel Collisions. *Journal of the Atmospheric Sciences*, 52(24):4523–4527.

Tan, I. and Storelvmo, T. (2019). Evidence of Strong Contributions From Mixed-Phase Clouds to Arctic Climate Change. *Geophysical Research Letters*, 46(5):2894–2902.

Tan, I., Storelvmo, T., and Zelinka, M. D. (2016). Observational constraints on mixed-phase clouds imply higher climate sensitivity. *Science*, 352(6282):224–7.

Tarr, R. S. and Martin, L. (1913). Glacial deposits of the continental type in Alaska. *The Journal of Geology*, 21(4):289–300.

Tatzelt, C., Henning, S., Welti, A., Baccarini, A., Hartmann, M., Gysel-Beer, M., van Pinxteren, M., Modini, R. L., Schmale, J., Stratmann, F., and Henning silviahenning, S. (2022). Circum-Antarctic abundance and properties of CCN and INPs. *Atmospheric Chemistry and Physics*, 22:9721–9745.

Taylor, J. W., Choularton, T. W., Blyth, A. M., Liu, Z., Bower, K. N., Crosier, J., Gallagher, M. W., Williams, P. I., Dorsey, J. R., Flynn, M. J., Bennett, L. J., Huang, Y., French, J., Korolev, A., and Brown, P. R. A. (2016). Observations of cloud microphysics and ice formation during COPE. *Atmospheric Chemistry and Physics*, 16(2):799–826.

Tian, P., Liu, D., Bi, K., Huang, M., Wu, Y., Hu, K., Li, R., He, H., Ding, D., Hu, Y., Liu, Q., Zhao, D., Qiu, Y., Kong, S., and Xue, H. (2022). Evidence for Anthropogenic Organic Aerosols Contributing to Ice Nucleation. *Geophysical Research Letters*, 49(17):e2022GL099990.

Tobo, Y., Adachi, K., Demott, P. J., Hill, T. C. J., Hamilton, D. S., Mahowald, N. M., Nagatsuka, N., Ohata, S., Uetake, J., Kondo, Y., and Koike, M. (2019). Glacially sourced dust as a potentially significant source of ice nucleating particles. *Nature Geoscience*, 12.

Tobo, Y., Prenni, A. J., DeMott, P. J., Huffman, J. A., McCluskey, C. S., Tian, G., Pöhlker, C., Pöschl, U., and Kreidenweis, S. M. (2013). Biological aerosol particles as a key determinant of ice nuclei populations in a forest ecosystem. *Journal of Geophysical Research: Atmospheres*, 118(17):10,100–10,110.

Tunved, P., Nilsson, E. D., Hansson, H.-C., Ström, J., Kulmala, M., Aalto, P., and Viisanen, Y. (2005). Aerosol characteristics of air masses in northern Europe: Influences of location, transport, sinks, and sources. *Journal of Geophysical Research: Atmospheres*, 110(D7).

Turner, D. D. and Blumberg, W. G. (2019). Improvements to the AERIoe Thermodynamic Profile Retrieval Algorithm. *IEEE Journal of Selected Topics in Applied Earth Observations and Remote Sensing*, 12(5):1339–1354.

Turner, D. D. and Löhnert, U. (2014). Information Content and Uncertainties in Thermodynamic Profiles and Liquid Cloud Properties Retrieved from the Ground-Based Atmospheric Emitted Radiance Interferometer (AERI). *Journal of Applied Meteorology and Climatology*, 53(3):752–771.

Twomey, S. (1977). The Influence of Pollution on the Shortwave Albedo of Clouds. *Journal of the Atmospheric Sciences*, 34(7):1149–1152.

UNCCD (2022). Sand and Dust Storms Source Base-map Visualization Tool. https://maps.unccd.int/sds/.

Vali, G. (1971). Quantitative Evaluation of Experimental Results an the Heterogeneous Freezing Nucleation of Supercooled Liquids. *Journal of the Atmospheric Sciences*, 28(3):402–409.

Vali, G. (1996). Ice Nucleation — a review. *Nucleation and Atmospheric Aerosols*, pages 271–279.

Vali, G. (2014). Interpretation of freezing nucleation experiments: Singular and stochastic; sites and surfaces. *Atmospheric Chemistry and Physics*, 14(11):5271–5294.

Vali, G. (2019). Revisiting the differential freezing nucleus spectra derived from drop-freezing experiments: Methods of calculation, applications, and confidence limits. *Atmospheric Measurement Techniques*, 12(2):1219–1231.

Vali, G., DeMott, P. J., Möhler, O., and Whale, T. F. (2015). Technical Note: A proposal for ice nucleation terminology. *Atmospheric Chemistry and Physics*, 15(18):10263–10270.

van den Broeke, M., Bamber, J., Ettema, J., Rignot, E., Schrama, E., van de Berg, W. J., van Meijgaard, E., Velicogna, I., and Wouters, B. (2009). Partitioning Recent Greenland Mass Loss. *Science*, 326(5955):984–986.

van den Broeke, M. R., Enderlin, E. M., Howat, I. M., Kuipers Munneke, P., Noël, B. P. Y., van de Berg, W. J., van Meijgaard, E., and Wouters, B. (2016). On the recent contribution of the Greenland ice sheet to sea level change. *The Cryosphere*, 10(5):1933–1946.

Van Tricht, K., Lhermitte, S., Lenaerts, J. T. M., Gorodetskaya, I. V., L'Ecuyer, T. S., Noël, B., van den Broeke, M. R., Turner, D. D., and van Lipzig, N. P. M. (2016). Clouds enhance Greenland ice sheet meltwater runoff. *Nature Communications*, 7(1):10266.

Vassel, M., Ickes, L., Maturilli, M., and Hoose, C. (2019). Classification of Arctic multilayer clouds using radiosonde and radar data in Svalbard. *Atmospheric Chemistry and Physics*, 19(7):5111–5126.

Vergara-Temprado, J., Miltenberger, A. K., Furtado, K., Grosvenor, D. P., Shipway, B. J., Hill, A. A., Wilkinson, J. M., Field, P. R., Murray, B. J., and Carslaw, K. S. (2018). Strong control of Southern Ocean cloud reflectivity by ice-nucleating particles. *Proceedings of the National Academy of Sciences*, 115(11):2687–2692.

Vergara-Temprado, J., Murray, B. J., Wilson, T. W., O'Sullivan, D., Browse, J., Pringle, K. J., Ardon-Dryer, K., Bertram, A. K., Burrows, S. M., Ceburnis, D., Demott, P. J., Mason, R. H., O'Dowd, C. D., Rinaldi, M., Carslaw, K. S., Browse, J., Pringle, K. J., Ardon-Dryer, K., Bertram,

A. K., Burrows, S. M., Ceburnis, D., Demott, P. J., Mason, R. H., Rinaldi, M., and Carslaw, K. S. (2017). Contribution of feldspar and marine organic aerosols to global ice nucleating particle concentrations. *Atmospheric Chemistry and Physics*, 17(5):3637–3658.

Volmer, M. and Weber, A. Z. (1926). Nucleus Formation in Supersaturated Systems. *Zeitschrift für Physikalische Chemie*, 119:277–301.

von der Weiden, S.-L., Drewnick, F., and Borrmann, S. (2009). Particle Loss Calculator – a new software tool for the assessment of the performance of aerosol inlet systems. *Atmospheric Measurement Techniques*, 2(2):479–494.

Wagner, R., Kiselev, A., Möhler, O., Saathoff, H., and Steinke, I. (2016). Pre-activation of ice-nucleating particles by the pore condensation and freezing mechanism. *Atmospheric Chemistry and Physics*, 16(4):2025–2042.

Welti, A., Bigg, E. K., DeMott, P. J., Gong, X., Hartmann, M., Harvey, M., Henning, S., Herenz, P., Hill, T. C. J., Hornblow, B., Leck, C., Löffler, M., McCluskey, C. S., Rauker, A. M., Schmale, J., Tatzelt, C., van Pinxteren, M., and Stratmann, F. (2020). Ship-based measurements of ice nuclei concentrations over the Arctic, Atlantic, Pacific and Southern oceans. *Atmospheric Chemistry and Physics*, 20(23):15191–15206.

Welti, A., Lüönd, F., Kanji, Z. A., Stetzer, O., and Lohmann, U. (2012). Time dependence of immersion freezing: An experimental study on size selected kaolinite particles. *Atmospheric Chemistry and Physics*, 12(20):9893–9907.

Westbrook, C. D. and Illingworth, A. J. (2013). The formation of ice in a long-lived supercooled layer cloud. *Quarterly Journal of the Royal Meteorological Society*, 139(677):2209–2221.

Wex, H., Huang, L., Zhang, W., Hung, H., Traversi, R., Becagli, S., Sheesley, R. J., Moffett, C. E., Barrett, T. E., Bossi, R., Skov, H., Hünerbein, A., Lubitz, J., Löffler, M., Linke, O., Hartmann, M., Herenz, P., and Stratmann, F. (2019). Annual variability of ice-nucleating particle concentrations at different Arctic locations. *Atmospheric Chemistry and Physics*, 19(7):5293–5311.

Whale, T. F., Holden, M. A., Wilson, T. W., O'Sullivan, D., and Murray, B. J. (2018). The enhancement and suppression of immersion mode heterogeneous ice-nucleation by solutes. *Chemical Science*, 9(17):4142–4151.

Whale, T. F., Murray, B. J., Sullivan, D., Wilson, T. W., Umo, N. S., Baustian, K. J., Atkinson, J. D., Workneh, D. A., Morris, G. J., O'Sullivan, D., Wilson, T. W., Umo, N. S., Baustian, K. J., Atkinson, J. D., Workneh, D. A., and Morris, G. J. (2015). A technique for quantifying heterogeneous ice nucleation in microlitre supercooled water droplets. *Atmospheric Measurement Techniques*, 8(6):2437–2447.

Widener, KB. and Johnson, K. (2005). Millimeter Wave Cloud Radar (MMCR) Handbook. Technical Report DOE/SC-ARM-TR-018, 948372.

Wieder, J., Ihn, N., Mignani, C., Haarig, M., Bühl, J., Seifert, P., Engelmann, R., Ramelli, F., Kanji, Z. A., Lohmann, U., and Henneberger, J. (2022). Retrieving ice-nucleating particle concentration and ice multiplication factors using active remote sensing validated by in situ observations. *Atmospheric Chemistry and Physics*, 22(15):9767–9797.

Wilson, T. W., Ladino, L. A., Alpert, P. A., Breckels, M. N., Brooks, I. M., Browse, J., Burrows, S. M., Carslaw, K. S., Huffman, J. A., Judd, C., Kilthau, W. P., Mason, R. H., McFiggans, G., Miller, L. A., Najera, J. J., Polishchuk, E., Rae, S., Schiller, C. L., Si, M., Temprado, J. V. J. V., Whale, T. F., Wong, J. P. S., Wurl, O., Yakobi-Hancock, J. D., Abbatt, J. P. D., Aller, J. Y., Bertram, A. K., Knopf, D. A., Murray, B. J., Nájera, J. J., Polishchuk, E., Rae, S., Schiller, C. L., Si, M., Temprado, J. V. J. V., Whale, T. F., Wong, J. P. S., Wurl, O., Yakobi-Hancock, J. D., Abbatt, J. P. D., Aller, J. Y., Bertram, A. K., Knopf, D. A., and Murray, B. J. (2015). A marine biogenic source of atmospheric ice-nucleating particles. *Nature*, 525(7568):234–238.

Winker, D. M., Pelon, J., Coakley, J. A., Ackerman, S. A., Charlson, R. J., Colarco, P. R., Flamant, P., Fu, Q., Hoff, R. M., Kittaka, C., Kubar, T. L., Treut, H. L., Mccormick, M. P., Mégie, G., Poole, L., Powell, K., Trepte, C., Vaughan, M. A., and Wielicki, B. A. (2010). The CALIPSO Mission: A Global 3D View of Aerosols and Clouds. *Bulletin of the American Meteorological Society*, 91(9):1211–1230.

Xi, Y., Xu, C., Downey, A., Stevens, R., Bachelder, J. O., King, J., Hayes, P. L., and Bertram, A. K. (2022). Ice nucleating properties of airborne dust from an actively retreating glacier in Yukon, Canada. *Environmental Science: Atmospheres*.

Young, G., Jones, H. M., Darbyshire, E., Baustian, K. J., McQuaid, J. B., Bower, K. N., Connolly, P. J., Gallagher, M. W., and Choularton, T. W. (2016). Size-segregated compositional analysis of aerosol particles collected in the European Arctic during the ACCACIA campaign. *Atmospheric Chemistry and Physics*, 16(6):4063–4079.

Zhao, X. and Liu, X. (2022). Primary and secondary ice production: Interactions and their relative importance. *Atmospheric Chemistry and Physics*, 22(4):2585–2600.

A

Appendix to Chapter 2

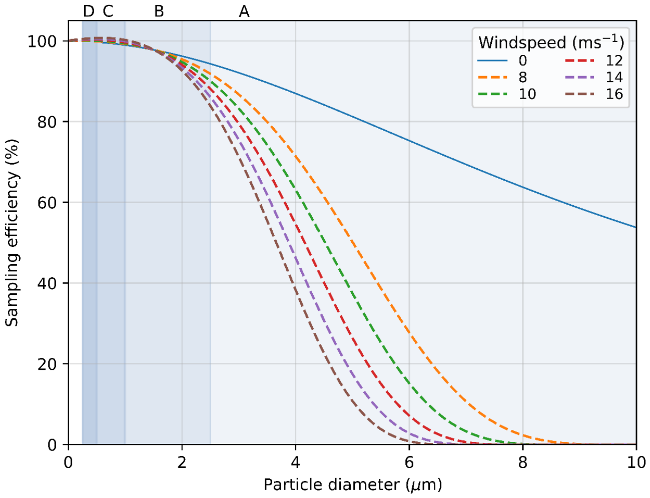

Fig. A.1.: Sampling efficiency of the impactor at different wind speeds. Shaded regions represent the different size bins of the impactor (A: > 2.5 μm, B: 1-2. μm, C: 0.5-1 μm, D: 0.25-0.5 μm)

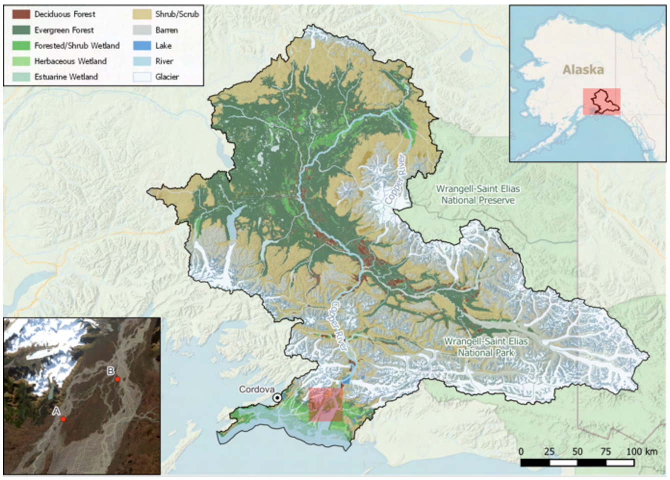

Fig. A.2.: Map of the Copper River watershed showing vegetation types. Land cover data from U.S. Geological Survey National Land Cover Database (NLCD), geospatial data such as waterways, boundaries and National Parks from State of Alaska Open Data Geoportal, background map from MapTiler and OpenStreetMap, lower left inset derived from Landsat 8 Collection 2 Tier 1 calibrated top-of-atmosphere (TOA) reflectance

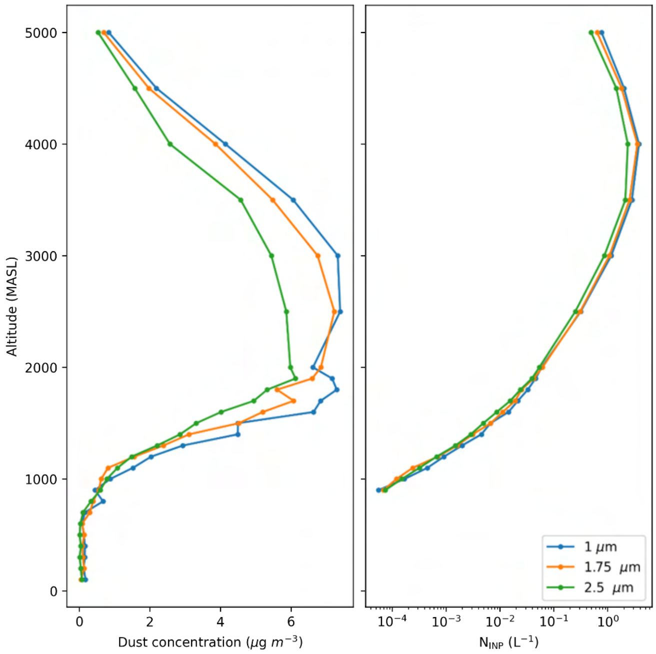

Fig. A.3.: Comparison of modelled dust concentration and N_{INP} with varying mean particle size in 10 day FLEXPART simulations starting on 14th October 2019. All model parameters are the same as for runs presented in the main body of the paper, including a total emitted mass of 15 kt.

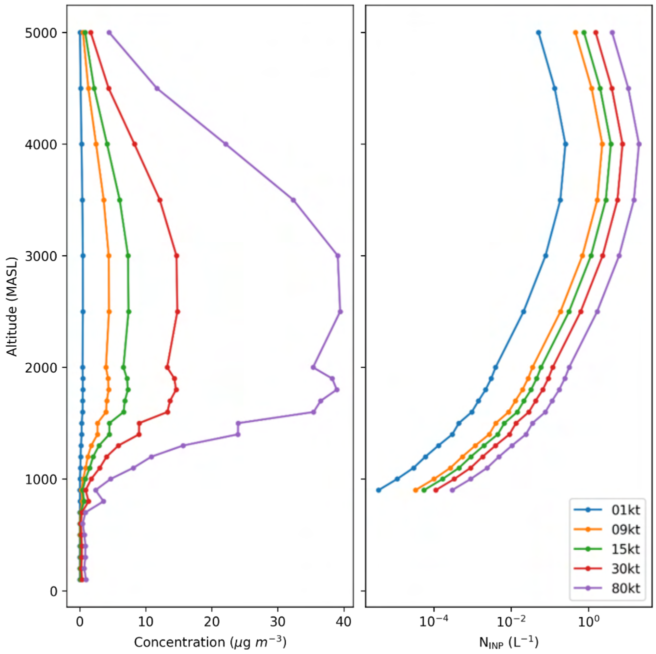

Fig. A.4.: Comparison of modelled dust concentration and N_{INP} with varying initial dust emissions mass in 10-day FLEXPART simulations starting on 14th October 2019. All model parameters are the same as model runs presented in the main body of the paper, including a mean particle size of 1 μm.

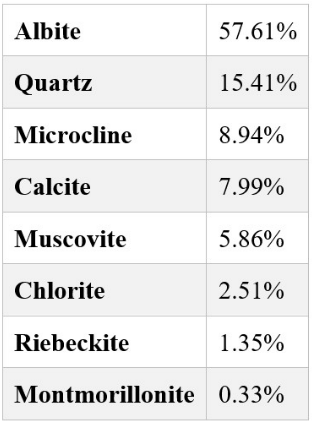

Albite	57.61%
Quartz	15.41%
Microcline	8.94%
Calcite	7.99%
Muscovite	5.86%
Chlorite	2.51%
Riebeckite	1.35%
Montmorillonite	0.33%

Fig. A.5.: Results of X-Ray diffraction on 45 μm surface samples showing the percentage of each mineral in the sample determined using Total Pattern Analysis Solutions (TOPAS) analysis of Rietveld refinement of powder X-ray diffraction (XRD) patterns

B

Background subtraction

Raw data from INP droplet freezing experiments needs to go through multiple steps to finally arrive at a usable INP concentration, one part of this is background subtraction. This is where the background INP activity, determined from handling blanks, is removed from the sample data. This appendix includes details of this process, adapted from an instructional jupyter notebook available on my GitHub. The steps involved are explained using three experiments from one sample and handling blanks collected at Summit Station, Greenland as an example.

1. Prepare sample data

The raw data contains a record of the temperature at which each droplet in the experiment froze, which can be expressed in terms of the fraction of frozen drops at each temperature ($f_{ice}(T)$):

$$f(T) = 1 - \frac{N(T)}{N_{tot}} \tag{B.1}$$

where $N(T)$ is the number of unfrozen droplets at temperature T, N_{tot} is the total number of droplets.

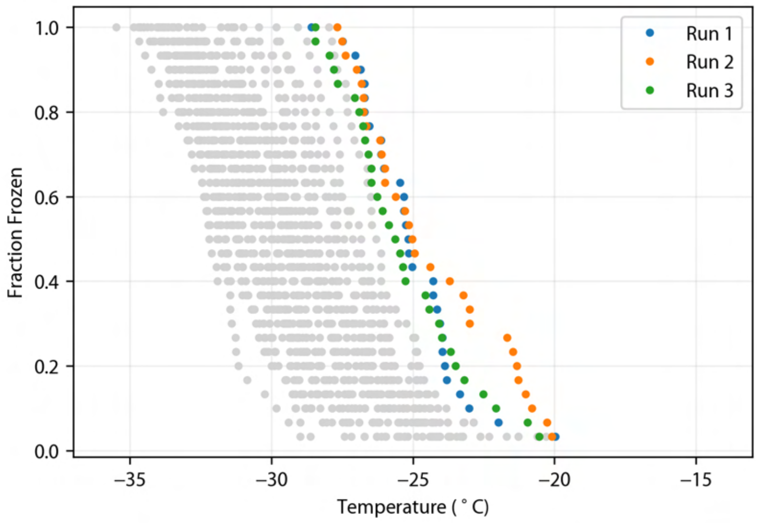

Fig. B.1.: Fraction frozen for three repeat experiments for one sample and all handling blanks (in grey)

1.1 Bin data and combine repeat runs

In order to do the background subtraction we need all the data to be in the same temperature bins. The temperature interval is chosen based on the dataset such that there are not too many bins with 0 counts, but not a huge number of counts in the bins (Vali, 2019). In this case, temperature bins of 1°C are used.

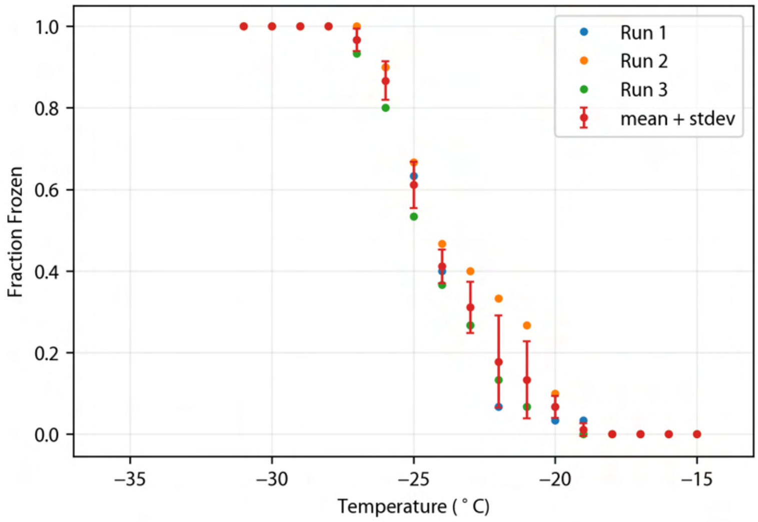

Fig. B.2.: Fraction frozen after data has been binned into 1°C temperature bins. The mean and standard deviation is determined by calculating the mean and standard deviation of the number of freezing events in each bin.

1.2 Calculate the differential nucleus spectrum ($k(T)$)

Next, we need to calculate $k(T)$. This value represents the differential nucleus spectrum; the number of sites active within the interval T to $T + \Delta T$. This is different to $K(T)$ which is the cumulative nucleus spectrum. Most INP data is shown in the cumulative space however in order to compare samples to the background you need to compare $k(T)$ at each temperature interval and subtract the background from this, rather than from the cumulative $K(T)$. Figure 4 in Vali (2019) gives a good example of why we use $k(T)$ and not $K(T)$. $k(T)$ is given by the following equation:

$$k(T) = -\frac{1}{V_d \cdot \Delta T} \cdot \ln \left(1 - \frac{\Delta N}{N(T + \Delta T)}\right) \tag{B.2}$$

where V_d is the droplet volume, ΔT is the width of the temperature bins, ΔN is the number of droplets that froze in that temperature bin and N is the total number of droplets unfrozen at temperature $T + \Delta T$.

1.3 Calculating errors

a) Samples with repeat experiments

When samples are in suspension it is common to do multiple μL-NIPI experiments for each sample. For example, in the analysis for Chapters 2 and 3 of this thesis, experiments were repeated three times. To combine them, the mean counts are calculated in each temperature bin and the mean is used to calculate a mean $k(T)$. The variability associated with these runs is then represented by the standard deviation of the counts ($\sigma_{\Delta N}$) and used to calculate the error in $k(T)$ ($\sigma_{k(T)}$):

$$\sigma^2_{k(T)} = \left[\frac{1}{V_d \Delta T} \cdot \frac{1}{N(T+\Delta T) - \Delta N_T}\right]^2 \sigma^2_{\Delta N_T} \tag{B.3}$$

b) Samples without repeat experiment

In some cases, such as when using the droplet-on-filter technique, the experiments can only be done once. This means error bars cannot be represented using a standard deviation of the measurements. Instead, $\sigma_{\Delta N}$ is calculated based on the fact that the number of freezing events per temperature interval is discrete and independent of the other intervals and so should be expected to follow a Poisson distribution. A Poisson distribution is calculated like so:

$$P(x, \lambda) = \frac{\lambda^x e^{-\lambda}}{x!} \tag{B.4}$$

where x is the number of occurrences, λ is the expected number of occurrences, e is Euler's number and ! is the factorial function. By using observed counts in each interval, ΔN, as the expected value, λ, we can generate a range of Poisson distributed numbers for each temperature interval. The standard deviation of these values is then $\sigma_{\Delta N}$ used in Eq. B.3 to calculate $\sigma_{k(T)}$

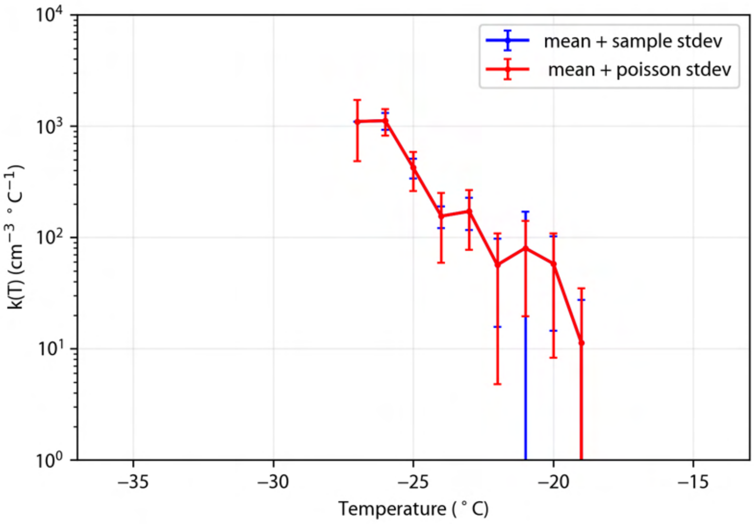

Fig. B.3.: Mean differential spectrum ($k(T)$) for the three experiments, with errors bars representing the standard deviation of the experiments (blue) and calculated based on a Poisson distribution of counts (red)

2. Prepare background data

2.1 Bin handling blank data and calculate background $k(T)$

In order to compare our sample data to the handling blanks we need an 'average' background. To calculate this we bin the handling blank data into the same temperature intervals as the sample data, then calculate the mean counts and standard deviation counts of all the handling blanks and finally calculate the mean $k(T)$ of the handling blanks.

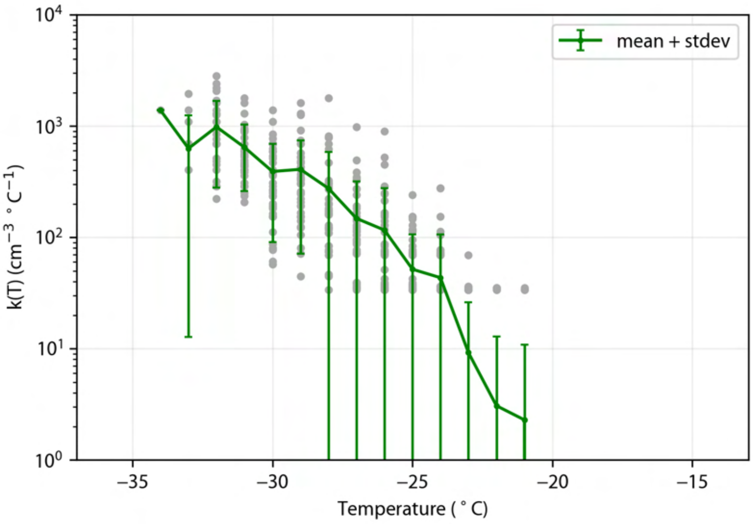

Fig. B.4.: Mean $k(T)$ for all handling blanks. Error bars represent the standard deviation

3. Background subtraction and INP calculation

3.1 Subtract background from sample data

Next the mean background $k(T)$ values are subtracted from the mean sample $k(T)$ values to get our background subtracted, $k(T)_{sub}$, values:

$$k(T)_{sub} = \overline{k(T)}_{sample} - \overline{k(T)}_{bg} \tag{B.5}$$

Total error for $k(T)_{sub}$ is calculated by combining the sample standard deviation (or Poisson error) and the background standard deviation in quadrature:

$$\sigma_{tot} = \sqrt{\sigma^2_{sample} + \sigma^2_{bg}} \tag{B.6}$$

3.2 Calculate the cumulative spectrum ($K(T)$)

After the background subtraction has been applied, $k(T)_{sub}$ can be converted back to a cumulative value, $K(T)$. This is the cumulative spectrum, meaning the number of sites active above T per unit sample volume. There are a number of ways to calculate $K(T)$, including directly from $f_{ice}(T)$:

$$K(T) = -\frac{1}{V_d} \cdot \ln(1 - f(T)) \tag{B.7}$$

However, since we already have $k(T)$ we can simply perform a numerical integration:

$$K(T) = \sum_{0}^{T} k(T)_{sub} \cdot \Delta T \tag{B.8}$$

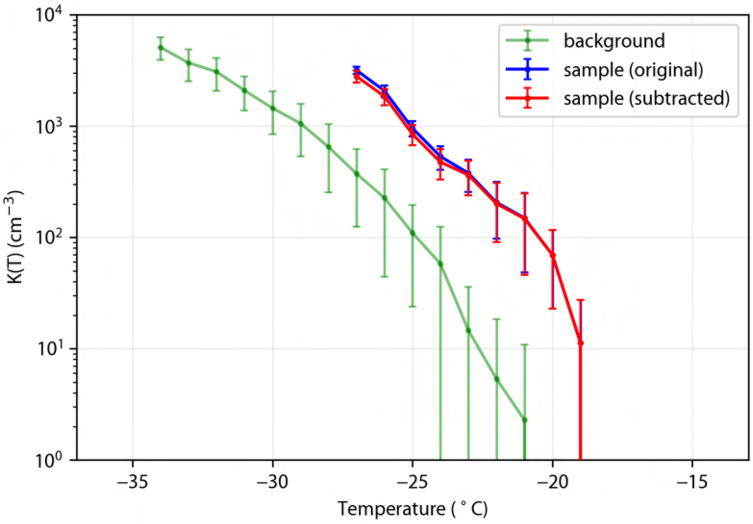

Fig. B.5.: Mean cumulative spectrum ($K(T)$) before (blue) and after (red) background subtraction

3.3. Calculate INP concentrations

Finally, INP concentrations are calculated.

3.3a wash-off samples

For samples prepared using the wash-off method (like at Summit), we use the following equation:

$$N_{\text{INP}}(T) = -\frac{\ln(1 - f(T))}{V_d} \cdot \frac{V_w}{V_a} \tag{B.9}$$

This can also be shown as:

$$N_{\text{INP}}(T) = K(T) \cdot \frac{V_w}{V_a} \tag{B.10}$$

where $N_{\text{INP}}(T)$ is the concentration of INPs at temperature T, V_w is the volume of water used to wash the samples from the filters and V_a is the volume of air sampled corrected to standard temperature and pressure.

3.3b Droplet-on-filter samples

For the drop-on method (e.g. for FAAM filter samples) the equation is:

$$N_{\text{INP}}(T) = K(T) \cdot \frac{V_d A_{fil}}{V_a \alpha} \tag{B.11}$$

Where V_d is the droplet volume, V_a is the volume of air sampled, A_{fil} is the area of filter exposed to aerosol particles (11 ± 2 cm^2) and α is the area of each droplet exposed to the filter (0.9 ± 0.1 mm^2 1 μ droplets).

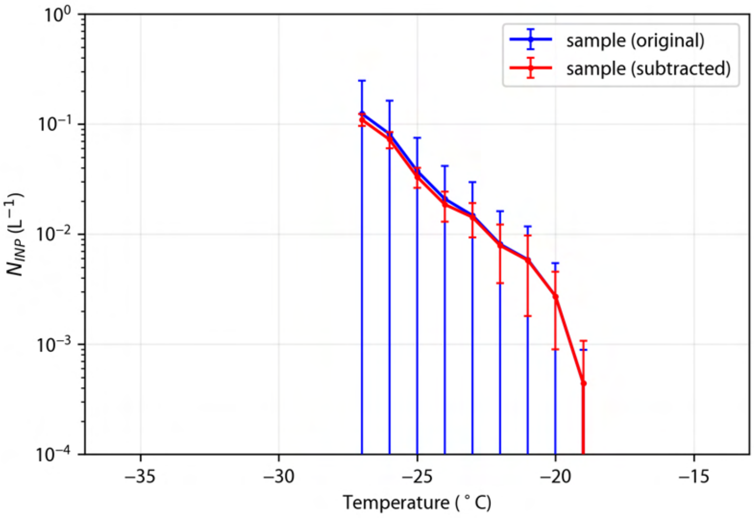

Fig. B.6.: Ice-nucleating particle concentration before (blue) and after (red) background subtraction.

In this example, there is only a very minor difference after the background subtraction has been applied because the data is well above the mean background. However, when the data is closer to the background there can be a larger difference. When the data falls entirely within the background, the data is consistent with a measurement of zero but the top of the error bars represents a possible upper limit, an example of this is shown in Fig. B.7.

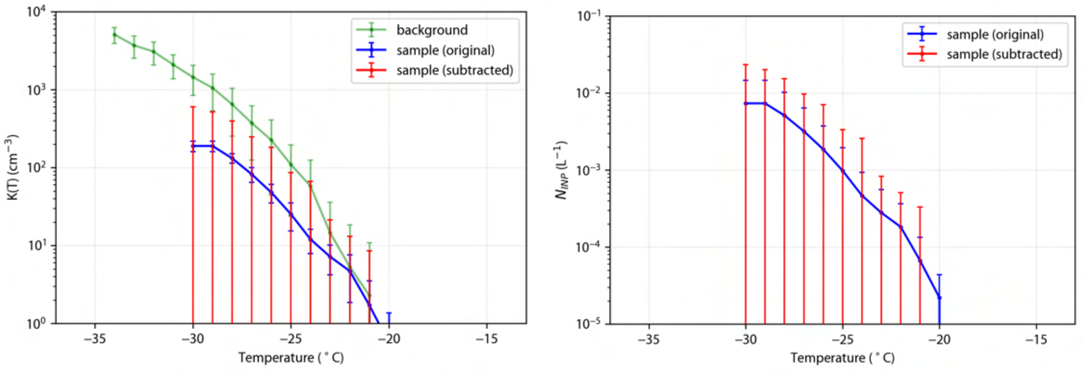

Fig. B.7.: $K(T)$ and N_{INP} before (blue) and after (red) background subtraction for a case where the data all falls below the mean background

C

Automatic droplet freezing detection

Previously, analysis of the video output of droplet freezing experiments as used in this thesis required significant manual input, each frame of the video was checked for freezing events and manually recorded with a mouse click. This is time-consuming and subject to human error, especially when there are a large number of droplets present and freezing events are easy to miss. Previous attempts to automatically analyse these videos had been unsuccessful, however, most of these used motion detection applied to the whole frame of the video to detect changes. This leads to incorrect detection of freezing events due to vibrations in the video, changes to lighting, frost formation on the cold stage and other potential movements. Additionally, freezing events are often missed due to the small change compared to variations in the whole frame. To solve this, I applied a different approach by first detecting the droplets in the frame and then using the change in pixel value within these droplets when freezing occurs to detect freezing events.

C.1 Droplet detection

A key step in the detection of freezing events is first being able to accurately detect droplets within the frame. To do this I used a circle hough transform, a feature extraction technique used in digital image processing to detect circles in images. The openCV python package was used to apply this technique (Bradski, 2000). In some cases, droplets were incorrectly detected and required manual correction. This was achieved by creating a graphical user interface (GUI), as shown in Fig. C.1, with the capability to manually add or remove droplets. The droplet detection threshold can also be adjusted, to account for the differences between the wash-off and droplet-on-filter techniques.

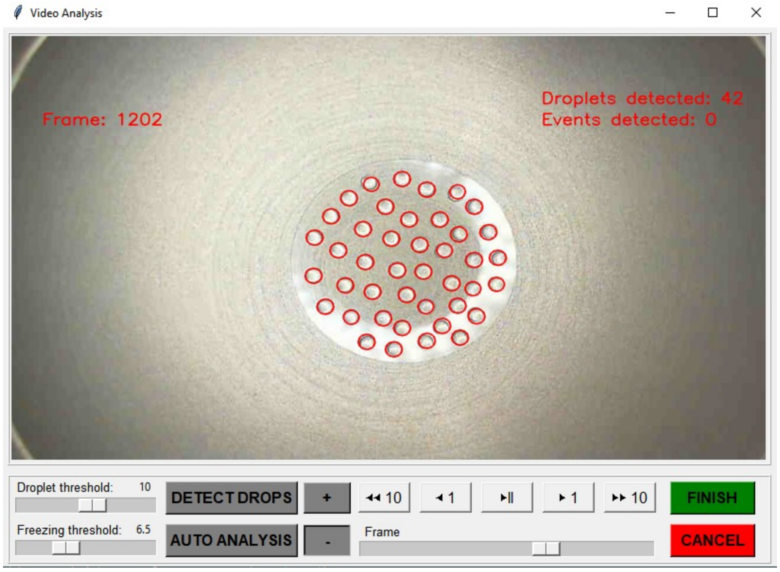

Frame: 1202

Droplets detected: 42
Events detected: 0

Droplet threshold: 10
Freezing threshold: 6.5

Fig. C.1.: Droplets detected and marked in red using graphical user interface for analysis of droplet freezing experiment videos

C.2 Freezing event detection

Once the droplets have been detected, methods to detect freezing can be applied to each droplet individually. In this case, we exploit the fact that droplets change colour as they freeze. First, the images are converted to grayscale images so that each pixel has a value between 0 and 255, where 0 is black and 255 is white. In experiments using the University of Leeds Microlitre by immersed particle instrument (μL-NIPI), droplets get darker when they freeze meaning the mean pixel value within the droplet reduces, as demonstrated in Figure C.2. This was implemented by calculating the mean pixel value in each droplet in each frame and then comparing it to the preceding frame. When the change from one frame to the next exceeds a certain threshold then a freezing event is recorded.

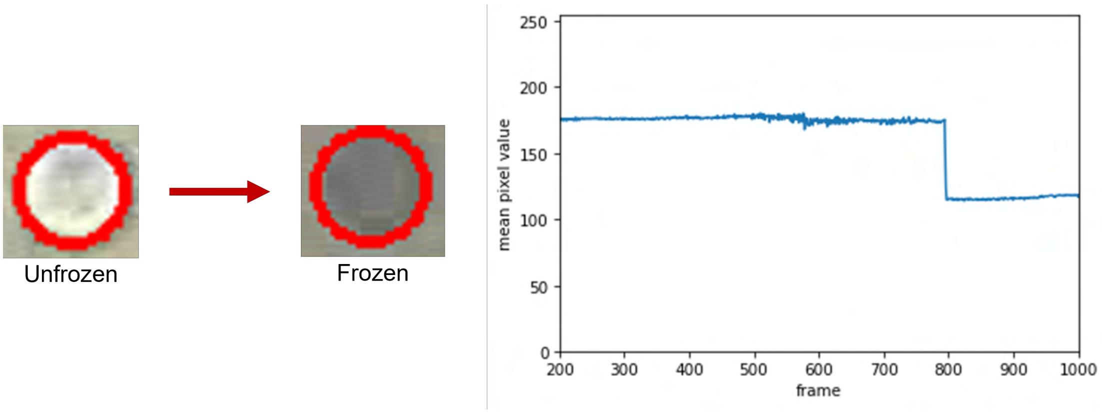

Fig. C.2.: Example of change in colour as a droplet freezes (left) and decrease in mean pixedl value (right)

To ensure that the event is not detected multiple times as the droplet fully freezes once a freezing event has been detected in a droplet it is no longer ‘watched’ by the programme. Once the frame in which each droplet freezes has been identified, the temperature of the cold stage at the time of each freezing event is retrieved from the cold stage temperature log which is recorded at the same time as the video. In the GUI, droplets are marked in blue (see Fig. C.3) once they have been detected as frozen so that incorrectly identified or missed events can be identified and manually corrected. However, this is rarely required; in a test of 20 experiments each containing approximately 50 droplets, 2 events were incorrectly identified. In addition, comparisons between the previous manual method and this automatic detection method show good agreement. An example of such a comparison is shown in Fig. C.4.

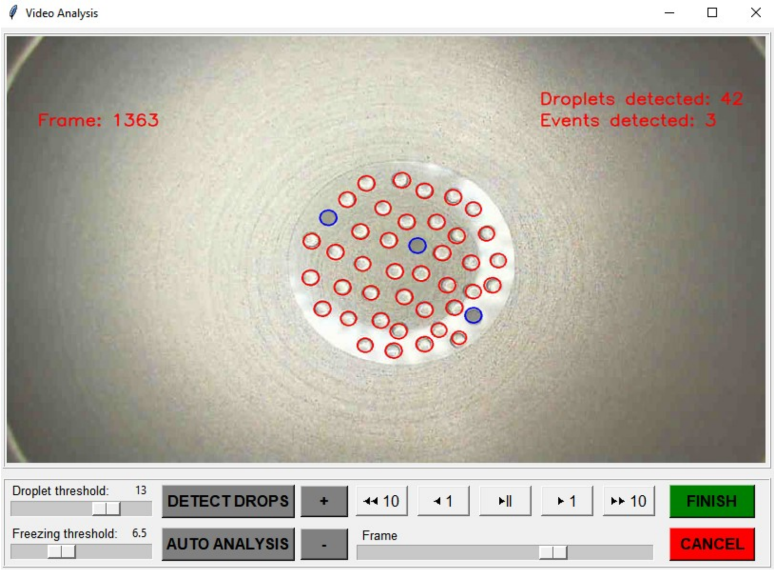

Frame: 1363

Droplets detected: 42

Events detected: 3

Droplet threshold: 13

Freezing threshold: 6.5

Fig. C.3.: Detected freezing events in blue during the automatic analysis of droplet freezing experiment video

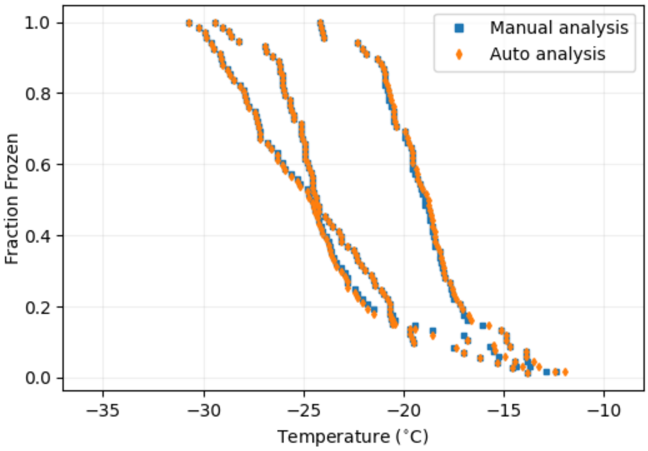

Fig. C.4.: Comparison of fraction frozen curves for videos analysed manually (blue) and using the automatic approach (orange)